Brunel University London

Structural Health Monitoring of High-temperature Pipelines using Piezoelectric Ultrasonic Guided Wave Transducers

Author:
Anurag DHUTTI

Supervisors:
Prof. T.H. GAN
Prof. W. BALACHANDRAN

A thesis submitted in fulfilment of the requirements
for the degree of Doctor of Philosophy

in the

Brunel Innovation Centre
Department of Electronic and Computer Engineering

April 21, 2024

Declaration of Authorship

I, Anurag DHUTTI, declare that this thesis titled, "Structural Health Monitoring of High-temperature Pipelines using Piezoelectric Ultrasonic Guided Wave Transducers" and the work presented in it are my own. I confirm that:

- This work was done wholly or mainly while in candidature for a research degree at this University.

- Where any part of this thesis has previously been submitted for a degree or any other qualification at this University or any other institution, this has been clearly stated.

- Where I have consulted the published work of others, this is always clearly attributed.

- Where I have quoted from the work of others, the source is always given. With the exception of such quotations, this thesis is entirely my own work.

- I have acknowledged all main sources of help.

- Where the thesis is based on work done by myself jointly with others, I have made clear exactly what was done by others and what I have contributed myself.

Signed:

Date: 21 April 2024

"Keep your face always toward the sunshine and shadows will fall behind you."

Rabindranath Tagore

BRUNEL UNIVERSITY LONDON

Abstract

College of Engineering, Design and Physical Sciences

Department of Electronic and Computer Engineering

Doctor of Philosophy

Structural Health Monitoring of High-temperature Pipelines using Piezoelectric Ultrasonic Guided Wave Transducers

by Anurag DHUTTI

This thesis focusses on the development of high temperature piezoelectric transducers for monitoring of pipes using fundamental torsional guided waves in the 20-100 kHz frequency range, with the ability to operate at temperatures up to 600°C. A combined numerical and experimental approach is employed to design, optimise, and characterise non-resonant transducers for high-temperature torsional operation. Additionally, the guided wave monitoring capabilities of an existing transducer system are demonstrated at temperatures up to 150°C. Thermal stability is evaluated through long-term experiments with simulated defects and field conditions in a power plant, achieving a defect sensitivity of 1% cross-sectional change with the proposed temperature compensation and defect detection approach. Multiphysics finite element models of the transducer are developed and verified, and the approach is applied to optimise the transducer design by eliminating undesired mode coupling. The findings are initially applied to a guided wave monitoring system for ambient temperatures. The modified bismuth titanate and gallium phosphate piezoelectric materials are then used to develop high-temperature transducers, which are characterised and verified for continuous operation at 350°C and 600°C. The results show promising ultrasonic performance, defect sensitivity, and stability for guided wave monitoring applications, enhancing confidence in the technique for use at higher operating temperatures.

Acknowledgements

First of all, I thank God for giving me the strength and intelligence to walk through this challenging endeavour. To my beloved parents, your constant support, love, and encouragement have been my pillars of strength. Thank you for believing in me, making sacrifices to support my journey that has made me the person I am today. I would like to thank my brother, Anuj Dhutti, for his constant support and motivation. To my omorfi partner, Vaso, for standing by my side, providing support, and more importantly, being patient throughout these years.

I am grateful to my supervisors, Prof. Wamadeva Balachandran (Bala) and Prof. Tat-Hean Gan, for offering me remarkable opportunities to delve into the world of ultrasonics and explore novel industrial applications. Their mentoring, guidance, and support have been pivotal throughout this journey to complete this thesis. Without their insightful discussions, review of this work, and encouragement, this achievement would not have been possible.

A special thanks goes to Abbas Mohimi, my first mentor, who kept me motivated and provided essential support from the beginning, laying the foundation for this work.

Many thanks to Borja Hernandez, Ashley Jolley, and the engineering staff at SSE and Tupras for their support in facilitating the guided wave monitoring trials. It was great to have the opportunity to experience the operational environment and gain a wider perspective.

I extend my gratitude to colleagues within the Brunel Innovation Centre (BIC), Plant Integrity (PI), TWI Ltd., including Alex Haig, Keith Thornicroft, Hugo Marques, Matthew Deere, Makis Livadas, Mario Kostan, Saiful Asmin Tumin, Shehan Lowe, Marco Zennaro, Marco Berchiolli, Muntasir Hashim, Shahroukh and many others, for their invaluable contributions, thoughtful discussions, camaraderie, and support. Your presence made my time at Brunel University and TWI an immensely rewarding experience.

Contents

List of Figures

List of Tables

Abbreviations

2D   Two Dimensional. 58
3D   Three Dimensional. 77

BAW   Bulk Acoustic Wave. 48
BSS   Baseline Signal Subtraction. 60

CSA   cross-sectional area. 4
CTE   Coefficient of thermal expansion. 53
CVD   Chemical vapor deposition. 53
CWT   Continuous Wavelet Transform. 40

DTW   Dyanamic Time Warping. 60
DWT   Discrete Wavelet Transform. 40

EMAT   Electromagnetic acoustic transducers. 5
EMI   Electromechanical Impedance. 21
EMIS   Electromechanical Impedance Spectroscopy. 10
EOC   Environmental and operational condition. 7

FEA   Finite Element Analysis. 2
FFT   Fast Fourier Transform. 39
FOM   Figure of Merit. 22

GWT   Guided wave testing. 4

HAZ   heat affected zone. 3
HT   High Temperature. 7
HTP   high temperature pipeline. 1

LDV   Laser Doppler Vibrometry. 77

NDT   Non-destructive testing. 4

O&M   operational and maintenance. 1
OBS   Optimum Baseline Selection. 59

PUT   Piezoelectric Ultrasonic Transducer. 8
PVD   Physical Vapor Deposition. 25
PWAS   Piezoelectric Wafer Active Sensor. 52

RMS   Root Mean Square. 39

SAFE   Semi-analytical finite element. 31
SAW   Surface Acoustic Wave. 47
SCC   stress corrosion cracking. 3
SCNR   Signal to Coherent Noise Ratio. 52
SHM   Structural health monitoring. 6
SLDV   Scanning Laser Doppler Vibrometry. 10
SNR   Signal to Noise Ratio. 28
STFT   Short-Time Fourier Transform. 39

TCF   Temperature coefficients of frequency. 158
TFR   Time-frequency response. 40
TOA   Time of Arrival. 35
TPP   thermal power plants. 1
TS   Thickness Shear. 73
TS-mode   Thickness-shear mode. 12

UGW   Ultrasonic guided wave. 5
UT   Ultrasonic testing. 4

List of Symbols

A	Signal amplitude	mV
A_D	Defect Signal Amplitude	mV
A_N	Noise Signal Amplitude	mV
$A_v(\omega)$	Signal amplitude as a function of angular frequency	V
C	Capacitance	F
d_{ij}	Piezoelectric Charge constant with $\vec{S}$ in i and $\vec{E}$ in j	C/N or m/V
D	Electric Displacement	m
$F(m,n)$	Flexural wave mode of mth order n family	-
g_{ij}	Piezoelectric voltage constant with $\vec{E}$ in i and $\vec{T}$ in j	Vm/N or m^2/C
GND	Ground	-
k_{ij}	Electromechanical coupling factor: $\vec{E}$ in i by applied $\vec{T}$ in j	-
K^T	Relative Dielectric Constant (at constant $\vec{T}$)	-
$L(0,n)$	Axially symmetric Torsional wave mode of nth order	-
μ	Poisson's ratio	-
ρ	Density	kg/m^3
$\vec{E}$	Electric Field Strength	N/C
$\vec{P}$	Direction of Polarisation	-
$\vec{S}$	Strain	m/m
$\vec{s}$	Elastic compliance	m/N
$\vec{s}$	Elastic stiffness	N/m^2
$\vec{T}$	Stress	N/m^2
t	Time	s
T	Temperature	°C
T_c	Curie Temperature	°C
$T(0,n)$	Axially symmetric Longitudinal wave mode of nth order	-
λ	Wavelength	m
ω	Angular Frequency	rad
f	Frequency	Hz
f_a	Anti-resonance frequency	Hz
f_r	Resonance frequency	Hz
k	Wave number	-
v_l	Longitudinal velocity	m s^{-1}
v_s	Shear velocity	m s^{-1}
E	Young's Modulus	GPa
ΔL_{shear}	Displacement of shear piezoelectric	m
ϵ_0^T	Permittivity of ceramic material (at constant $\vec{T}$)	F/m

Chapter 1

Introduction

1.1 Overview

The opening chapter of this thesis delves into the motivation behind the implementation of structural health monitoring for high-temperature pipelines. It assesses existing commercially available technologies, reviews their performance characteristics, and examines their limitations. It outlines the aims and specific objectives of the study and provides an overview of the research methodology used. It highlights the contributions of this study to existing knowledge, accompanied by a list of publications resulting from this research effort. An outline of the thesis is also provided to help the reader navigate the document.

1.2 Motivation for Research

Thermal power plants (TPP) operate with the energy produced by a heat source[1] and are critical to global energy supply, as they generate nearly 80% of global demand [1, 2]. The heat source generates high-temperature, high-pressure steam in the boiler that is channelled to the steam turbines using high temperature pipelines (HTPs) to produce electricity. There is strong motivation to improve plant efficiency to reduce CO_2 emissions and power production costs to remain competitive. This has led to higher process temperatures, pressures, and cyclic schedules. However, utilities are reducing operational and maintenance (O&M) costs by optimising inspection and maintenance procedures and deferring the replacement or maintenance of expensive components.

TPP with super-critical steam (24-25 MPa, 540-560°C) can achieve higher efficiency than subcritical power plants [3]. Efficiency can be further increased with ultra-supercritical (30 MPa, 600°C) TPP [4]. In the next decade (by 2030), other

---

[1]Heat source in the TPP are powered by coal, natural gas, oil, biomass or a nuclear reactor.

advanced ultra-supercritical TPP (35 MPa, 700°C) are expected to enter the operation and reach even higher efficiency [5]; however, a significant challenge lies in the limitations of the materials used under these conditions.

TPP includes several complex metallic structures, and during their operational lifetime, they are subjected to various degradation mechanisms. Damage to these metallic structures is inevitable and, when unnoticed, could result in catastrophic consequences. Each TPP has several kilometres of HTPs, including steam tubes, superheater tubes, headers, and steam transfer pipes. These pipes operate at temperatures up to 600°C and provide critical connections between the feed water pumps, the boiler or heat exchanger, and the turbine, as illustrated in Figure 1.1.

① Steam boiler ② Electrostatic ③ Combustion turbine ④ Alternator ⑤ Transformer ⑥ Condenser ⑦ Cooling tower
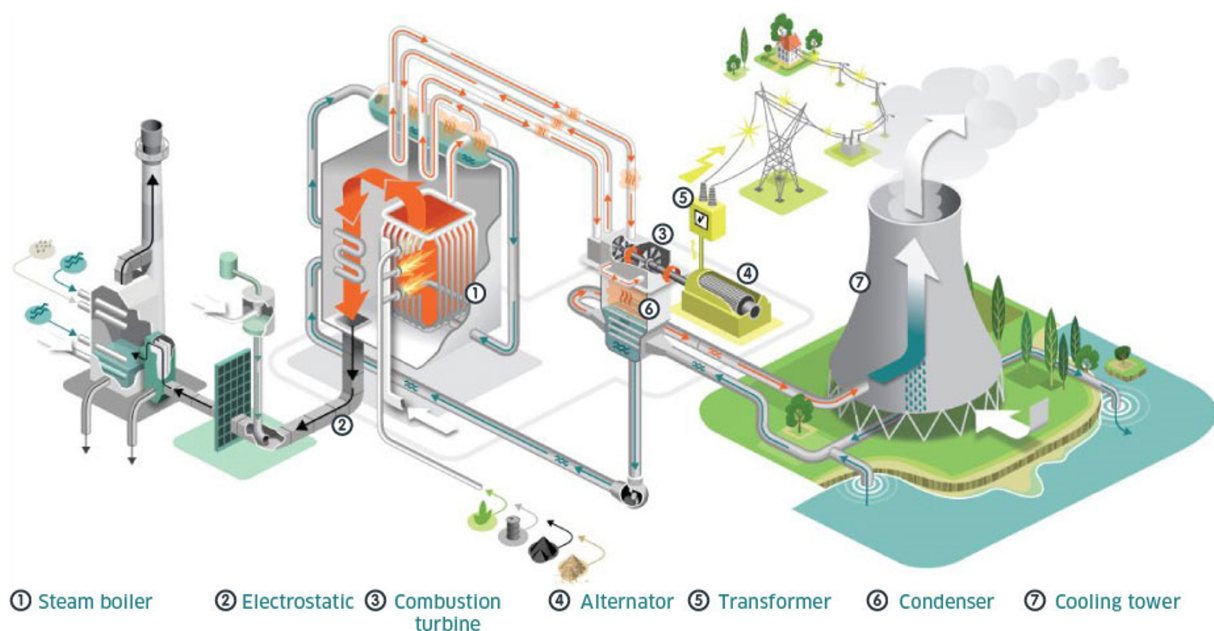
FIGURE 1.1: Thermal power plant operating with energy produced by a steam boiler, whereby the steam is transmitted through high-temperature pipelines and activates a turbine to drive an alternator generating electricity [6].

Similarly, in refineries, the temperature of the oil furnace outlet is 350-360°C. These HTPs are of particular concern, as they experience extreme temperatures and pressures and suffer continuous cyclic loading through vibrations experienced in operational conditions [7]. As a result, HTPs are known to develop defects through a variety of damage mechanisms, including creep, fatigue, creep fatigue, thermal fatigue, and corrosion [8, 9, 10, 11].

A Finite Element Analysis (FEA) study on damage analysis of a heat-resistant steel (10CrMo910) operating at 540°C with internal pressure of 9.8 MPa formulated the service life to be 34.2 years [12]. However, most TPPs have an average operating age of more than 30 years [13]. Many operators extend the lifetime beyond their original

design life to improve economic viability and increase profitability [14]. However, harsh operating conditions and the ageing infrastructure have increased the probability of failure which have severe consequences. The severity of failure depends on the content of the pipe (pressure, temperature, and toxicity) and the impact on production, health and safety, the environment, potential outages, and equipment costs [15]. The failure to detect such defects in HTP has resulted in catastrophic failures (examples in Figure 1.2) every year, causing loss of life and widespread power cuts with environmental damage and adverse financial consequences due to plant unavailability.
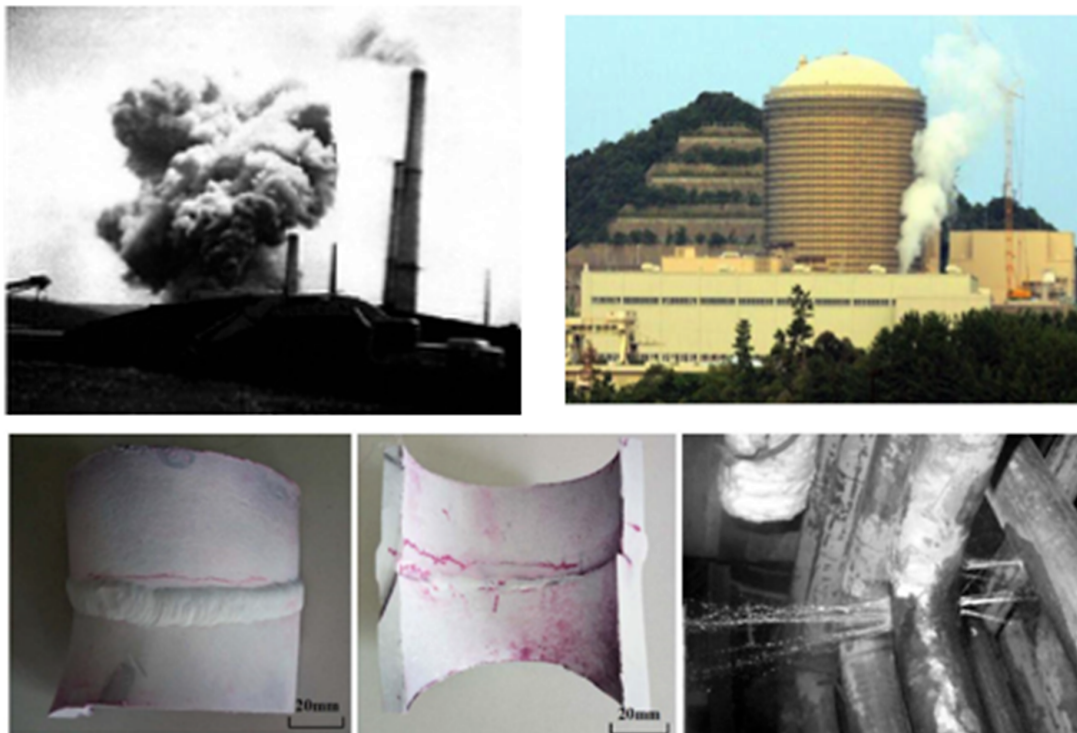
FIGURE 1.2: Examples of HTP failure: (top-left) vapor line corrosion failure caused explosion in Narco refinery [16]; (top-right) pipe rupture in Mount Storm TPP that led to the explosive release of steam [17]; (bottom-three) crack appearance on the outer and inner walls of a furnace tube [18].

Root-cause analyses of super-heated boiler tube failure indicated that thermal shock[2] and differential thermal expansion were responsible for crack initiation [19]. High pH values for steam have also been reported to cause stress corrosion cracking (SCC) in heat affected zones (HAZs) [18]. The requirement to assess the structural integrity of critical pipelines has encouraged research and development activities for their inspection and monitoring technologies.

---

[2]The thermal shock was caused by the return of condensate along the pipe, which flashed off as steam that produced rapid surface cooling.

1.3 Current Industrial Approach

Non-destructive testing (NDT) includes several analysis techniques for the evaluation of the material or the structure without affecting or degrading the functional performance of the structure [20]. These have become a necessary industrial operation to assess critical components for their fitness for service. Several high resolution NDT techniques are now standardised, including radiographic X-ray testing [21], magnetic particle testing [22], eddy current testing [23], and Ultrasonic testing (UT) [24]. Current industrial standards suggest implementing these NDT techniques for routine pipeline inspection.

Inspection of pipelines using conventional UT and high-resolution techniques requires repeated access to the pipes. Repeated access may include the removal of insulation, the erection of scaffolds for difficult-to-access locations, or the excavation of the ground for buried pipes, which can be time-consuming, expensive, and can put the safety of the operator at risk. Only a few high-risk points are generally inspected and an undetected defect can increase the probability of pipeline failure [25]. Recent developments are advancing the application of NDT techniques for in-service inspection of HTPs but are limited to temperatures below 250-300°C [26, 27].

1.3.1 Pipeline Inspection and Monitoring using Guided Waves

This thesis focusses on Guided wave testing (GWT), which is a modern NDT technique that employs low-frequency ultrasonic signals in the kilohertz range and offers long-range inspection of structures. GWT was first introduced for pipeline inspection in the early 1990s, but has continued to evolve for inspection and monitoring applications[3] to structural components of various geometries[4] and materials [29].

Advances in GWT technology have led to the introduction of commercially available pipeline inspection systems and the development of national and international standards such as ISO 18211:2016 [30]. These systems are now widely adopted by the Oil and Gas industry for periodic off-load inspections. They have demonstrated reliable defect detection capabilities for corrosion and erosion-type defects that remove around 3-9% of the pipe cross-sectional area (CSA).

---

[3]An overview of the existing literature reveals that more than 2000 papers have been published in the last decade (2012-2022) on GWT and over 500 for guided wave monitoring. This was determined by a Scopus search conducted in January 2023.

[4]Recently the research has expanded the application of GWT to storage tanks, bridges, rail, ship hull, aircraft, and containment structures [28].

Various transduction technologies for the generation and detection of Ultrasonic guided wave (UGW) have been developed, including Electromagnetic acoustic transducers (EMAT) [31] and magnetostrictive devices [32, 33]. Recent development has also expanded their application to high temperatures using active cooling [34, 35]. However, they require high drive levels due to inefficient electromechanical coupling, have poor signal-to-noise ratios, and are very sensitive to perturbations in sensor lift-off. This study will focus on piezoelectric transduction, which is used in most commercial systems due to its high efficiency, high temperature stability, low cost, simple signal conditioning, compact size, and ease of integration.

The current study is based on the Teletest system, developed by Plant Integrity Ltd., now acquired and rebranded by Eddify Technologies [36]. The components of the Teletest system are shown in Figure 1.3, including the pulser receiver unit that controls the transducer array, collar arrays of different pipe sizes, and transducer modules containing piezoelectric transducers that are attached to the pipe to generate and sense UGW signals.
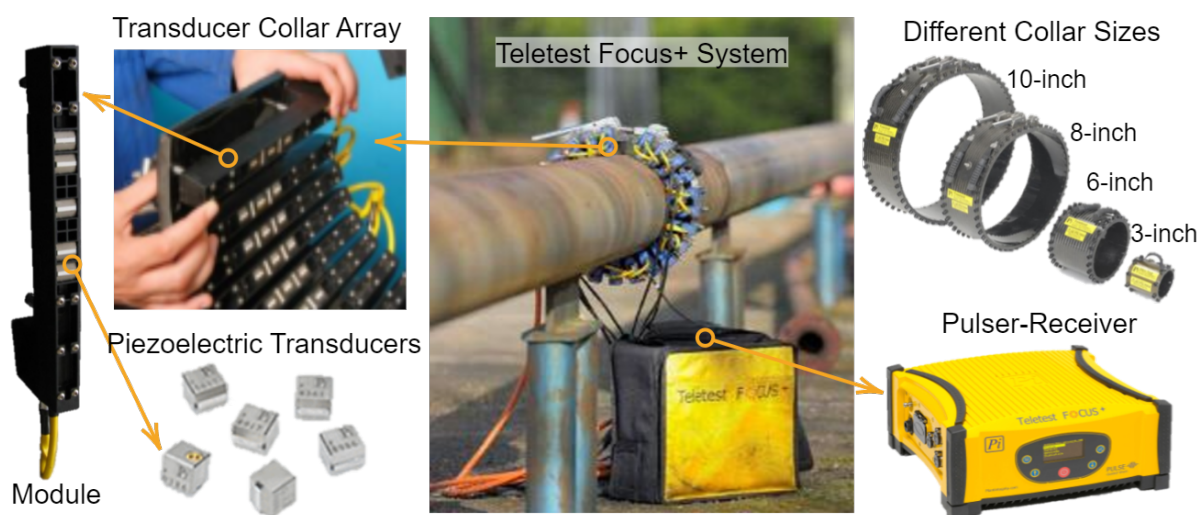
FIGURE 1.3: Teletest GWT system and its components including transducer collar array for different pipe sizes with multi-mode transducer modules housing piezoelectric transducers and pulser-receiver unit [37].

Traditionally, GWT has been carried out as a discrete inspection of HTP during planned maintenance outages under ambient temperature conditions. Their high-temperature operation is limited mainly due to the transduction system; however, recent developments have extended their application to intermittent[5] use at high temperatures up to 400°C [39, 38].

---

[5]The test duration including system installation and measurement capture is limited to five minutes above 300°C. After that, the transducers would be damaged by overheating [38].

GWT requires access to the pipe surface for sensor installation and minimal surface preparation. Detachable sensors and instrumentation are installed on the pipe to transmit UGWs, which travel along the pipe and are confined within the walls of the pipe. Any detected change in the area of the cross section reflects an echo. Thus, any existing defects are identified by analysing the signals received. The requirement of continuously assessing the integrity of critical pipelines has encouraged research and development of damage prognosis systems [40, 41].

Structural health monitoring (SHM) is a methodology that uses permanently installed sensor systems that allow frequent inspections of the structure while in service. Changes in acquired measurements enable early defect detection. Monitoring of defects and severity can transform maintenance management from a schedule-driven to an optimised condition-based implementation. Several pipeline monitoring technologies have been developed based on acoustic emission, fibre optic sensors, and guided wave sensors [42]. Examples of commercially available guided wave inspection and monitoring systems are shown in Figure 1.4 and their performance characteristics are given in Table 1.1.
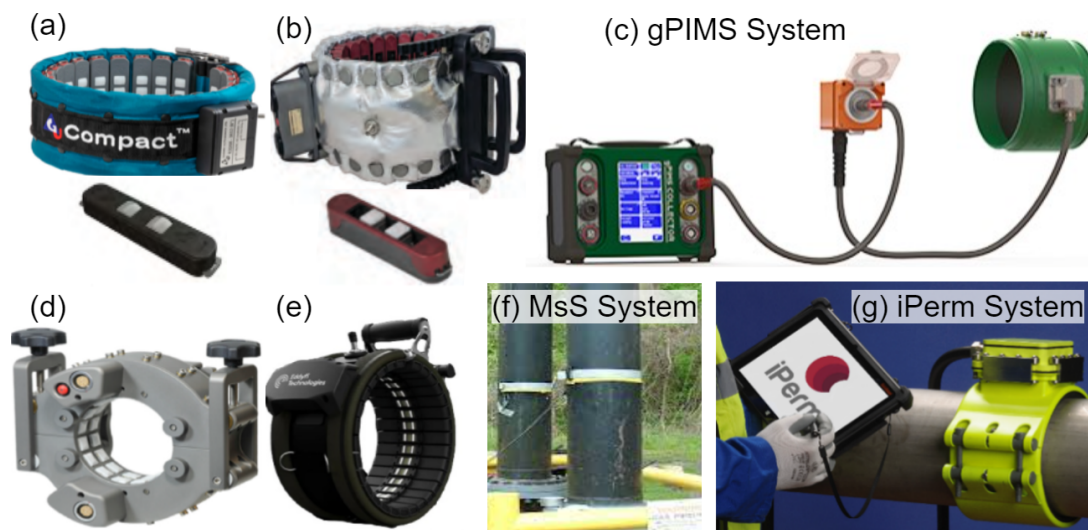
FIGURE 1.4: Examples of UGW pipeline inspection and monitoring systems and transducer arrays: (a) Compact, (b) HT Inflatable Ring, (c) gPIMS and (d) HT EFC Solid Ring by Guided Ultrasonics Ltd. [43]; (e) Sonyks by Eddyfi [36]; (f) MsSR3030 by Guided Wave Analysis LLC [44]; and (g) iPerm System [45].

Permanently installed sensors produce more repeatable measurements as the variability introduced by sensors and their coupling or installation are minimised. The repeatability of the measurement can significantly improve the defect detection characteristics by comparing it with historical measurements [46]. A study showed that an average 7dB increase in defect sensitivity could be achieved over conventional guided wave inspection [47]. However, this required signal processing techniques to

compensate for signal changes due to Environmental and operational condition (EOC). This also assumes that the ultrasonic performance of the sensor system is not degraded over time and that the system can perform reliably under EOC.

TABLE 1.1: Commercial pipe monitoring systems, their underlying technology, operating temperature range, inspection range and defect sensitivity.

System	Technology	Max Temp	Range and Sensitivity
MsS (SwRI) [44]	Electromagnetic	N/A	150 m; 2-3% CSA
HotSense (Ionix) [48]	Ultrasonic	380-550 °C	>2.5 mm; 0.05 mm
WT210 (Emerson) [49]	Ultrasonic	600°C	3-100 mm; 10 m
Permamount (Eddify) [50]	Ultrasonic	200°C	N/A; N/A
gPims (GUL) [51]	Ultrasonic	90°C	60m; 1% CSA

An example of one such system is the gPIMS developed by Guided Ultrasonic Ltd. [52]. The gPIMs system is limited to operating at temperatures below 90°C and is therefore not suitable for HTP. The permamount system [53] developed by Plant Integrity Ltd. has been reported to operate at temperatures up to 200°C. However, no stability analysis was performed over an extended period of time. The magnestrostrictive technology employed by MsS offers low output power, significantly limiting the inspection range. The acoustic emission technique offers a limited range in a noisy environment and requires complex signal processing.

1.3.2 Limitations and Challenges

Despite recent advances in GWT technology using piezoelectric transducers that have made it a promising tool for SHM, there are still some challenges that need to be addressed [54]. Some challenges are inherent in techniques based on UGW, whereas some are relevant for High Temperature (HT)-SHM applications. These are listed below.

- Inherent UGW related challenges including multi-mode propagation and mode conversion due to interaction with geometric features and dispersive behaviour that require complicated signal interpretation. This can be further complicated by ineffective excitation and isolation of the desired wave mode or cancellation of unwanted wave modes.

- The development of transducers for HT-SHM application with suitable functional ultrasonic performance. This includes challenges associated with the integration of high-temperature piezoelectric materials, which possess a lower

electromechanical efficiency and offer weaker transduction performance. Their construction into transducer, packaging, and application over wide temperature ranges can affect electrical continuity, piezoelectric properties, and acoustic coupling to the structure, and lead to irreversible transducer performance degradation. Transducers must operate reliably during prolonged exposures to extreme EOCs with no instability and performance drifts to ensure consistency of the measurements and the sensitivity of the defect over time.

- Monitoring data interpretation challenges, including the influence of temperature on UGW propagation. Instability in the transducer response can mask small defect signals or lead to false defect detection. Advanced signal processing routines are required to compensate for changes arising from EOCs.

- Design challenges for the transduction system to be mechanically durable and low profile to allow mounting in restricted or confined areas. It must also have a modular transducer design for application to different pipe sizes.

1.4 Aim and Objectives

This thesis is devoted to developing an SHM system based on GWT for pipelines operating at high temperatures up to 350°C and ultra-high temperatures up to 600°C. The primary focus is designing, developing, and verifying a HT-Piezoelectric Ultrasonic Transducer (PUT) that can form the core of the GWT transduction system required to enable SHM of HTP. The desirable specifications of the transducer system were defined by an industrial partner and are listed in Table 1.2.

TABLE 1.2: Transducer system specifications defined by an industrial partner.

Characteristic	Specification	Notes
Frequency Range	30-120 kHz	Broadband capability
Wave mode	$T(0,1)$	Complete pipe CSA coverage and simple signal interpretation.
Acoustic Coupling	Dry-coupling	Rapid installation with minimal surface preparation
Temperature	350°C	HTPs application in Oil&Gas
	600°C	UHTPs application in NPPs
Operational Life	>2 years	
SNR and Sensitivity	30 dB and 3% CSA	Provide >6dB signal difference

The development of the HT-UGW transducer aimed to meet these overarching system requirements while addressing the current challenges described in the previous section. The development and fabrication of the transducer involves the selection and characterisation of suitable materials along with numerical and experimental techniques for their design and validation against target specifications. The complete application of the GWT-SHM system on HTP under representative EOC was also desirable to verify the transduction system. The key objectives of this research are the following.

- Investigation of the current state-of-the-art high-temperature piezoelectric ultrasonic transducers and their SHM applications, including signal processing techniques for defect detection in varying EOC.

- Development of a numerical and experimental approach to design and characterise a high-temperature piezoelectric ultrasonic transducer for guided wave application that focuses on performance parameters relevant to T(0,1) mode excitation.

- Characterisation of the existing Teletest transducer and GWT system in representative EOC for SHM application on a HTP.

- Design and numerical optimisation of a high temperature piezoelectric ultrasonic transducer for continuous operation at 350°C and 600°C.

- Development of a transducer fabrication process to manufacture prototype transducers and conduct design verification for the HT-SHM application through performance characterisation at target temperatures and over extended periods.

- Study the performance of the complete GWT system in representative EOC for SHM application on a high-temperature pipe.

- Make appropriate recommendations for future work on this subject.

1.5 Research Methodology

To address the challenges associated with the development of HT-UGW piezoelectric transducers and their application for SHM of HTP, a unified numerical and experimental methodology is established, as illustrated in Figure 1.5. These methods are used throughout this thesis to characterise piezoelectric materials and transducer performance for the generation and sensing of the desired UGW at high temperatures. The numerical approach is based on multiphysics FEA for characterising the design of

the transducer and for analysis of the influence of temperature on electromechanical and ultrasonic performance. The experimental approach includes characterising the electromechanical properties of piezoelectric materials as a function of temperature using Electromechanical Impedance Spectroscopy (EMIS), the vibrational response as a function of frequency using Scanning Laser Doppler Vibrometry (SLDV), and the ultrasonic performance for the transmission and reception of desired guided wave modes under target operating conditions.
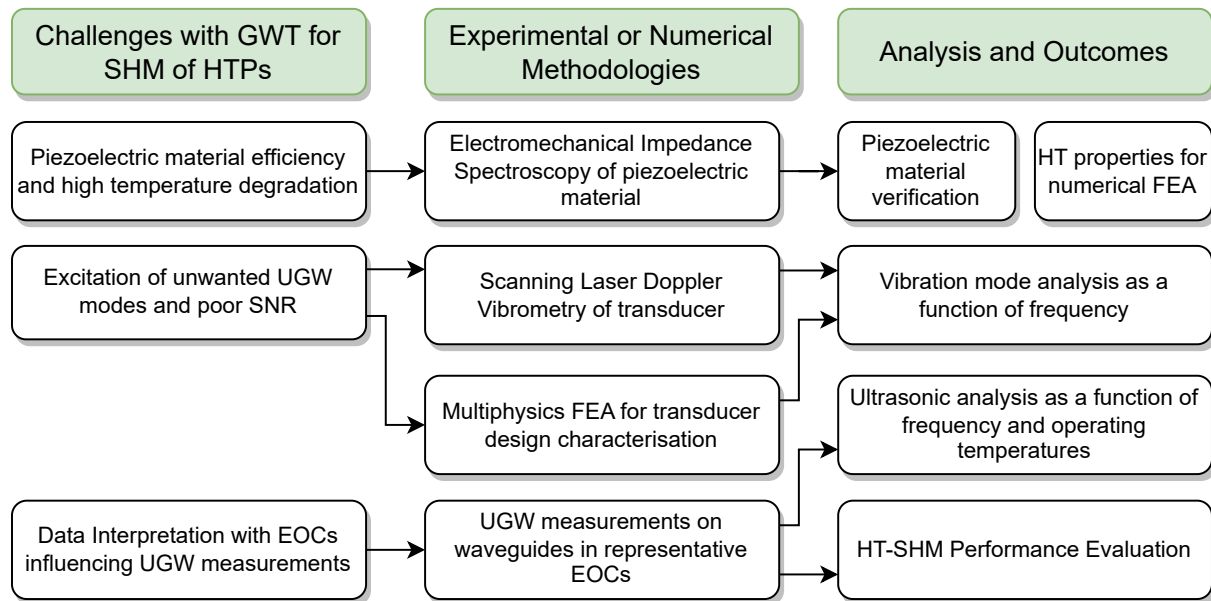
FIGURE 1.5: The unified numerical and experimental methodology followed for the design and analysis of the high temperature ultrasonic guided wave piezoelectric transducer.

These numerical and experimental design characterisation methodologies are validated through application on an existing transducer. Analysis also provided a better understanding of the dynamic vibration response of the transducer and the limitations for high-temperature operation. The methods are used to optimise the transducer design parameters, verify new piezoelectric materials, and aid in the design of new transducers with enhanced temperature capabilities. An experimental approach was also developed to investigate the influence of high temperatures on the performance of a complete GWT system for SHM on HTPs. This characterises the ultrasonic performance for the desired UGW in a pipe under representative EOCs to analyse the defect sensitivity as a function of temperature.

1.6 Thesis Outline

This thesis is structured in nine chapters, as illustrated in Figure 1.6, which also shows how the results or findings of one chapter are used in the studies conducted in other chapters. Chapter 2 provides the relevant theoretical background on piezoelectric ultrasonic transducers and GWT. The characteristics of UGW modes in pipes, including their dispersive behaviour and their transduction using a piezoelectric transducer, are explained. The signal processing methods used in GWT for defect detection in the SHM application are also described. Chapter 3 reviews the recently published literature on high-temperature piezoelectric materials and transducers and the application of GWT for SHM in varying EOC.

In Chapter 4, the methodology for the design and characterisation of the HT-UGW transducer is established and the unified numerical and experimental approach is explained. The development of the multiphysics FEA piezoelectric transducer model and the experimental methods for the characterisation of the transducer are described and applied to a simple piezoelectric PZT-5A wafer transducer.
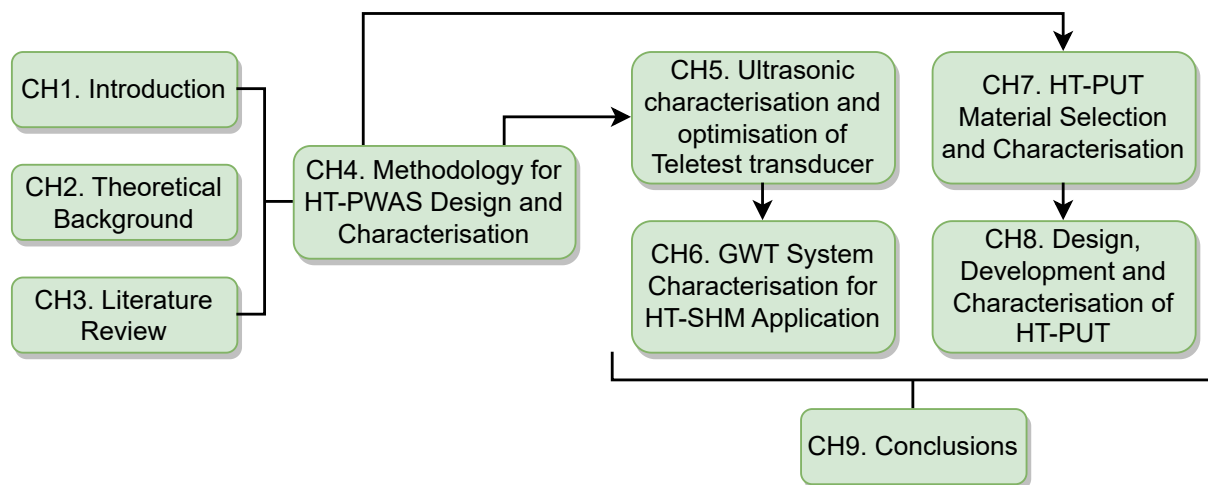
FIGURE 1.6: Structure of the thesis showing the interrelation of findings and inputs to other chapters.

In Chapter 5, the established methodology is used to characterise the Teletest transducer. Numerical parametric studies are carried out to analyse the influence of different design parameters to optimise the electromechanical and vibrational frequency response for transduction of the torsional UGW mode. The optimised transducer design was used in GWT for SHM under ambient operating conditions.

In Chapter 6, the application of the existing HT -UGW transducer within a complete GWT system for SHM of HTPs is evaluated in representative EOC. System performance, including sensitivity to defects as a function of temperature, is assessed

with artificially introduced defects in the pipe. Additionally, the stability of the entire GWT system is investigated at high temperatures in a power plant.

Chapter 7 focuses on the selection and characterisation of new high temperature piezoelectric materials for the design of HT-UGW for continuous operation at 350°C and 600°C, respectively. Their high-temperature electromechanical properties are characterised as functions of temperature up to their respective target temperatures and for extended periods to verify their performance for transducer development.

The design of the complete transducer, including material selection and the design of passive transducer layers, is reported in Chapter 8. Prototype HT-UGW transducers are manufactured, and their ultrasonic performance is characterised at the target operating temperatures. The research conclusions are discussed in Chapter 9, where contributions to knowledge are thoroughly reviewed in the broader context of the published literature. Finally, recommendations are offered for future research work.

1.7 Contributions to Knowledge

1.7.1 Research Contribution

The research focusses on the design and characterisation of a HT-UGW piezoelectric ultrasonic transducer for SHM application on HTPs. This research made the following contributions to knowledge:

- Developed and validated multiphysics FEA models of piezoelectric materials and transducers to simulate the high temperature electromechanical and ultrasonic performance for operation at high temperatures in Thickness-shear mode (TS-mode).

- Characterised the existing Teletest transducer and the complete UGW system for HT-SHM application through investigation of the transducer and the system for the excitation of the torsional guided wave mode at HT and reliability over time.

- Characterised modified bismuth titanate and gallium phosphate piezoelectric materials at high temperatures up to 350°C and 600°C and evaluated their performance for TS-mode operation.

- Designed and developed HT-UGW piezoelectric transducers and demonstrated stable ultrasonic performance for SHM application at 350°C and 600°C.

1.7.2 Publications from PhD

Journal Publications

AD1 A. Dhutti, S.A. Tumin, W. Balachandran, J. Kanfoud, T.H. Gan, Development of ultrasonic guided wave transducer for monitoring of high-temperature pipelines, Sensors, vol. 19(24), 5443, 2019. [Link to article]

AD2 A. Dhutti, S. A. Tumin, A. Mohimi, M. Kostan, T. H. Gan, W. Balachandran, and C. Selcuk, Development of low-frequency high-temperature ultrasonic transducers for in-service monitoring of pipework in power plants, Procedia Engineering, vol. 168, no. 0, pp. 983986, 2016. [Link to article]

AD3 M. Kostan, A. Mohimi, C. Nageswaran, A. Dhutti, T. H. Gan, L. Wrobel, and C. Selcuk, High-temperature gallium orthophosphate transducers for NDT, Procedia Engineering, vol. 168, no. 0, pp. 987990, 2016. [Link to article]

Conference Publications

AD4 A. Dhutti, S. A. Tumin, T.H. Gan, J. Kanfoud, and W. Balachandran. "Comparative study on the performance of high-temperature piezoelectric materials for structural health monitoring using ultrasonic guided waves." In Proceedings of the 7th Asia-Pacific Workshop on Structural Health Monitoring, Hong Kong, China, pp. 12-15. 2018. [Link to article]

AD5 A. Dhutti, T. H. Gan, W. Balachandran, and J. Kanfoud. "High-temperature performance of ultrasonic guided wave system for structural health monitoring of the pipeline." In Proceedings of the 7th Asia-Pacific Workshop on Structural Health Monitoring, Hong Kong, pp. 12-15. 2018. [Link to article]

AD6 A. Dhutti, T.H. Gan, W. Balachandran, Effect of electrode configuration on high-temperature thickness-shear Gallium Orthophosphate transducer, Multidisciplinary Digital Publishing Institute Proceedings. Vol. 1. No. 4. 2017. (Also presented at Eurosensors XXXI Conference, Paris, September 2017) [Link to article]

AD7 A. Dhutti, T.H. Gan, A. Mohimi, and J. Kanfoud, Investigation of high-temperature performance of ultrasonic guided wave system for in-service condition monitoring of pipework in thermal power plants, In Proceedings of the First World Congress on Condition Monitoring, London, June 2017.

AD8   A. Dhutti, T.H. Gan, A. Mohimi, W. Balachandran, Development of a GWT system with enhanced high-temperature condition monitoring performance, presented at NSIRC Conference, Cambridge, June 2016.

AD9   Dhutti, A., Kanfoud, J., Gan, T. H., Hernandez, B., Mudge, P. (2018, July). iPerm: A Guided Wave Pipeline Monitoring Tool for the Oil and Gas Industry. In Proceedings of the 9th European Workshop on Structural Health Monitoring, EWSHM, Manchester, UK (pp. 10-13). [Link to article]

AD10   Hernandez, B., Dhutti, A., Gan, T. H. (2018). iPerm: Guided wave pipeline monitoring tool. Impact, 2018(9), 15-17.[Link to article]

Book Chapters

AD11   A. Dhutti, S. Lowe, S., and T.H. Gan, Monitoring of Critical Metallic Assets in Oil and Gas Industry Using Ultrasonic Guided Waves. In Advances in Structural Health Monitoring. InTechOpen. 2019. [Link to book chapter]

AD12   A. Dhutti, T. H. Gan. "Pipeline Health Monitoring to Optimise Plant Efficiency." In Power Plants in the Industry. InTechOpen, 2019. [Link to book chapter]

Chapter 2

Theoretical background

2.1 Introduction

This research involves two fundamental aspects of physics, namely UGW and piezoelectricity. The theoretical background presented in this chapter is illustrated in Figure 2.1 and will be referred to in the following chapters of the thesis. The chapter starts with an introduction of guided wave behaviour in cylindrical pipe-like structures and their application for GWT. Then, piezoelectric materials and principles are described, with a focus on electromechanical properties related to the design of PUT for the transduction of UGW. The chapter concludes with a discussion of signal processing techniques that allow efficient analysis of acquired ultrasonic signals for GWT and SHM applications.

Piezoelectric Ultrasonic Transducers	Guided Wave Testing	Signal Processing for Ulrasonic Guided Waves
Piezoelectricity and Material Types	Bulk Waves and Guided Waves	Discrete Pulse Excitation in Frequency Domain
Piezoelectric Properties &Operating Modes	Cylindrical Guided Wave Modes	Hilbert Transform for Envelope Detection
Piezoelectric Electromechanical Characterisation	Propagation Velocity and Dispersion Curves	Signal to Noise ratio in UGW Measurements
Transducer Design and Construction	Guided wave mode selection & excitation	Time Frequency Domain Analysis
Transducer Characteristics for Ultrasonic Application	Guided wave mode propagation	

FIGURE 2.1: Theoretical topics covered in the background to guided wave monitoring of pipes using piezoelectric ultrasonic transducers.

2.2 Piezoelectric Ultrasonic Transducers

2.2.1 Piezoelectricity and Types of Piezoelectric Materials

Piezoelectricity is a phenomenon in which certain materials generate an electric charge when subjected to mechanical stress or pressure (direct piezoelectric effect). On the contrary, these materials can also undergo mechanical deformation when an electric field is applied to them (inverse piezoelectric effect). Piezoelectric materials can thus convert electrical energy into mechanical energy and vice versa.

Piezoelectric materials are non-conducting and possess dielectric properties. On the basis of their composition and structure, piezoelectric materials can be characterised as single crystals, piezoceramics, thin-film piezoelectrics, composites, and polymers. Each has its own advantages and limitations, and the choice depends on the specific requirements of the application [55]. This research focusses on piezoceramics and single crystals, as they offer superior piezoelectric properties for high-performance applications where sensitivity and precision are vital.

Piezoceramics are poly-crystalline ferroelectric structures composed of randomly orientated dipoles (positive and negative poles separated by a distance) in unit cell-like structures called domains. They have isotropic properties on a macroscopic scale with no net polarisation. They exhibit reorientable spontaneous polarisation produced by the domain walls of the crystal structure. They are polarised by applying a strong electric field at high temperatures, aligning the dipoles parallel to the field. After poling, the dipoles stay almost in exact alignment, giving the ferroelectric ceramic a permanent polarisation and thus making it piezoelectric. The most used ferroelectric materials are Lead Zirconate Titanate ($Pb[Zr, Ti]O_3$), generally known as PZT, and Barium Titanate ($BaTiO_3$).

Single crystals are inherently anisotropic and possess spontaneous polarisation because of their non-centrosymmetric crystalline structure. As an example, the trigonal structure of the quartz unit cell (SiO_2) is shown in Figure 2.2. It is longer in the vertical direction, resulting in a net electrical polarisation of the bulk material. When a mechanical force is applied to piezoelectric materials, the dipoles within the material create charges at the two ends of the material. These charges can be accessed by connecting electrodes, as illustrated in the figure.
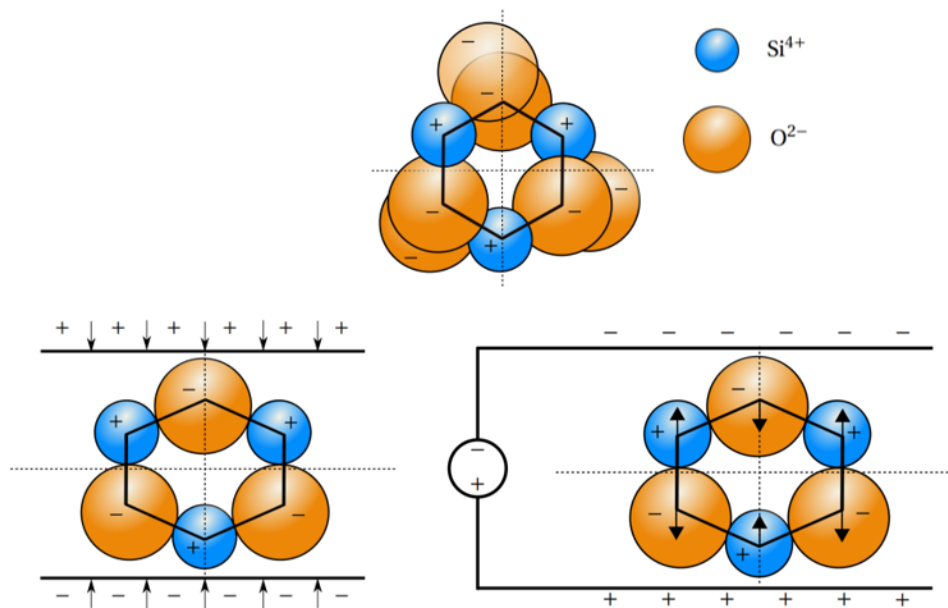
FIGURE 2.2: Silicon and oxygen arrangement in α-Quartz and illustration of direct and inverse piezoelectric effect [56]

In comparison to single crystals, piezoceramics are low-cost and can be formed into intricate shapes. However, they provide worse reproducibility because of complex ceramic processes, loss of piezoelectric behaviour above the Curie temperature, and practical limitation below this temperature. They also possess higher temperature coefficients, higher electrical conductivity compared with those of single crystals, and pyroelectric behaviour (change in surface charge in response to change in temperature).

Their fast response time, high conversion efficiency, low cost, and compact size have led to various sensors, actuators, and transducer applications. Pressure, force or vibration sensors use the direct piezoelectric effect [57], while the inverse piezoelectric effect forms the basis for actuators, such as displacement actuators for industrial process control and vibration cancellation in aerospace systems [58]. Transducer applications, such as bioimaging equipment and NDT, use the same material to perform direct and inverse piezoelectric operations for actuating and sensing surface acoustic waves or ultrasonic waves, respectively [59].

2.2.2 Piezoelectric Properties and Operating Modes

The electromechanical characteristics of piezoelectric materials are described by various interrelated coefficients standardised by the IEEE [60]. These coefficients include piezoelectric, dielectric, and elastic material properties. The electromechanical behaviour of piezoelectric materials can be expressed by coupling the electrical and

mechanical constitutive relationship in Equation (2.1). This describes both direct and inverse piezoelectric effects.

$$\begin{bmatrix} \vec{S} \\ \vec{D} \end{bmatrix} = \begin{bmatrix} s^E & d^T \\ d & \epsilon^T \end{bmatrix} \begin{bmatrix} \vec{T} \\ \vec{E} \end{bmatrix} \tag{2.1}$$

Electrical displacement $\vec{D}$ is the electric charge per unit of area and is measured in $[C/m^2]$. Permitivity ϵ^T is measured under constant stress, electric field $\vec{E}$ is measured in $[V/m]$, and stress $\vec{T}$ in $[N/m^2]$. The piezoelectric charge (or strain) constant, d, is the polarisation generated per unit of applied mechanical stress and is measured in $[C/N]$ or $[m/V]$). The vector $\vec{S}$ is the strain, s^E is the elastic compliance in a constant electric field $\vec{E}$ (strain per unit of stress) $[m^2/N]$, and d^T is the transpose of d. Direct and inverse piezoelectric effects are equal in magnitude.

These parameters are tensor quantities and define the three-dimensional behaviour of piezoelectric materials. They are described using the axes designation and the deformation direction illustrated in Figure 2.3. These directions follow the Cartesian coordinate system where the x, y, and z axes are identified as 1, 2 and 3, respectively. The shear planes are indicated by 4, 5, and 6 and are perpendicular to axes 1, 2 and 3, respectively. By convention, the direction of polarisation is defined as axis 3.
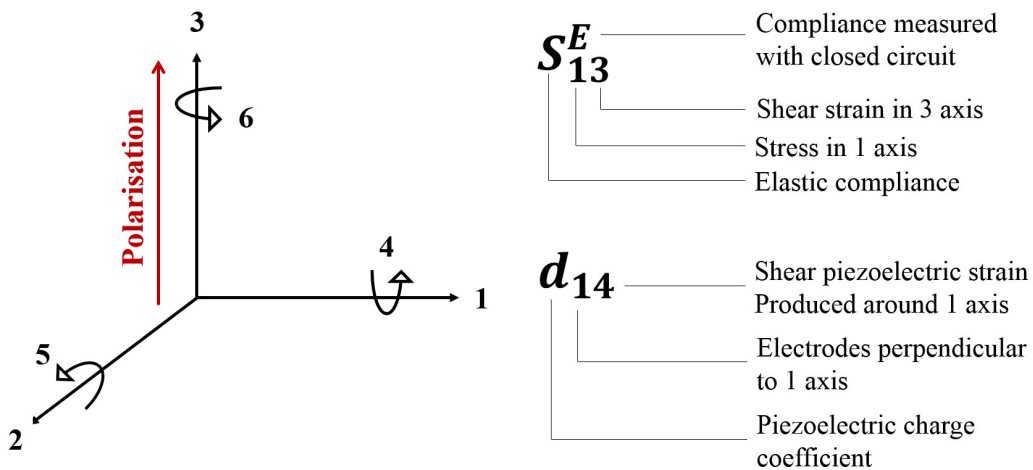
FIGURE 2.3: Coordinate system used to define piezoelectric properties and example representation.

The strain $\vec{S}$ and stress $\vec{T}$ are vectors with six components where the first three denote the normal deformation along the $x-$, $y-$ and $z-$ directions, and the next three indicate the shear deformation around the $x-$, $y-$ and $z-$ axes. The electric field $\vec{E}$ and the electrical displacement $\vec{D}$ are vectors with three components, normal to the $x-$, $y-$ and $z-$ axis. The material parameters s^E, d, and ϵ_T are rank 4, 3 and 2 tensors, respectively. They are represented using the abbreviated Voigt subscript, whereby the

first subscript denotes the direction of the electrical quantity (electrical displacement $\vec{D}$ or the electric field $\vec{E}$). The second subscript denotes the direction of the mechanical quantity (the strain $\vec{S}$ or the stress $\vec{T}$). Therefore, the complete description of the piezoelectric behaviour in Equation (2.1) is described in matrix form by Equation (2.2) and Equation (2.3).

$$
\begin{bmatrix} D_x \\ D_y \\ D_z \end{bmatrix} = \begin{bmatrix} d_{11} & d_{12} & d_{13} & d_{14} & d_{15} & d_{16} \\ d_{21} & d_{22} & d_{23} & d_{24} & d_{25} & d_{26} \\ d_{31} & d_{32} & d_{33} & d_{34} & d_{35} & d_{36} \end{bmatrix} \begin{bmatrix} T_{xx} \\ T_{yy} \\ T_{zz} \\ T_{yz} \\ T_{xz} \\ T_{xy} \end{bmatrix} + \epsilon_0 \begin{bmatrix} \epsilon^T_{r11} & \epsilon^T_{r12} & \epsilon^T_{r13} \\ \epsilon^T_{r21} & \epsilon^T_{r22} & \epsilon^T_{r23} \\ \epsilon^T_{r31} & \epsilon^T_{r32} & \epsilon^T_{r33} \end{bmatrix} \begin{bmatrix} E_x \\ E_y \\ E_z \end{bmatrix} \tag{2.2}
$$

$$
\begin{bmatrix} S_{xx} \\ S_{yy} \\ S_{zz} \\ S_{yz} \\ S_{xz} \\ S_{xy} \end{bmatrix} = \begin{bmatrix} s^E_{11} & s^E_{12} & s^E_{13} & s^E_{14} & s^E_{15} & s^E_{16} \\ s^E_{21} & s^E_{22} & s^E_{23} & s^E_{24} & s^E_{25} & s^E_{26} \\ s^E_{31} & s^E_{32} & s^E_{33} & s^E_{34} & s^E_{35} & s^E_{36} \\ s^E_{41} & s^E_{42} & s^E_{43} & s^E_{44} & s^E_{45} & s^E_{46} \\ s^E_{51} & s^E_{52} & s^E_{53} & s^E_{54} & s^E_{55} & s^E_{56} \\ s^E_{61} & s^E_{62} & s^E_{63} & s^E_{64} & s^E_{65} & s^E_{66} \end{bmatrix} \begin{bmatrix} T_{xx} \\ T_{yy} \\ T_{zz} \\ T_{yz} \\ T_{xz} \\ T_{xy} \end{bmatrix} + \begin{bmatrix} d_{11} & d_{21} & d_{31} \\ d_{12} & d_{22} & d_{32} \\ d_{13} & d_{23} & d_{33} \\ d_{14} & d_{24} & d_{34} \\ d_{15} & d_{25} & d_{35} \\ d_{16} & d_{26} & d_{36} \end{bmatrix} \begin{bmatrix} E_x \\ E_y \\ E_z \end{bmatrix} \tag{2.3}
$$

Based on the symmetry of their crystal structure; various d_{ij} components are mutually dependent or zero. For example, quartz with a trigonal crystal structure only has five non-zero d_{ij} components, of which only two (d_{11} and d_{14}) are independent (Equation 2.4). An overview of the symmetry constraints on piezoelectric tensors for various crystal point groups is given in [61]. In contrast to single crystals like Quartz, Piezoceramics are given artificial polarisation and exhibit rotational symmetry around the poling axis '3'-direction. All directions perpendicular to the poling direction are considered as the '1'-direction. This results in a d matrix of the form in Equation (2.5).

$$
d = \begin{bmatrix} d_{11} & -d_{11} & 0 & d_{14} & 0 & 0 \\ 0 & 0 & 0 & 0 & -d_{14} & -2d_{11} \\ 0 & 0 & 0 & 0 & 0 & 0 \end{bmatrix} \tag{2.4}
$$

$$
d = \begin{bmatrix} 0 & 0 & 0 & 0 & d_{15} & 0 \\ 0 & 0 & 0 & d_{15} & 0 & 0 \\ d_{31} & d_{31} & d_{33} & 0 & 0 & 0 \end{bmatrix} \tag{2.5}
$$

From the piezoelectric constant matrix for ceramic materials, it can be seen that there are three non-zero elements: d_{33}, d_{31} (equal to d_{32}), and d_{15} (equivalent to d_{24}). This suggests that electromechanical coupling operates in three basic modes, called longitudinal ("33"), transverse ("31"), and shear ("15"). These modes of operation apply coupling between the mechanical and electric domains in various directions, as illustrated in Figure 2.4. In the d_{33} mode, the deformation and electric field are in the '3'-direction, parallel to the polarisation. In d_{31} mode, the electric field is parallel to the polarisation, and the relevant deformation is perpendicular to the polarisation in the '1'-direction. The longitudinal and transverse modes are coupled, as the deformation along the poling axis inherently results in deformation in a perpendicular direction.
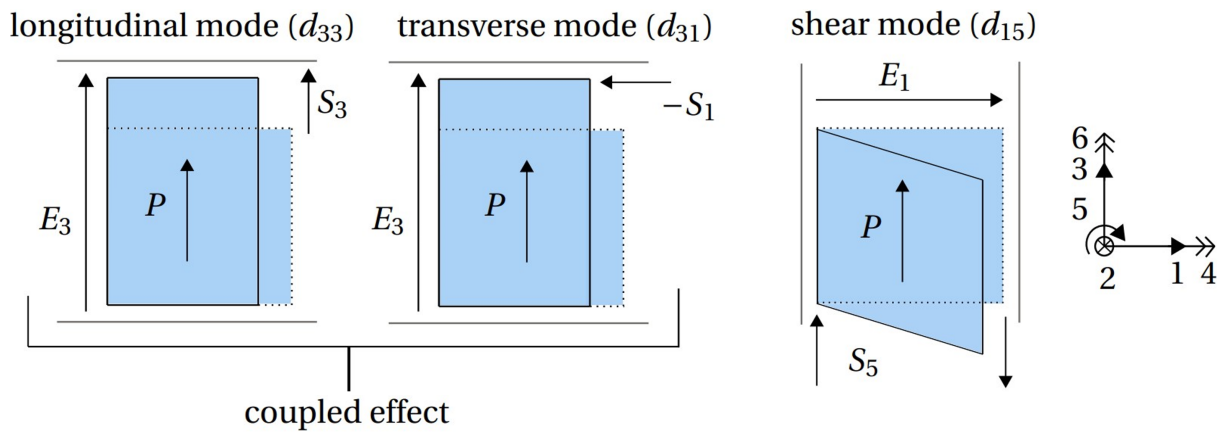
FIGURE 2.4: Electromechanical coupling of longitudinal (d_{33}) and transverse (d_{31}) modes; and the thickness-shear (d_{15}) mode of operation of piezoelectrics [56].

This work focusses on the shear mode of operation, where the electric field is applied perpendicular (subscript 1) to the polarisation direction, and the shear deformation is around the other perpendicular axis. The two-port equation for the shear mode, with the electrical port (D, E) in the '1' direction and the mechanical port (S, T) in the '5' direction, is written as:

$$\begin{bmatrix} \vec{S_5} \\ \vec{D_1} \end{bmatrix} = \begin{bmatrix} s_{55}^E & d_{15} \\ d_{15} & \epsilon_{11}^T \end{bmatrix} \begin{bmatrix} \vec{T_5} \\ \vec{E_1} \end{bmatrix} \tag{2.6}$$

Several studies have classified vibration modes in piezoelectric plates operating in the thickness-shear mode of varying aspect ratios analytically and experimentally [62]. Parameters that govern the TS-mode of the piezoelectric element include its thickness, physical aspect ratio, the direction of polarisation (for ferroelectric materials), and the angle at which the element is cut (for single crystals). The direction perpendicular to the most prominent face is the cut axis. The shear mode is less sensitive to the temperature dependence of the polarisation (pyroelectric effect). Furthermore, the

shear mode is neither affected by deformation in the other directions nor causes unwanted deformation in the other directions. Ceramics can be used with positive and negative voltages for shear mode, thus providing a more significant actuation. However, one limitation is associated with the shear mode: during operation, re-polarisation may occur along the '1' axis in case large voltages are developed.

2.2.3 Piezoelectric Electromechanical Characterisation

When an alternating field (AC voltage) is applied, the dimensions change at the cycling frequency of the field and result in dynamic mechanical vibration. If the drive frequency of the field is adjusted to the mechanical resonance frequency of the device, a large resonating strain is generated. This phenomenon of strain magnification due to the accumulation of input energy is called piezoelectric resonance. The frequency at which the piezoelectric vibrates most readily is called the resonance frequency. The material is most efficient at converting electric energy into mechanical energy at this frequency.

Multiple resonances are observed in piezoelectric devices related to their geometry, density, and elastic constants. The dynamic response of the piezoelectric material can be captured by measuring the EMIS. For a piezoelectric plate of thickness t and electrode area A, vibrating in TS-mode, the electromechanical impedance Z as a function of frequency is described by Equation (2.7), whereby f_r and f_a are the characteristic resonance and anti-resonance frequencies.

$$z(\omega) = \frac{t}{i\omega\epsilon^S A}\left[1 - k^2\frac{\tan(\frac{\omega}{4f_a})}{(\frac{\omega}{4f_a})}\right] \tag{2.7}$$

A typical EMIS of a piezoelectric plate operating in TS-mode is shown in Figure 2.5 with annotations to the characteristic resonance frequencies. The Electromechanical Impedance (EMI) versus frequency plots are generally presented on a logarithmic scale to emphasise the weaker excitable modes, including any an-harmonics, spurious, or unwanted modes. The observed resonances are associated with ultrasound reflection within the ceramic body, resulting in their vibration modes. The resonance at the lowest frequency corresponds to the motion in the largest dimension of the ceramic. When a piezoelectric device is mounted on a mechanical structure, the mechanical boundary conditions of the material change, as do the behavioural properties of the loaded piezoelectric device.
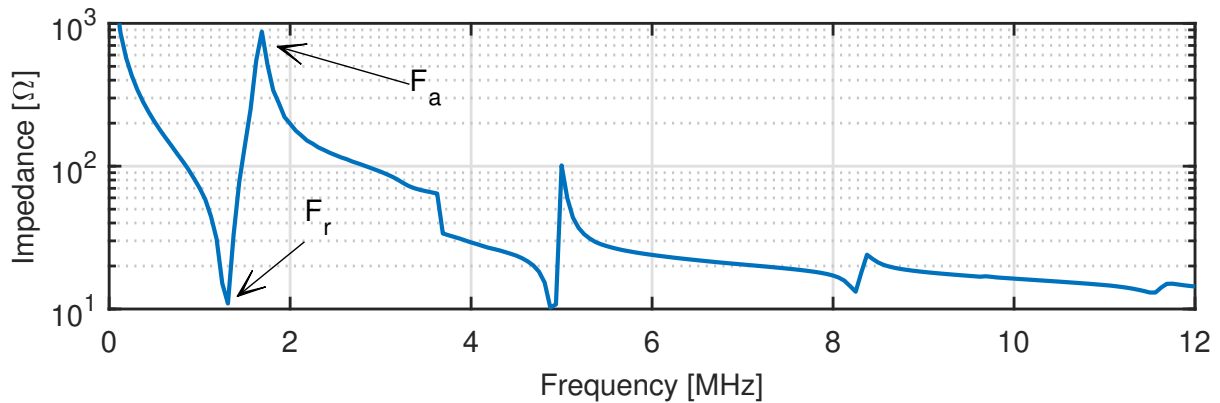
FIGURE 2.5: Example electro-mechanical impedance response of a TS-mode piezoelectric material showing TS-mode resonances and highlighting the characteristic resonance (F_r) and anti-resonance (F_a) frequencies of the fundamental resonance.

A useful guide for the selection of an appropriate piezoelectric material is its Figure of Merit (FOM). The key elastic, dielectric and piezoelectric material properties and their relation and significance to the transducer application are given in Table 2.1.

TABLE 2.1: Piezoelectric material FOM along with their relation and significance for transducer application.

Piezoelectric FOM	Relation	Significance
Strain constant (d)	$x = dE$	Measure of strain induced by an external electric field. Signifies the performance as an actuator.
Voltage constant (g)	$E = gX$	Measurement of the electric field induced by an external stress. Signifies the performance as a sensor.
Coupling coefficient (k)	$k^2 = \frac{\epsilon^T - \epsilon^S}{\epsilon^T}$	Measure of the fraction of mechanical energy converted into electric energy and vice versa.
Frequency constant (N)	$N_i = \frac{V_i}{2}$	Related to wave speed in the material and used to determine the fundamental resonance frequency.
Dielectric constant (K^T)	$K^T = \epsilon^T / \epsilon_0$	Measurement of the capacity of the materials to hold charge.

The characteristic frequencies of the EMI response can be used to derive these properties. The coefficients relevant for the shear mode of thickness vibration are taken from the British Standards documents with reference code BS EN 50324-2:2002 [63]. Their relationship with the piezoelectric plate geometry, characteristic frequencies, and interrelationship with other FOM are given in Table 2.2.

TABLE 2.2: Piezoelectric material FOM for TS-mode operation along with their relation to geometric properties and their interrelationship with other FOMs.

Piezoelectric TSM FOM	Relation
Elastic compliance at constant $\vec{D}$ (S_{55}^D)	$S_{55}^D = \frac{1}{4\rho F_a^2 t^2}$
Electromechanical coupling factor (k_{15})	$k_{15} = \sqrt{\frac{\pi}{2}\frac{F_r}{F_a}\cot(\frac{\pi}{2}\frac{F_r}{F_a})}$
Elastic compliance at constant $\vec{E}$ (S_{55}^E)	$S_{55}^E = \frac{S_{55}^D}{1-k_{15}^2}$
Piezoelectric charge constant d_{15}	$d_{15} = k_{15}\sqrt{\epsilon_{11}^T S_{55}^E}$
Free electric permittivity (ϵ_{11}^T)	$\epsilon_{11}^T = C^T\frac{t}{A}$
Clamped electrical permittivity	$\epsilon_{11}^S = \epsilon_{11}^T(1-k_{15}^2)$
Voltage constant (g_{15})	$g_{15} = \frac{d_{15}}{\epsilon_{11}^T}$

For piezoelectric materials in Class 32, TS-mode of vibration can be obtained using Y-cut plates with electrode surfaces on the plane normal to the direction x_2. The electric field is applied in the x_2 direction, which results in a mechanical displacement in the x_1 direction. The independent materials constants for the y-cut resonators are reduced to c_{66}, $e_{26} = e_{11}$ and $\epsilon = \epsilon_{22} = \epsilon_{11}$. These piezoelectric properties and their derivation are given in Table 2.3.

TABLE 2.3: Piezoelectric material FOM for TS-mode operation for Y-cut single crystals along with their relation to geometric properties and their interrelationship with other FOMs.

Piezoelectric TSM FOM	Relation
Eigenfrequency of TS-mode harmonic (f_n)	$f_n = n\frac{v}{2h}, v = \sqrt{\frac{c_{66}^D}{\rho}}$
Electromechanical coupling factor (k_{26})	$k_{26}^2 = \frac{\pi}{2}\frac{f_r}{f_a}tan(\frac{\pi}{2}\frac{\Delta f}{f_a})$
Elastic constants (c_{66}^E)	$c_{66}^E = (1-k_{26}^2)\rho f_p t^2, c_{66}^D = 4\rho(tf_r)^2$
Piezoelectric constant (e_{26})	$\frac{k_{26}^2}{1-k_{26}^2} = \frac{e_{26}^2}{\epsilon_{22}^S c_{66}^E}$
Elastic compliance (S_{66}^E)	$S_{66}^E = \frac{1}{(4\rho t^2 f_a^2(1-k_{26}^2))}$

2.2.4   Influence of Temperature on Piezoelectric Materials

The effects of temperature on piezoelectric materials can be explained using the theory of propagation of acoustic waves in crystals [64]. Temperature creates a biased field that leads to geometrical and physical non-linearity. The geometric non-linearity occurs because of a change in shape from the anisotropic dilation of the piezoelectric crystal; this change affects the acoustic wave path and increases the attenuation. Physical non-linearity arises from thermal expansion, weakening the chemical bonds between atoms. This physical non-linearity and chemical instability increase electrical conductivity, and excessive charge carriers can lead to chemical decomposition and ionic defects [65]. For ferroelectrics, the temperature can result in the depinning of the domains or by the motion of the domain wall, causing the dielectric loss to increase. As the temperature increases, the orientation of the domains becomes more random, causing a loss in polarisation and reducing the piezoelectric effect. Moreover, above a specific temperature, the Curie temperature (T_c), the asymmetric crystal structure undergoes a phase transition to a high-symmetry paraelectric phase, where all piezoelectric activity disappears, causing irreversible material failure.

Due to these geometric and physical non-linearities caused by temperature, piezoelectric materials have temperature-dependent dielectric, piezoelectric, and electromechanical properties [66].   Significant temperature variation of these properties can highlight the degradation of the piezoelectric effect, for example, the elastic constant of quartz changes significantly across the α-β transition [67]. These temperature effects can grow with a high electric field, compressive mechanical bias, or mechanical loading.   Variation in temperature may also produce pyroelectric charges that can influence the piezoelectric effect.   Many ferroelectrics become conductive at high temperatures, leading to charge drifts and partial loss of signal. The conductivity problem can be aggravated during operation in an atmosphere with a low oxygen content. Many oxygen-containing ferroelectrics can rapidly lose oxygen and become semiconductive. Thus, the limitation of piezoelectric materials at high temperatures is governed by increased electrical conductivity, mechanical attenuation, and variation of piezoelectric properties [68].

The temperature coefficients of these piezoelectric properties are essential to predict their high-temperature electromechanical performance and suitability for HT-PUT application. The temperature coefficients of these properties can be derived using Equations (2.8) and (2.9).

$$T(P)^{(n)} = \frac{1}{P_0 n!} \left(\frac{\delta^n p}{\delta \theta^n} \right)_{\theta = T_0} \tag{2.8}$$

$$P(T) = P(T_0) + \sum_{n=1}^{3} T(P)^{(n)}.(T - T_0)^n \tag{2.9}$$

Where $T(P)^{(n)}$ is the temperature coefficient of the nth order of the material property P, T_0 is the reference temperature (usually 25°C), and the property $P(T)$ at temperature T can be calculated using these coefficients.

2.2.5 Transducer Design and Construction

A PUT employs the piezoelectric material to generate a mechanical (acoustic) signal from an electrical input or an electrical signal from a mechanical input, allowing the transmission and reception of ultrasonic signals. Their design requires multidisciplinary knowledge and consideration of acoustics, vibration, materials, signal processing, and electronics drive requirements. There is no standard tool or methodology available for their design and thus is primarily empirical with some established rules and fundamental theoretical understanding. These empirical design rules have generally been applied to resonant transducers that are used for ultrasonic testing in the MHz range. The construction of a typical PUT includes five key components: a face plate, a piezoelectric element, a damping block, a casing and electrical connections, as illustrated in Figure 2.6.
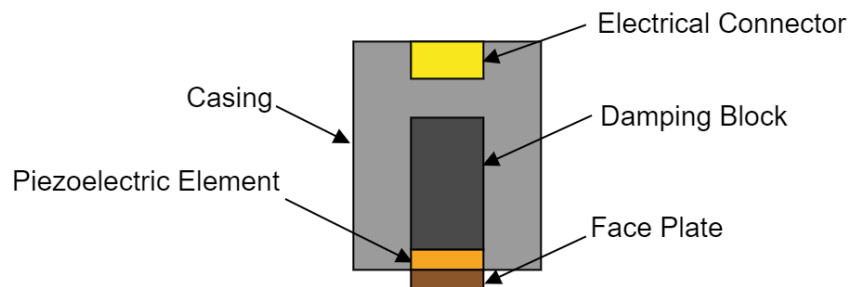
FIGURE 2.6: Construction of a generic piezoelectric transducer.

Piezoceramics of thickness in the range of 0.1 to 1 mm are used for the resonant PUT operating in the thickness mode in the frequency range of 1 MHz to 5 MHz. The piezoelectric materials require electrodes to allow the transfer of an electrical pulse to and from the transducer. This is achieved by applying thin-film electrodes of about $100nm$ thickness using the Physical Vapor Deposition (PVD) method. The live connection is generally made through a wire, and the grounding is carried out through the casing.

The casing provides mechanical support for the entire transducer and electrical shielding for the piezoelectric element. For resonant transducers, an additional

backing layer made of soft materials, such as epoxy loaded with heavy particles (e.g. tungsten fillers) is used. This serves a dual purpose in damping piezoceramics as piezoceramics have low internal damping and a typical mechanical quality factor of $\approx$ 80 [69]. This prevents ringing and achieves the excitation of short pulses to achieve the desired axial resolution.

The front layer also called the face plate, is used for wear protection and is generally made from a durable and corrosion-resistant material. For specific applications, including immersion, angle beam, and delay line transducers, the face plate also functions as an acoustic transformer[1] between the piezoelectric material and the medium through which the wave propagates.

Adhesives are used to assemble these transducer layers and can also be used as a mechanical coupling for permanently mounted transducers. Epoxy resins and cyanoacrylates are the two most commonly used adhesives and a bond line thickness of 10-120 μm is generally used. Studies have shown that the ultrasonic performance is greatly affected by the thickness and shear modulus of the adhesive layer [70, 71, 72]. Adhesives are viscoelastic and their influence on ultrasonic performance is frequency-dependent. The ultrasonic performance is more sensitive to the shear modulus at high frequency (>500 kHz) and only slightly affects the signals at low frequency (<100 kHz). At lower frequencies, the signal with thin adhesive bond lines is stronger than for those with thicker adhesive bond lines. Adhesive de-bonding or uneven distribution or air cavities have a negative impact on the ultrasonic amplitude and can also introduce a phase offset [73, 74].

The PUT transducer used in the commercial Teletest system employs PZT-5A elements that operate in TS-mode. The transducer layers are illustrated in Figure 2.7. The rectangular PZT-5A plate used in the transducer is of dimensions 13 mm x 3 mm x 0.5 mm. The piezoelectric plate is coated with nickel electrodes with a wraparound configuration that allows ground and live electrical connections to be made on the same 13 mm x 3 mm surface. An aluminium oxide (Al_2O_3) wear plate is bonded to the PZT-5A plate using a nonconductive epoxy. A stainless steel block of dimensions 13 mm x 12 mm x 12 mm is used as a backing layer to house the piezo-wear plate assembly and provide an electrical connection to the piezoelectric plate.

---

[1]Resonant transducers use a face plate of thickness equal to a quarter of the wavelength and an intermediate acoustic impedance between the piezoelectric layer and the load medium to improve the power transmission.
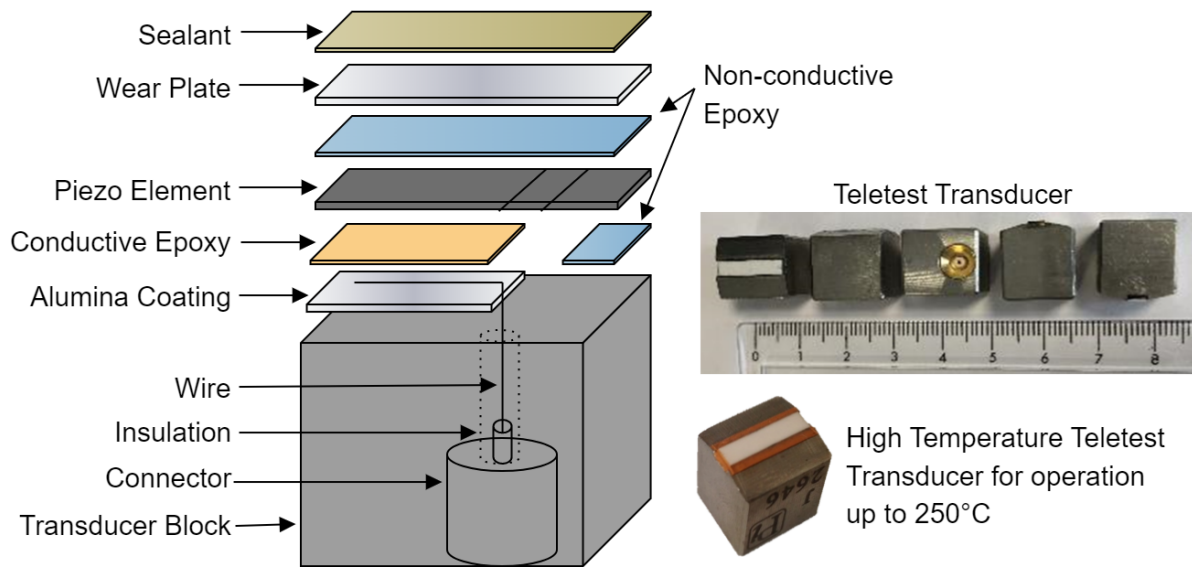
FIGURE 2.7: Schematic of the Teletest shear piezoelectric transducers show different layers. Images showing the (a) Teletest transducers and (b) high-temperature variant for operation up to 250°C.

The steel backing block has a through hole feature where the connector is fitted. A nickel wire is soldered to the connector and fed through to the top of the backing block. A section of the upper face of the backing block has an Al_2O_3 coating to provide electrical insulation and the nickel wire is placed on this coated section. A layer of non-conductive epoxy is applied on top of the wire, and a layer of conductive epoxy is used on the other side where the wrap-around electrode of the PZT-5A element joins the backing block. Thus, the steel backing serves as the ground connection to complete the circuit. A sealant is applied to the sides of the piezo-wear plate assembly to avoid moisture ingress.

2.2.6 FEA for Transducer Design

In a multi-layered piezoelectric transducer, the resonances in the frequency response function are associated with the coupling of vibration modes (eigenmodes) of the different transducer layers. For prototyping and design verification, manufacturing new transducers can be expensive and time-consuming, as many transducers may need to be manufactured and tested to find the optimal design.

Several methods have been developed to simulate piezoelectric transducers, including analytical methods based on the equivalent circuit model, mathematical models using the coupling of modes theory and FEA. Analytical methods are based on one- or two-dimensional models and are suitable for only simple geometries. They cannot be applied when anisotropic materials, nonuniform physical features, or

boundary conditions are involved. However, the FEA method provides a direct numerical approach and is implemented in several commercial software and allows the development of representative multiphysics piezoelectric transducer models.

Commercial FEA software, including ANSYS, ABAQUS, COMSOL, and OnScale [75], have the ability to model piezoelectric materials. Several studies have reported using FEA methods to analyse and optimise piezoelectric transducer designs and have demonstrated an exceptional ability to predict the transducer response through experimental validation [76]. These include the analysis of transducers with complicated geometries and their radiated sound fields as functions of frequency for different geometric features and wave propagating mediums. Studies have also employed FEA in combination with optimisation algorithms to define design parameters that maximise ultrasonic performance while minimising electrical input [77, 78].

2.2.7 Transducer Characteristics for Ultrasonic Application

The suitability of PUT depends on its sensitivity, dimensions, frequency bandwidth, and type of contact between the transducer surface and the object under investigation. Piezoelectric materials with large electromechanical coefficients (e.g. PZT-5A) are generally used for their design to achieve high ultrasonic output and therefore Signal to Noise Ratio (SNR). Their performance characteristics also depend on the interactions between their electrical, mechanical, acoustic, and thermal response functions. For example, the electrical input impedance is a function of frequency and several peaks and troughs are observed in their response functions. The transducer frequency response should be near-linear in the operating frequency range, as neighbouring resonance frequency can influence the measurement quality. It can cause mode coupling, frequency jumps, and activity dips in the sensor transfer function.

For low frequency application, the transducers operate at frequencies much lower than their first resonance frequency, and therefore the unevenness of their frequency response is much above the operating frequency range. These are also called non-resonant wideband transducers and use piezoceramics with planar dimensions in the order of several millimetres and can achieve UGW sensitivity with a broadband frequency response in the 20 kHz to 1 MHz range.

The mechanical wave generated within the piezoelectric element can be coupled to the structure by dry coupling (with high pressure), fluid coupling, or solid coupling. Generally, a couplant, usually a gel, is used for high-frequency longitudinal

applications. The coupling of shear waves requires an interface with a high modulus of rigidity, which is commonly achieved by mechanical bonding using adhesives or dry coupling with an external load. For high-temperature applications of PUT, stability of mechanical bonding, piezoelectric properties, and high electrical resistivity (low dielectric loss) are required to achieve a stable thermal response to maintain their ultrasonic performance. A review of high-temperature piezoelectric materials and low-frequency wideband non-resonant transducers is given in Chapter 3.

2.3 Ultrasonic Guided Wave Testing

2.3.1 Bulk Waves and Guided Waves

The term "ultrasound" refers to the propagation of mechanical stress waves in a medium. Two types of ultrasonic waves can propagate in isotropic solids: bulk waves and guided waves [79]. Bulk waves travel in infinite media and are not governed by boundaries. In homogeneous and isotropic materials, there are only two bulk wave modes, longitudinal (or compression) and shear waves. Bulk ultrasonic waves have different propagation speeds, which can be calculated analytically from the material properties of the propagating medium.

The velocity of compression waves (V_l) and shear waves (V_s) in an isotropic solid material is related to the Young's modulus (E), Shear modulus (G), density (ρ) and Poisson's ratio (μ). It is given by Equation (2.10) and Equation (2.11), respectively. The longitudinal and shear velocities of a typical carbon steel material are around 5800 m/s and 3200 m/s, respectively.

$$V_l = \sqrt{\frac{E(1-\mu)}{\rho(1+\mu)(1-2\mu)}} \tag{2.10}$$

$$V_s = \sqrt{\frac{E}{2\rho(1+\mu)}} = \sqrt{\frac{G}{\rho}} \tag{2.11}$$

Bulk waves travel through a material unaffected by the material boundaries. On the contrary, UGW propagate along the layers throughout the thickness of the structure and can cover large distances. The wavelength of UGW modes is large, usually comparable to the dimensions of the structure. Unlike bulk waves, an infinite number of guided wave modes can propagate in a structure.

2.3.2 Cylindrical Guided Waves Modes

In cylindrical pipe-like structures, there are three categories of guided wave modes based on their displacement patterns [80]. These are axially symmetric wave modes: longitudinal (*L*) and torsional (*T*); and non-axially symmetric flexural (*F*) modes, as illustrated in Figure 2.8. Looking down the pipe from one end, the *L* wave mode can be visualised as a travelling bulge, the *F* wave flexing the pipe in many directions, and the *T* wave as a twisting motion. The dominant particle motion of a longitudinal wave mode is axial and radial, whereas the torsional mode generates tangential displacement in the cross section of the pipe.
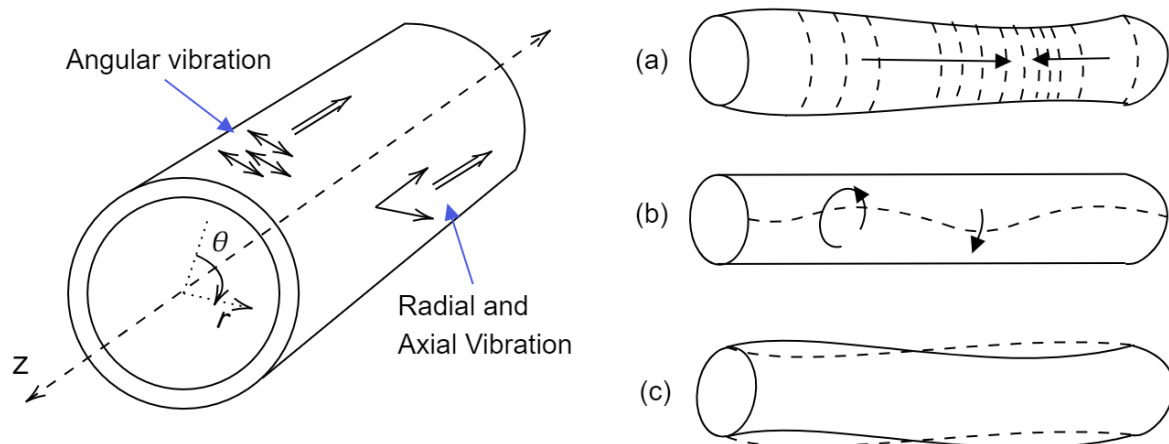
FIGURE 2.8: Illustration of the guided wave modes propagating a pipe-like structure (a) Longitudinal modes with axial and radial displacement, (b) Torsional modes with displacement in the tangential direction, and (c) flexural modes with a complex displacement varying along the circumference.

The wave modes are designated with two numbers, as defined by Meitzler [81]. The first number is the circumferential wavenumber (also known as the order), and the second denotes the sequential mode. The torsional $T(m,n)$ and longitudinal $L(m,n)$ wave modes are axially symmetric ($m = 0$); therefore, their displacement does not vary around the circumference and only changes along the thickness. For example, the $T(0,1)$ mode has a uniform rotational displacement throughout the thickness of the wall of the pipe. Wave modes of an order greater than zero, for example, $F(1,2)$, are not axially symmetric and have a non-uniform displacement distribution along the thickness.

2.3.3 Propagation Velocity and Dispersion Curves

The velocity of the guided wave modes depends not only on the material properties but also on the geometry of the structure. At a given frequency, multiple guided wave modes can be present, and the velocity of these modes can change with frequency. This response is due to the nonlinear relationship between the wavenumber or spatial frequency of the wave modes (k) and the temporal frequency (ω).

When an ultrasonic pulse is transmitted, it will contain many frequencies, due to its finite length as opposed to a continuous sinusoidal wave at a single frequency. The propagation properties of the guided wave modes are described by the phase velocity (V_p) and the group velocity (V_g). The velocity of a single peak within a pulse (or phase within the wave packet) is termed phase velocity and is described by Equation (2.12). The velocity of the pulse (or wave packet) is called the group velocity (v_g), and is given by Equation (2.13).

$$V_p = \frac{\omega}{k} \tag{2.12}$$

$$V_g = \frac{\delta \omega}{\delta k} = V_p + \frac{\delta V_p}{\delta V_k} * k \tag{2.13}$$

The pulse may not travel at the phase velocity of the transmitted centre frequency. If the phase and group velocities are different ($v_p \neq v_g$), the pulse is said to be dispersive. Dispersion elongates the wave packets, increasing the envelope and lowering its amplitude as different frequency components within the wave travel at different velocities. However, if $v_p = v_g$, the wave packet will travel dispersion-free, and the shape of the wave packet will be maintained as it propagates [82]. Dispersion degrades the resolution of the UGW response, as it causes signals to spread over time or space and, consequently, contributes to coherent noise [83].

Dispersion curves are used to illustrate the variation in v_p and v_g of each wave mode over a range of frequencies. The dispersion curves are well-known for simple plate and pipe like structures. Semi-analytical finite element (SAFE) methods have become convenient for computing the dispersion curves of a homogeneous waveguide. They are available through open-source commercially available software such as Disperse [84] and GUIGUW [85]; and can also be generated using commercial FEA software using Floquet boundary conditions [86]. These softwares can calculate the dispersion curves of complex geometries with arbitrary cross-section and multi-layer structures. The dispersion curves of a 4" Schedule 40 pipe are shown in Figure 2.9.
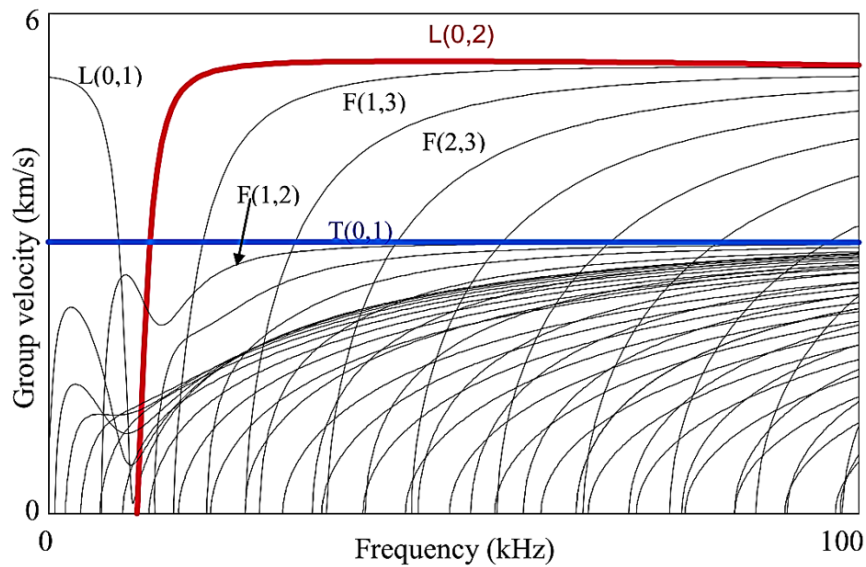
FIGURE 2.9: Dispersion curves for a 4-inch NPS Schedule 40 steel pipe [87].

The dispersion curve shows the presence of more than 50 wave modes below 100 kHz. For non-dispersive wave modes in a particular frequency range, the phase velocity dispersion curve will be flat with v_p close to v_g, which can be seen with the highlighted fundamental torsional $T(0,1)$ and longitudinal $L(0,2)$ modes above a frequency of around 20 kHz. On the contrary, dispersive wave modes spread in space over time as they have frequency-dependent velocities and different v_p and v_g.

2.3.4 Guided Wave Mode Selection and Transduction

Axisymmetric wave modes are preferred for GWT because they provide full circumferential coverage with their uniform displacement throughout the thickness of the pipe wall. Their sensitivity to defects on the inner or outer surface of the pipe is the same. There are three axisymmetric wave modes, $L(0,1)$, $L(0,2)$, and $T(0,1)$, in this frequency range commonly used for GWT. A single transducer excites all UGW modes (axisymmetric and non-axisymmetric) within the frequency bandwidth of the excitation signal [88]. The excitation of multiple wave modes and their dispersive nature make the measurements complex and their interpretation challenging.

A single-wave mode is typically used for GWT to determine the time of arrival of an echo. An array of transducers is used to selectively excite axisymmetric wave modes and suppress non-axisymmetric wave modes. It has been shown that the generation of non-axisymmetric flexural modes $F(n,1)$ present in the excitation frequency region can be avoided when more than n transducers are used around the circumference [89].

For example, a 16-transducer array is required for a 4-inch NPS Schedule 40 pipe that has a cutoff frequency of $F(16,1)$ at 96 kHz.

When an axisymmetric wave is generated at a given pipe location, it travels in both directions. For time-of-flight analysis of ultrasonic measurements, it is desirable to control the directionality of guided waves. This has been achieved by combining two arrays of transducers separated by a specified axial separation (quarter wavelength), generating waves that cancel in one direction and add constructively in the other [87]. A mathematical interpretation of this is explained in [90].

The initial application of GWT employed the $L(0,2)$ wave mode due to its faster velocity and relatively constant phase velocity at high frequencies [91, 92, 93]. Two circumferential rings of the transducer were used to obtain unidirectional propagation (by applying time delays and phase manipulation between the two transducer rings) and achieved distances of almost fifty metres with 70 kHz signals. However, the presence of the second axially symmetric mode $L(0,1)$ and dispersion characteristic limited the operation at lower frequencies and complicated the interpretation of the results.

Subsequent testing methodologies used the fundamental axisymmetric torsional wave mode $T(0,1)$, which is nondispersive throughout the frequency range [94]. Thus, the excitation of the $T(0,1)$ mode can be isolated from other modes, thus simplifying the interpretation of the signal. Torsional forcing can be achieved by rotating the shear transducer used for the $L(0,2)$ mode by 90°to apply the force in the circumferential or tangential direction rather than axially as illustrated in Figure 2.10.
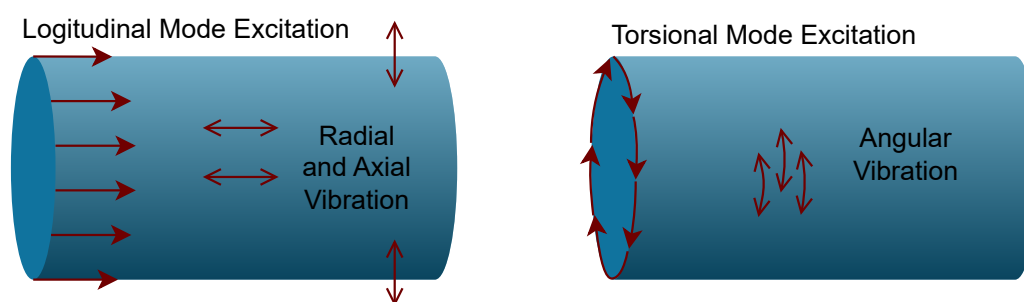
FIGURE 2.10: Schematic diagram showing the excitation of axisymmetric Longitudinal and Torsional modes on a pipe.

Studies have been conducted to explore the potential of the $T(0,1)$ mode in the MHz frequency range, which can lead to improved axial resolution [95]. But in the context of GWT, $T(0,1)$ is generally used at frequencies lower than 120 kHz [96]. For standard NPS pipe sizes, there are no higher-order torsional modes in the range of

UGW frequencies. For example, the cut-off frequency of the higher order torsional mode $T(0,2)$ is greater than 300 kHz for a 3-inch NPS Schedule 40 pipe [97]. Being the only torsional mode in the frequency range of interest, only two rings of transducers are required. The torsional mode has an additional advantage; it is not influenced by the presence of fluid inside the pipe, unlike the $L(0,2)$ mode due to its radial displacement.

2.3.5 Guided Wave Propagation

The propagating ultrasonic guided waves are affected by the characteristics of the pipe and GWT analyses these reflections to identify a potential flaw. Several studies have explored the interaction of axisymmetric wave modes with defects and features in pipes such as flanges and pipe supports [89, 98]. When an axisymmetric wave mode $T(0,1)$ or $L(0,2)$ is incident on an axisymmetric feature such as the flange or uniform weld; only axisymmetric modes are reflected. This interaction is described by the reflection coefficient, which is the ratio of the reflected and incident wave amplitudes. However, defects such as localised corrosion or features such as pipe supports are generally non-axisymmetric and lead to a complex ultrasonic response due to mode conversion [99]. With non-axisymmetric defects, apart from the reflection of part of the incoming wave, energy is also converted to other modes, e.g., flexural modes [100]. Analysis of these flexural modes can provide further information on the circumferential extent of the defect. Defects with a smaller circumferential extent will generate larger-amplitude flexural modes. FEA methods are generally used to calculate the reflection coefficients [101]. These studies have shown that the reflection from axial defects varies as a function of its dimensions to the wavelength due to the interference between the waves reflected from the two ends of the defect.

The interaction of the $T(0,1)$ wave mode with non-axisymmetric defects such as cracks, notches, and holes has been extensively studied [102, 103, 104]. It can be interpreted that the most influential factor on the reflection coefficient is the reduction in the cross-sectional area of the pipe. However, other features such as the shape of the defect, its axial extent, and frequency also have an effect on the reflection of the torsional mode [101]. The cross-section loss and reflection coefficients may be similar for deep-localised defects and much larger but shallower defects, although the former is more critical. Thus, the reflected wave amplitude can only give an indication of the size and severity of the defect.

2.3.6 Effect of Temperature on Guided Waves

Temperature can influence UGW by changing the amplitude and phase of the signals [105]. This is due to the mechanical properties of the pipe, the ultrasonic transducers, and their bonding. Changes in signal amplitude are generally due to changes in the temperature-dependent properties of the ultrasonic transducer, particularly piezoelectric and adhesive materials [106]. However, with small temperature variations of a few degrees, the effect on the performance of the transducer is significantly less than that on wave propagation [107]. It is possible to minimise these variabilities by carefully selecting adhesives and transducer materials.

The phase change in the transducer signals is mainly attributable to the change in wave propagation velocity due to changes in the mechanical properties of the pipe [46]. The relevant mechanical properties of the pipe are the elastic and shear moduli, acoustic absorption, and density. Thermal expansion changes the propagation distance directly and indirectly through changes in pipe thickness. These, in turn, affect the dispersion curves and velocity of the guided waves.

Temperature influence can be described by considering two Hanning-windowed tone-burst signals, s_x and s_y, representing the baseline and the current signal, respectively. The current signal is measured at a different temperature, so it expands in time by δt, which is the time shift, represented by:

$$s_1 = u_0 h(t) sin\omega t \tag{2.14}$$

$$s_2 = u_0 h(t) sin\omega (t + \delta t) \tag{2.15}$$

where $h(t)$ is the Hanning window function, u_0 is the signal amplitude, ω is the angular frequency, and t is time. The relationship between the time (difference in Time of Arrival (TOA)) of the signal and the change in temperature can be written as follows.

$$\delta t = \frac{d}{V_p}(\alpha - \gamma)\delta T \tag{2.16}$$

Here, δt is the difference in the arrival times of the signals when the structure changes temperature as δT. d is the distance propagated by the wave of phase velocity V_p. α is the thermal expansion coefficient and γ is the phase velocity change coefficient. γ is

usually significantly greater than α; therefore, from Equation (2.16), it can be seen that the change in wave velocity contributes to the time shift due to temperature variations.

This relation suggests that an increase in temperature will always result in a positive δt, as this will increase the propagation path due to thermal expansion of the structure and reduce the phase velocity. The effect of temperature variation increases with an increase in distance propagated by the wave, as the time shift is directly proportional to the propagation distance. Also, the inverse relation to the wave velocity suggests that the faster modes will be less affected than the slower ones.

The temperature-related shift of the UGW signals can be observed as a change in the instantaneous phase. The TOA of a wave packet is shown to have a linear relationship with temperature, within a limited temperature range. Therefore, the instantaneous phase difference of two UGW signals with different temperatures is proportional to the temperature difference. This can be expressed as follows:

$$args_2(t) - args_0(t) = \frac{T_2 - T_0}{T_1 - T_0}[args_1(t) - args_0(t)] \tag{2.17}$$

Where $s_0(t)$, $s_1(t)$ and $s_2(t)$ are the UGW signals at temperatures T_0, T_1 and T_2, respectively, arg denotes the instantaneous phase of the signal.

These temperature-influenced changes in the UGW signals, including phase shift, arrival time, and signal amplitude, can decrease the sensitivity and probability of detecting damage. Signal processing methods are employed to reduce these temperature effects and maintain sensitivity, and are introduced in Section 2.4.5.

2.4 Signal Processing for UGW

UGW measurements produce low signal amplitudes and are often influenced by several sources of electrical noise. When a defect appears in the structure under study, the amplitude and frequency of its corresponding ultrasonic echo signal change. Several signal processing methods are available to extract these damage-sensitive features from the time, frequency, or time-frequency domains. Here, the fundamentals of signal processing methods used to analyse UGW measurements in this thesis are briefly discussed. The review of recent work on signal processing for EOC (e.g. temperature) compensation and approaches for damage detection and monitoring using historic SHM data are given in Chapter 3.

2.4.1 Discrete Pulse Excitation in the Frequency Domain

To achieve the highest possible resolution, the ultrasonic excitation signals should be short. However, short pulses have a large bandwidth in the frequency domain, presenting issues if the transducer has a limited bandwidth or if dispersive wave modes can be excited in the frequency range. Generally, a compromise is made and the excitation signal consists of a few cycles. A window function is applied to the high-frequency carrier wave to generate a discrete excitation signal, often called a tone burst signal. Hanning window is a standard[2] window function used in the UGW application, as it significantly suppresses the frequencies of the side lobe. The Hanning window $\omega(t)$ is defined as [109]:

$$\omega(t) = \frac{1}{2}(1 - cos(\frac{2\pi f_c}{N})) \tag{2.18}$$

Here, f_c is the frequency of the carrier sine wave and N is the number of cycles of the Hanning window signal. The frequency content is a broadband signal, since the window function is applied to the carrier harmonic signal. The frequency domain $F(\omega)$ of the Hanning windowed signal $f(t)$ is defined by:

$$F(\omega) = \int_{-\infty}^{\infty} f(t).e^{-i\omega t}dt \tag{2.19}$$

The main frequency content of the tone burst signal is centred on the carrier frequency f_c. The bandwidth of the main lobe is related to the number of cycles and has a range of $\pm(2f_c/N)$ [110]. This bandwidth is generally used to apply the appropriate filtering of the acquired signal. The presented work utilises Hanning window modulated toneburst signals as excitation signals. An example of a five-cycle 27 kHz Hanning windowed tone-burst signal, and its frequency domain, is shown in Figure 2.11.
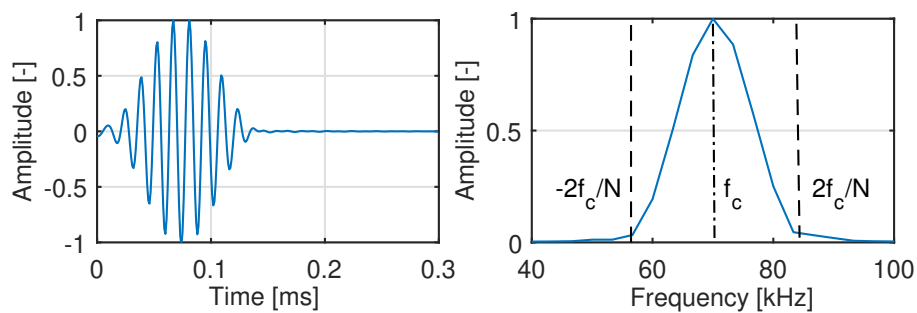
FIGURE 2.11: A 70kHz 10 cycle Hanning modulated tone burst excitation signal and the frequency content of the signal showing the bandwidth on the right.

---

[2]Several other window functions such as Gaussian and Reicker are also available [108].

2.4.2 Hilbert Transform for Envelope Detection

It is often desirable to recover the envelope of a measured ultrasonic signals to analyse the signal amplitude and arrival time. A commonly used method for envelope detection is the Hilbert transform [111]. The Hilbert transform $f_1(t)$ of a real signal $f(t)$ is given by convolution:

$$f_1(t) = -\frac{1}{\pi} \int_{-\infty}^{\infty} \frac{f(x)}{t-x} dx \tag{2.20}$$

The Fourier transform of $f(t)$ and $f_1(t)$ is $F(\omega)$ and $F_1(\omega)$ respectively and are related in the frequency domain by the following expression:

$$F_1(\omega) = j.F(\omega).sgn(\omega) \tag{2.21}$$

Where sgn(ω) is the Signum function, the Hilbert transform recovers the imaginary part of the signal. Then, both the phase and the envelope can be calculated as the Hilbert transform of the signal is known. An example with two UGW signals measured at different ambient temperatures along with their detected envelope and phase are shown in Figure 2.12.
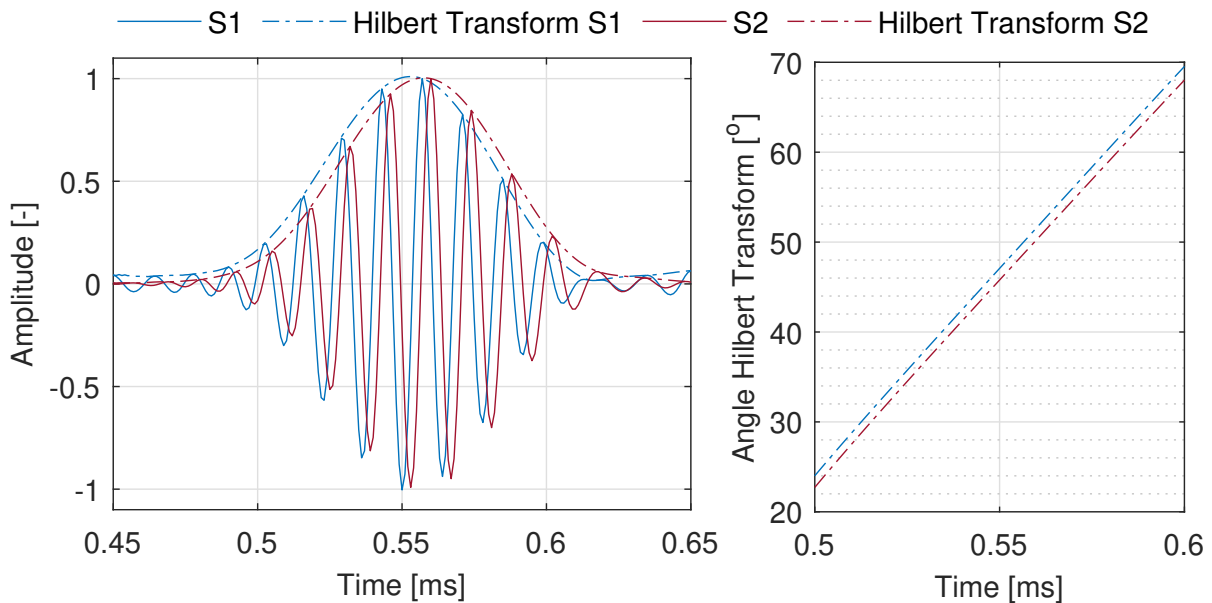
FIGURE 2.12: Ultrasonic guided wave measurement at 35 kHz with ambient temperature variation showing time of arrival and phase difference using amplitude and angle derived using the Hilbert transforms of measurements.

2.4.3 Signal-to-Noise Ratio in UGW Measurements

By definition, SNR is the power of the useful signal relative to the power of unwanted interference [112] and is generally evaluated as the ratio of Root Mean Square (RMS) value. As the UGW signals contain discontinuous wave packets, RMS does not represent the actual signal power. Therefore, for the UGW application, SNR is calculated using the signal amplitude ratio to the noise RMS value using Equation (2.22). To achieve a suitable defect sensitivity GWT application require large SNR; for example, torsional wave pipe inspection requires a SNR greater than 40 dB [113].

$$\text{SNR (dB)} = 20 \cdot \log_{10}\left(\frac{\text{Signal Amplitude}}{\text{Noise RMS}}\right) \tag{2.22}$$

Signal filtering is usually performed on the signal acquisition instrument (electrical analogue filtering) or during post-processing (digital filter) to improve SNR the ultrasonic measurements. Measurement SNR can be further improved when the excitation signal level is increased; hence, larger signal amplitudes are recorded[3]. Furthermore, SNR of the measurement can also be increased by performing averages of the acquired signals. The measured noise is incoherent and can gradually be decreased by averaging, whereas the signal amplitude remains unchanged. However, this assumes that the EOC effect does not change the signal during the averaging process. Ultrasonic measurements may also contain coherent noise due to unwanted mode or signal dispersion, which are challenging to isolate and filter.

2.4.4 Time-Frequency Domain Analysis

Time frequency analysis extends the time domain and frequency domain analysis by representing how the frequency content of the signal changes over time. This representation is generally displayed as a spectrogram or time-frequency plot. Short-Time Fourier Transform (STFT) is a common time-frequency analysis. It divides the signal in the time domain into small overlapping windows and computes the Fast Fourier Transform (FFT) for these windows. When the window is moved along the signal, a time-frequency plot is created showing how the frequency components change over time. The STFT provides good frequency resolution at the cost of time resolution, as longer windows yield better frequency information but lose temporal details, while shorter windows provide better temporal details but lose frequency accuracy.

---

[3]The excitation signal levels are often limited due to instrumentation and safety constraints [114].

The wavelet transform is another method used to analyse the frequency content of a signal at different resolutions. It utilises wavelet functions with varying scales and positions to achieve this. The wavelet transform offers a more balanced compromise between time and frequency resolution compared to STFT [115]. Continuous Wavelet Transform (CWT) and Discrete Wavelet Transform (DWT) are two different mathematical formulations of the wavelet transform. CWT is computationally expensive, but offers a higher resolution time-frequency analysis compared to DWT. As the CWT algorithm automatically adjusts the window length based on the local frequency scale, it offers better resolution for signals with large frequency changes compared to STFT. CWT is used to perform the time-frequency analysis of the ultrasonic measurements in the presented work.

In CWT, a wavelet function, $\psi(t)$, is used, which is also known as the Mother Wavelet. This wavelet function is oscillatory and localised in both time and frequency. It has a centre frequency and bandwidth. The CWT examines a signal, $x(t)$, by scaling and shifting the wavelet function across the signal. This produces a set of wavelets, each of which represents the signal at a different scale and position. The mathematical expression of CWT is:

$$CWT(a,b) = \int [x(t) * \psi * [\frac{(t-b)}{a}]]dt \qquad (2.23)$$

where a represents the scale factor by which the wavelet is stretched or compressed, b represents the translation (position), and $*$ denotes the complex conjugate. The CWT provides a time-frequency representation of the signal, where the scale parameter a corresponds to the frequency and the translation parameter b corresponds to the time. By varying a and b, a 2D representation showing how different frequency components of the signal evolve over time can be obtained. An example of CWT based on Time-frequency response (TFR) of an ultrasonic measurement is shown in Figure 2.13.
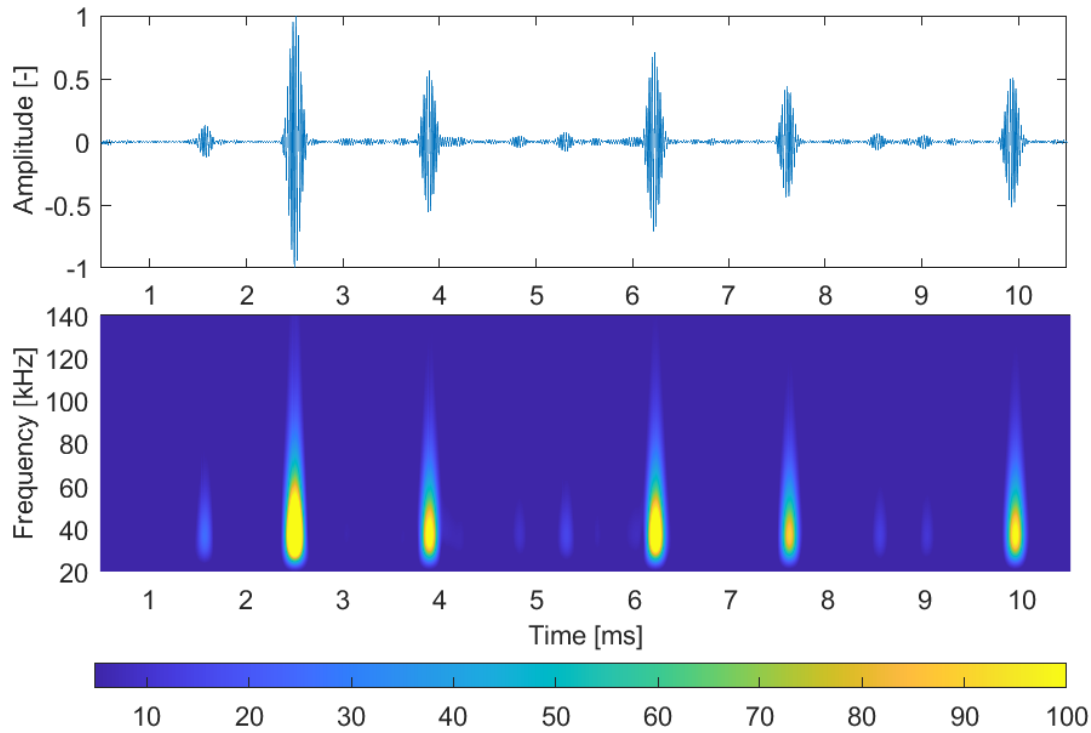
FIGURE 2.13: Example of ultrasonic guided wave measurement with 10 cycles 35 kHz Hanning modulated toneburst showing multiple reflections in the time series and the corresponding time frequency representation using continuous wavelet transform.

2.4.5 Baseline Subtraction and Temperature Compensation

The monitoring signals based on UGW are analysed to provide information on the presence of a defect and information on its type, location, and severity. The most common signal processing technique for SHM applications that use GWT is the baseline subtraction method [46]. Initially, a signal is collected when the structure is known to be in a defect-free state. This baseline signal is then compared with subsequent measurements using various techniques. The difference between two time domain signals, $s_1(t)$ and $s_2(t)$ is computed as:

$$Err = 20log\frac{\|(|s_2(t) - s_1(t)|)\|_\infty}{\|(|s_1(t)|)\|_\infty} \tag{2.24}$$

where $\|.\|_\infty$ is the l_∞ - norm of a vector. Ideally, any change in the ultrasonic signal refers to a change in the structure alone. However, UGW data are susceptible to changes in EOCs such as temperature, humidity, pressure, vibration, and flow, which influence electronic devices, the behaviour of the transducer, and even the structure itself. Of these EOCs, temperature has a dominating effect, as described in Section 2.3.6.

The decibel values (dB) of the residual signal are generally calculated using envelope detected amplitudes relative to those of a known feature in the baseline signal. This relation is given by:

$$res_{dB}(t) = 20log10\left(\frac{|s_a(t)|}{|b_a(t = p/v_{gr}^{T0})|}\right) \tag{2.25}$$

The relationship between the baseline subtraction residual and the temperature can be described by subtracting the signal $s_2(t)$ from $s_1(t)$ and defining $U_0 = u_0 h(t)$:

$$s_2 - s_1 = U_0(sin\omega(t + \delta t) - sin\omega t) \tag{2.26}$$

where $h(t)$ is the Hanning window function, u_0 is the signal amplitude, ω is the angular frequency, and t is time. If δt is small enough, a small angle approximation can be used:

$$|s_2 - s_1|_{max} = 2\pi f U_0 \delta t \tag{2.27}$$

Where f is the frequency and from Equation (2.26), it can be seen that if two waves of equal amplitude arrive in phase, the amplitude of the residual signal will double. This suggests that the residual signal is proportional to the temperature difference between the current signal and the baseline, the number of overlapping arrivals and the excitation frequency. The number of reflectors in complex structures increases; therefore, interference will occur more frequently, increasing the subtraction residual of the baseline. Taking into account $\lambda = v/f$, for non-dispersive modes (with a velocity constant with frequency), the residual for a given propagation distance is directly proportional to frequency. This is an important issue to consider when choosing the mode and frequency of the guided wave monitoring system.

These temperature-induced variations in UGW measurements can lead to a significant subtraction residual that can mask the damage response or lead to false diagnostics [116]. This is illustrated in the example shown in Figure 2.14.
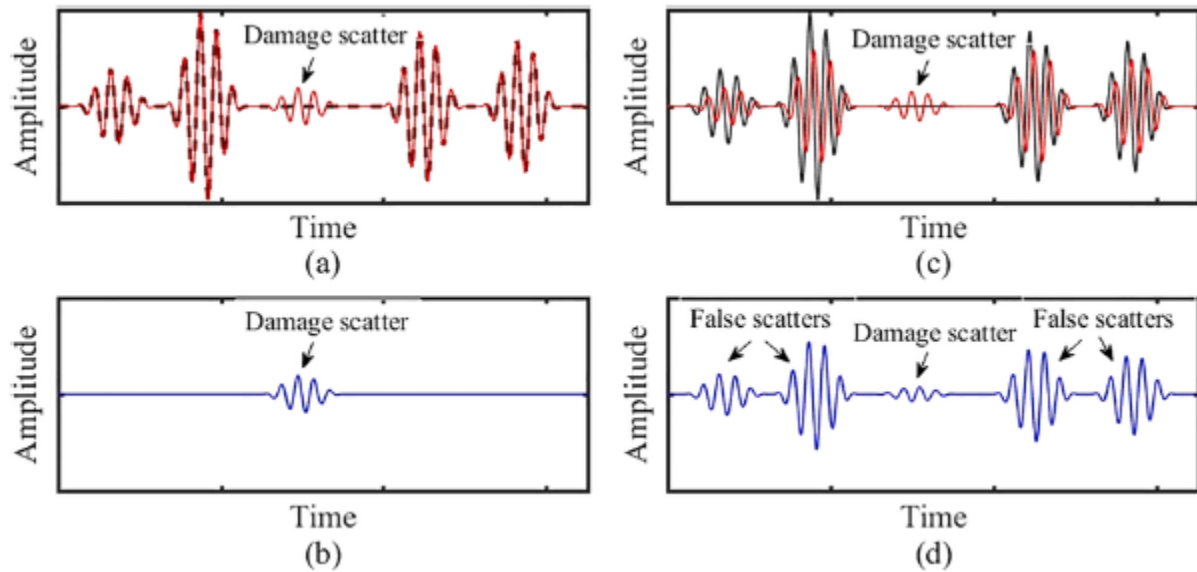
FIGURE 2.14: (a) Baseline and current signals, obtained from the same EOCs or after temperature compensation; (b) residual signal derived from subtracting signals in (a); (c) baseline and current signals obtained from different EOCs or without temperature compensation; (d) residual signal derived from subtracting signals in (c) [117].

It is therefore crucial to minimise the residual from the subtraction between the signals measured from the undamaged structure at varying temperatures. Baseline subtraction is generally used with temperature compensation techniques, and depending on their effectiveness, the residual signal will change only due to a structural change. Various compensation and signal processing techniques have been developed to overcome the effect of temperature and are reviewed in Chapter 3.

2.5 Summary

This chapter summarised the relevant theoretical background on PUT, UGW and signal processing. These are the enabling technologies for the application of GWT for SHM of HTPs and are referred to in the rest of the thesis. The piezoelectric theory is introduced to understand the behaviour of the material at high temperatures and its application for the design of PUT. An overview of GWT technology covered the fundamental theory of UGW in pipes, the components of the system, and the desired performance parameters for HT-SHM application. The fundamentals of the ultrasonic signal processing techniques applied for GWT under varying temperature conditions are discussed.

Chapter 3

Literature Review

3.1 Introduction

This chapter reviews the most significant work related to the present research on the application of GWT to SHM of HTPs. Critical review has been documented in areas where contributions to knowledge have been made by the thesis. The review covers published research[1] on the topics shown in Figure 3.1. This included HT piezoelectric materials, HT-PUT design, modelling and development, and UGW application for SHM at varying temperatures, including temperature compensation and defect detection techniques.
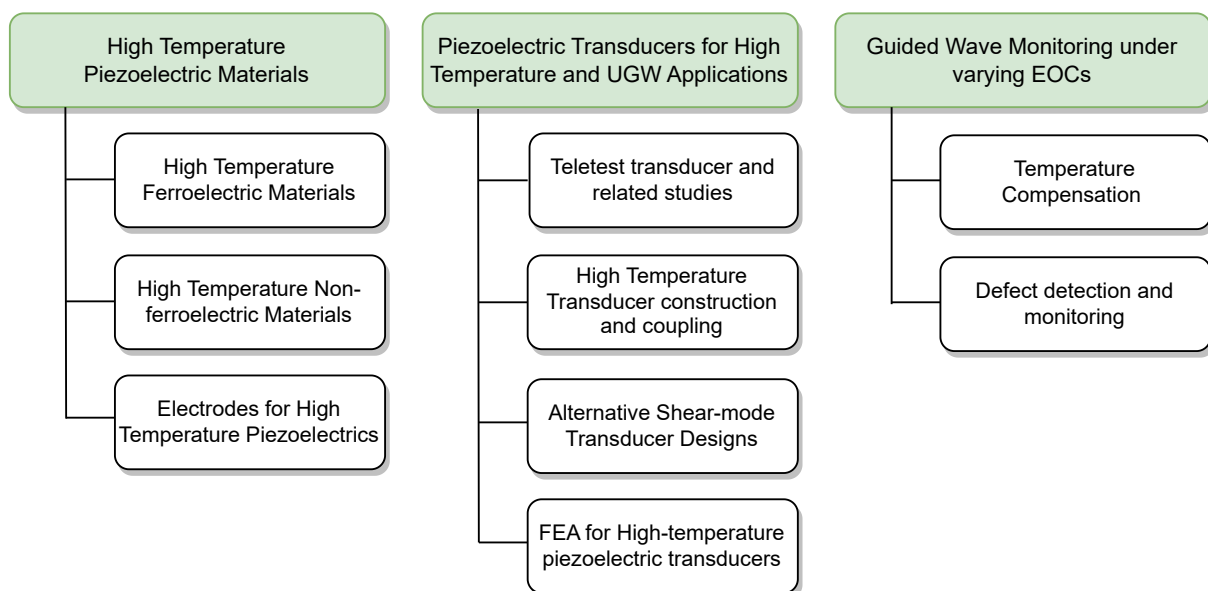
FIGURE 3.1: Topics covered in the literature review for structural health monitoring of high temperature pipelines using ultrasonic transducers.

---

[1]The presented research and development activities were completed in 2019 but this review includes the reported research and findings till 2022.

3.2 High Temperature Piezoelectric Materials

Increasing demand for the monitoring of critical structures in aerospace, material processing, and power plants; has led to the research and development of novel HT piezoelectric materials. These materials have been used in accelerometers, pressure sensors, and ultrasonic transducer applications. This review focusses on polycrstalline ferroelectrics and piezoelectric single crystals and considers both commercially available and those under development. The following sections provide a critical review of these materials, including their electromechanical properties for operation in TS-mode and limitations relevant for the HT-PUT application.

3.2.1 Ferroelectrics Materials

Ferroelectrics offer high piezoelectric performance, but their operation at high temperature is limited due to the Curie temperature and can degrade over time due to domain-related thermal ageing, as described in Chapter 2. Significant research has been done to develop ferroelectric materials with high Curie temperatures [118, 119, 120]. Depending on the crystalline structure, these materials can be classified into the following categories.

Polycrystallines with Perovskite and Tungsten Bronze Structures

Ferroelectrics with perovskite structure (ABO_3) can achieve high sensitivity but offer poor temperature stability. The most widely used Lead Zirconate Titanate ($Pb(Zr, Ti)O3$ or PZT) belongs to this category and offers a high electromechanical coupling $k \approx 70\%$ and a piezoelectric coefficient $d \approx 370pC/N$. However, with a $T_c \approx 350°C$, they are limited for long-term operation below $(1/2T_c)$, above which they are known to undergo thermally activated ageing [121]. Lead titanate ($PbTiO_3$ or PT) is another example with $T_c = 490°C$, however, undergoes sudden dielectric losses at 350°C [122]. Studies have also observed that the influence of temperature is more significant at low frequencies and increased over a period of 36 hours [123]. Bismuth-based perovskite (BS-PT) has also been extensively studied, but $T_c = 450°C$ limits its HT operation [124, 125].

Ferroelectrics with tungsten bronze and oxygen octahedral structures (AB_2O_6), such as lead metaniobate ($PbNb_2O_6$), offer a high piezoelectric coefficient (d_{15}=95pC/N; k_{15}=0.25; g_{15}=31$mV.m/N$) [126]. However, their high temperature operation is restricted due to $T_c \approx 460°C$ and high conductivity above 300°C.

Ferroelectrics with perovskite layer structure (*PLS*) have a general formula $A_2B_2O_7$. They have better temperature stability compared to perovskites but offer lower sensitivity. Two compounds of this family - $Sr_2Nb_2O_7$ and $La_2Ti_2O_7$ are well recognised due to their very high T_c of approximately 1300°C and 1500°C, respectively. They offer $d \approx 3pC/N$ and a high electrical resistivity of the order $10^8 \Omega m$ at 500°C and $10^7 \Omega m$ at 700°C. Their proposed operating temperatures are in the 900°C range. However, the growth of good quality crystals is a challenge due to the high melting points of these compounds, and therefore fabrication is limited to thin film techniques such as sol-gel [127].

Bismuth Layer Structured Ferroelectrics

Bismuth-layer-structured ferroelectrics (BLSF) is a family of piezoelectric materials that includes compounds such as $Bi_4Ti_3O_{12}$ (BIT), $SrBi_2Ta_2O_9$ (SBT), $CaBi_2Nb_2O_9$ (CBN), Bi_3TiNbO_9, $CaBi_4Ti_4O_{15}$ (CBT). They possess low dielectric permittivity and piezoelectric properties (e.g. CBN has $d = 5pC/N$) but offer high T_c of up to 950°C and low ageing rates. Doping can improve their piezoelectric properties, but with a compromise to T_c, resulting in a range of d and T_c of $10 - 45pC/N$ and 500-900°C [128]. Modifications to BIT with suitable doping have achieved $d \approx 20pC/N$ with $T_c = 650°C$ and several modifications are now commercially available. A study evaluated two such commercially available BIT maetrials and showed a stable response up to 500°C where the values of k_t and d_{13} ranged between 0.19-0.23 and 1.3-4.6pC/N, respectively [129]. Although they have shown improved temperature stability; thermal ageing limits their application to below 600°C. A study of high temperature endurance of BIT showed a decrease in performance (5%) for 34 days with an average temperature of 365°C [130]. Limited studies have evaluated their ageing response over extended time periods.

Crystals with Corundum structure

Piezoelectric crystals with a corundum structure (point group $3m$) include Lithium Niobate ($LiNbO_3$) and Lithium Tantalate ($LiTaO_3$) with T_c of 1150°C and 700°C, respectively. Lithium Niobate has $d_{15} = 68pC/N$, which is much higher than its $d_{33} = 6pC/N$, and therefore has been extensively studied for TS-mode operation in transducers. Studies have reported a variation in TS-mode electromechanical coupling factor of 45-70% with variation less than 2% up to 500°C [131]. However, it is known to suffer from chemical decomposition at 600°C due to oxygen loss [132]. This results in a decrease in resistivity, variations in electromechanical performance, and increased attenuation. A study investigated the losses and the ageing response of a

$LiNbO_3$ device up to 450°C for more than 10 days [133]. Continuous performance degradation below 450°C was reported and described due to chemical decomposition above the congruent melting point of 300°C.

3.2.2 Non-ferroelectric Materials

The limitations of ferroelectric materials motivated research on several innovative single-crystalline piezoelectric materials that are structurally and compositionally stable, can retain their piezoelectricity at higher temperatures and offer excellent thermal stability. Many articles have reported a comprehensive review of recent developments in high-temperature crystals [134, 135, 120].

Quartz and Tourmaline

Quartz (SiO_2) belongs to the triclinic crystal system (point group 32), and was one of the first discovered piezoelectric single crystals. Synthetic quartz is hydrothermally grown and different crystal cuts have been used for a variety of applications; for example, AT-cut quartz is used in TS-mode for oscillators in clock sources, and ST-cut quartz has a zero temperature coefficient and is used for Surface Acoustic Wave (SAW) devices. However, it offers a low piezoelectric coefficient $d_{11} \approx 2.3pC/N$, undergoes mechanical twinning at 300°C and phase transition at 537°C from $\alpha-$ quartz to its non-piezoelectric $\beta-$ form [136]. Tourmaline belongs to the symmetry $3m$ and has a piezoelectric coefficient $d_{33} = 1.8pC/N$. Tormaline does not undergo twinning or phase change, but its application is limited because of its strong pyroelectric effect and the difficulty of growing crystals of usable sizes. Lithium Tetraborate ($Li_2B_4O_7$) belongs to the tetragonal symmetry $4mm$ and does not undergo phase transition until its melting point at 917°C. It has been reported to have $d_{33} = 19.5pC/N$, but is not suitable for low-frequency applications due to high levels of ionic conductivity [137].

Gallium Phosphate and other Quartz Analogues

Quartz-like crystals such as gallium orthophosphate ($GaPO_4$), berlinite ($AlPO_4$) and gallium arsenate ($GaAsO_4$) can be synthesised using hydrothermal processes. $GaPO_4$ shows features similar to quartz, such as a high electrical resistivity and a mechanical quality factor, but it also exhibits high electromechanical coupling and greater piezoelectric sensitivity until the phase transition α to β occurs around 970°C [138]. It offers high electrical resistivity, low acoustic losses, no pyroelectricity, and thermally stable properties, for example, a constant value of d_{11} (two times as quartz) up to 700°C. An X-cut $GaPO_4$ resonator was investigated for phased arrays and displayed

encouraging results for the SHM application [139, 140, 141]. A 3 mm x 12 mm x 1 mm plate with platinum electrodes (100 nm thick) was used for HT-EMI characterisation at temperatures up to 580°C. A stable electromechanical response with k_t of 7.5%, d_{11} of 4 pC/N and elastic properties S_E^{11} and C_E^{11} of 19 pm^2/N and 61.6 GPa, respectively, was reported. The physical and electromechanical characterisation of the material with high-temperature exposure to 705°C did not show an effect on the microstructure or chemical composition of the material [142]. The temperature limit is due to the decrease in the mechanical quality factor due to the increase in structural disorder at temperatures above 700°C [120]. It is commercially available from Roditi [143] and Piezocryst Advances Sensorics [144].

In 1994, AVL developed the first commercial product, GM12D, an uncooled pressure sensor for combustion engines. Since then, $GaPO_4$ has been explored for a large field of HT resonator applications, including temperature-compensated cuts for Bulk Acoustic Wave (BAW), SAW and microbalance devices operating at temperatures up to 720°C [145, 146, 147]. Previous work has investigated $GaPO_4$ as a pressure transducer and has evaluated its quality factor and sensitivity to temperature and pressure variations [148]. Studies have investigated singly rotated Y-cut $GaPO_4$ resonators with different angles and reported that the Y-11°cut is 100 times less sensitive to temperature compared to AT-cut quartz [149].

Langasite, Melitite and Rare-earth Oxyborate

LGS has been thoroughly reviewed and its performance has been compared to $GaPO_4$ and shows more promising performance [150]. Dielectric constant 3 times as $GaPO_4$, piezoelectric constant 2 times as $GaPO_4$. High-temperature SAW sensors based on LGS crystals have been developed and evaluated at temperatures up to 850°C [151]. The study showed good performance for the SAW application for continuous operation up to 600°C. The sensing performance of langasite sensors can be limited due to its relatively low electrical resistivity and low quality factor at elevated temperatures, which result from the transport and diffusion of oxygen ions in the lattice [152].

$RECa_4O(BO_3)_3$ - (RECOB, Re:rare-earth elements) has promising dielectric, piezoelectric, and electromechanical properties up to 1000°C. $YGdCOB$ has demonstrated a variation in d_{26} of less than 5% [135]. Yttrium calcium oxyborate (YCOB) is one of the rare-earth calcium oxyborate single crystals which has gained special attention for ultra-high temperature applications. YCOB is known to be a promising candidate for HT sensors due to its stable piezoelectric properties and no phase transformation before the melting temperature of 1500°C. The temperature

independence of their electromechanical properties ($k = 15\%$ and $d = 4pC/N$) was demonstrated to be up to 950°C [153]. A study developed a TS-mode accelerometer for vibration detection applications and tested at temperatures up to 1000°C at frequencies ranging from 50-350 Hz [154]. Stable performance was observed by a 9-hour test at 1000°C that demonstrates the reliability of the accelerometer prototype.

$Yb^{3+}:Ca_3NbGa_3Si_2O_{14}$ ($Yb^{3+}:CNGS$) single crystal is relatively new with an operating temperature range of up to 800°C. A study characterised their electromechanical properties using HT-EMIS. The observed variation in dielectric constant (ϵ_{11}/ϵ_0; 17.89 to 21.78), elastic constant (s_{11}; 9.01 to 9.57 pm^2/N) and piezoelectric coefficients (d_{11}; 3.87 to 5.10 pC/N) was relatively low in the 20-30% range [155]. $Ca_3TaGa_3Si_2O_{14}(CTGS)$ is another single crystal that has been characterised at temperatures up to 900°C [156] and demonstrated good temperature stability. The divergence in the elastic stiffness constant, piezoelectric constant (e_{11}) and dielectric constant was up to 20%, 16% and 9%, respectively. The dependence of temperature on the electromechanical properties of calcium yttrium aluminate ($CaYAl_3O_7$) has also been characterised up to 500°C [157]. The electromechanical coupling k and the piezoelectric coefficient d varied by $\approx 20\%$ at 500°C, while the elastic constant was stable with a variation of less than 4%. $SrGdGa_3O_7$, $SrLaGa_3O_7$ and $BaLaGa_3O_7$ have high piezoelectric coefficients (d_14 = 14.5, 13.7, 12.3 pC/N, respectively), which are much higher than those of Quartz (2.3 pC/N), Gallium Phosphate (4.5 pC/N) and LGS (6.3 pC/N). However, these crystals are not commercially available.

Aluminium Nitride and Gallium Nitride

Aluminium Nitride (AlN) and Gallium Nitride (GaN) belong to the point group $6mm$ and have d_{14} of $9.7pC/N$ and $6.4pC/N$, respectively. High temperature operation of GaN is limited to around 350°C due to intrinsic carrier concentration, which can significantly reduce the sensor output, as seen in a previous study [158]. AlN suffer oxidation even at ambient temperatures, but have been successfully applied in a hydrogen or carbon dioxide environment at temperatures up to 1100°C [159]. The piezoelectric properties of AlN have been characterised at temperatures up to 1000°C [160]. A moderate variation in the electromechanical coupling of 17% was observed. However, the variation in d was much higher ($\approx$ 60%) and the dielectric values increased sharply after 800°C, which was described due to the strong pyroelectric effect. The application of AlN and GaN is limited to thin films due to difficulties in the manufacture of good quality crystals, as defects develop due to their low resistivity [161]. A study using a AlN transducer for ultrasonic application demonstrated pulse-echo measurements with minimal degradation up to 750°C and

with acceptable performance up to 950°C [162]. A high temperature endurance study using *AlN* showed an increase in performance by 11% over 35 days with an average temperature of 441°C [130].

A summary of HT ferroelectric and single crystal piezoelectric materials, together with their TS-mode electromechanical properties and high temperature limitations, is given in Table 3.2.

TABLE 3.1: TS-mode FOMs of candidate high-temperature ferroelectric materials along with references to temperature limitations.

Material	T_c/T_p	T_o	High Temperature Limitation	d_{15}	g_{15}	k_{15}
Lead Zirconate Titanate	350	200	Accelerated ageing [163]	710	41	0.77
Bismuth Titanate	600	500	Low electrical resistivity [68]	14	10	0.08
Lead Metaniobate	400	300	Suffers high conductivity [164]	95	31	0.25
Lithium Niobate	1142	600	Chemical decomposition [132]	69	91	0.6
Lithium Tantalate	1500	900	Dielectric loss [137]	-	-	-
Quartz	570	300	Mechanical twinning at T_o and $\alpha - \beta$ phase transition at T_p [136]	2.3 (d_{11})	50 (g_{33})	0.08 (k)
Langasite	1300	700	Frequency shifts caused by changes in oxygen stoichiometry at high temperatures[165, 166]	4.5 (d_{11})		0.12 (k_{22})
Tourmaline	900	450	Strong pyroelectric effect and difficult to grow in suitable sizes [164]	1.8 (d_{33})		
Lithium Tetraborate	920	500	Not suitable for low-frequency applications [137]	19.5 (d_{33})	220 (g_{33})	-
Aluminium Nitride	2000	700-1000	Suffers from oxidation when approaching T_r [162]	5.6 (d_{33})		0.2 (k_{33})
Gallium Phosphate	970	700-900	Stable thermal response but lower sensitivity [138]	4.5 (d11)	-	0.16 (k_{33})

3.2.3 Electrode materials for high-temperature piezoelectrics

The electrodes applied to the piezoelectric material should remain stable under high temperatures and exhibit good adhesion and high conductivity. The primary cause of deterioration in thin-film electrodes at elevated temperatures is agglomeration, which is a surface diffusion-driven capillarity process due to dewetting. Other failure mechanisms, such as oxidation, evaporation, stress, and inter-layer reaction, are also present, but are not as influential [167]. For HT applications, many metallic (platinum, palladium and iridium), metal alloy (platinum - 10% rhodium), and conductive ceramic electrodes (lanthanum strontium manganite - LSM and silicon-alumina nitrogen - *SiAlON*) have been studied for temperatures up to 1000°C [168, 169]. Platinum is the most commonly used thin film electrode for operation at temperatures

of up to 650°C due to its excellent electrical properties, high melting point, and resistance to oxidation. However, at temperatures greater than 700°C it degrades due to agglomeration, even with an additional titanium adhesion layer [170, 171]. Studies have also shown that Pt film agglomeration can worsen with an electrode thickness less than 100 nm [172]. The stability of platinum films was demonstrated for a Langasite-based surface acoustic wave device at temperatures up to 600°C. The combination of layered ($Pt/Zr; Pt/ZrO_2$) and alloy electrodes (Pt 5% and 10% Au; Pt 10% Rh) hindered the agglomeration of the Pt films and extended the long-term operation from 600°C to 950°C [173].

3.3 Piezoelectric Transducers for HT-UGW Application

A range of HT active and passive piezoelectric sensors have been developed for applications including accelerometer, surface acoustic wave sensor, ultrasound transducer, acoustic emission sensor, gas sensor and pressure sensor for operation at temperatures up to 1,250°C [167]. The primary focus of this review was on the PUT design for the transduction of torsional guided wave modes in pipes for HT-SHM application. However, due to limited research in this area, this review was extended to studies on the development of HT-PUT for high-frequency ultrasonic applications. The design of transducers for selective generation of shear modes for high-wave mode purity is also reviewed. The fundamental piezoelectric component of HT-PUT can be developed using materials described in Section 3.2. The challenge lies in the selection of compatible high-temperature materials for passive transducer components, their bonding, and sufficient and stable ultrasonic performance for the desired application. It is extremely challenging to achieve long-term stability of the measurement system, especially when transducers operate in harsh conditions. Only a few studies have investigated the high-temperature ultrasonic performance of piezoelectric transducers, and even fewer have investigated the long-term stability at high temperatures. The reported designs are discussed including material selection, numerical modelling, assembly procedures, performance characteristics, and limitations.

3.3.1 Teletest transducer and related studies

The maximum operating temperature of the Teletest transducer described in Chapter 2 is limited due to the low glass transition of the epoxies used in its construction. A study investigated their ultrasonic performance at temperatures up to 225°C by analysing the amplitude of the excited UGW signal [174]. Ultrasonic signals were

shown to degrade by 60% at 100°C, by around 85% at 160°C and ultimately failed at 225°C. The study extended the operating temperatures of the Teletest transducer by replacing epoxies and sealants with high-temperature alternatives and the proposed designs are show in Figure 3.2. Modified transducers were shown to operate at temperatures of up to 250°C with less than 10% decrease in signal amplitude. Their performance was also investigated when subjected to thermal cycling and ageing at 250°C. An initial decrease in ultrasonic output of 20% was observed during thermal cycling, but afterward a stable response was observed for 35 days at 250°C.

Another HT-PUT design using lithium niobate as a piezoelectric crystal has been reported for operation at temperatures up to 580°C [175]. The lithium niobate piezoelectric plate was bonded to an aluminium oxide backing using the vacuum brazing technique. The design omitted a wear plate to minimise the number of transducer layers for the brazing process. The transducers were shown to work at temperatures up to 580°C, although with a reduction in ultrasonic output of 50%. Furthermore, an unexpected decrease in performance ($\approx$ 80%) was observed around 350°C which was explained due to the known oxygen loss problem with lithium niobate material.

FIGURE 3.2: Previously developed HT-UGW transducers using PZT-5A for operation at 250°C and Lithium Niobate at 580°C [174].

The ultrasonic performance of the Teletest transducers has been characterised at high temperatures up to 250°C [174]. Pitch catch measurements were recorded on a bar waveguide using a reference PZT Piezoelectric Wafer Active Sensor (PWAS), which was kept under ambient conditions. The peak-to-peak amplitude of the first arriving UGW mode was analysed to assess transmission and reception performance at a single operating frequency of 70 kHz as a function of temperature. Signal degradation less than 10% decrease in signal amplitude. However, the excited-wave modes and their variation as a function of temperature and temperature over time were not evaluated. These performance characteristics are related to Signal to Coherent Noise Ratio (SCNR), which is a crucial parameter that governs the sensitivity to defects for UGW applications.

3.3.2   Transducer construction for HT application

Polymer-based piezoelectrics such as polyvinylidene fluoride ($PVDF$) and its copolymers and composites have been developed and offer flexible transducers, but their operation is limited to moderately high temperatures in the range of 100-150°C [176]. Simple PZT-based PWAS with epoxy adhesives have been used for space SHM applications with temperatures ranging between -70 and +150°C [177]. For operation at temperatures up to 200-300°C, several designs of ultrasonic transducers have been reported using single element $BS - PT$, $PZT - 5A$ piezoelectric materials [178, 179]. These reported designs use ceramic or metal backing and high-temperature conductive and isoluating epoxies. The bulk piezoceramic range from thickness 0.1-1 mm for operation in the 1-3.5 MHz operation. A number of HT-PUT designs for flow metre application in liquid-metal-cooled reactors with operating temperature ranges of 180-300°C in sodium and 450°C in the Pb/Bi alloy [180, 159]. The transducer designs incorporated PZT, $LiNbO_3$, $GaPO_4$, AlN, and sodium bismuth titanate materials for operation in the 2-5 MHz frequency range. Additional copper layers have been used to improve the adhesion quality between internal components and avoid failures such as electrode delamination due to thermal stresses during multiple heating-cooling cycles [181]. Although a performance degradation of around $12dB$ was observed at 225°C, it was completely recovered when the transducer cooled to ambient temperature and demonstrated relatively good repeatability during different heating cycles.

Transducers with thin and thick film ceramics manufactured using spray-on technologies (for example Chemical vapor deposition (CVD) and sol-gel) have been developed using HT piezoceramics (bismuth titanate, AlN, etc.) for temperature ranges 600-1150°C [182, 183, 184, 185]. Spray-on deposition techniques offer a cost-effective way to fabricate transducers and combine the fabrication of piezoelectric materials and the bonding process and have been successfully applied to engineering structures for ultrasonic SHM applications [186]. They offer stable bonding and good acoustic coupling, provided that Coefficient of thermal expansions (CTEs) are compatible with the substrate. These spray-on fabrication techniques are limited to thin film deposition with typical thicknesses in the range of 10 to 200 μm to avoid delamination and fracture failures. This limits their application to high-frequency applications within the 1-30 MHz frequency range and hence have only been applied for thickness measurements and corrosion mapping applications.

Several studies have designed and developed transducers with delay lines (also called wave guides or buffer rods) to isolate the transducer from high operating temperatures. Piezoelectric materials such as $PbNb_2O_6$, $BS - PT$ have been used for

operating temperatures ranging from 215-400°C [187, 188]. Transducer designs have also combined sol-gel-sprayed PZT, bismuth titanate, and lithium niobate piezoceramics with delay lines for operation up to 150°C, 400°C and 800°C, respectively [189]. However, limited studies have been conducted to investigate long-term stability. The delay line solution only works well at high frequencies (2-10 MHz) when the waveguide dimensions are proportional to the ultrasonic wavelength in the rod and are also not suitable for low-frequency applications.

Several HT-PUT design have been reported using $LiNbO_3$ crystal with Z-cut, 30°Y-cut, and 36°Y-cut. Z-cut crystal has been bonded directly using ceramic adhesives for 4-8 MHz operation at temperatures up to 1000°C [190]. The design with 30°Y-cut used a porous zirconia-based backing layer and an alumina matching layer assembled through brazing [191]. The study reported a loss of signals above 200°C due to coupling instability, although the transducer was functional at 600°C. Another transducer for 3MHz operation used 36°Y cut with Pt coating and Ti adhesion layer with powdered steel with calcium aluminate cement as backing [192]. Dry coupling was achieved using 50 thick silver foil and ultrasonic performance was demonstrated up to failure at 650-750°C. Thermal cycling at 500°C resulted in a degradation of 2.3-5.6dB after 3-6 cycles. Stable performance was demonstrated at 550°C for 1 month, but at 650°C 36dB degradation was observed within 14 days. The low resistivity of $LiNbO_3$ can limit their use as a low-frequency device, and the evaporation of Li that starts around 300°C restricted their continuous operation at higher temperatures [120].

A comparative study developed HT-PUTs with materials $YCa_4O(BO_3)_3$, $LiNbO_3$ and AlN, in which a wave spring was used to compress the piezoelectric material onto the substrate [193]. Longevity of several days was observed when the temperature was below 560°C, while the springs provided a pressure of 150 psi. Ultrasonic performance was also characterised by "cook and look" tests after heat treatment of 950°C for 24 h and 1000°C for 48 h. All three candidate materials showed stable ultrasonic performance, and YCOB exhibited the least change in properties.

A newly grown single piezoelectric crystal $YSr_3(PO_4)_3$ (YSP) was used to fabricate an X-cut YSP wafer of dimensions $5mm$ x $5mm$ x $1mm$ (f_r = 346 kHz) for operation in face shear mode for transduction of SH_0 UGW [194]. The reported d_{14} of YSP is 9.7 pC/N and the wafer transducer was able to achieve highly directional SH_0 waves in the frequency range of $300 - 400kHz$. The stability at high temperature was demonstrated to be up to 800°C with variation in dielectric losses of less than 1% and piezoelectric properties of less than 10% and resisitivity of ($2.3x10^7 \Omega cm$), which is comparable to $GaPO_4$. However, no ultrasonic characterisation was reported at high temperatures.

Piezoelectric sensors with bismuth titanate have been tested in a nuclear reactor for a period of 448 days. During this time, the sensors were subjected to temperatures in the range of 400-450°C and neutron flux comparable to that of a commercial reactor [195]. A previous study used *BIT* to develop a high-temperature transducer that demonstrated stable performance over time at 350°C [196]. The design and fabrication of a wideband $GaPO_4$ transducer using a porous ceramic backing for operation at $2.8MHz$ have been reported [197]. An operating temperature range of 700-800°C was achieved; however, no high-temperature ultrasonic measurements were presented.

TABLE 3.2: Reported high-temperature piezoelectric transducer designs and their temperature limitations.

Piezoelectric Material	Passive Materials	Construction	Bonding	Frequency [Hz]	T_{max} [°C]	Thermal Stability	Ref
PZT	-	PWAS	Adhesive	-	100-120°C	Low	[198, 199]
PZT	-	Sprayed	Not required	-	150°C	N/A	[189]
BIT	-	Sprayed	Not required	-	300°C	N/A	[189]
$LiNbO_3$	-	Sprayed	Not required	-	800°C	N/A	[189]
AlN	Pt coated SiO_2	Sprayed	0.5-2μm	N/A	1150°C	N/A	[182]
BIT	Pt coated SiO_2	Sprayed	120μm	6 MHz	600°C	Good (7 days)	[183]
$LiNbO_3$	Zirconia backing	Brazing	PWAS	200-600°C	Coupling failure (200°C)		[191]
$GaPO_4$	None	PWAS	Adhesive	-	435°C	Adhesive failure	[142]
BS-PT	Aluminium	PWAS	HT epoxies	4MHz	200°C (50% amplitude reduction)	N/A	[178]
PZT-5A	Ceramic backing	Delay line	HT Epoxies	3.5MHz	300°C	N/A	[179]
$LiNbO_3$	-	PWAS	Ceramic adhesive	4-8MHz	300-600°C	Li evaporation (300°C)	[190, 120]
$LiNbO_3$	Calcium aluminate cement backing	PWAS	Dry coupling silver foil (50m)	3MHz	650-750°C	1 month (550°); 14 days (36dB degradation at 650 °C)	[192]

3.3.3 Transducer coupling for HT application

For the acoustic coupling of PUT to the substrate, standard bonding methods include epoxies, but these are generally limited to around 100-120°C due to their glass transition temperature. High-temperature epoxy and thermosetting polymer have been used for HT-PUT. The thickness and shear modulus of the adhesive have an effect on the transmission of guided ultrasonic waves [71]. Bonding layers with

uneven distribution or air pockets can significantly reduce transducer performance. Although techniques such as EMI characterisation and time-domain terahertz spectroscopy can be used to quantitatively assess adhesive bonds and ensure consistency [73]. Several studies have investigated the thermal stability of adhesive bonding PUT and for application UGW and have demonstrated excellent short-term performance, but its performance fluctuates with temperature and degrades over time even in the ambient temperature ranges. The amplitude and phase of UGW can vary and degrade, complicating their use for HT-SHM applications [198, 199, 200, 107].

Other methods include regular soldering, diffusion bonding, ultrasonic welding, cementing, sol-gel, and vacuum brazing. A comprehensive review of these high-temperature ultrasonic transducer bonding techniques and designs can be found in [119]. Glass solder can be used up to 500°C, but it can react chemically with other components. A study compared bonding and brazing methods for use in HT-PUT and compared solder, ceramic, and gold indium as joining materials for ceramic and steel [201]. *PZT* was bonded with a solder bond and *LiNbO*$_3$ with a ceramic or gold-indium bond and showed a stable response up to 250°C and 400°C, respectively.

A study used 36°Y cut *LiNbO*$_3$ and investigated various adhesives and brazing alloys to achieve stable acoustic coupling [202]. The transducer for operation at temperatures up to 700-800 °C was achieved with a porous ceramic backing and an alumina matching layer. However, the long-term durability under steady-state conditions at elevated temperature was not evaluated. A study used *GaPO*$_4$ for HT-PWAS for ultrasonic application SHM, however, adhesive failure caused premature loss of ultrasonic performance at 435°C [142].

An alternative for high-temperature operation is a dry-coupled transducer, where the ultrasonic energy is transmitted by pressing the transducer to the structure. A study investigated the use of silver foil for dry transducer coupling and evaluated the influence of transducer component alignment, cyclic clamping, component roughness, and component flatness [203]. A clamping force of 25 MPa was required with high hardness and surface finish of precision aligned material for plastic deformation of foil asperities to produce echoes SNR greater than 25 dB compared to 32 dB when all transducer interfaces were coupled with an ultrasonic gel. Studies have shown that even a small air gap (>0.01μm) can substantially reduce the acoustic energy for operation in the MHz range and may require pressures of up to 300 MPa [204].

3.3.4 Alternative Shear-mode Transducers for UGW Application

Traditionally, thickness-poled d_{15} PZT PWAS has been used for the generation and detection of UGW [205]. These were also assembled into arrays for the generation of longitudinal wave modes in pipes [91]. Transducers with in-plane polarisation in the pipe circumferential direction were used for torsional wave modes [206]. However, in-plane poled PWAS can generate unwanted lamb wave modes, and their dispersive characteristics can significantly increase coherent noise and restrict their application [207]. Recent studies have optimised PWAS designs for the selective generation and detection of shear wave modes.

A study compared conventional thickness poled (d_{15}) with two new types of shear mode: poled in the plane (d_{15}) and face shear (d_{24}), for the generation and reception of $SH0$ waves through FEA and experiments [208]. All three variants were of the same dimensions. The thickness poled generated SH_0 coupled with lamb wave modes. The d_{24} provided a higher purity of the $SH0$ wave with high energy efficiency. Of the thickness-poled and in-plane-poled d_{15} wafers, the in-plane generated a higher amplitude and acceptable SNR but both generated $SH0$ waves coupled with lamb wave modes with relatively low energy conversion efficiency.

Geometric optimisation has also been performed on a rectangular piezoelectric plate to obtain a directional $SH0$ transducer with a signal amplitude of at least $20dB$ higher than the lamb modes confirmed by FEA and experiments [209]. The dimensions of $PZT - 5H$ PWAS polarised along the L direction were $L = 25.4mm$, $W = 3.9mm$, and $T = 1mm$, where W was selected to be $\lambda/2$ and L close to an integer multiple of λ for 400kHz. However, the design was optimised for a single operating frequency, and the purity of the wave mode will not be maintained at different operating frequencies.

A study proposed a bidirectional SH_0 dual wafer PWAS made up of two rectangular face shear (d_{24}) PZT plates of dimensions $L = 24.8mm$, $W = 6.2mm$, $T = 1mm$ [210]. Dimensions were not required to be multiples of λ as the symmetric shear stresses distributed along the width were eliminated due to destructive interference of the two wafers. FEA and experimental studies of the transducer on a plate confirmed a highly directional SH_0 output with no additional wave modes over a wide frequency range from $150kHz$ to $250kHz$. This approach could also be applied to cylindrical pipe-like structures.

3.3.5   FEA for HT-PUT design

Several studies have reported using methods FEA to analyse and optimise piezoelectric transducer designs and have demonstrated an exceptional ability to predict the response of the transducer through experimental validation [76]. However, very limited studies have used FEA for the design and analysis of HT-PUT.

A semi-analytical FEA model has also been used to simulate the effect of temperature on the generated and received UGW using PZT in the temperature range of -40 to 60°C [211]. The effects of temperature were introduced through temperature-dependent dielectric permittivity, piezoelectric coefficient, adhesive stiffness, and thermal expansion. However, such a semi-analytical approach is limited to simple isotropic piezoelectric structures with poling in normal direction.

FEA has been applied to evaluate complex piezoelectric geometries and different crystal cuts. A study analysed the orientation of HT piezoelectric crystals, lithium niobate, and Langasite in the propagation of acoustic waves for a SAW device using Comsol [212]. Different crystal cuts were evaluated, and the capability of identifying optimal crystal orientation for the given application was demonstrated.

An FEA of a PZT-5A ultrasonic transducer immersed in liquid sodium evaluated the effect of transmitted and received signals at temperatures up to 200°C [213]. A Two Dimensional (2D) model was used and incorporated thermal expansion, temperature-dependent piezoelectric material, and degradation of the bonding by the introduction of air pockets. Temperature-dependent piezoelectric properties resulted in an insignificant reduction in signal amplitude of around $1 - 2dB$ in the temperature range considered. The simulated debonding resulted in increased ringing in the signal, as the transducer appeared to be lightly damped, which increased the acoustic noise and reduced the transducer bandwidth.

The effects of temperature-dependent piezoelectric losses on resonance and antiresonance frequencies, admittance amplitudes, and ultrasonic amplitude of a bismuth titanate material [214]. Elastic losses $tan\phi$ in s_{11}^E; dielectric losses $tan\delta$; and piezoelectric losses $tan\theta$ in d_{31} were evaluated in orders of magnitude 0. 1%, 1%, and 10%. The greatest impact of these three losses was on the amplitude at antiresonance. Only the elastic losses affected the sound level at the resonance frequency and the admittance at every frequency.

3.4 Guided Wave Monitoring

Several investigations have been conducted to investigate temperature-induced changes in the propagation of UGW. A study characterised the temperature dependence of longitudinal and shear wave velocity as $-0.8m/s$ and $-0.44m/s$ respectively in a carbon steel material within the 0-50°C temperature range [215]. These temperature-induced variations can adversely affect the sensitivity of defect detection. A study characterised the effect of temperature variation on guided waves at ambient temperatures of up to 70°C, and the observed effect of temperature effect was much more pronounced than damage from drilled holes [216].

3.4.1 Temperature Compensation Techniques

Optimum Baseline Selection (OBS) is a data-driven technique that selects a baseline signal from a large data set of signals collected from the structure at different temperatures. The optimal baseline is selected to minimise differences relative to the test signal for that temperature. Different implementations of OBS have been reported with selection criteria based on the mean square deviation or the maximum residual amplitude [106, 113]. The detection of notch- and hole-type defects was demonstrated on a plate. It was shown that a detection probability of more than 95% can be achieved with a temperature variation of more than 30°C. The ambient temperatures were 5-40°C. A similar approach has been applied for the detection of simulated corrosion-type defects of increasing severity in pipes under ambient temperature conditions [217]. Experimental studies have shown that the OBS method performs well for variations in ambient temperature; however, a temperature step of less than 1°C was required to achieve the desired residual levels [218]. Signal subtraction using signal envelopes gave a significant improvement in sensitivity over raw signal subtraction, but at the expense of introducing blind spots [46]. A study achieved a residual of $-38dB$ with ΔT=0.5°C which worsened to -34dB with ΔT=1°C [219]. Compensation performance can degrade with time due to the influence of temperature degradation on the measurement system [220]. An impractical number of baselines may be necessary to ensure acceptable results, which is not always feasible in practical engineering applications.

Methodologies based on the signal stretch are the most widely used temperature compensation technique. Several approaches based on stretching in the time, frequency, and scale domains have been presented in the literature [221]. In time-domain stretching, the signal delay is estimated as a function of time through local coherence using methods such as short-time cross-correlation, which is

subsequently used to stretch either the baseline or the current signal. The frequency domain stretching is performed by stretching the frequency axis by changing the frequency step size. Optimal stretch is achieved when the residual signal is minimised in time, or maximum correlation is achieved between the spectra of the two signals. The scale transform method is computationally efficient, since it uses FFT to estimate the stretch factor. Stretch-based methods are effective only for small temperature changes and their performance deteriorates for large temperature variations, large propagation distances, and high frequencies. A modified stretch-based temperature compensation procedure has been proposed for wave velocity and transducer phase response [222]. This approach varied the phase change of the current signal and demonstrated an improvement in residual signal levels at higher temperature differences compared to the standard Baseline Signal Subtraction (BSS). Residual levels were reduced to half at $\Delta T = 15°C$ in the temperature ranges of 7-28°C or 35-55°C. A Dyanamic Time Warping (DTW) method has also been applied to adjust misaligned guided wave data [223]. This was compared with the scale transform BSS and achieved better temperature compensation performance for higher frequencies with temperature variation with a baseline of more than 25°C.

Temperature compensation techniques with optimal baseline selection have been used to increase the allowable temperature gaps between baseline signals and reduce the number of signals in the database. A combination of OBS and BSS provides an effective temperature compensation strategy and allows a reduction in the required baseline signals. Several studies have applied a combination of stretch-based compensation and OBS to provide enhanced temperature compensation while requiring a limited baseline data set [46, 116, 218]. However, these techniques are affected by the complexity of the signals, wave mode purity, and changes in the transducer response.

Physics-based compensation techniques are based on the reconstruction of transducer signals at different temperatures. One such technique considered the influence of temperature on the physical properties of the base substrate, the piezoelectric transducer, and the adhesive interface [224]. Although good agreement with experiments have been observed, such techniques require prior measurements and are limited to simple structural geometries and boundary conditions with a modest temperature range within $\pm 50°C$.

TABLE 3.3: Studies on temperature compensation for guided wave monitoring.

Application	Temp Comp	Defect Detection	Temp Range	Sensitivity	Monitoring Period	Ref
Diffuse UGW	OBS + BSS	NMSE	5-40°C	95% POD of 1-2 mm with Δ T=30°C	N/A	[106]
Diffuse UGW	OBS + BSS	RMS	ΔT=8°C	5-10 mm	3 weeks	[113]
Diffuse UGW	OBS + BSS	RMS	22-32°C	22 mm	1 week	[220]
UGW on airframe panel	OBS + BSS	Max residual	ΔT=4-5°C	N/A	3 weeks	[219]
Diffuse UGW	OBS + BSS	Max Residual	10-20°C with ΔT=0.16°C	N/A	2-3 days	[225]

3.4.2 Pipeline monitoring in varying EOCs

Only limited monitoring studies have been performed using UGW on pipes operating in the above ambient temperature ranges. A study used a magnetostrictive patch sensor for a small diameter stainless steel tube used for gas transfer in silicon wafer manufacturing with up to 150°C operating temperatures [226]. Ultrasonic measurements using 1MHz frequency $T(0,1)$ excitation were recorded at each 1°C temperature increase. A combination of OBS and BSS was used to demonstrate the sensitivity of defects on pitting type defects of 2% CSA over the entire temperature range. Location-specific temperature compensation (LSTC) of UGW signals has also been proposed that applies compensation at each axial location considering samples of the signal separately [227]. A curve is derived to show how the expected signal amplitude at each location in the absence of damage varies with temperature and can compensate for temperature-dependent coherent noise more effectively. LSTC has been used with OBS for bulk waves and has been demonstrated for defect detection in the 20-70°C temperature range [228]. LSTC and OBS have also been applied to a pipeline SHM in the temperature range of 30-90°C and a defect sensitivity of 0.1% CSA has been demonstrated [229]. Such techniques could be applied for much higher temperature ranges. Statistical pattern recognition techniques such as outlier analysis have also been applied using machine learning techniques [230, 231, 232]. Several signal features are extracted for damage classification and can achieve a defect sensitivity less than 1% CSA. However, to implement such an approach, large data sets of the structure with known types and levels of damage are required.

3.5 Gaps in the Literature

From the review of high-temperature materials and their transducer applications, operating temperatures of more than 1000°C have been achieved but developed for resonant operation in the MHz frequency range where the electromechanical efficiency is high. Very few studies have characterised the ultrasonic performance with long-term operation at temperatures above 300°C. Limited research has been done on the application of piezoelectric materials operating in TS-mode for the design of a low frequency broadband transducer for HT application but with limited analysis of the thermal stability of FOMs such as mode purity or SNR which are crucial for UGW-SHM application. Alternative TS-mode piezoelectric designs have been proposed to improve mode purity, but are limited to PZT-5A wafers and their operation at ambient temperatures. Furthermore, no significant work had been done to study the effect of temperatures on a piezoelectric transducer-based system and temperature compensation techniques for a UGW based SHM system above ambient temperature conditions and under varying damage conditions.

Chapter 4

Methodology for HT-PWAS Design and Characterisation

4.1 Introduction

The scope of this chapter is to establish a numerical and experimental approach for the design and characterisation of HT-PWAS that can be used as an active element in an UGW-PUT to achieve the design specifications introduced in Chapter 1. The numerical characterisation methodology is based on the multiphysics FEA approach and focuses on assessing the electromechanical dynamic performance of PWAS relevant to the HT-UGW application. The experimental characterisation includes Electromechanical Impedance Spectroscopy (EMIS) for resonance analysis and Scanning Laser Doppler Vibrometry (SLDV) for vibrational frequency response analysis for guided wave performance assessment. Both numerical and experimental methodologies are developed to characterise the design of PWAS as a function of temperature and operating frequency.

4.1.1 Motivation

The elastic, dielectric, and electromechanical properties of piezoelectric materials depend on their polarisation and mode of operation as described in Chapter 2. These properties are also temperature-dependent, due to changes in the electrical properties at high temperatures that affect the mechanical behaviour and vice versa. Variation of these properties can limit their high-temperature application due to increased electrical conductivity and mechanical attenuation.

These piezoelectric properties can be used as FOMs to evaluate their performance in a particular mode of operation for HT-PUT devices. Several studies have been conducted on PZT-5A-type piezoelectric materials, and their HT material properties

are available for operation in TS-mode. A study characterised the ten mutually independent piezoelectric coefficients of the PZT-5A using EMI at temperatures up to 195°C [233]. It was also shown that each piezoelectric coefficient varied differently at high temperatures compared to its baseline value at ambient temperature, and some displayed a non-linear temperature behaviour. This highlights that the temperature coefficients of piezoelectric properties available in literature may apply to a limited temperature range.

For newly developed HT piezoelectric materials, their properties are generally not available for a particular mode of operation or the desired temperature range. Even for well-known materials, not all relevant properties are available from their datasheets, and the actual values may deviate from those specified as a result of differences in shape, electrodes, and polarisation. Therefore, it is essential to derive a complete data set of the TS-mode properties as a function of temperature and characterise any deviation in performance due to temperature coupling effects.

For ultrasonic applications, it is also critical to assess the dynamic behaviour of the piezoelectric material to assess the ultrasonic output. Multiphysics FEA can consider all design parameters and EOCs by coupling the relevant associated physics. This numerical approach enables an accurate simulation of the transducer's dynamic behaviour and can identify design parameters for potential performance improvements. The literature reviewed in Chapter 3 has shown that the multiphysics FEA approach can be used to accurately simulate the high temperature electromechanical behaviour of piezoelectric materials using temperature-dependent properties.

4.1.2 Aims and Objectives

This chapter seeks to create a numerical and experimental approach for the design and evaluation of a piezoelectric ceramic wafer transducer for the HT-UGW application. The numerical and experimental design characterisation methodology was developed and validated using PZT-5A PWAS from an existing Teletest transducer through the following objectives.

(1) Establish a multiphysics finite element model of a PWAS to characterise electromechanical response as a function of frequency and temperature.

(2) Extend (1) and perform multiphysics finite element modelling to study the influence of the passive layer on the vibrational response of PWAS.

(3) Develop an experimental method to evaluate the electromechanical response of a PWAS and characterise the TS-mode properties of the piezoelectric material at high temperatures.

(4) Establish an experimental method to characterise the vibrational frequency response of PWAS to interpret the excitation of the ultrasonic wave mode.

(5) Validate the numerical and experimental approach by evaluating the PZT-5A PWAS from the existing Teletest transducer design; by comparing the simulated response of the models in (1) and (2) with measurements using (3) and (4), respectively.

4.2 Overview of the proposed methodology

The proposed design characterisation methodology for the HT-UGW piezoelectric transducer combines numerical, experimental, and analytical techniques. Characterisation of the transducer design is focused on analysing the FOM derived from the transducer design specifications described in Chapter 2. These include electromechanical properties for TS-mode operation at high temperatures, resonance and vibration frequency response in the frequency range of interest for UGW and ultrasonic performance of the transducer for excitation of the $T(0,1)$ wave mode.

This design characterisation methodology is established using a simple PZT-5A PWAS from the Teletest UGW transducer described in Chapter 2. This allowed validation experiments to be performed on the well-known and readily available PZT-5A material. The design characterisation also allowed for a better understanding of the current design parameters and provided a baseline for comparing the performance with different HT-UGW transducer designs.

The numerical characterisation methodology was established using the COMSOL Multiphysics finite element modelling software package [234]. First, an FEA model of a piezoelectric plate operating in TS-mode is developed. This model was used to analyse the vibrational response of the piezoelectric plate and to evaluate changes in electromechanical performance with increasing temperatures. An experimental setup was established to measure the EMI response at high temperatures. The HT-EMI measurements were compared with the simulated response for model validation. The HT-EMI measurements were also used to characterise the HT elastic, dielectric and piezoelectric material properties. The measured HT properties are compared with those reported in the datasheet or other studies to validate the experimental methodology.

The piezoelectric plate model was then advanced to study the influence of the passive transducer layer (wear plate) on the vibrational and frequency response. Frequency domain studies were performed on developed models to evaluate the vibration response in the 20 to 100 kHz frequency range. The simulation patterns were examined to understand the excitation of the potential UGW modes and to evaluate the effect of the passive transducer layers on TS-mode performance for UGW application. The simulated vibration response was validated through SLDV measurements on transducer sub assembly.

4.3 FEA of HT-PUT

4.3.1 Piezoelectric material modelling using COMSOL

This study used COMSOL Multiphysics simulation software to characterise the piezoelectric transducer. The Piezoelectric Device module was used to simulate the electromechanical behaviour of the piezoelectric device. This multiphysics module combines Electrostatics and Solid Mechanics physics by coupling the structural and electrical domains. This electromechanical coupling of the piezoelectric material is defined by the relation between the material stress and its permittivity under constant stress or between the material strain and its permittivity under constant stress, described in Section 2.2.2. An electrical input to the piezoelectric material will result in a forced vibration based on the piezoelectric properties, crystal orientation, and mechanical boundary conditions. The influence of temperature is incorporated with thermal expansion of the piezoelectric device and the introduction of temperature-dependent material properties. Since the HT-UGW application will operate piezoelectrics at a much lower frequency, structural damping due to internal friction and resulting vibration-induced heating is ignored. The multiphysics setup is shown in Figure 4.1.
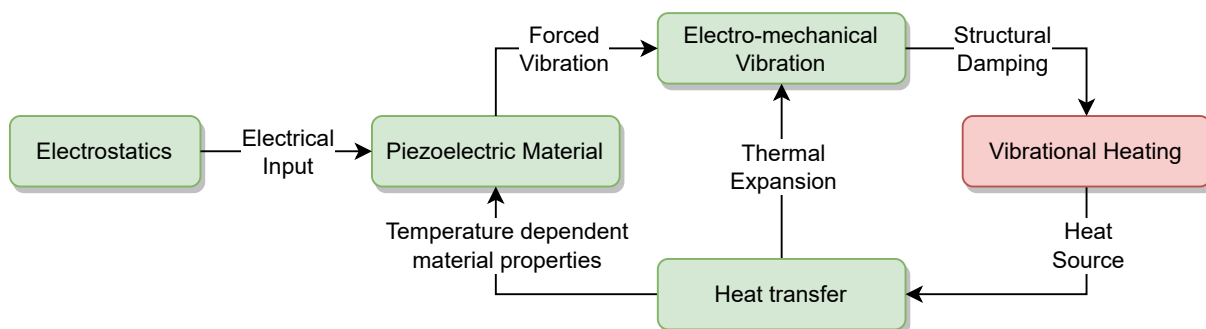
FIGURE 4.1: Multiphysics finite element modelling approach used for high temperature piezoelectric materials.

4.3.2 Geometry and mesh consideration

This study considered the PZT-5A piezoelectric plate of the Teletest transducer as PWAS. The geometry of PZT-5A PWAS was modelled as a rectangular plate with a length, width and thickness of 13*mm*, 3*mm*, and 0.5*mm*, respectively. The rectangular geometry included two edges on one of the length-width surfaces to model the boundaries of the wrapped-around electrodes. The CuNi electrodes of PWAS were not included in the model as an additional layer. It was assumed that their thickness of 150*nm* did not contribute significantly to electromechanical behaviour. The geometry of PWAS was set with the length (longitudinal dimension) along the geometric Z axis to model the polarisation along its length.

The piezoelectric plate was discretised with a fine-mapped mesh to achieve uniform meshing throughout its rectangular geometry. Previous studies have indicated different recommendations for mesh size, ranging from 8 elements to more than 20 elements per wavelength [235]. Initially, a mesh size equivalent to 10 elements per wavelength was used and was later optimised through a mesh analysis study. For the mesh size equivalent to 10 elements per wavelength, a maximum element size of 0.05 mm was used to capture any vibration modes for a maximum operating frequency of 12 MHz. The geometry of the PZT-5A PWAS model with dimensions, meshing, and an example of the displacement profile showing the TS-mode vibration response is shown in Figure 4.2.

FIGURE 4.2: FEA model geometry, meshing and vibrational response of the PZT-5A piezoelectric wafer transducer.

4.3.3 Piezoelectric material properties

Depending on the known properties of the piezoelectric material, either of the stress-charge or strain-charge relations could be used to define the piezoelectric domain in the model. For this study, the stress-charge relation was used and this material model required density, elastic compliance (s^E), coupling matrix (d) and relative permittivity (ϵ^T). Heat transfer physics was introduced to model the effect of high temperatures on the piezoelectric material. It included temperature-dependent properties of the piezoelectric material and thermal expansion as a result of an external heat source. The vibration-induced heat of the piezoelectric PWAS was not considered as the heat source and the viscoelasticity-based losses were ignored.
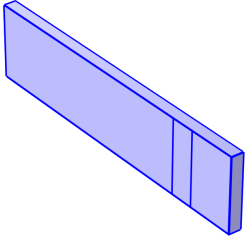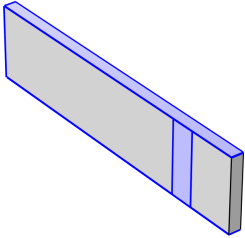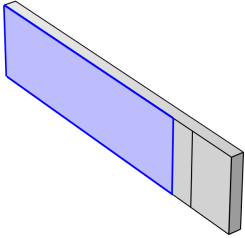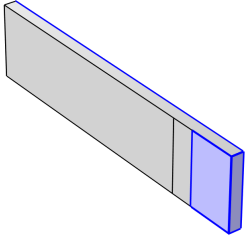
The material properties for PZT-5A, including the elastic, piezoelectric and dielectric properties, were obtained from the supplier data sheet [236]. Piezoelectric material losses were included in the dielectric, elastic, and piezoelectric properties. The model accounted for internal losses in the piezoelectric material using isotropic elastic and dielectric loss factors of 0.0006 and 0.004.

PZT-5A CTEs were coupled with the dimensions of the plate to model the unconstrained volumetric thermal expansion of the piezoelectric plate. The CTE of PZT-5A is a rank 2 tensor with two independent coefficients. These material properties were set up as analytical functions of temperature using their respective temperature coefficients. Assuming zero loss in mass of the PZT-5A element at high temperatures, the change in density (factor of 10^{-6}) was ignored and a constant density of 7500 kg/m^3 was used for HT simulations.

4.3.4 Boundary conditions

The Piezoelectric Devices module accepts the transducer drive conditions and circuit parameters from the Electric Circuit module. An AC voltage source built into the Electrical Circuit module provides an excitation signal to the piezoelectric device. The input and output impedances of the piezoelectric device change according to the excitation frequency of the drive circuit. These changes affect the charges generated at the output, which are coupled with the Electric Circuit module and used to analyse the electrical characteristics of the transducer. Similarly, the generated electrical displacement is coupled with the Solid Mechanics module and used to analyse the mechanical characteristics of the transducer. Representative electrical boundary conditions were applied to the piezoelectric plate model, as shown in Table 4.1.

TABLE 4.1: Boundary conditions applied to the PZT-5A piezoelectric wafer transducer model.

Physics	Domain or Geometry	Comment
Piezoelectric Material Model		The PZT-5A plate was modelled as a piezoelectric domain. The plate length was aligned along the geometric +Z direction to achieve length polarisation.
Zero Charge		The zero-charge node added zero surface charge density conditions on the boundary, enabling floating potential implementation using a terminal node.
Terminal		Terminal nodes were applied to the selected boundary of the piezoelectric domain to implement a connection to the external circuit.
Ground		Ground node was applied on the top wrapped around surface of the piezoelectric domain to implement zero potential boundary conditions.

Electrical ground and terminal boundary conditions were applied to the surfaces of the piezoelectric plate representing the wrapped-around electrode configuration. A zero initial charge condition was applied to all other edges.

4.3.5 Electromechanical analysis

Frequency domain analysis was used to study these electromechanical characteristics parametrically in the frequency spectrum. It allowed the analysis of the electrical load dependence and displacement of the PWAS transducer as a function of the operating frequency. The electrical load dependence was used to analyse the frequency response and impedance spectrum of the transducer. At the same time, electrical displacement patterns of the transducer surface were used to analyse the vibrational modes.

Frequency domain analysis was performed to evaluate the electromechanical response of PWAS. Two studies in the frequency domain were performed, one to simulate the full resonance spectrum of EMI and the other for the analysis of vibrational modes. The first study was conducted within the 40 Hz to 12 MHz frequency range in steps of 15 kHz. The simulated EMI response was then analysed for the resonance frequencies of TS-mode.

The second study in the frequency domain was performed from 20 kHz to 100 kHz in steps of 2 kHz to evaluate the electrical displacement pattern of the vibration modes of the piezoelectric plate. The displacement components on the geometric X, Y and Z axes were averaged on the surface of the piezoelectric plate or the transducer face plate, as they would be in contact with the waveguide during the UGW application. The displacement fields and the associated vibration modes were analysed as a function of frequency to identify any electromechanical resonances and interpret the UGW mode being excited by the transducer.

4.3.6   Piezoelectric plate resonance analysis

A mesh analysis study was conducted to ensure appropriate discretisation of the piezoelectric domain to capture its dynamic electro-mechanical behaviour accurately. Previous modelling studies have shown that the number of mesh elements in the thickness direction significantly affects the response of the simulated TS-mode response [237]. Therefore, the mesh refinement study was carried out by analysing the simulated EMI response and characteristic frequencies with increasing mesh elements (N_{el}) along the thickness.

The resonance frequency of the second harmonic was chosen as the characteristic frequency because it was more significantly affected by the thickness than by the fundamental resonance. The results of the mesh analysis are shown in Figure 4.3. They indicate that at least twelve mesh elements ($N_{el} \geq 12$) along the thickness dimension were required to accurately simulate the amplitude and frequency of the second harmonic of TS-mode.
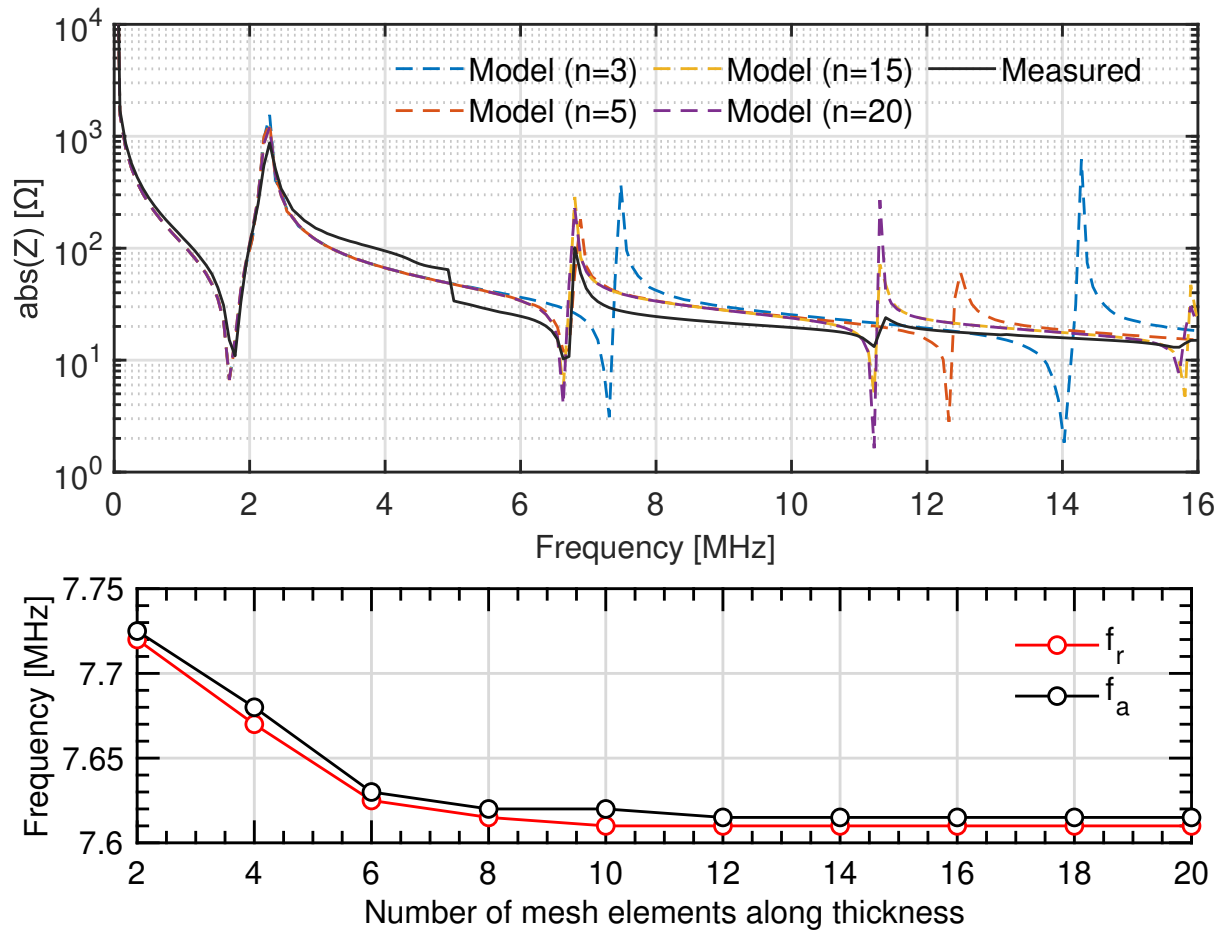
FIGURE 4.3: Mesh analysis study showing the effect of increasing number of mesh elements in the thickness direction on the (top) PZT-5A PWAS EMI response and (bottom) second TS-mode resonance harmonic frequency.

Twelve mesh elements along the thickness translated to a cubic mesh element of 42 μm, resulting in 263,000 total elements for the piezoelectric plate model. This mesh size equated to 14 elements per wavelength at the highest frequency of interest. The piezoelectric material model used in all subsequent FEA studies in the reported work was optimised in the same way.

4.4 TSM electromechanical FOM characterisation

The EMIS method was chosen for the characterisation of the properties of the piezoelectric material as a function of temperature. The EMIS measurements can be analysed to calculate the piezoelectric, electromechanical, dielectric, and elastic properties following BS EN 50324-2:2002 [63], as described in Chapter 2.

4.4.1 HT-EMIS measurement apparatus

An Agilent 4294A impedance analyser was used to measure impedance spectra. The impedance analyser provided a constant voltage signal of 0.5V at the selected frequency to the piezoelectric material. The magnitude and phase of the steady-state current drawn from the piezoelectric material were recorded and converted into real and imaginary parts of the impedance. The frequency was increased, and the process was repeated for the entire frequency range. In this way, variations in the electrical impedance over the selected frequency range, known as impedance spectra, were obtained. Piezoelectric samples were placed inside a Carbolite LHT6-30 furnace for HT measurements using a purpose-built jig [175]. The measurement system and test setup used for EMIS on piezoelectric plates are shown in Figure 4.4.
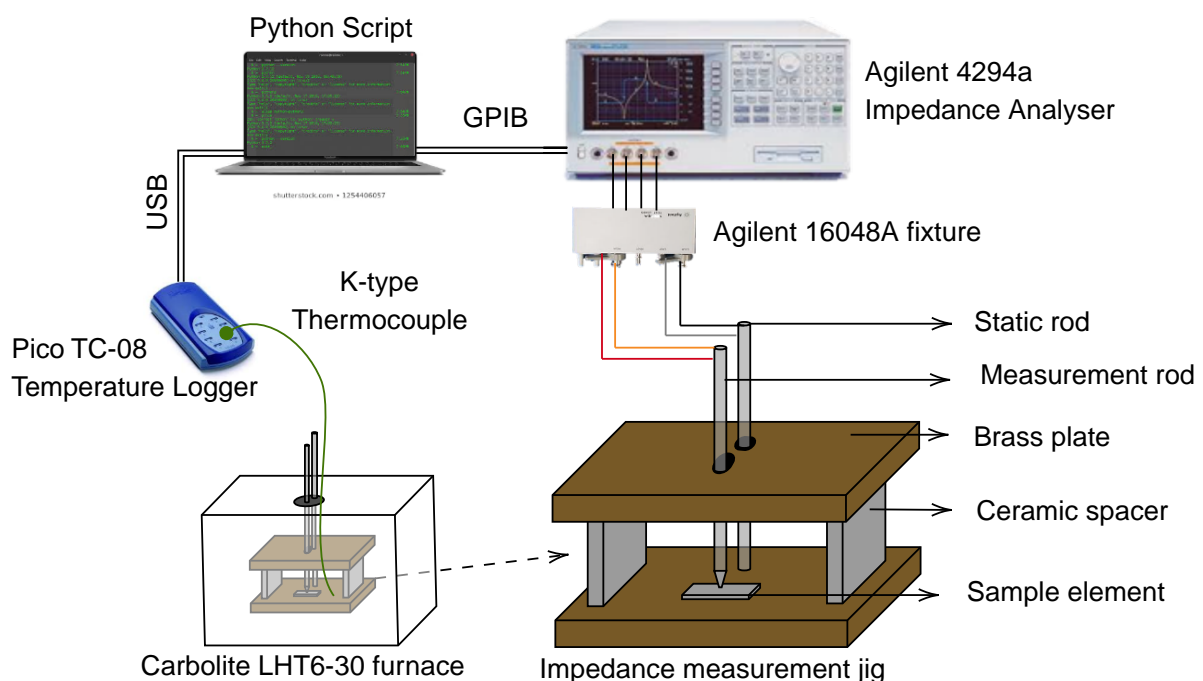
FIGURE 4.4: Experimental setup for HT-EMIS used for the characterisation of piezoelectric materials.

The jig consisted of two brass plates separated by a ceramic spacer. Two rods provided electrical connections to the piezoelectric element placed on the bottom plate. One rod, named the static rod, was screwed into the bottom brass plate and provided the ground terminal connection. The second rod, called the Measurement rod, was movable through a channel cut into the top brass plate of the jig, allowing it to be placed on the terminal electrode of the piezoelectric element under test. The wires were attached to the two rods using screw-terminal connectors. Electrical connections were made between the impedance analyser and these rods through an

Agilent 16048A fixture, suitable for measurements from 40 kHz to 12 MHz. The test jig was placed inside the furnace with two rods that extended out for calibration. Alumina plates were added between the shelf and the jig for electrical isolation.

A digital interface controlled the furnace temperature and the temperature of the specimen was measured using a K-type digital thermocouple using a Pico TC-08 temperature logger. A temperature ramp-up rate of 5°C/min was used, and measurements were made once a thermal equilibrium was achieved. Before each HT measurement, the jig was calibrated using open and short-circuit compensation to remove the parasitic impedance of the test jig. The measurement rod was lifted to rest in the channel groove for open-circuit measurement, and for short-circuit measurement, the rod rested on the bottom brass plate. The HT measurement recorded capacitance at 1 kHz and EMI in the frequency range of 40 Hz to 12 MHz with 15-kHz steps. Data collection was automated using a Python script, whereby a GPIB interface was used for data acquisition from the Impedance Analyser. A USB serial interface was used to capture temperature measurements from the Pico logger.

4.4.2 HT-EMI measurements of PZT-5A wafer transducer

The described experimental setup was used to measure the HT-EMI response of the PZT-5A plate from the Teletest transducer. EMI measurements were taken at ambient temperatures up to 350°C in increments of 50°C. The impedance response as a function of frequency at increasing temperatures is shown in Figure 4.5. A decreasing trend of characteristic resonance frequencies in the Thickness Shear (TS) mode and anti-resonance frequencies (f_r, f_a) with a negative frequency shift can be observed with increasing temperature.
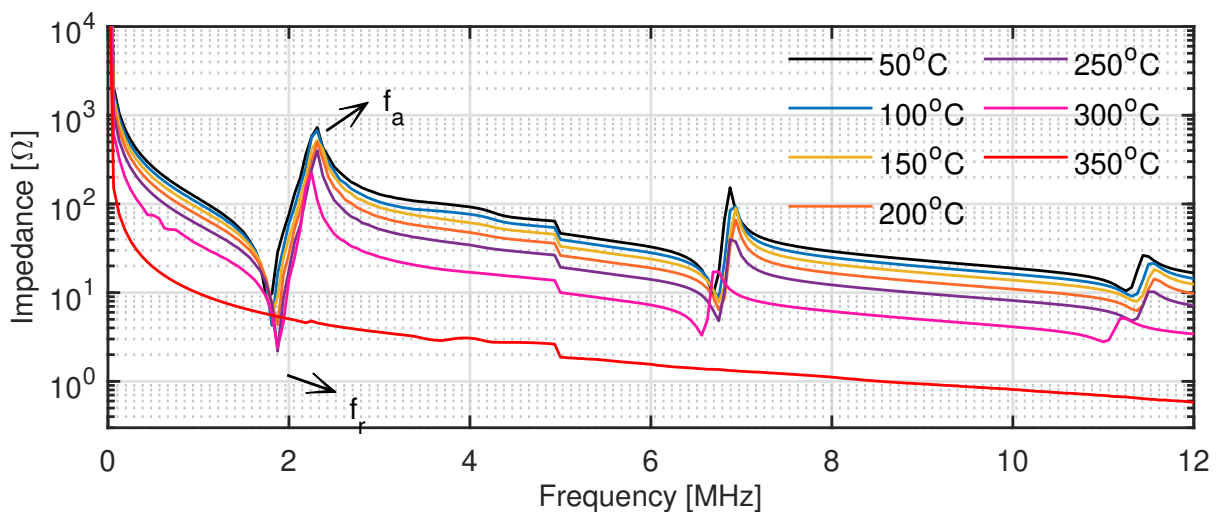
FIGURE 4.5: EMIs spectra measurements of the PZT-5A piezoelectric wafer transducer at temperature increments of 50°C up to 350°C.

Frequency shifts were significantly higher for TS-mode harmonics at higher frequencies. These horizontal shifts in the impedance spectrum are associated with changes in the structural and electromechanical properties of the piezoelectric material. In addition to the frequency shifts in the impedance resonances, a reduction in the impedance amplitude was also observed as a result of the increase in capacitance. The reduction in impedance showed a linear response with an increase in temperature to 300°C and a significant drop after that. At 350°C, the material loses its resonance behaviour and is no longer piezoelectric. The observed Curie point is in agreement with T_c of 340°C provided in the material data sheet [238].

4.4.3 Derivation of TSM electromechanical properties

HT dielectric, elastic and piezoelectric material properties were calculated using the formulae mentioned in Chapter 2. The CTEs in the material datasheet were used to calculate the dimensions of the piezoelectric plate for each temperature increase. The characteristic frequencies and capacitance were measured at 1 kHz.

The datasheet for Pz27 provided by Meggitt [239] only provides two TS-mode FOM, k_{15} and d_{15}. Measurements of FOM from the PZT sample matched well and were within the variation of $\pm 5\%$ stated in the datasheet. Similar Navy II soft PZT materials are also available from other suppliers, such as K350 from Piezo Technologies [240] and EBL [241]. Their datasheets provided some additional TS-mode FOM, which are also compared to the measured FOM. Although direct comparison is not possible as they are different PZT materials, this indicates the reliability of measurements and compares other available PZT materials.

TABLE 4.2: TS-mode electromechanical properties of PZT-5A derived from EMIS and compared with those available from datasheets and literature.

	k [-]	d [pC/N]	g [Vm/N]	K^T [-]	K^S [-]	Vs
Measured	0.69	527	375	1587.1	881.3	1710.3
Datasheet [241]	0.69	584	382	1725	-	-
Pz27 [239]	0.7	500	-	-	-	-
K350 [240]	0.67	570	400	1750	795	1880

The EMI response of PZT-5A PWAS was simulated for temperatures of 25°C to 350°C in steps of 50°C, using the high temperature material properties of PZT-5A. Frequency domain analysis was performed within a frequency range of 40 Hz to 12 MHz in steps of 15 kHz to match the frequency resolution of the experiments. The electrical impedance data from the solved models was extracted using the global evaluation

function using the inverse of terminal admittance ($es.Y_{11}$) parameter in Comsol. The comparison of the simulated and measured electrical impedance as a function of frequency at temperatures of 25°C, 250°C, and 350°C is shown in Figure 4.6. The simulated HT-EMI was in good agreement with the measured response. There was a slight difference between the measured and simulated resonance frequencies and impedance amplitude, but the trend with increasing temperature was accurately simulated.
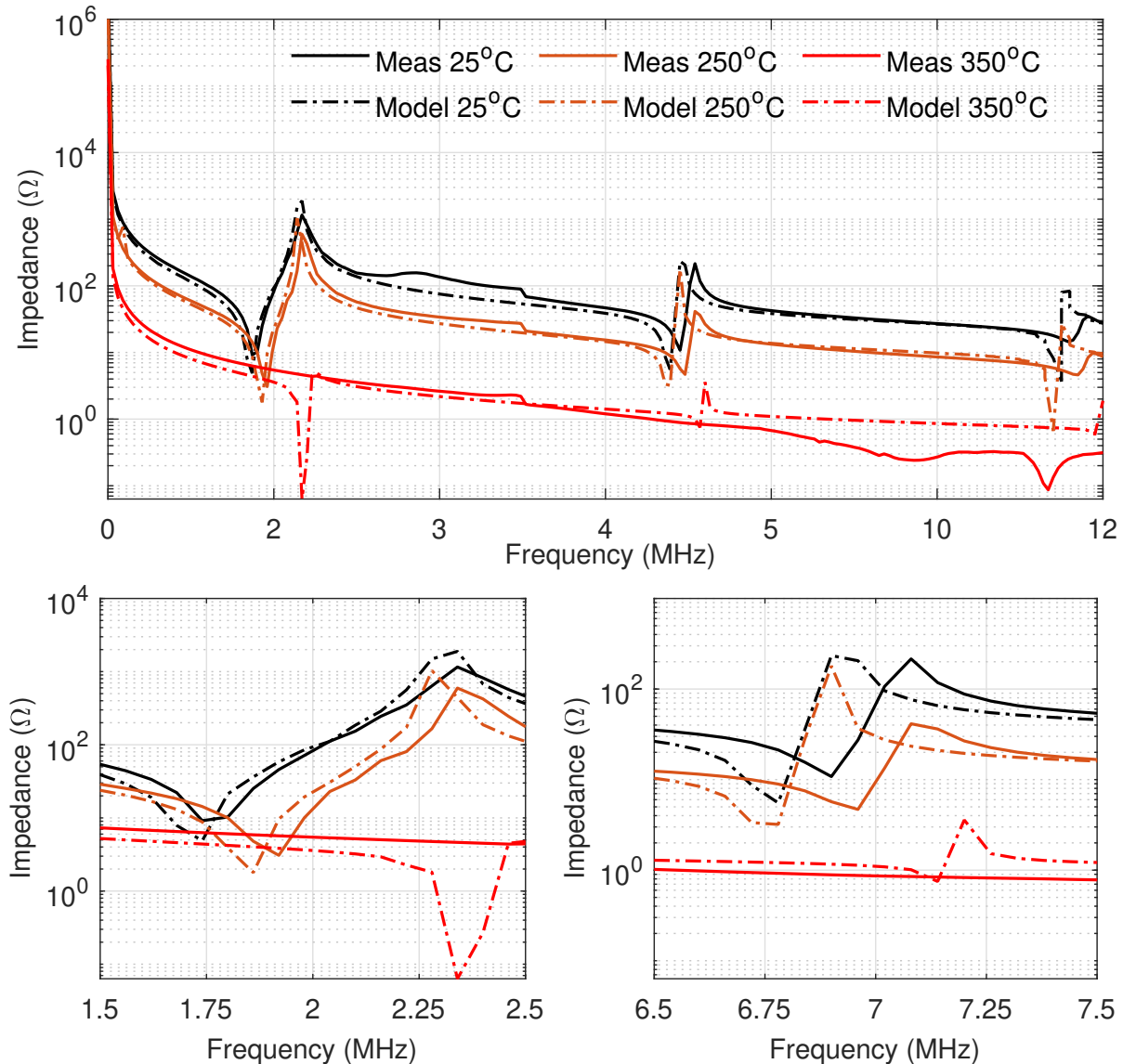
FIGURE 4.6: Comparison of simulated and measured high temperature electromechanical impedance response of PZT-5A wafer transducer.

At 350°C, the simulated impedance loss complies with the measured response. However, the modelled results still indicate the presence of resonance, because the piezoelectric losses are not simulated as a function of temperature. At temperatures

up to 300°C, the difference in the simulated resonance frequency for the fundamental and second harmonic TS-mode resonance was less than 5% and around 15%, respectively. These minor differences may be associated with manufacturing variability that may have affected the dimensions of the plate and electrodes.

The capacitance and characteristic frequencies as a function of temperature were extracted for ten PZT-5A samples to assess the variability of the measurement. This was compared to the modelled response and is shown in Figure 4.7. The variation between the measured results is shown using shaded areas and the simulated response is within the measured range, confirming the accuracy of the simulated temperature response.
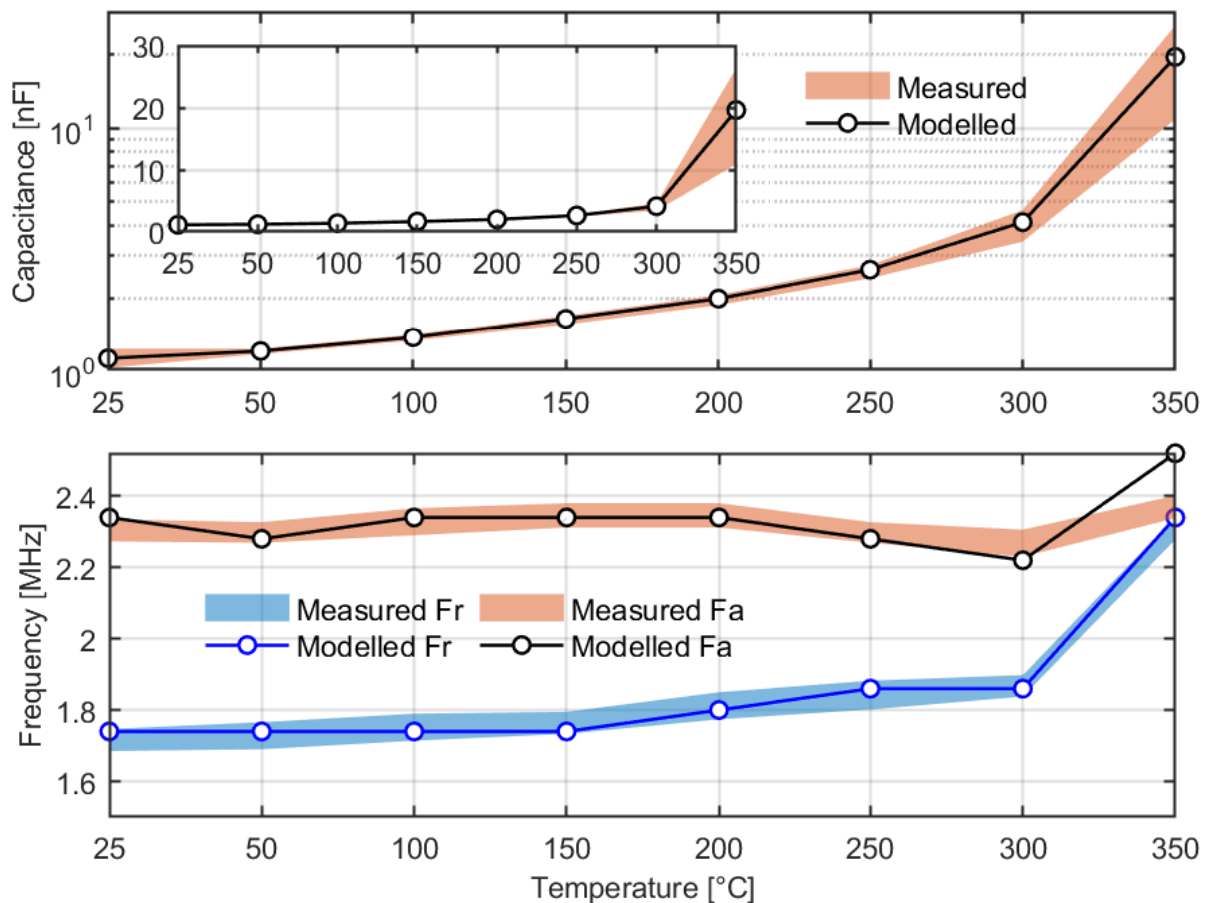
FIGURE 4.7: Capacitance and characteristic frequency derived from HT-EMI measurements on five PZT-5A piezoelectric wafer transducers at temperatures up to 350°C and their comparison with simulated response.

4.5 Vibrational response characterisation

In this study, vibrational characterisation is carried out using SLDV, a scientific instrument used to make noncontact vibration measurements of a surface. SLDV allows for Three Dimensional (3D) vibration measurements of small target areas without mass loading and is ideal for characterising the vibrational response of ultrasonic piezoelectric transducers.

4.5.1 SLDV measurement apparatus

The vibration response of the transducer as a function of the operating frequency was measured using a Polytec PSV-400 3D-Laser Doppler Vibrometry (LDV). The experimental setup used to measure the electrical displacement fields of the transducer surface is shown in Figure 4.8. The PSV-400 LDV has three laser scanning heads that employ wavelength $633nm$ lasers, which can measure a displacement amplitude range between $1nm$ to $40\mu m$. These scanners measured the three velocity components, and the surface displacement is obtained by orthogonal decomposition. The Polytec Vibrometer contains a velocity decoder to process acquired Doppler signals with spectral resolution of $1Hz$.
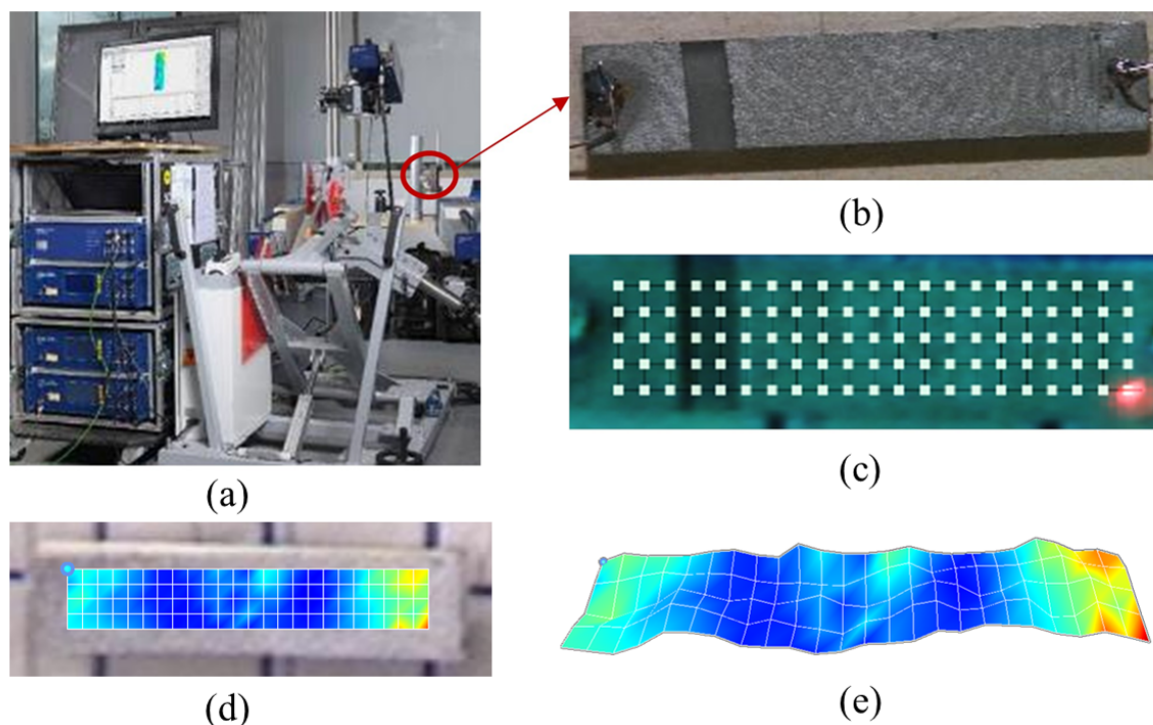
FIGURE 4.8: SLDV experimental setup showing (a) Polytec PSV-400 equipment, (b) PZT-5A PWAS transducer under test, (c) array of scan points, (d) PZT-5A PWAS with wear plate showing (e) example 3D measurement.

Teletest Focus pulser-receiver unit was used as an external function generator to provide excitation signals to the transducer under test. A PC was used to control the software for the Teletest unit to configure the parameters of the ultrasonic signal. A Hanning window five-cycle signal of centre frequency was used in the range $20kHz$ to $150kHz$ for transducer excitation to cover the entire frequency range of interest for UGW application. The Teletest unit was connected to the PSV as an external trigger to ensure that measurement recording was in sync with transducer excitation.

A camera installed on the top head was used to visualise the transducer under test, and a geometric scan unit was used to control the transducer's distance from the vibrometer. There is a periodic variation of the laser intensity with the stand-off distance. Although the results can be obtained with any stand-off distance, the recommended optimal distance is calculated using the relation $D = 0.099 + (n * 0.204)$ as recommended in the PSV-400 user manual [242]. Here D is the optimal stand-off distance, and n is an integer value. A standoff distance of 2.55m with $n = 1$ was chosen for the transducer under test to achieve the best SNR.

The laser beams from the three scanner heads were focused on the active surface of the piezoelectric device. A two-dimensional and then a three-dimensional alignment was conducted to line up the laser beams from the left and right laser heads with the beam from the top laser head. The calibration procedures followed are described in the user manual [242]. Measurements were recorded after the highest possible resolution of $0.1mm$ was achieved, which was indicated by a perfect alignment of 100% in the PSV software. The PSV system software was used to set a sampling frequency of 5.12 MHz, an average of 512 acquisitions for each measurement to reduce random noise. A bandpass filter with a limit of $[f_c \pm 2f_c/n]$ was used to capture the frequency band corresponding to the excitation signal provided by the Teletest unit.

An array of scan points are added to the piezoelectric device to cover the active surface area for 3D velocity or displacement measurements. For each scan point, the vibration amplitude are extracted from the Doppler shift of the reflected backscattered laser beam due to the motion of the surface. The Polytec vibrometer software was used to acquire and process three-dimensional velocity or displacement measurements caused by electrical excitation of the transducer. Vibrational mode shapes were also visualised using Polytec software post-processing tools. Displacement field measurements for different excitation signals were transformed into the frequency domain, which provided the displacement spectrum as a function of frequency.

4.5.2 Vibrational response of PZT-5A PWAS

The PZT-5A PWAS was suspended in air by securing the cables to a foam support layer to ensure acoustic isolation. An array of scanning points was added to the surface of the piezoelectric wafer transducer. A minimum of 100 points were considered adequate to map the active surface area of dimensions 13*mm* x 3*mm*. A frequency domain analysis was performed on the PZT-5A piezoelectric wafer transducer model within the 20 to 150 kHz frequency range to determine its electromechanical resonances and displacement patterns. The measured eigenmodes of the PZT-5A piezoelectric wafer transducer are shown in Figure 4.9 and compared with those simulated with the transducer model. Four resonance modes were observed at around 40, 60, 90 and 130 kHz. The simulated eigenmodes matched well with those measured and their displacement patterns were accurately captured. The difference in eigenfrequency was less than 12% in all resonance modes and around 1.5% for the mode without out-of-plane displacement.
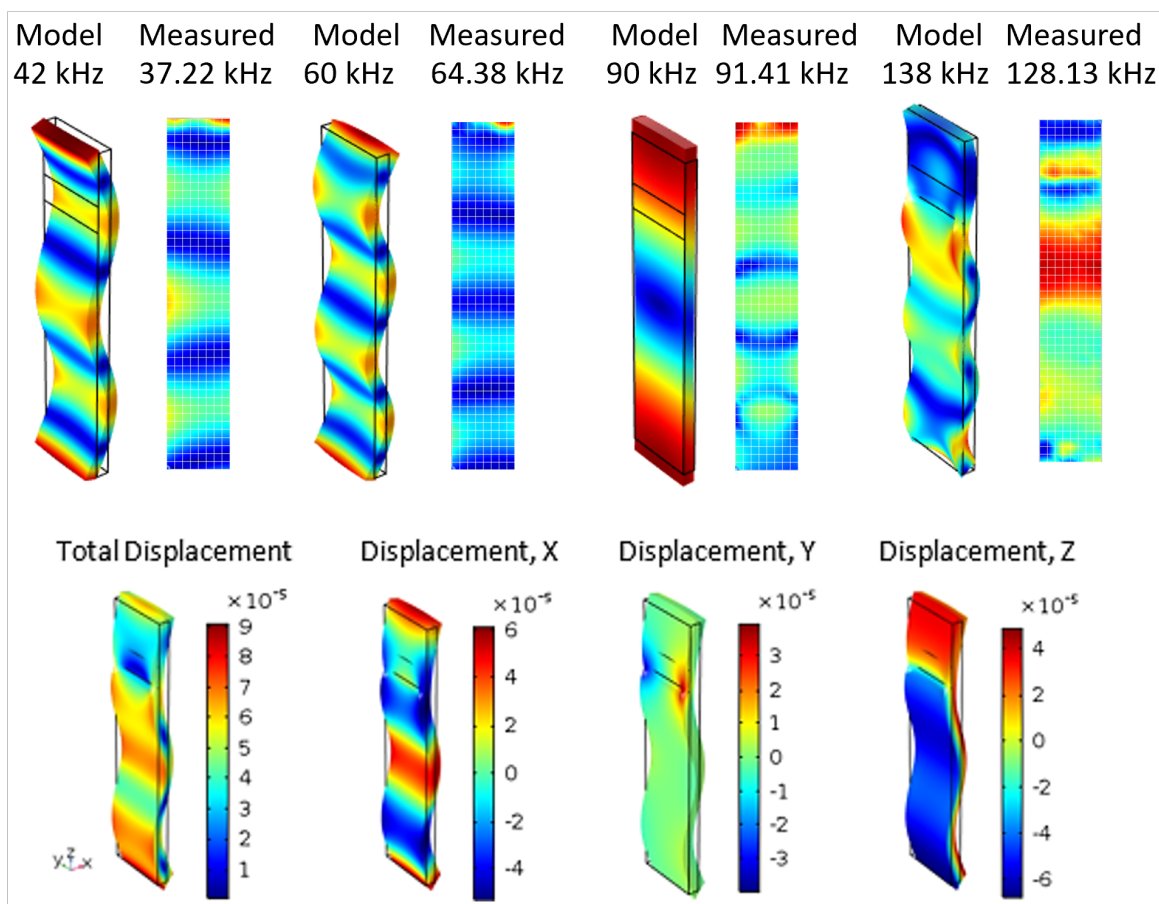
FIGURE 4.9: Simulated and measured eigenfrequencies and the vibrational response of the PZT-5A piezoelectric wafer transducer. The bottom shows the simulated three-dimensional displacement fields for non-resonance operation at 50 kHz.

The results suggest that the wires soldered onto the piezoelectric wafer transducer may have affected the out-of-plane displacement. The total displacement and the electrical displacement fields simulated in the three directions are shown at a non-resonant frequency of 50 kHz. This highlights that there is a significant out-of-plane displacement (X) of a magnitude similar to that of the in-plane shear displacement (Z) and the lateral displacement (Y) is concentrated around the gap between the wraparound electrodes. The in-plane shear displacement (Z) is concentrated on the positive electrode surface and in the opposite direction for the wrapped-around ground electrode, which may decrease the overall in-plane shear vibration of the piezoelectric wafer transducer.

The 3D-LDV measurements were averaged across all measurement points on the active transducer surface to derive three-dimensional displacement fields as a function of the operating frequency. Similarly, the simulated electrical displacement fields from the model were averaged across the surface area. The measured and modelled in-plane and out-of-plane displacement fields were normalised to the maximum value of the simulated in-plane displacement at around 90 kHz. The frequency spectrum of the simulated and measured displacement fields is compared in Figure 4.10. The comparison shows a good correlation in terms of resonance frequencies and the relation between the in-plane and out-of-plane displacement.
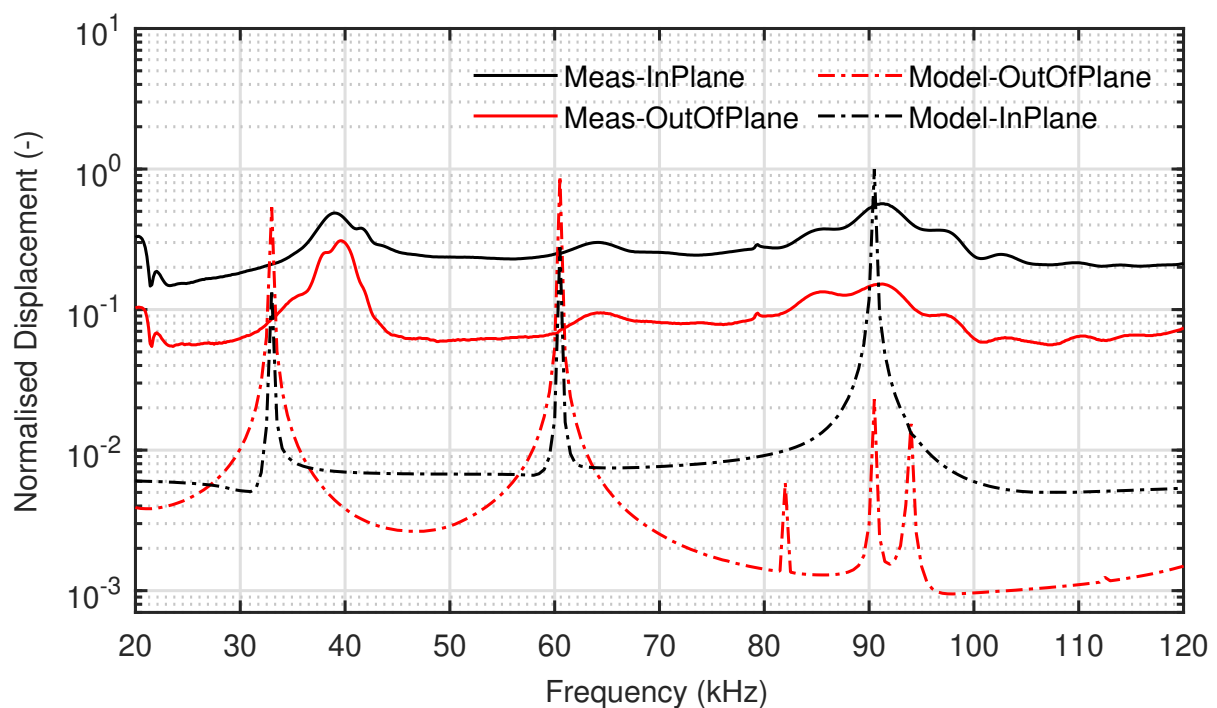
FIGURE 4.10: Comparison of the measured and simulated in-plane and out-of-plane displacement and frequency response of the PZT-5A piezoelectric wafer transducer.

Apart from a slight shift in frequency response, as highlighted by the eigenfrequencies, there is an order of magnitude difference between the magnitudes of the measured and simulated displacement fields. The peaks and troughs in the measured response are also less pronounced. This may be due to the measurement error or damping effect of the soldered wires on the piezoelectric wafer transducer that is not considered in the model. Nevertheless, the model depicted the out-of-plane vs. in-plane displacement ratio reasonably well in the frequency ranges without resonances.

4.5.3 Vibrational response PZT-5A PWAS with wear plate

SLDV measurement and numerical analysis was performed on an Alumina wear plate bonded on the PZT-5A PWAS. Even with the addition of a wear plate, there were some vibration modes with significant out-of-plane motion, as shown in Figure 4.11. The 26 kHz, 69 kHz, and 130 kHz wave modes show significant out-of-plane motion. An example of a displacement pattern for non-resonance operation is shown for 30 kHz. The displacement fields on the geometric axes X, Y, and Z are shown separately.
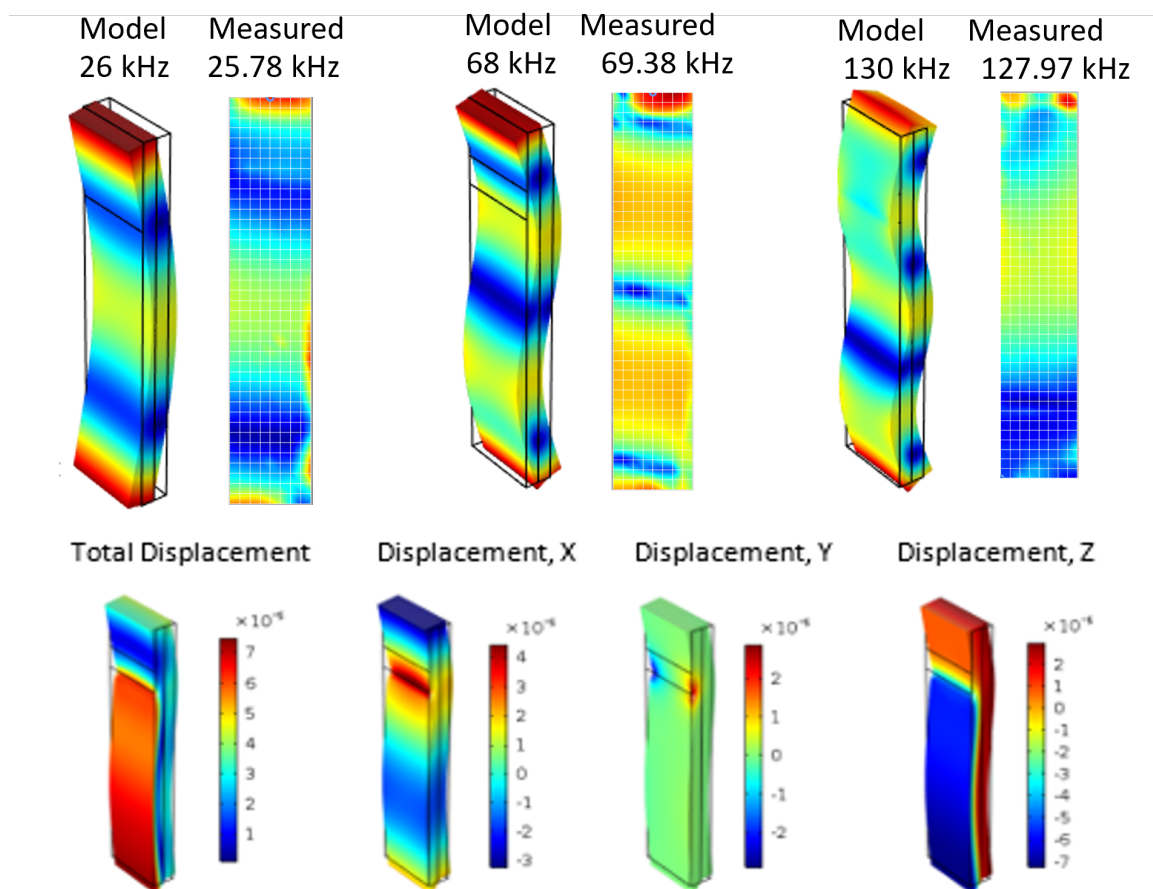
FIGURE 4.11: Eigenmodes of the PZT-5A plate bonded to Alumina wear plate and displacement fields for non-resonance operation at 50 kHz.

The frequency spectrum of the simulated and measured displacement fields is compared in Figure 4.12. The comparison shows a good correlation in terms of resonance frequencies and the relation between the in-plane and out-of-plane displacement spectrum. The most significant in-plane shear displacement was around $5\mu m$ along the Z axis. This is responsible for generating the desired Torsional guided wave mode on pipes. An out-of-plane displacement along the X axis of approximately $1.5\mu m$ was observed in the gap between the positive and negative electrodes of the piezoelectric plate. This out-of-plane displacement caused by the wrapped-around electrode configuration can be detrimental, leading to the generation of unwanted longitudinal waves in pipes.
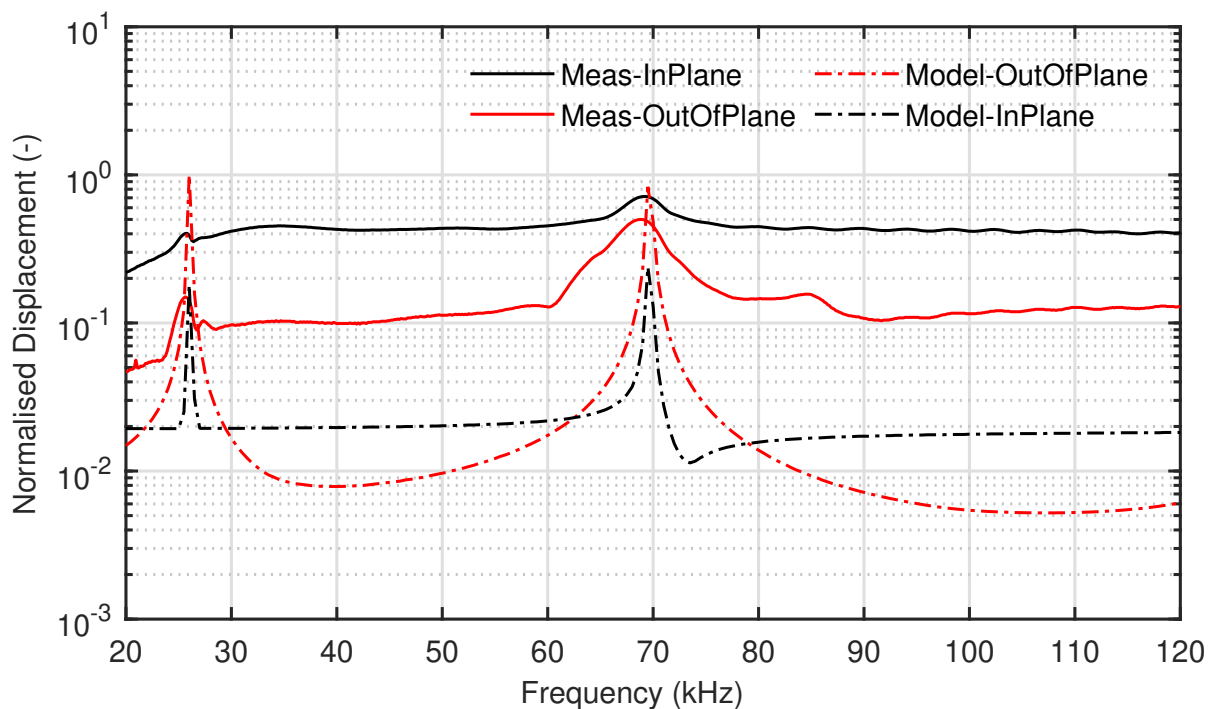
FIGURE 4.12: Comparison of the measured and simulated in-plane and out-of-plane displacement and frequency response of the PZT-5A piezoelectric wafer transducer with Alumina wear plate.

4.6 Transducer Ultrasonic Characterisation

4.6.1 Experimental setup

An experimental setup was developed to collect UGW measurements and characterise the ultrasonic frequency response of the piezoelectric transducers. The setup required a waveguide on which the transducer under test would transmit and receive the ultrasonic-guided waves. A waveguide with a profile smaller than that of a full-scale pipe was required to test the transducers in a confined space of an environmental chamber. A 12mm square bar was chosen as the waveguide as it provides a flat surface to allow easier positioning and dry coupling of the transducer. The dispersion curves of this bar waveguide were calculated for the transducer excitation frequency range (20 to 120 kHz) using GUIGUW and indicate the presence of three UGW modes. The group velocity and phase velocity dispersion of these modes, along with their displacement profile, are shown in Figure 4.13. The three wave modes shown in blue, green, and black are equivalent to the longitudinal, torsional, and flexural wave modes in a pipe, respectively. Therefore, the guided wave measurements on this bar waveguide represent those on the pipe of a similar wall thickness.
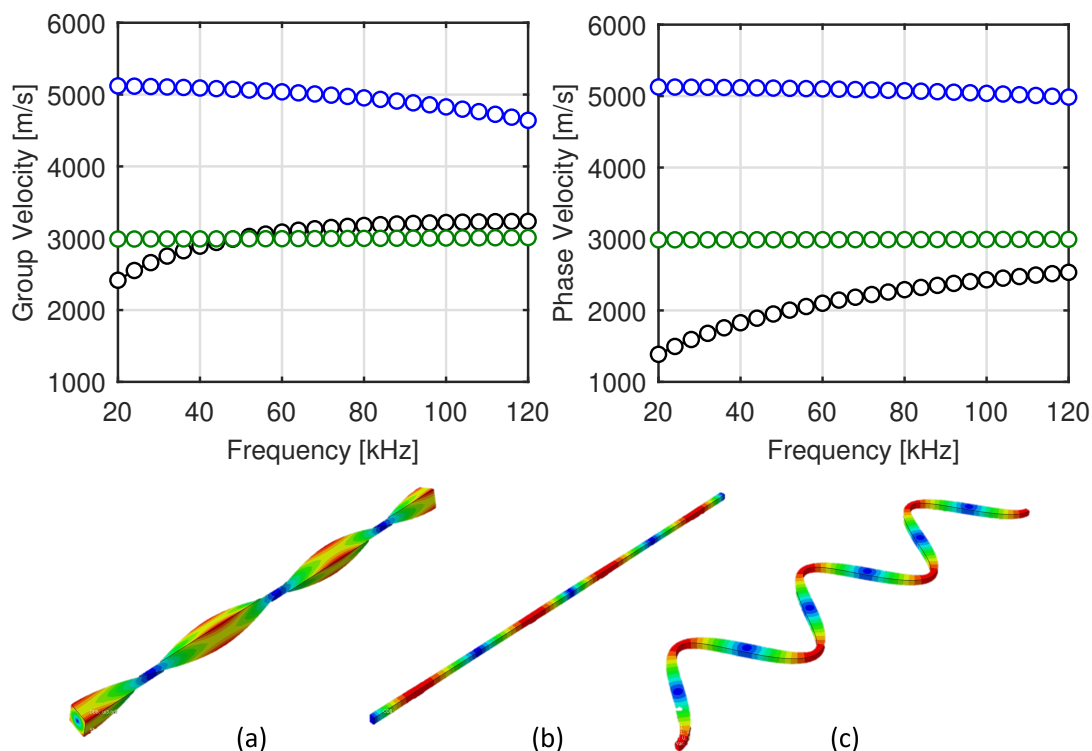
FIGURE 4.13: Dispersion curves and guided wave mode shapes of a $12mm^2$ square steel bar used as a waveguide for ultrasonic measurements. The group and phase velocity of the three wave modes are colour-coded with (a) $T(0,1)$ in green (b) $L(0,1)$ in blue and $F(1,1)$ in black.

These dispersion curves are used to calculate the expected time of flight of these UGW modes. A length of 1.5 m was chosen for the square bar to allow for the propagation of UGW without destructive interference from a reflection. This was calculated using a 5-cycle Hanning windowed wave packet traveling at the $L(0,1)$ mode velocity at 20 kHz, that is, the lowest frequency of interest with the largest wavelength of 0.25m. Thus, excitation signals of five cycles will ensure effective mode separation throughout the frequency range for the chosen length of the bar waveguide.

The experimental apparatus is shown in Figure 4.14. An assembly of PZT-5A and face plate was connected on a custom-built flexible connector. The transducer under test was connected to the Teletest Focus Pulser-Receiver unit using a coaxial cable. The Pulser-Receiver unit provided the electrical excitation of 5 cycle tone bust signal of the different centre frequencies and collected the received pulse-echo ultrasonic measurements.
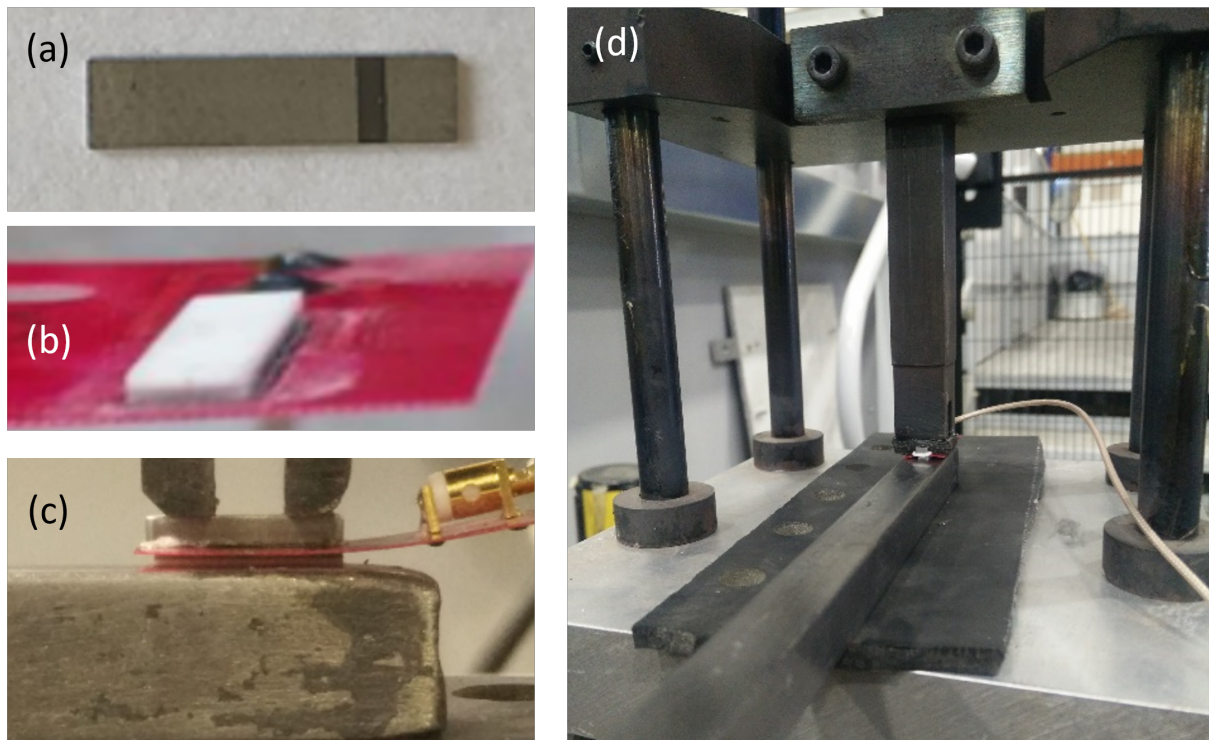
FIGURE 4.14: Experimental setup used for UGW characterisation on a 12 mm square steel bar of length 1.5 m showing the (a) PZT-5A PWAS from the Teletest transducer (b) PWAS and face plate assembly on a custom flexible connector (c) dry coupled on the bar using (d) normal force applied using free weights.

4.6.2 UGW Measurements and Analysis

Ultrasonic pulse echo measurements were acquired at different excitation frequencies of centre frequencies of 35 to 80 kHz in 5-kHz increments to evaluate the transducer frequency response and to assess the different wave modes excited in the waveguide. For each pulse-echo measurement, an averaging of 128 signals was used, as it was sufficient to remove any incoherent noise. A transmitter gain of 30dB to 70dB was considered. The pulse-echo signal amplitude and SNR as a function of the excitation frequency were analysed for different transmitter gain settings. The results are shown in Figure 4.15, which indicates that a 50dB gain offered a suitable trade-off of high signal amplitude and SNR. A significant drop in SNR was observed at 70 kHz regardless of the gain settings. This may be due to the out-of-plane displacement of the PZT-5A and the wear plate assembly as observed in both the simulated and measured vibrational frequency response in free air.
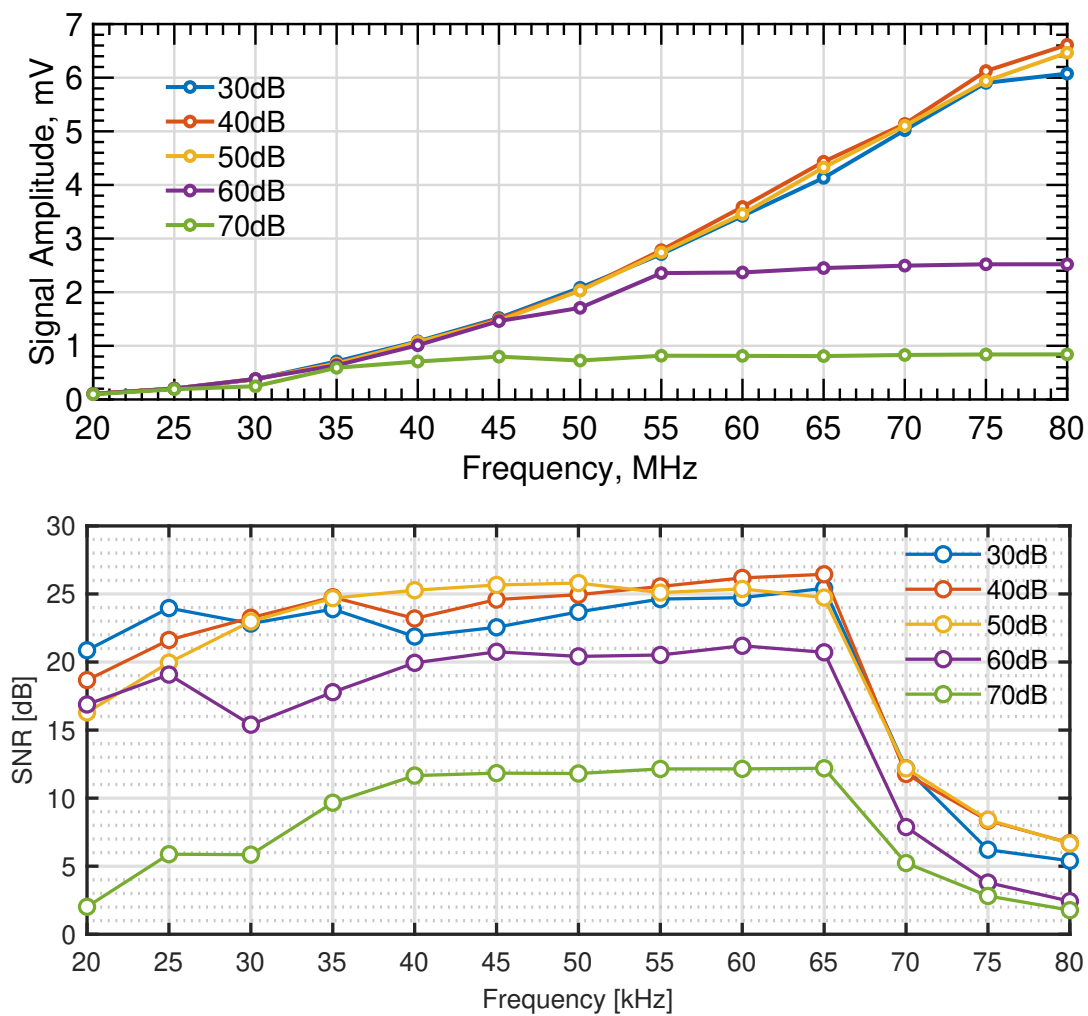
FIGURE 4.15: Pulse echo signal amplitude and SNR as a function of excitation frequency performed at different transmitter gain settings.

Time frequency analysis was performed on the collected pulse-echo measurements. Each ultrasonic measurement was first filtered with a narrow band filter of $(\pm 2 * f_c/5)$ where f_c is the centre frequency of the excitation signal. The signals were then normalised to the amplitude of reflection from the end of the bar. The TFR analysis of the measurements is shown in Figure 4.16. Three distinct UGW reflections were seen at around 0.5 ms, 0.8 ms, and 1.25 ms. The reflection at 0.5 ms and 1.25 ms correspond to the $L(0,1)$ wave mode of velocity around 5000m/s reflections with round trip distances of 3 m and 6 m, respectively. It is important to note that the L(0, 1) modes were excited due to the axial orientation of the transducer vibrating in TS-mode.
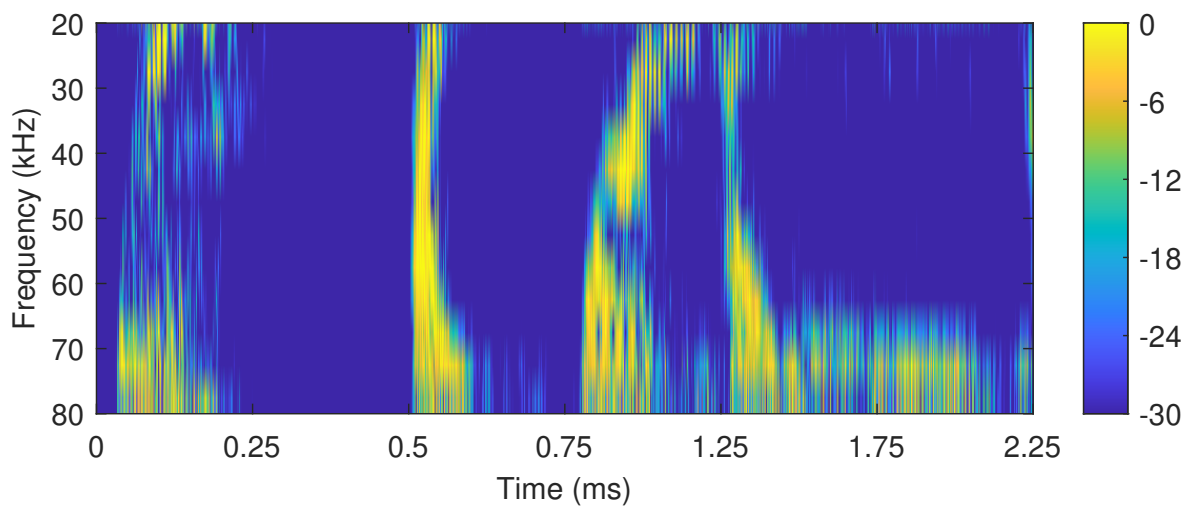
FIGURE 4.16: Time frequency representation of the ultrasonic pulse echo guided wave measurements using PZT-5A wafer transducer.

A dispersive UGW reflection was observed around 0.8 ms. The time of flight analysis from the bar-end reflection indicates the group velocity of around 3750 m/s, which implies that this mode conversion occurred when $L(0,1)$ reflected from the end of the bar. This may be the $F(1,1)$ or $T(0,1)$ wave mode or a superposition of the two. However, it can be observed that noise between the three reflections increased significantly beyond the 60 kHz operating frequency. This increased coherent noise is likely caused by the excitation of multiple wave modes due to the out-of-plane displacement of the PZT-5A and the wear plate assembly, as observed in the simulated and SLDV measurements.

4.7   Summary

This chapter presented a unified numerical and experimental methodology for the design and characterisation of an HT-PWAS transducer for UGW application. Characterisation parameters were chosen for HT-TS-mode operation for the transduction of $T(0,1)$ guided wave mode on HTPs. The methodology involved analysis of the electromechanical impedance, vibrational behaviour, and UGW response as a function of frequency. These characterisation methodologies are applied and validated using a PZT-5A PWAS used in the Teletest transducer.

The TS-mode piezoelectric properties of PZT-5A derived from EMIS at ambient temperature compared well to those reported in the datasheet. These properties were derived as a function of temperature from HT-EMI and were introduced as temperature-dependent properties into the model. The simulated high-temperature response, including resonance frequencies and capacitance, was within measurement variations and less than 5% at temperatures up to 300°C.

The simulated vibration frequency response of PWAS and the influence of the wear plate accurately captured the vibration modes and resonances measured using 3D-SLDV. This allowed the interpretation of the vibration modes of the transducer and can be used to characterise the purity of TS-mode and thus the torsional guided wave mode. The simulated response and the LDV frequency response indicated the presence of out-of-plane vibration around 70 kHz, which was confirmed by the UGW measurements on a waveguide. This is detrimental to the UGW application around that frequency range, as it introduces unwanted wave modes.

The numerical FEA approach provides an appropriate tool for simulating the dynamic electromechanical response piezoelectric devices as a function of frequency and temperature and can be used to study different transducer materials and their design parameters to evaluate and optimise performance for HT-UGW applications. This is applied to characterise and optimise the Teletest transducer in Chapter 5 and for the analysing HT piezoelectric materials in Chapter 7.

Chapter 5

Ultrasonic characterisation and optimisation of Teletest transducer

5.1 Introduction

This chapter applies the design characterisation methodologies established in Chapter 4 to optimise the design of an existing Teletest transducer. The validated PZT-5A PWAS FEA model is used to analyse the influence of design parameters of the PWAS and passive transducer layers on the electromechanical and vibrational response of the transducer. Parametric design studies are conducted to maximise in-plane vibration over out-of-plane vibration to optimise operation in TS-mode and achieve higher SNR for transduction of the torsional wave mode. The formulated design hypotheses are validated by experimental measurements, whereby the optimised transducer performance is characterised and compared with the current Teletest transducer. The amplitude of the ultrasonic signal and the wave mode response are evaluated as a function of frequency to analyse the SCNR of the transducer. An application of the optimised transducer design for GWT is presented.

5.1.1 Motivation

PUT have a complex, multi-layered structure, and their characteristics depend on the interaction between its electrical, mechanical, and thermal properties. A typical transducer has active piezoelectric and passive layers as described in Chapter 2. The design parameters of each transducer layer, such as material and geometry, affect their natural frequencies and mode shapes. This, in turn, affects the vibrational and electromechanical frequency response of the transducer and thus their ultrasonic performance in the given application.

The numerical FEA approach to optimising the design of the transducer can significantly reduce the time and cost involved in the mechanical and electrical design process, especially when complex designs are involved. Numerical studies can evaluate different parameters of the transducer design to improve its electromechanical and ultrasonic performance, which would lead to a more effective UGW application with improved accuracy and sensitivity to defects, and a wider range of inspection.

For ultrasonic applications, if there is resonance in the operating frequency range, i.e. if the excitation frequency of the transducer matches the natural frequencies, it can lead to excessive vibration, increased stresses, and reduced ultrasonic efficiency. For a UGW transducer designed to operate in TS-mode for the excitation of the $T(0,1)$ wave mode in pipes, it is critical to ensure that a non-resonant behaviour is achieved in the operating frequency range $(20 - 100kHz)$ and that no vibration mode is coupled with TS-mode. This coupling can lead to the excitation of unwanted guided wave modes that can degrade the purity of $T(0,1)$ and therefore limit SCNR and overall system performance. If a resonance does exist, it is crucial to analyse its origin, so it can be mitigated by choosing a different geometry or damping materials in the transducer to ensure stable operation.

Electrical connections using wrap-around or edge electrodes are common to simplify transducer assembly and reduce transducer footprint. However, this electrode configuration results in non-uniform electric fields at the edges of the piezoelectric plate. Previous studies have shown that electrodes wrapped around can significantly degrade electromechanical performance [243, 244]. From the numerical studies performed on PZT-5A PWAS in Chapter 5, it was evident that the wraparound electrode design led to the introduction of out-of-plane resonances, which can have a negative impact on TS-mode and the purity of the wave mode. A study evaluated a modification of the Teletest transducer with PZT-5A PWAS with a parallel electrode and analysed the UGW modes excited in a plate with a single excitation frequency of $90kHz$ [245]. Although the signal amplitude and SNR are not reported, the purity of the SH_0 wave mode was significantly improved with a parallel electrode, showing promising results for further investigation.

A previous study investigated the mechanical resonances within the Teletest transducer and the influence of the dry coupling force using FEA which was validated with LDV measurements [246]. Eigenfrequency analysis of the Teletest transducer with steel backing of dimensions $L = 14mm$, $W = 14mm$, $T = 12.5mm$ indicated the lowest resonance frequency at around 80 kHz in free air. However, an additional contact resonance at 20kHz was introduced when constrained with dry

coupling   force.   A   parametric   study   on   the   width   considered
$W = [6mm, 7.5mm, 10mm]$ and this additional resonance was found to increase with
reduced width. It was also shown that an asymmetry in the backing mass caused by
the connector hole generated an imbalance and a rotational moment in the transducer.
The influence of the backing layer and materials is not adequately reported in the
literature. Therefore, the design parameters of the backing layer are also of interest for
this investigation.

5.1.2   Aims and Objectives

The purpose of this study was to understand the influence of the design parameters
of PUT on the electromechanical and vibrational characteristics for GWT application,
and propose design improvements to optimise the ultrasonic performance for the
transduction of the $T(0,1)$ mode. For this study, the following specific objectives were
set:

(1) Application of the PZT-5A PWAS model of Chapter 4 to study the influence of the
parameters of the piezoelectric wafer design, including dimensions, polarisation,
and electrode configuration.

(2) Analyse the natural frequencies of the backing layer of different dimensions and
their influence on the vibrational response of the transducer.

(3) Validate the design hypothesis of (1) through experimental analysis of optimised
piezoelectric wafer design parameters.

(4) Propose a optimised transducer design with the hypothesis of (1) and (2) by
characterising the performance for UGW application.

5.2   FEA of Teletest Transducer

5.2.1   Geometry and Mesh

The PZT-5A PWAS and Al_2O_3 face plate model from Chapter 4 was advanced to
study the Teletest transducer. The transducer geometry was simplified to include only
the stainless steel backing block and excluded the adhesive layers and electrical
connections. The adhesive layers were approximately $100\mu m$ thick and the connector
was pressfit and not mechanically coupled to the body of the transducer. Therefore, it
was assumed that their contribution to the structural stiffness of the transducer and
its motion was negligible. Although the connector housed on the backing of the

transducer was excluded, the shape of the access hole in the backing layer was preserved to achieve representative physical properties.

This simplified geometry of the transducer significantly reduced the meshing requirement and the number of elements and nodes. The PZT-5A piezoelectric plate and the wear plate were discretised using the fine-mapped mesh optimised in Chapter 4. The backing layer of the transducer was discretised using a tetrahedral mesh that efficiently covered the slots and access holes in the backing layer. A higher mesh density was used in the regions near the piezoelectric layer where the most significant displacement was expected. The geometry of the transducer model with dimensions, meshing, and an example of simulated displacement profile showing the TS-mode vibration response is shown in Figure 5.1.
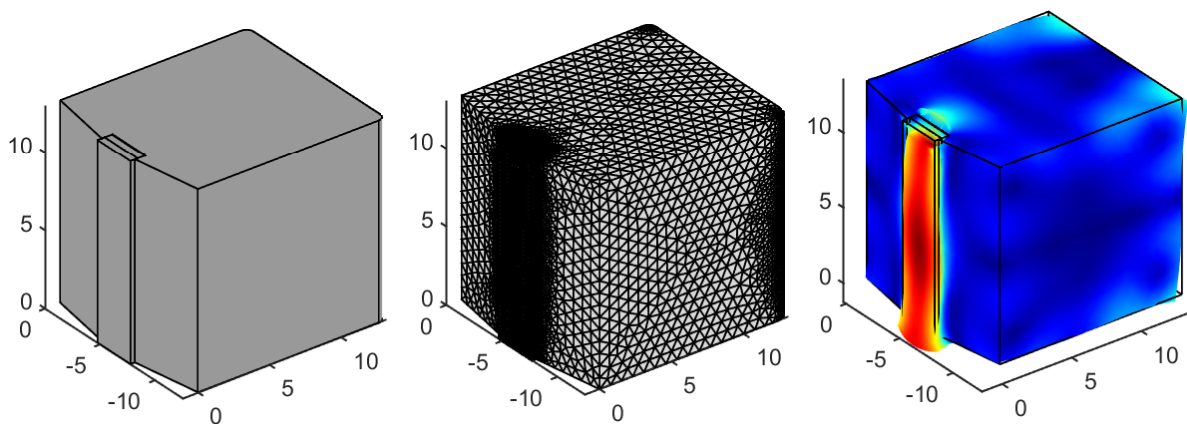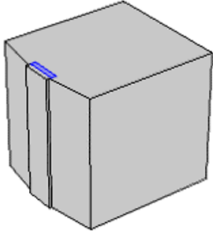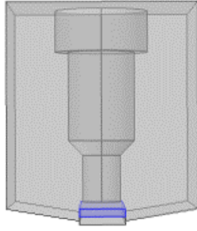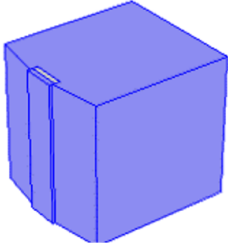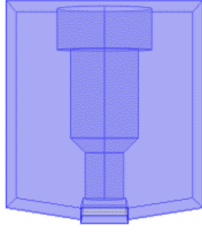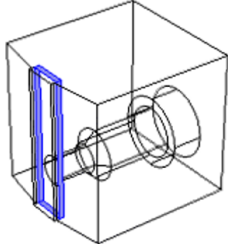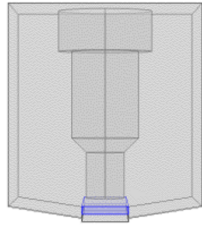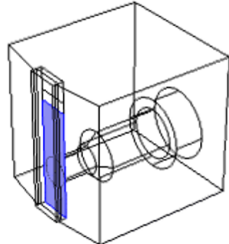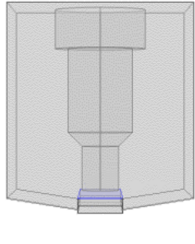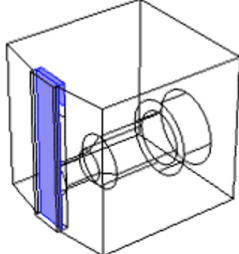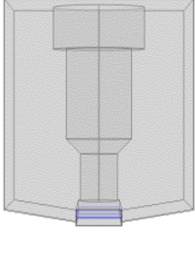
FIGURE 5.1: Geometry of the transducer being studied and incremental models of the piezoelectric plate, wear plate assembly and complete transducer.

5.2.2 Boundary Conditions

The three layers of the transducer were defined as explicit domains, where the piezoelectric plate was modelled as a piezoelectric domain, and the rest of the transducer was modelled as a linear elastic domain. The Form Union operation in COMSOL created a single transducer object with the sequence of joined domains. The form-union case assumes that domains cannot move or slide relative to each other; thus, the internal friction between the bonded surfaces was ignored. The physics and boundary conditions applied to the transducer domains are shown in Table 5.1.

TABLE 5.1: Boundary conditions applied to the transducer model.

Physics	Domain or Geometry	Comment
Piezoelectric Material Model		The PZT-5A plate was modelled as a piezoelectric domain. The plate length was aligned along the geometric +Z direction to achieve length polarisation.
Linear Elastic Material Model		The non-piezoelectric layers - wear plate and backing layer were defined as a linear elastic domain.
Zero Charge		The zero-charge node added zero surface charge density conditions on the boundary, enabling floating potential implementation using a terminal node.
Terminal		Terminal nodes were applied to the selected boundary of the piezoelectric domain to implement a connection to the external circuit.
Ground		Ground node was applied on the top surface of the piezoelectric domain to implement zero potential boundary conditions.

5.2.3 Electromechanical Vibrational Analysis

Electromechanical analysis was performed to analyse the resonances and vibration modes of the transducer within the frequency range $20 - 160kHz$. A wider frequency range was used, as previous studies have found that resonances can shift to lower frequencies due to the applied dry coupling force [246].

The eigenmodes in the frequency range between 20 kHz and 150 kHz and their respective displacement patterns are shown in Figure 5.2. The results suggested five eigenmodes at 140 kHz, 142 kHz, 146 kHz, 150 kHz, and 152 kHz. It can be seen that the resonances around 140 and 150kHz show out-of-plane displacement is dominated and that this would lead to the generation of unwanted wave modes.
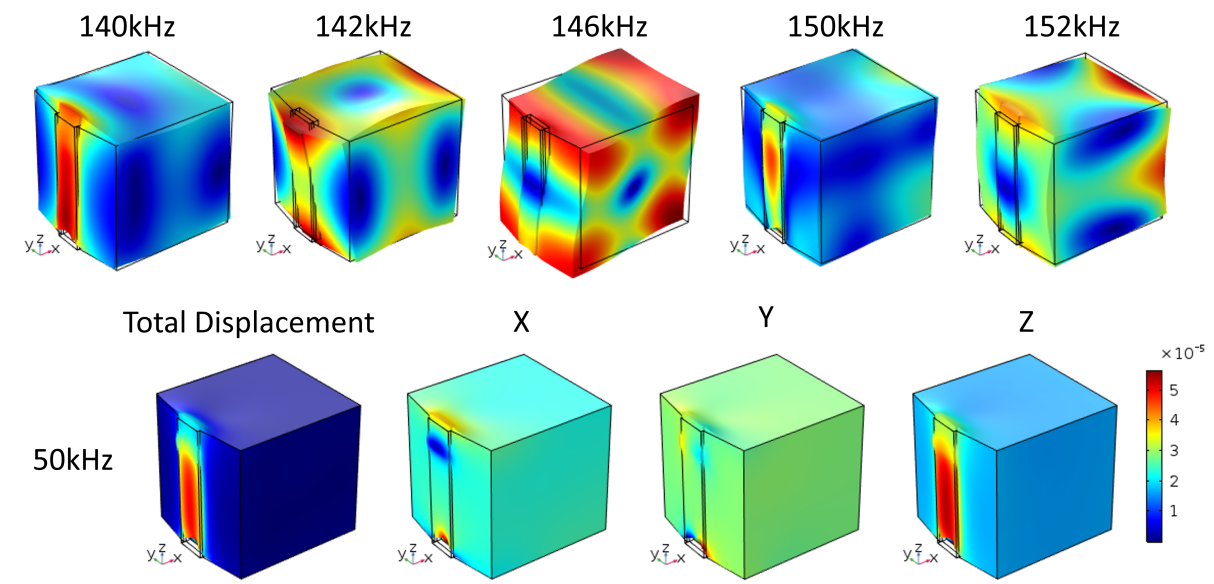
FIGURE 5.2: Vibrational response of the Teletest transducer at eigenfrequencies along with the displacement fields in a non-resonance frequency of 50kHz.

The three-dimensional displacement fields of the active transducer surface were calculated as a function of frequency as described in Chapter 4. The displacement of the face plate surface was averaged in the three directions shown as a function of frequency. The in-plane displacement and flat frequency response were seen in the 20-70kHz range, but resonances were observed at higher frequencies as seen in the displacement spectrum in Figure 5.3. From the displacement patterns, it is evident that these resonances occur in the stainless steel backing layer. However, these would influence the TS-mode vibration of the piezoelectric plate and thus can introduce unwanted wave modes. The displacement and deformation profiles of the contour curve show wave propagation over the piezoelectric material. Even in the nonresonant region, there is stress concentration around the gap between the wraparound electrode.
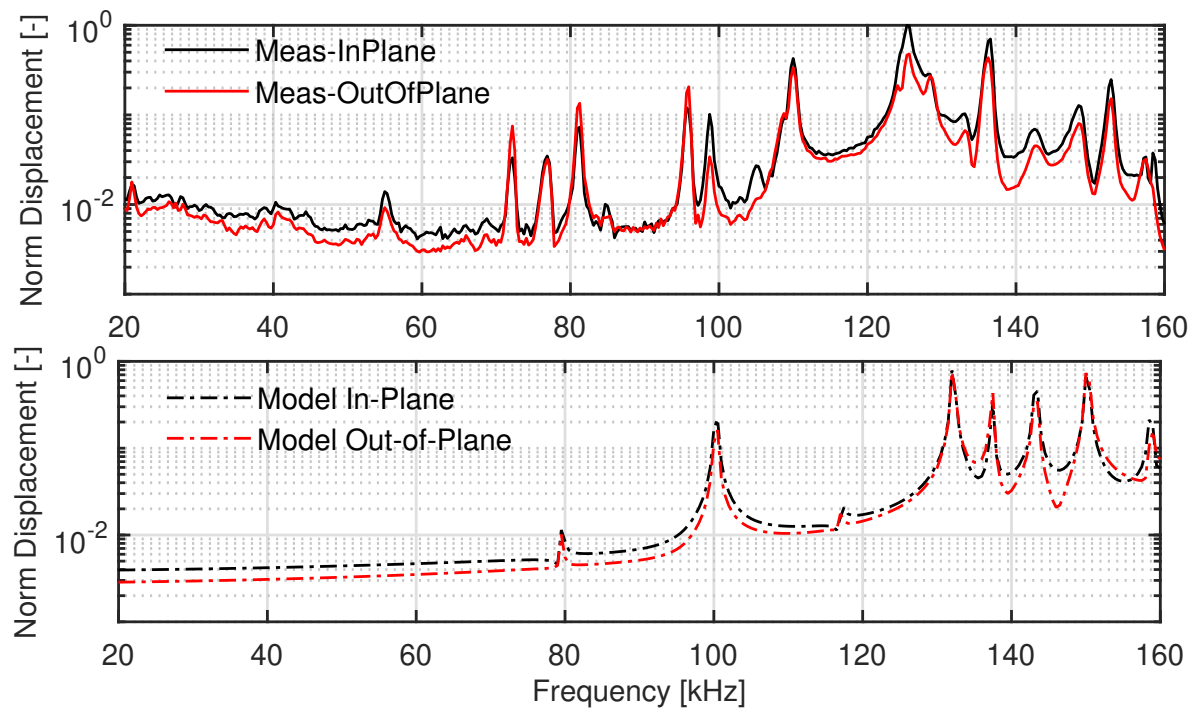
FIGURE 5.3: Measured and modelled in-plane shear and out-of-plane displacement fields averaged over the wear plate surface as a function of frequency.

5.3 Analysis of Transducer Design Parameters

This study used the current Teletest transducer as a baseline and investigated several design parameters to optimise ultrasonic performance. Transducer FEA models developed and validated in Chapter 4 were used for this optimisation study. The alternative design configurations are characterised and their performance is compared to that of the Teletest transducer. This numerical modelling then creates a design hypothesis for the HT-UGW transducer which is validated through experiments.

The transducer design has multiple degrees of freedom that can influence the transducer's ultrasonic performance. This includes dimensions and material for different components of the transducer, including the piezoelectric plate, the wear plate, and the backing layer, as illustrated in Figure 5.4.

Firstly, the design optimisation of the piezoelectric plate was performed by analysing the effect of the piezoelectric plate design variables, including plate dimensions, direction of polarisation, and electrode pattern. The design parameters evaluated in this study focus on the findings of the PZT-5A PWAS model developed in Chapter 4.
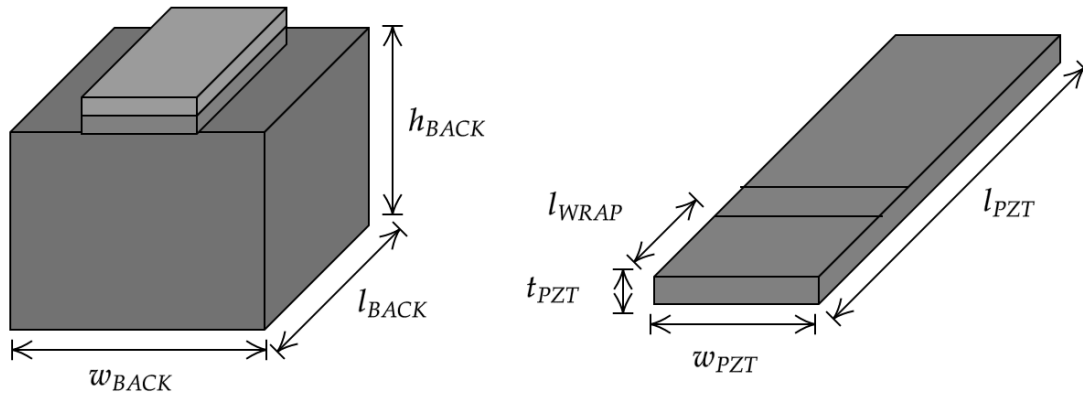
FIGURE 5.4: Design parameters of the transducer backing block and the piezoelectric element.

The dimensions of the backing layer should be minimised to reduce material and manufacturing costs and maintain the density of the transducer array required for smaller NPS pipes. The key transducer layers for the design of HT-UGW and their design parameters are listed in Table 5.2. The table indicates the design variables and parameters considered for the transducer design and compares them with those used in the current Teletest transducer.

TABLE 5.2: Design variables for modelling and analysis of HT-UGW transducer.

Transducer Component	Design Parameter	Teletest Transducer	Values Characterised
Piezoelectric Plate	Dimensions (mm)	$l_{pzt} = 13$ $w_{pzt}=3$ $t_{pzt}=0.5$	$l_{pzt}=[6,7,8,9,10]$ $w_{pzt}=[1,2,3,4]$ $t_{pzt}=[0.25, 0.5, 0.75, 1.0]$
	Polarisation Electrode	L-Polarised Wrap-around $l_{wrap} = 2$	L-Polarised, W-Polarised Parallel and Wrap-around $l_{wrap} = [0.5, 1, 1.5, 2]$
Backing Layer	Dimensions (mm)	$l_{back} = 13$ $w_{back}=12$ $h_{back}=12$	$l_{back}=[14, 15, 16]$ $w_{back}=[6, 7, 8, 9, 10, 11, 12]$ $h_{back}=[6, 7, 8, 9, 10, 11, 12]$

5.3.1 Piezoelectric Polarisation and Electrode

The PZT-5A piezoelectric plate of the current Teletest transducer is polarised along the longitudinal dimension of 13*mm*. When installed on the pipe, the length of the piezoelectric plate is aligned in the circumferential direction, and the shear motion in the length direction provides the tangential force for torsional mode excitation. This creates a contact length that is equal to the width of the piezoelectric plate. To maximise the contact, the piezoelectric plate can be polarised in the shorter lateral width direction, aligning it with the circumferential direction of the pipe. In this case, the contact length is equal to the length of the piezoelectric plate. The piezoelectric plate of the same dimensions and two described polarisation configurations along with the contact are illustrated in Figure 5.5.
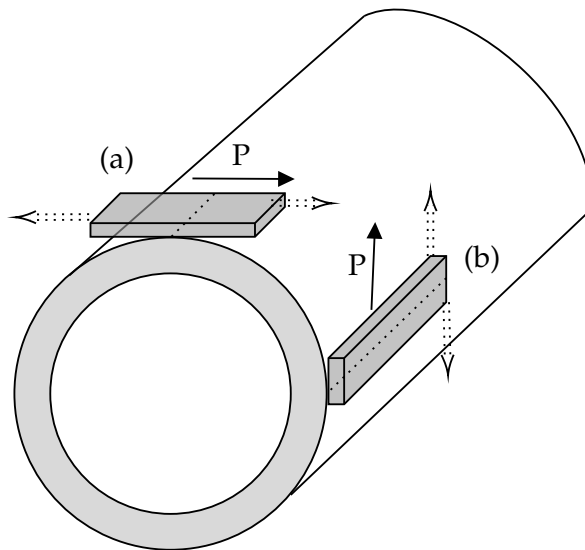
FIGURE 5.5: Illustration of the piezoelectric plates with (a) length polarisation and (b) width polarisation installed on the pipe for torsional mode excitation.

A dry coupling force is generally applied to the piezoelectric transducer for the transduction of guided waves. Under a coupling force, the contact surface area can be approximated using the Hertzian theory of elastic contact [247]. The theory and calculations for contact surface area between a cylinder and a flat plate are described in Appendix A.1. This theory can be used to calculate the expected contact area between the rectangular piezoelectric plate and a cylindrical pipe. This example calculation considers a 4-inch pipe (ϕ=114.3mm), a 13*mm* x 3*mm* x 0.5*mm* piezoelectric plate and a contact force of 200 N. The length polarised piezoelectric plate shown in Figure 5.5 (a) will have a contact area of ≈ 0.87 square millimetres, whereas the width polarised plate shown in Figure 5.5 (b) will have a contact area of ≈ 3.76 square, which is higher by a factor of 4.33.

The influence of the direction of polarisation on a piezoelectric plate was analysed using the PZT-5A PWAS model from Chapter 4. The eigenfrequency analysis was performed on the plate with polarization along the lateral 3*mm* width direction and compared to longitudinal polarisation. The vibration frequency response and displacement pattern for PZT-5A piezoelectric plates polarised in the length or width direction with parallel electrode configuration is shown in Figure 5.6.
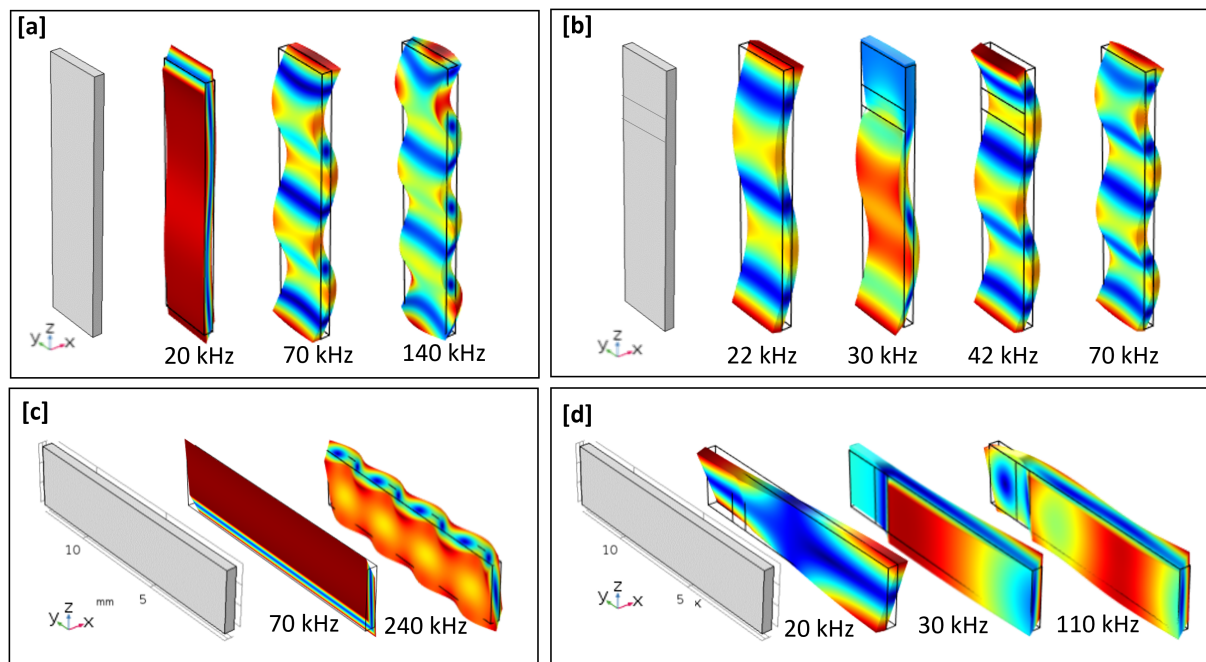
FIGURE 5.6: Vibrational analysis of PZT-5A PWAS eigenfrequencies with polarisation along the longitudinal 13mm length direction with (a) parallel electrodes and (b) wrap-around electrodes; and with lateral polarisation along the 3mm width direction with (a) parallel electrodes and (b) wrap-around electrodes.

For longitudinally polarised PWAS with a parallel electrode, two out-of-plane resonances were observed within the frequency range of interest at 20*kHz*, 70*kHz* and the next overtone at 140*kHz*. For the longitudinally polarised plate with wrapped around electrode, additional out-of-plane vibration modes at lower frequencies of 22*kHz*, 30*kHz* and 42*kHz* were introduced. With the laterally polarised PWAS , the first resonance with significant out-of-plane vibration was at 240*kHz*, which was outside the UGW frequency range. The wrap-around electrode configuration on the lateral polarised plate introduced out-of-plane vibrations at 20*kHz* and 30*kHz* as seen with the length-polarised plate, but the next overtone was at a much higher frequency of 110*kHz*. The simulated electromechanical impedance amplitude and the three-dimensional displacement components as a function of frequency for the four PZT-5A PWAS variants are shown in Figure 5.7.
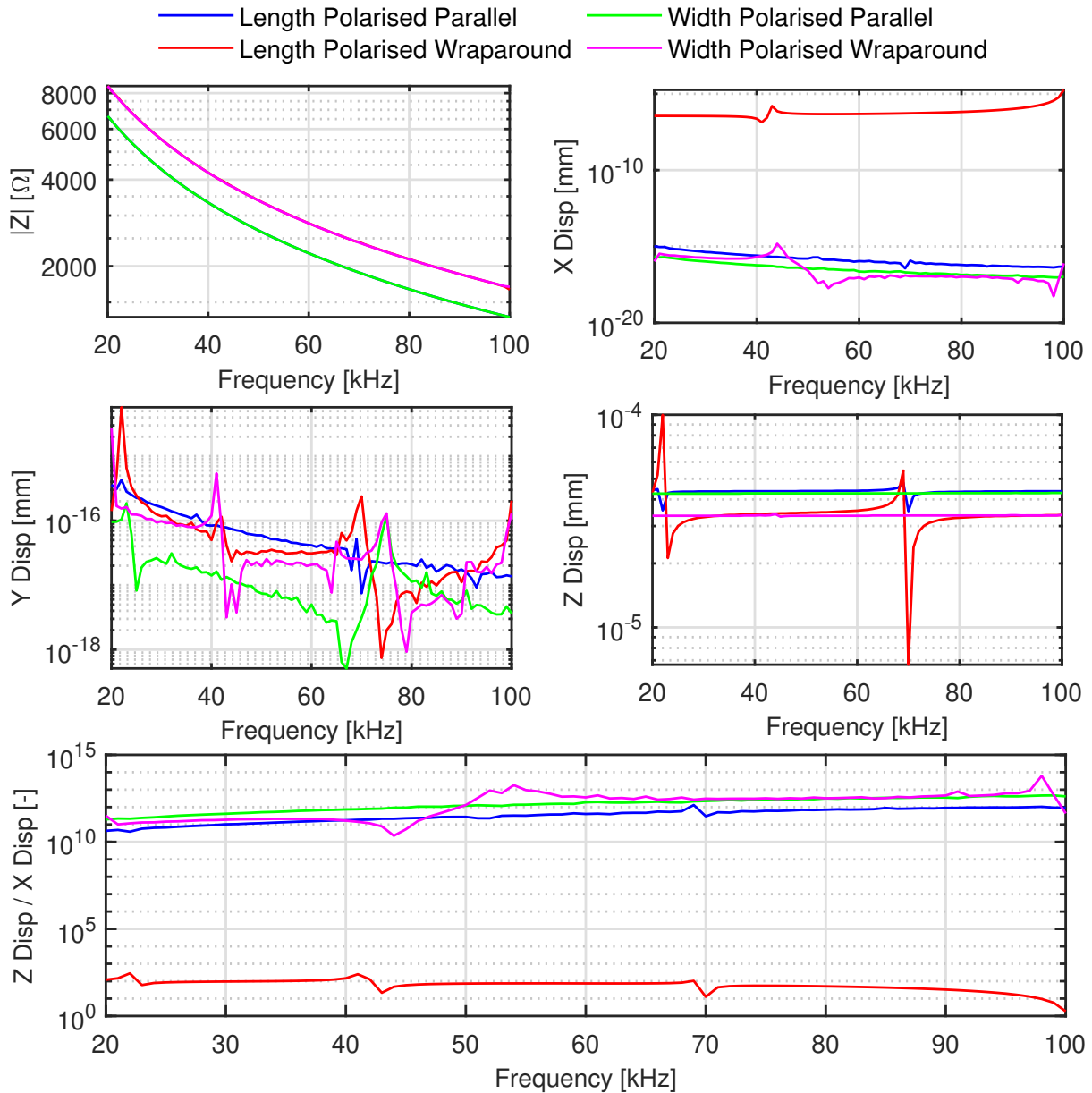
FIGURE 5.7: Simulated EMI and displacement fields as a function of frequency for the four PWAS designs considered with lateral or longitudinal polarisation with parallel or wrapped electrode configuration.

The impedance response of both length and width polarised plates was the same for each of the electrode configurations, suggesting that it is purely capacitive due to the difference in electrode area. The difference in impedance at $60kHz$ was $\approx 24\%$ with a corresponding difference in the electrode area of 26%. The out-of-plane displacement in the X direction was highest for the length-polarised wraparound plate and was orders of magnitude higher than the other variants. The out-of-plane displacement was around $0.45nm$ at $60kHz$ and was highest at $1.6nm$ at the resonance out of the plane at $42kHz$. The TS-mode in-plane shear displacement in the Z direction was also

comparable for both length and width polarised plates for each of the electrode configurations. The in-plane shear displacement was on the order of $44nm$ for the parallel electrode and $33nm$ for wrapped electrodes; a difference of around 28.5%. The reduction in in-plane shear displacement was more significant around the out-of-plane resonance frequencies of $22kHz$ and $70kHz$. The ratio of displacement in-plane to out-of-plane was assessed as TS-mode FOM. The ratio of in-plane over out-of-plane displacement shows that the current length polarised wrapped-around configuration had the worst performance by several orders of magnitude compared to the other variants. The width-polarised parallel electrode had a $11dB$ higher ratio compared to its respective wrap-around configuration.

A time domain analysis was performed by applying a five-cycle tone burst signal of $70kHz$ centre frequency on the length polarised PZT-5A PWAS in parallel and wrapped-around electrode configuration. The in-plane and out-of-plane displacements generated and the resulting charge are shown in Figure 5.8.
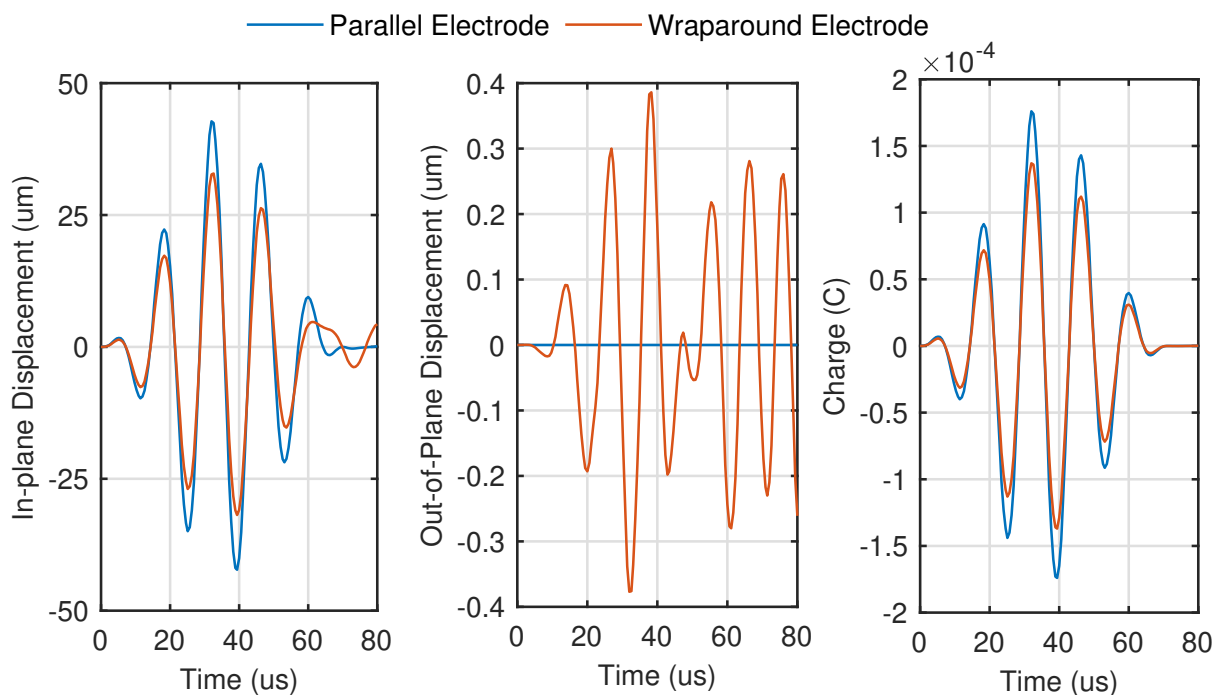
FIGURE 5.8: PZT transducer with parallel vs wrapped around in plane-shear and out-of-plane displacement pattern at a single frequency of 70 kHz model of parallel vs wraparound ultrasonic simulation

A significant increase in the out-of-plane displacement was observed with a wrap-around electrode, which could lead to the generation of longitudinal wave mode and, therefore, increased coherent noise. An in-plane to out-of-plane ratio suggests a theoretical SNR of 36.5dB that was increased by $\approx$16dB with the parallel electrode.

5.3.2 Wrap-around Electrode Design

The out-of-plane displacement coupled with TS-mode produced as a result of the configuration of the wraparound electrode can lead to the excitation of undesirable guided wave modes. This study evaluates the piezoelectric plate design with alternate electrode configurations. This is carried out by varying the design parameter l_{wrap} from the existing value of 2mm to 0.5mm in decrements of 0.5mm. This ressults in a decreased ground electrode and increased terminal or live electrode on the surface of the PWAS. The different wraparound electrode configuration considered are shown in Figure 5.9.

(A) 0.5 mm   (B) 1 mm   (C) 1.5 mm   (D) 2 mm
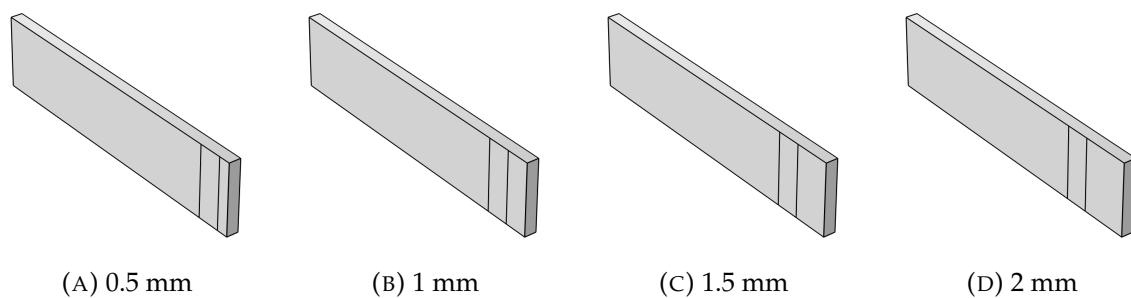
FIGURE 5.9: Geometry of PWAS designs with different wrapped around electrode configurations.

The analysis was carried out for both length-polarised and width-polarised plates. The results of the width-polarised variant are presented here, and the length-polarised showed similar response and are given in the Appendix A.4.2. The impedance, three-dimensional displacement, and electrical charge for the four wrapped-around configurations are compared in Figure 5.10.

The compared parameters had a nearly linear relationship with the reduction in l_{wrap} with a change of ≈3.5% per increment. The impedance of the variant 0.5mm was around 14% lower than 2mm and the corresponding increase in charge was 14pC to 16pC; and in-plane displacement increased from 33nm to 38nm. The in-plane over out-of-plane ratio highlights that the change in resonance around 40kHz but the ratio improved throughout the frequency range for the 0.5mm variant. The in-plane displacement of 38nm for the 0.5mm variant was still around 11% lower than the parallel electrode configuration (42.7nm) at 60kHz. The results show that better sensitivity and electromechanical performance can be achieved with an alternative electrode configuration with l_{wrap}, however, a parallel electrode provides a significantly higher improvement.
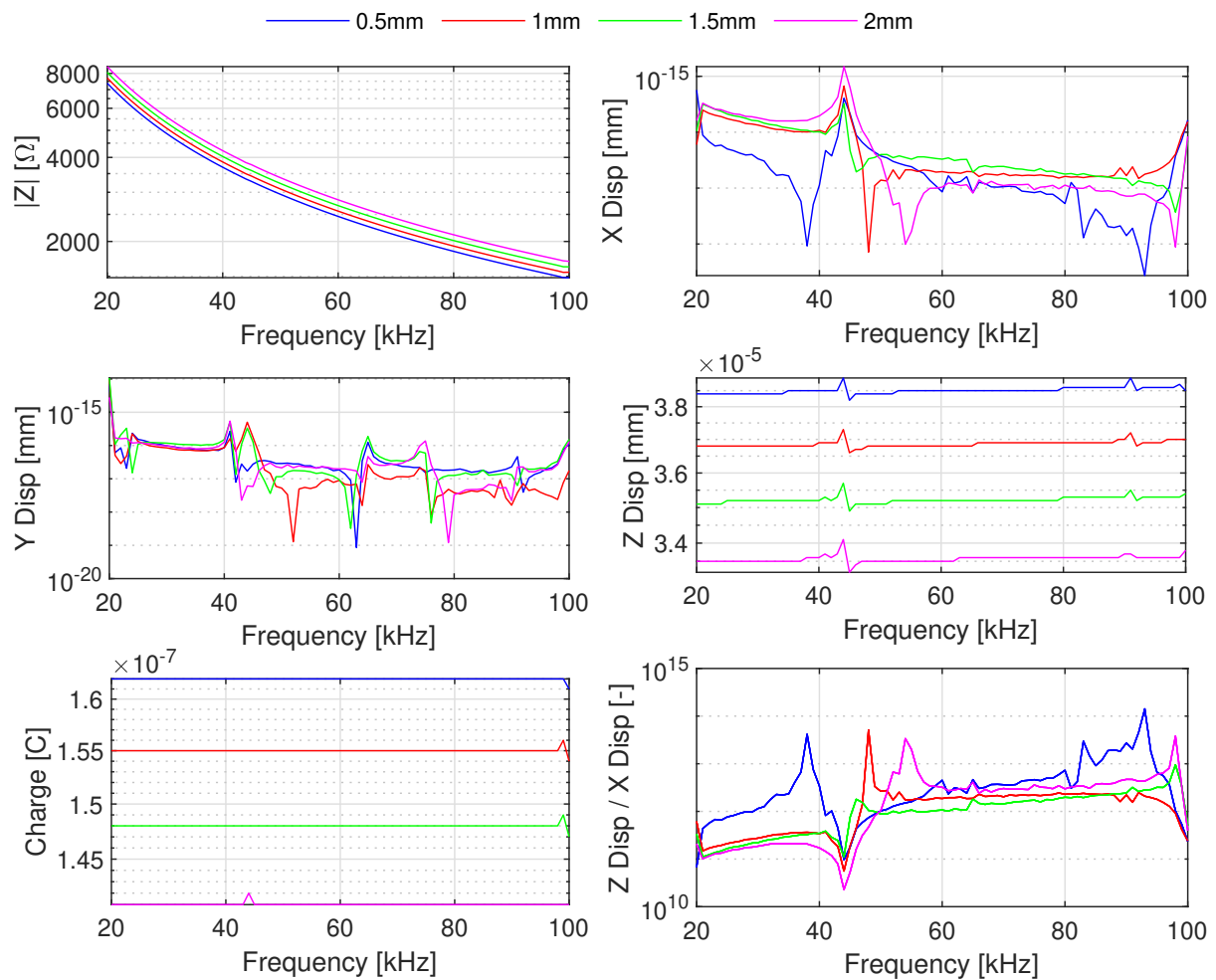
FIGURE 5.10: Simulated electromechanical impedance and displacement fields as a function of frequency for the four width polarised PWAS designs of different wrapped around electrode configuration.

5.3.3 Dimensions of the Piezoelectric Plate

The dimensions of the piezoelectric plate can also influence the coupling of different modes with the desired TS-mode for the generation of UGW and the sensitivity to the received UGW signals at different frequencies. A numerical parametric study was carried out to study the influence of the dimensions of the piezoelectric plate on their electromechanical performance for TS-mode operation. The influence of the dimensions of the piezoelectric plate was analysed using the PZT-5A plate model developed in Chapter 4. The dimensional parameters of the piezoelectric plate listed in Table 5.2 resulted in multiple combinations of the length, width and thickness of the piezoelectric plate. A total of 80 different piezoelectric plates were simulated. The terminal charge of each piezoelectric plate model and the displacement fields in-plane and out-of-plane were evaluated at a single frequency of 70 kHz and are shown in Figure 5.11.
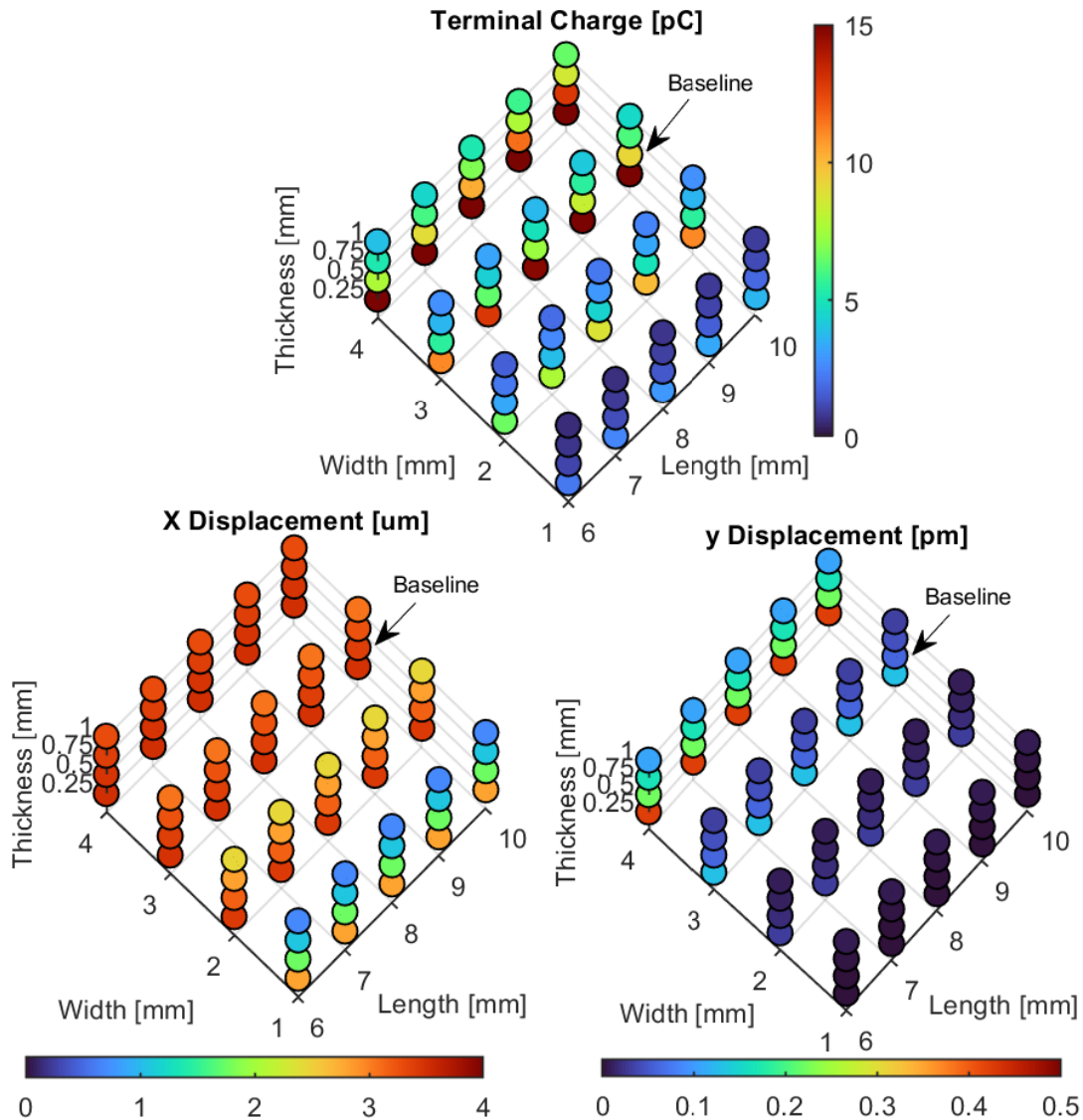
FIGURE 5.11: Effect of piezoelectric plate dimensions on the in-plane, out-of-plane displacement fields and terminal charge for a PZT plate polarised along the width dimension.

The terminal charge, in-plane and out-of-plane displacements for the current PZT-5A plate with dimensions $10mm$ x $3mm$ x $0.5mm$ were $12.8pC$, $3.46\mu m$ and $0.22pm$, respectively. The maximum displacement ratio in-plane over out-of-plane displacement ratio was achieved by $8mm$ x $0.5mm$ x $0.5mm$, but with a reduction in charge to $1.4pC$. The terminal charge was inversely proportional to the thickness of the plate and increased by 100% by reducing the thickness of the plate to $0.25mm$. The highest in-plane displacement was observed for 3.5 mm in width and $0.25mm$ in thickness. However, with a thickness of $0.25mm$, the out-of-plane displacement almost doubled. It is important to note that the in-plane displacement was directly proportional to the width of the piezoelectric plate, which was also the polarisation

direction. The in-plane and out-of-plane displacement did not change for a constant width and thickness, but the charge increased by 10% for each 1*mm* increase in length. For constant width and length and an increase in thickness from 0.25*mm* to 1*mm*, the in-plane displacement decreased by 5%; the out-of-plane displacement decreased from 190% to 50% and the charge from 200% to 50% of the current value.

5.3.4   Dimensions of Backing Layer

As seen with the FEA of the Teletest transducer, the shape and dimensions of the stainless steel backing resulted in natural frequencies just outside the operating frequency range for UGW. These resonances lead to a variation in the electromechanical performance of the transducer. The resonances may shift to lower frequencies in the operating range due to boundary conditions or temperature. This study analysed the natural frequencies of the stainless steel backing layer of different dimensions. The first six eigenfrequencies of the 13*mm* x 12*mm* x 10*mm* stainless steel backing of the Teletest transducer are shown in Figure 5.12.
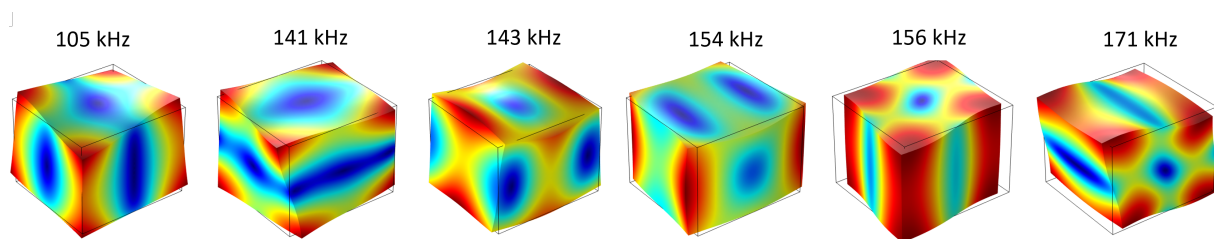
FIGURE 5.12: Eigenfrequencies of 13mm x 12mm x 10mm stainless steel backing block.

A parametric eigenfrequency analysis was performed on a fixed backing height of 10*mm* with varying length and width in the range of 7*mm* to 12*mm* with increments of 1*mm*. The lowest eigenfrequency corresponding to each backing shape is given in Figure 5.13. It can be seen that all the evaluated shapes had resonances above 120kHz and the highest was achieved for square geometries of 9*mm* x 9*mm* and 10*mm* x 10*mm*. This shows a dependency with the aspect ratio and suggests that a more even distribution of mass leads to symmetric vibration modes of higher frequencies.
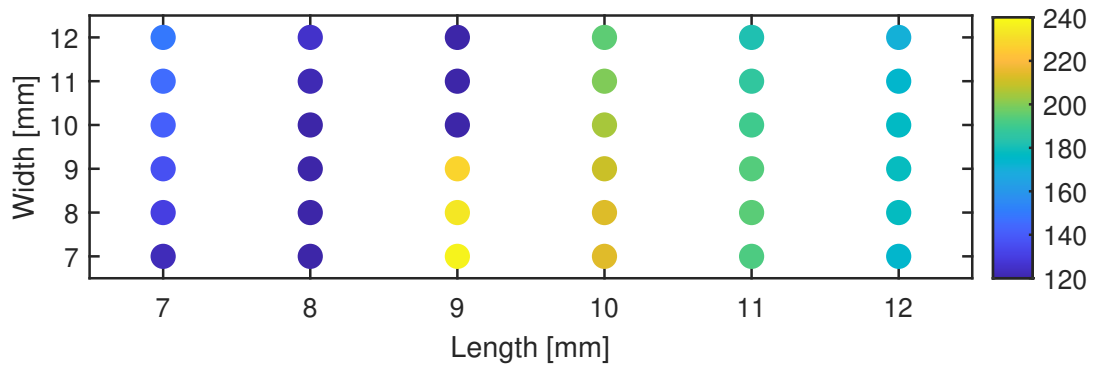
FIGURE 5.13: Eigenfrequencies of different length and width of the backing block for a fixed height of 10mm.

Next, an eigenfrequency analysis was performed on a block 10*mm* x 10*mm* of varying heights in the range of 1*mm* to 7*mm* with increments of 1*mm*. The first six resonance modes corresponding to each backing shape are shown in Figure 5.14. Reducing the height of the backing shows an increase in eigenfrequencies, with the lowest eigenfrequency doubling from 120*kHz* for 7*mm* height to 245*kHz* for 1*mm*. This is due to the reduced mass and increased stiffness of the block with decreasing height.
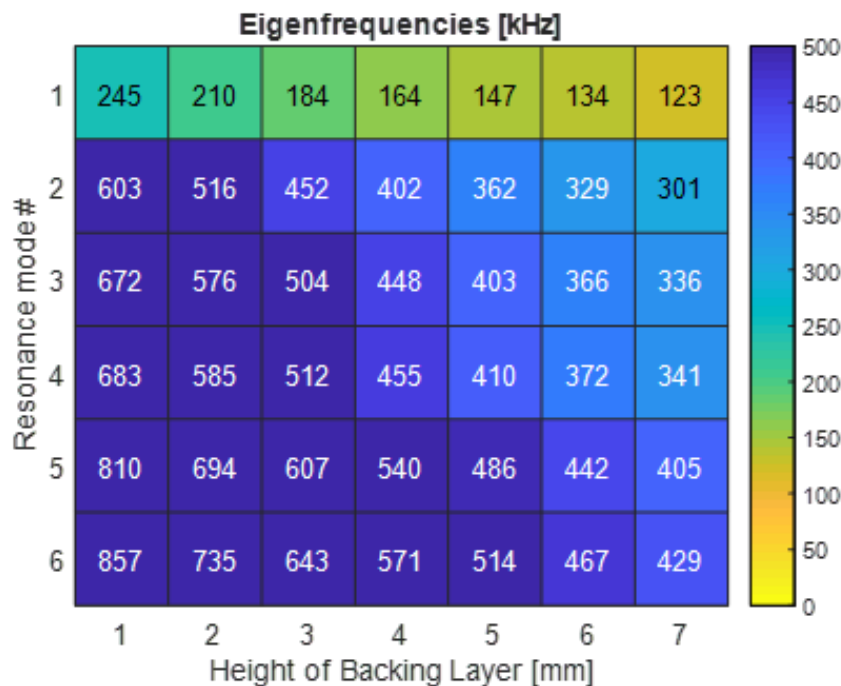
FIGURE 5.14: Analysis of first six eigenfrequencies of a stainless steel block of 13 mm length and 10 mm width of varying thickness ranging from 1 to 7 mm.

5.3.5   Alternative Transducer Designs

A frequency domain analysis was performed on a complete transducer with a PZT-5A PWAS of dimensions 10*mm* x 3*mm* x 0.5*mm* with parallel electrode in the width dimension sandwiched with the same dimensions wear plate. A square backing of 10*mm* x 10*mm* with heights in the range of 6*mm* to 12*mm* with increments of 2*mm* was considered for a parametric study. The electromechanical impedance response corresponding to each transducer variant is shown in Figure 5.15. It can be seen that the resonance in the backing at around 120*kHz* for the height of 12*mm* changes to a higher frequency around 150*kHz* with a backing height of 6*mm*. In-plane shear and out-of-plane displacement were averaged across the wear plate and compared for the transducer variants. It can be seen that the out-of-plane displacement was significantly reduced with a square backing of 10*mm* x 10*mm* x 10*mm*, resulting in the highest displacement ratio from the plane to the out of the plane. The difference in the ratio related to an improvement of ≈12.5dB. The results also confirmed the hypothesis of the square aspect ratio of the backing block and it's impact on the electromechanical response of the transducer.
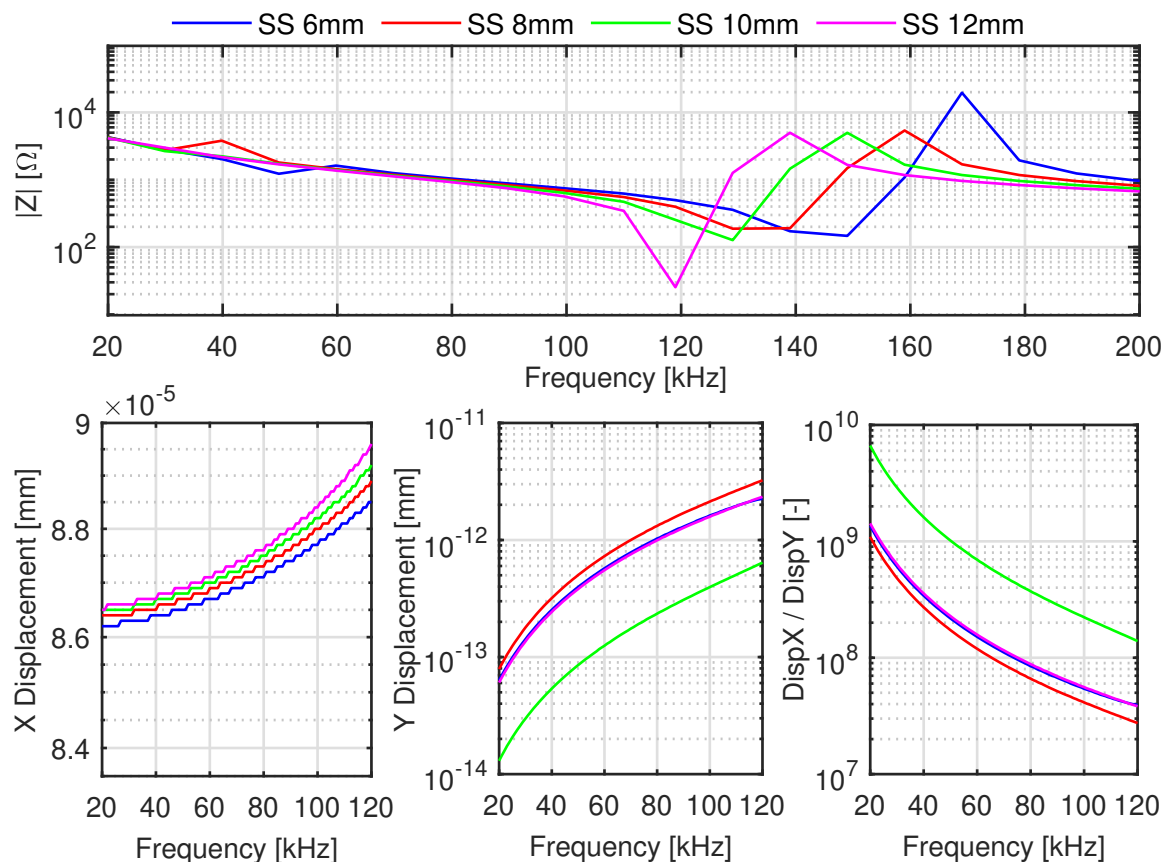
FIGURE 5.15: Electromechanical impedance and simiulated in-plane and out-of-plane displacement response of the alternative transducer designs.

5.4   Optimised Transducer Design and Application

The discussed parametric FEA studies guided the design of an optimised transducer. The results of FEA indicated that lateral-polarised PWAS with both wrapped-around and parallel electrode design resulted in a significant reduction in out-of-plane vibration compared to the current design. An alternative transducer and complete array design was developed using a width-polarised wraparound electrode PZT-5A PWAS. A smaller backing mass of dimensions 13*mm* x 3*mm* x 2*mm* was used and had no natural frequencies in the UGW operating range. The design and performance of the transducer is compared with the current Teletest transducer, but because of commercial sensitivity, the details of the transducer construction are not shared. The development work was covered under the H2020-EC-Horizon Fast Track to Innovation Programme [248, 249]. The EMIS of the width-polarised PZT-5A PWAS was compared with that of the length-polarised variant and is shown in Figure 5.16.
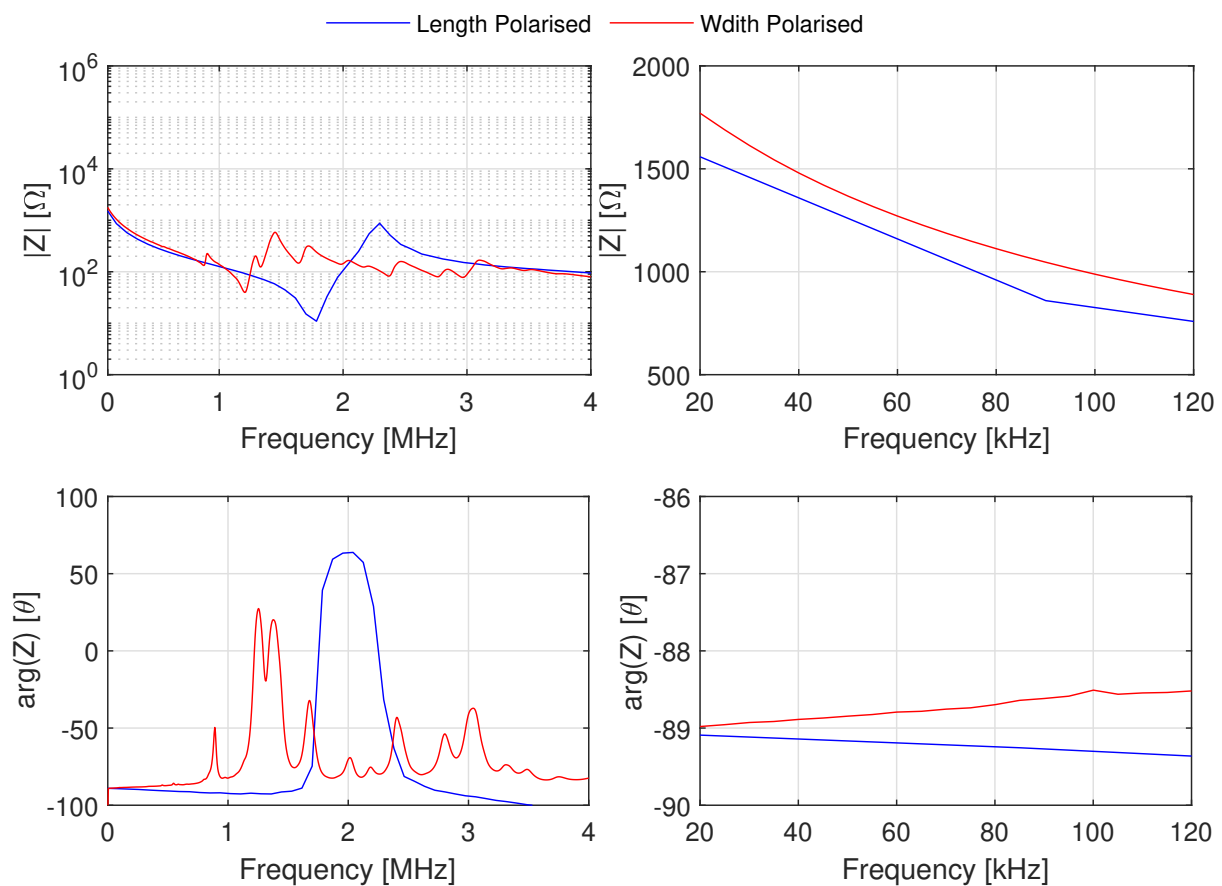
FIGURE 5.16: Comparison of EMI measurements of longitudinal and lateral polarised PZT-5A PWAS.

The EMI amplitude and phase are compared in the MHz and UGW kHz frequency range. The MHz frequency range shows multiple additional resonances at lower frequencies of around $900kHz$ with the width-polarised plate. In the UGW frequency range, no resonance is observed and the response is purely capacitive, as can be seen with a phase angle of approximately -90°. The impedance of the width-polarised was approximately 20% higher 1047Ω compared to 860Ω for the length-polarised at 100kHz. Since both piezoelectric plates had the same wrapped-around electrode and hence the capacitive area, this variation cannot be due to the dimensions and is likely a result of the direction of polarisation.

PZT-5A PWAS of dimensions $13mm$ x $3mm$ x $0.5mm$ with wrap-around CuNi electrodes sandwiched with Al_2O_3 of the same dimensions was acquired from PI Ceramics Gmbh and used for the new transducer design. The ultrasonic performance of the optimised transducer was characterised using the methodology described in Chapter 4 and compared to the Teletest transducer. Ultrasonic guided wave measurements were recorded in pitch-catch mode with a bonded PZT-5A PWAS used as a reference. An example of guided wave measurement where both the Teletest transducer and the optimised transducer were used as a transmitter with an excitation signal of 10-cycle toneburst of $70kHz$ is shown in Figure 5.17.
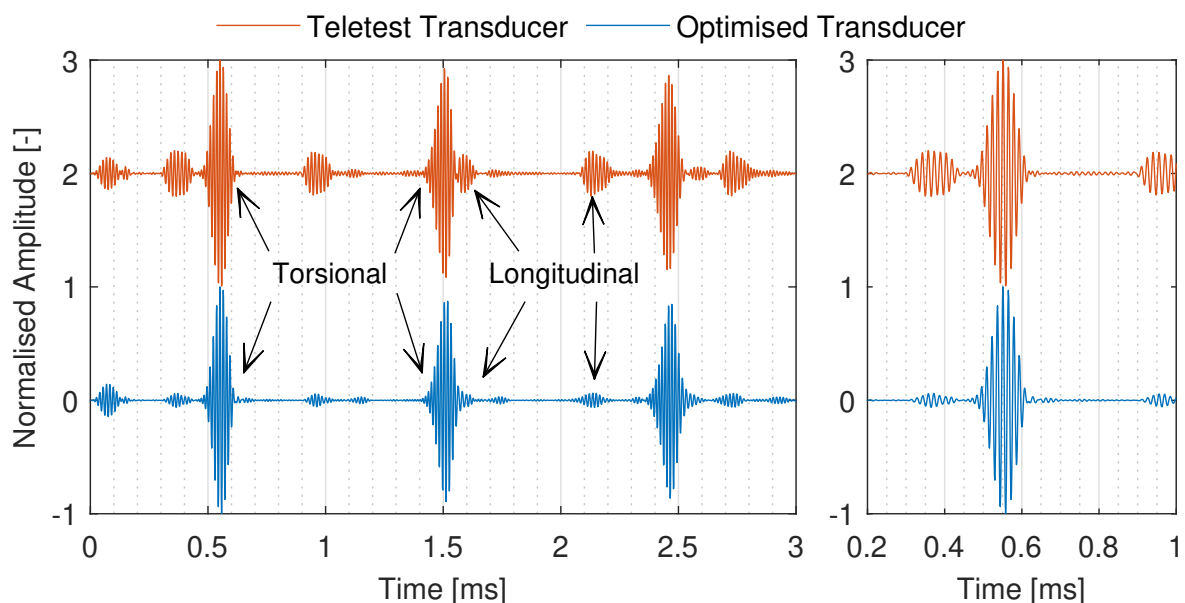
FIGURE 5.17: Comparison of transmitted UGW signal by the Teletest transducer and bespoke transducer with lateral polarisation showing the desired torsional and unwanted longitudinal wave modes.

The transmitted torsional signal with a velocity of $3000m/s$ and a travel distance of $1.5m$ can be seen arriving at $0.5ms$ and multiple reflections from the end of the bar can

be seen in increments of $1ms$. The longitudinal mode travelling at $5000m/s$ can be seen at $0.3ms$ and its reflections at increments of $0.6ms$. Excitation of this longitudinal mode is significantly reduced with the optimised design with a reduction in amplitude of around $10dB$ relative to the desired torsional mode.

A frequency sweep analysis was performed where both the Teletest transducer and the optimised transducer were used in pulse-echo mode and were individually characterised. Ultrasonic frequency sweep measurements were made using 10-cycle tone burst excitation signals with a centre frequency in the $20 - 120kHz$ frequency range in increments of $5kHz$. Each ultrasonic measurement was normalised to the first pulse echo reflection from the end of the bar arriving at $1ms$. The frequency response of the Teletest transducer and the optimised transducer is shown as a time-frequency response in Figure 5.18. Multiple torsional reflections can be seen at roughly $1ms$ intervals with a travel distance of $3m$. The response of the Teletest transducer shows a degradation in performance at frequencies higher than $70kHz$ probably due to resonances within the backing that caused ringing in the transducer. In contrast, the frequency response of the optimised transducer with a smaller backing shows consistent performance at frequencies up to $120kHz$. With an operating frequency in the range of $40kHz$ a significant drop in amplitude was observed.
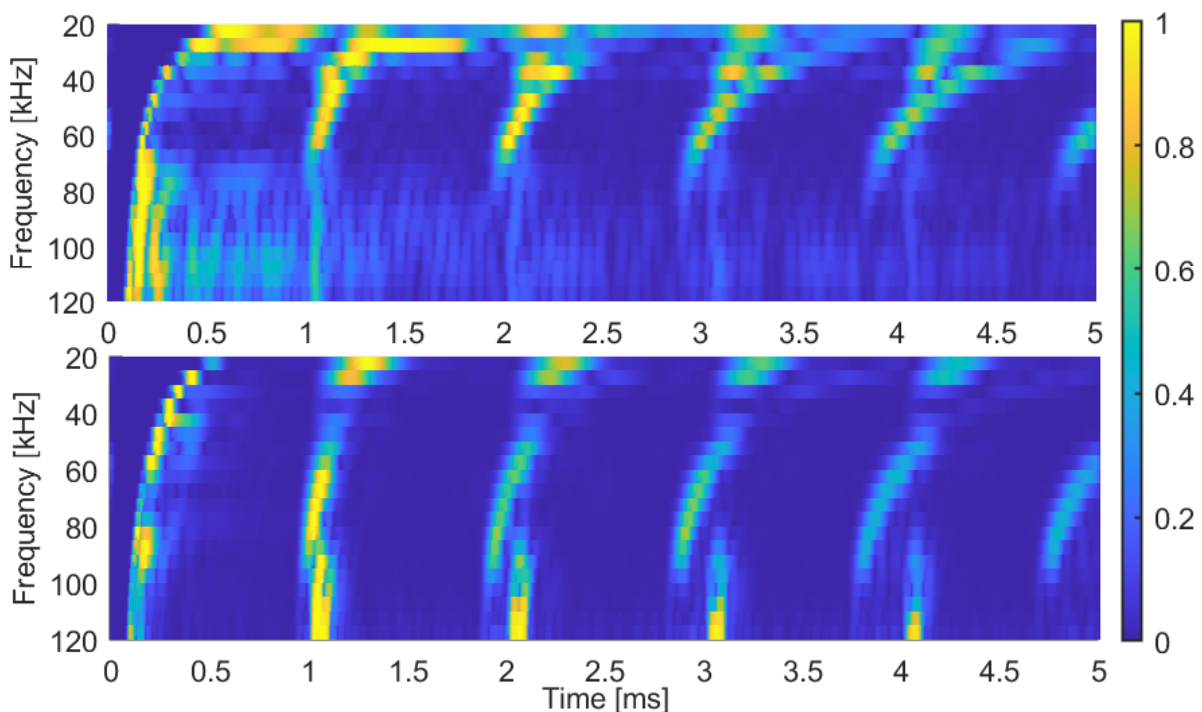
FIGURE 5.18: Comparison of the time-frequency response of the (top) Teletest transducer with the (bottom) optimised transducer.

This ultrasonic response is likely due to the coupling of the eigenfrequency of the width-polarised plate with a significant out-of-plane displacement reported earlier. Torsional reflection was coupled with a slightly slower flexural mode that has a similar velocity at higher frequencies. However, the flexural mode can be prevented by excitation using multiple transducers.

The optimised transducer was used in an array design using a flexible connector and a custom assembly procedure. The optimised transducer design achieved the design constraints due to the rest of the system. The design of the array using sandwiched PZT-5A PWAS, optimised backing layer and face plate is shown in Figure 5.19. An array of optimised transducers is shown as installed on a 6-inch NPS Schedule 40 pipe. The transducer array was part of a SHM system and its ultrasonic performance was demonstrated through SHM trials at a refinery [45].

FIGURE 5.19: Design and application of optimised transducer in an array for SHM application in a refinery.

5.5   Summary

The numerical methodology established in Chapter 4 is used to characterise the current Teletest transducer. Several FEA studies are carried out to analyse the design parameters of the piezoelectric PWAS and the backing layer by evaluating the influence of the design characteristics on the electromechanical and vibrational frequency response of the transducer. The design parameters investigated for PWAS included dimensions, polarisation direction, and electrode configuration. The results suggested improvement in TS-mode operation with width-polarised PWAS and further improvement with parallel electrode configuration by reducing unwanted out-of-plane vibration caused by wraparound electrodes. The physical dimensions of the backing layer and their influence on the electromechanical response of the transducer were also investigated. The FEA studies guided the development of an optimised transducer that achieved $10dB$ improvement in SNR and TS-mode purity for torsional operation and non-resonant behaviour in a wider $20 - 120kHz$ frequency range for SHM application using UGW.

Chapter 6

GWT System Characterisation for HT-SHM Application

6.1 Introduction

This study carried out an experimental characterisation of a transducer array for the application of SHM to HTPs. The transduction system consisted of an array of Teletest transducers characterised in Chapter 5 for the excitation and sensing of the $T(0,1)$ UGW mode in pipes. Characterisation of the transducer array is carried out through long-term UGW monitoring experiments on a full-scale pipe over a range of representative EOCs and a temperature of up to 150°C. The characterisation focused on the signal amplitude, purity of the $T(0,1)$ wave mode, thermal stability, and defect sensitivity.

The experimental investigation was first carried out in a laboratory setting where the Teletest transducer array was exposed to more than 1000 thermal cycles at temperatures of up to 150°C over a period of six months. The sensitivity of the system is evaluated using an artificially introduced defect of gradually increasing severity from 1% to 4% loss of cross-sectional area during the monitoring period. The baseline signal subtraction and temperature compensation methods introduced in Chapter 2 are applied to increase the defect sensitivity.

Another monitoring experiment was conducted on a HTP in an operational power plant. The transducer array experienced a daily thermal cycle of temperatures up to 180°C for more than a year. The ultrasonic measurements are analysed to evaluate the thermal stability, and the transducer behaviour over the monitoring is discussed.

6.1.1 Motivation

For the application of SHM to HTPs, it is desirable for the UGW system to operate reliably in the range of EOCs without any degradation in ultrasonic performance over time. For the SHM application, ultrasonic measurements of the transducer array are compared to a known baseline to identify and characterise any developing structural changes. Therefore, to produce reliable information, the SHM system must be able to differentiate changes due to damage from those caused by EOCs.

For an UGW transducer array, the inspection range and defect sensitivity are related to the amplitude and SNR of the ultrasonic signal. To achieve the highest level of purity for the generated axisymmetric $T(0,1)$ mode, it is essential that all transducers in the array have the same signal amplitude and phase. This is difficult to achieve due to the variability in the transducer output caused by manufacturing variation and its response to EOCs.

When transducers are exposed to significant temperature variations, their ultrasonic response is altered, leading to changes in their signal amplitude and phase. When the phase or amplitude of all transducers changes uniformly, compensation can be performed if a reference wave packet is present in the signal. However, temperature can result in uneven amplitude and phase changes among transducers in an array. When the excitation signal changes differently, it can lead to unwanted modes, such as flexural modes. These non-axisymmetric wave modes are usually dispersive and can significantly increase the coherent noise of the signal. This can significantly increase the variation from baseline, mask the information about the defect, and limit the damage sensitivity.

Repeated exposure to temperature changes can also degrade ultrasonic performance over time. Therefore, it is crucial to characterise the ultrasonic performance of the transducer array in EOCs and investigate its variation or degradation in performance at high temperatures and thermal stability over time for SHM application.

6.1.2 Aim and Objectives

This chapter aims to establish an experimental methodology to investigate the performance of a UGW system for the application of SHM on high temperature pipelines. The performance of the UGW system is characterised as a function of temperature, and its reliability is evaluated in the simulated and actual EOCs. The defect detection and sizing capabilities of the system are also evaluated by artificially introduced defects. The key objectives of this study were to:

(1) Establish an experimental setup to characterise an UGW system for HT-SHM application

(2) Assess the ultrasonic response of the transducer array in a range of operating temperatures and analyse the effect of temperature on velocity, amplitude, energy, phase, and SNR of the $T(0,1)$ wave mode.

(3) Assess the stability of the transducer array at high temperatures over time by evaluating $T(0,1)$ wave mode FOMs mentioned in (2), but at high temperatures over time.

(4) Evaluate the damage sensitivity of the high temperature UGW system as a temperature function and assess whether it is maintained under varying temperature conditions over time.

6.2 Ultrasonic Guided Wave Transducer Array

The HT transducer collar system was developed as part of the UltraSteamLine project [250] funded by Innovate UK. The transducer collar was designed for application on a 4-inch NPS pipe and was made of a two-part stainless steel frame that held transducer holder modules around the circumference of the pipe. The collar consisted of 16 modules, with two HT-UGW Teletest transducers housed in each of the modules to form the two-ring array, as shown in Figure 6.1. The 16 transducers in each ring were evenly distributed around the circumference.

The Teletest transducers operating in TS-mode provided a tangential force on the pipe surface for the excitation of the T(0,1) wave mode when provided with the same electrical input. The two rings were axially separated by 30 mm, and this separation was used to control the directionality of UGW. When released, the transducer holder module had springs calibrated to apply an axial force of 200 N on each transducer. This spring loading mechanism allowed the transducers to be dry coupled to the pipe.
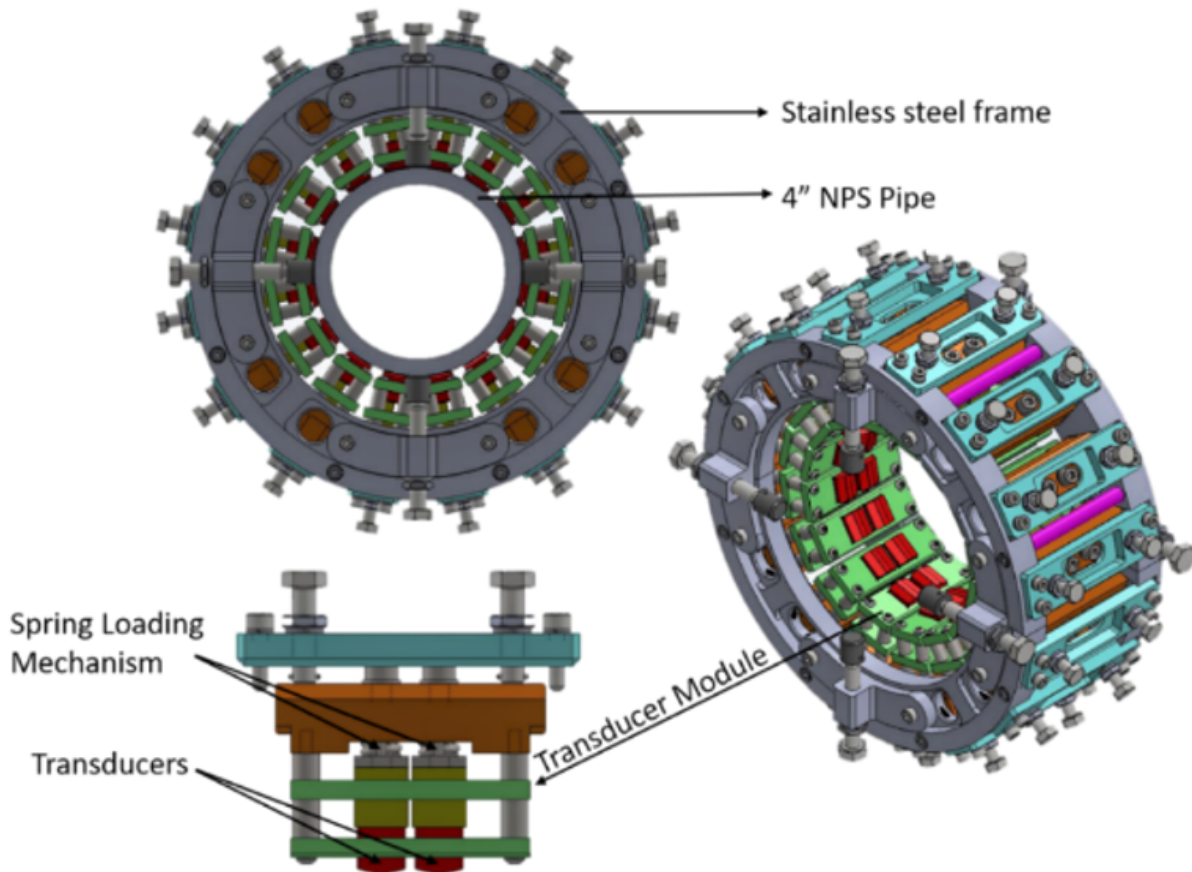
FIGURE 6.1: CAD drawing of the transducer collar array prototype designed for HT operation. It shows the key components, including the collar frame, transducer housing modules with spring loading mechanism and the piezoelectric ultrasonic transducers.

This investigation was carried out before developing HT-UGW transducers for 350°C and 600°C as described in Chapter 8. Therefore, the transducer array used in this study consisted of the existing HT variant of the Teletest transducers. The previous study that developed these transducers has reported stable transducer performance for 35 days at 250°C [174]. The transducer array was characterised at high temperatures of up to 250°C; however, no long-term monitoring experiments were performed. A field trial was attempted, but because operational temperatures reached 350°C, only measurements at ambient temperature were recorded before the transducers depolarised within the first 14 days.

6.3   System Characterisation in Simulated EOCs

6.3.1   Experimental Setup

The described transducer array was installed on a $6m$ long $4 - inch$ NPS schedule 40 pipe specimen near one end of the pipe. The transducer collar was connected to the Teletest Pulser-Receiver unit for ultrasonic transduction. Each ring was divided into eight segments of two transducers, each octant connected to a single channel in the pulser-receiver unit using high-temperature wires. HT operating conditions were simulated using flexible ceramic pad heaters that were wrapped around either side of the collar array. The experimental setup is shown in Figure 6.2.
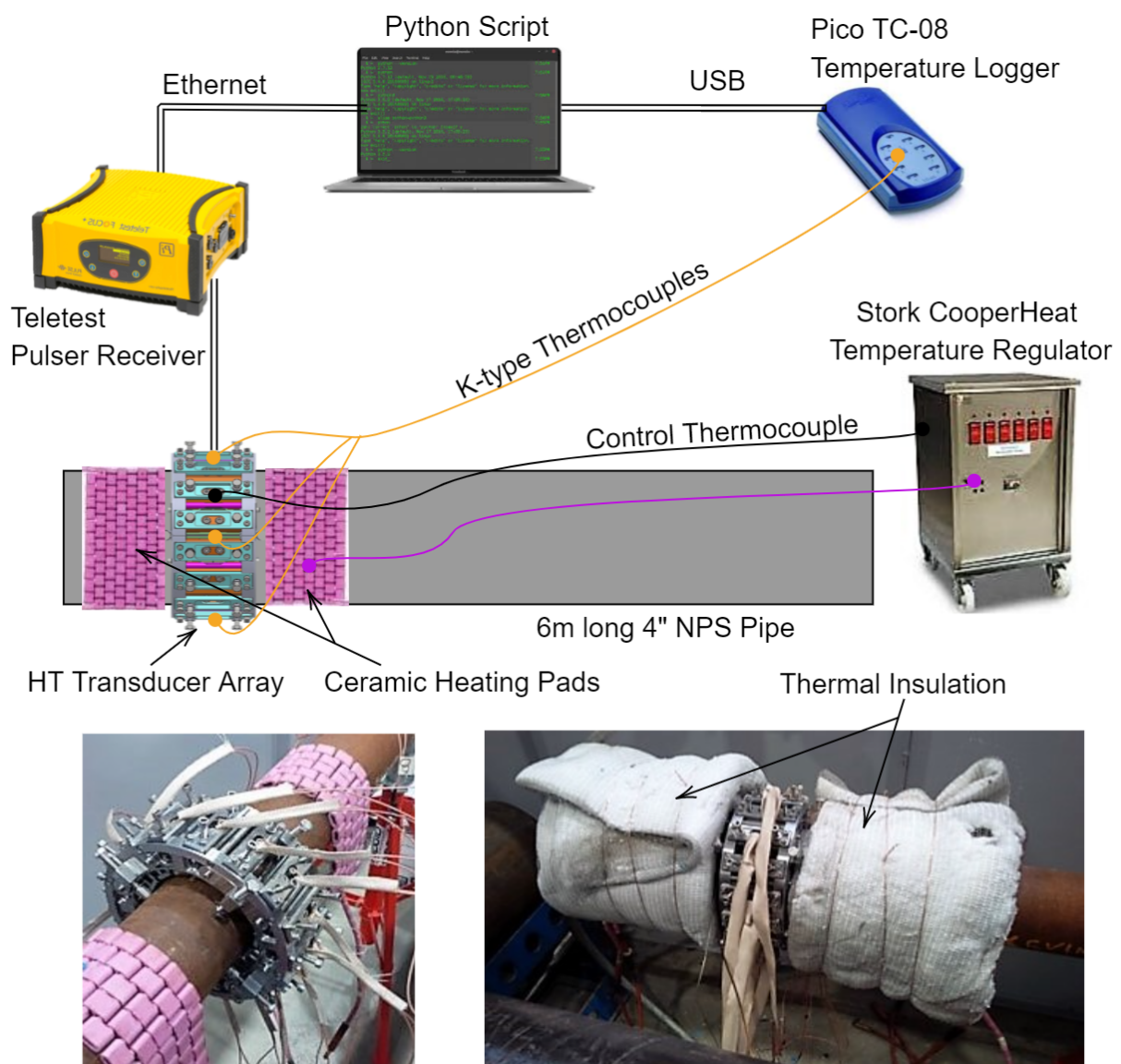
FIGURE 6.2: Experimental setup for high temperature guided wave monitoring showing the installation of transducer array, thermocouples, temperature regulator and their connection with the measurement equipment.

The heating mats were powered by a Stork Cooper Heat temperature regulator unit [251]. A temperature control thermocouple was welded to the centre of the transducer array to ensure uniform heat exposure to all transducers. The temperature reading of this thermocouple was used to control the relays to turn on the high-power input connected to the heating mats. The heating mats were covered with high temperature fibreglass insulation to minimise heat loss. Four K-type thermocouples were installed in each quarter of the collar array and connected to a Pico TC-08 logger to measure the temperature distribution around the circumference of the transducer array during the experiments.

The temperature regulator heated the mats until the temperature reading from the control thermocouple had reached the target temperature. The controller then turned on and off repeatedly to keep the temperature steady. After the temperature stabilised, the high temperature ultrasonic measurements were acquired. Measurements with 128 averages took less than 30 seconds, so the temperature did not change significantly during signal acquisitions.

6.3.2 HT-UGW Monitoring Data Collection

A data acquisition script was used to establish an automated test routine for data collection during the monitoring experiment. Ultrasonic measurements from the Teletest system and the corresponding temperature profile from the Pico data logger were recorded before and after each ultrasonic measurement. Ultrasonic measurements were acquired in pulse-echo mode and the transducers were excited with a ten-cycle Hanning modulated toneburst signals of centre frequencies of 40 kHz, 50 kHz, and 60 kHz.

The HT-UGW measurements were taken at increasing temperatures in steps of 25°C to 150°C and at 150°C over time. To investigate the sensitivity of the UGW system at high temperatures, a defect (as illustrated in Figure 6.3) was added and gradually increased during the monitoring experiment. This was done to determine the minimum level of damage that can be detected in representative EOC. An artificial crack-type saw-cut defect was introduced at $1m$ from the end of the pipe on the opposite side where the collar was installed. The length and depth of the sawn-cut defect were calculated using Equations (6.1) and (6.2), respectively.

$$y = 2R_0 \sin\left(\frac{\theta}{2}\right) \tag{6.1}$$

$$d = R_0 \left(1 - \cos\frac{\theta}{2}\right) \tag{6.2}$$
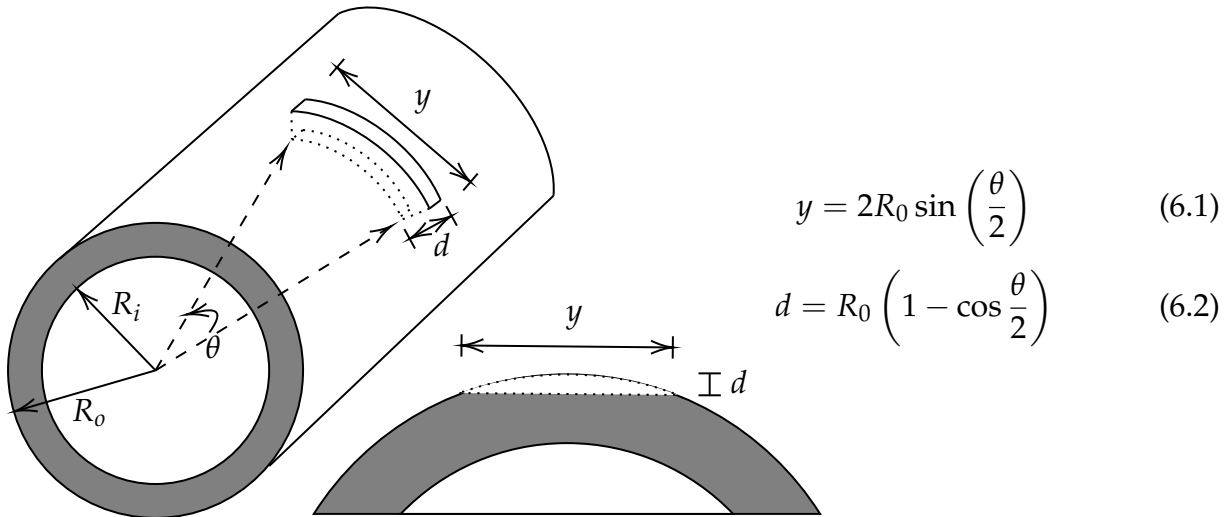
FIGURE 6.3: Schematic of the pipe cross-section showing the artificially introduced defect and its length (y) and depth (d) in the lateral and axial direction.

The size of the defect was gradually increased in 4 steps of loss of 1% CSA from 1% to 4% CSA to simulate the growth of the defect. The introduced saw cut defects of increasing size are shown in Figure 6.4.
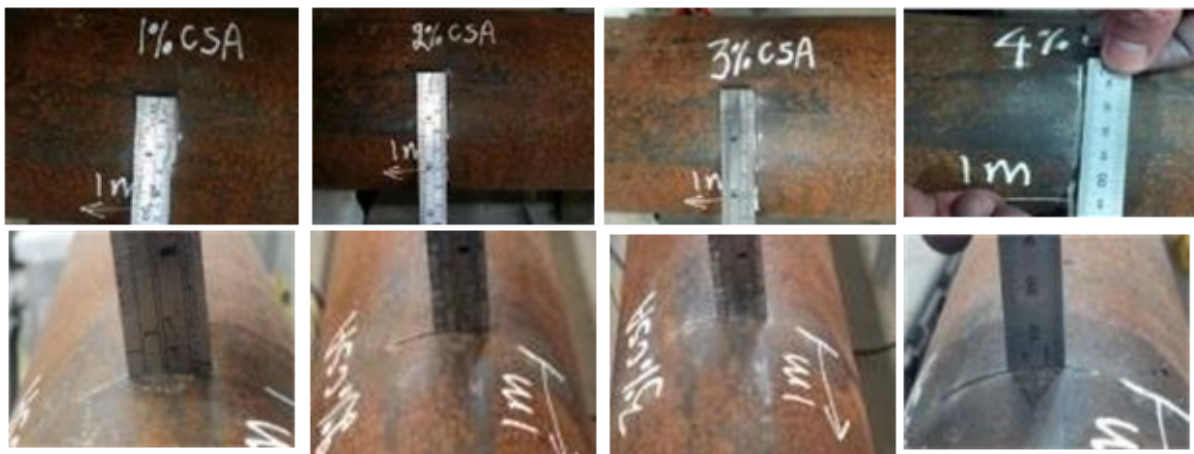
FIGURE 6.4: Artificial saw-cut defects of increasing size from 1% to 4% pipe CSA introduced 1 m away from the far pipe end during the monitoring experiment.

The monitoring experiment lasted more than 200 days, during which 12,000 ultrasonic data sets were collected. The temperature of the pipe during the experiment is shown in Figure 6.5. First, baseline ultrasonic measurements were taken from pristine pipe samples for 75 days. The baseline data set covered ambient and HT ultrasonic measurements covering a temperature range from 20°C to 150°C. The transducer array was exposed to three thermal cycles from ambient temperature to 150°C and 8,000 thermal cycles from 130°C to 150°C. The latter was due to the

on-off control of the temperature regulator. In summary, a total of 7000 baseline ultrasonic measurements were recorded. This dataset was used to analyse the influence of increasing temperature and thermal cycles on the ultrasonic performance of the transducer array. After baseline measurements, a saw cut defect of 1% CSA was introduced. This defect was gradually increased over 30 days in increments of 1% CSA at 1-week intervals up to 4% CSA, while ultrasonic measurements were continuously recorded.
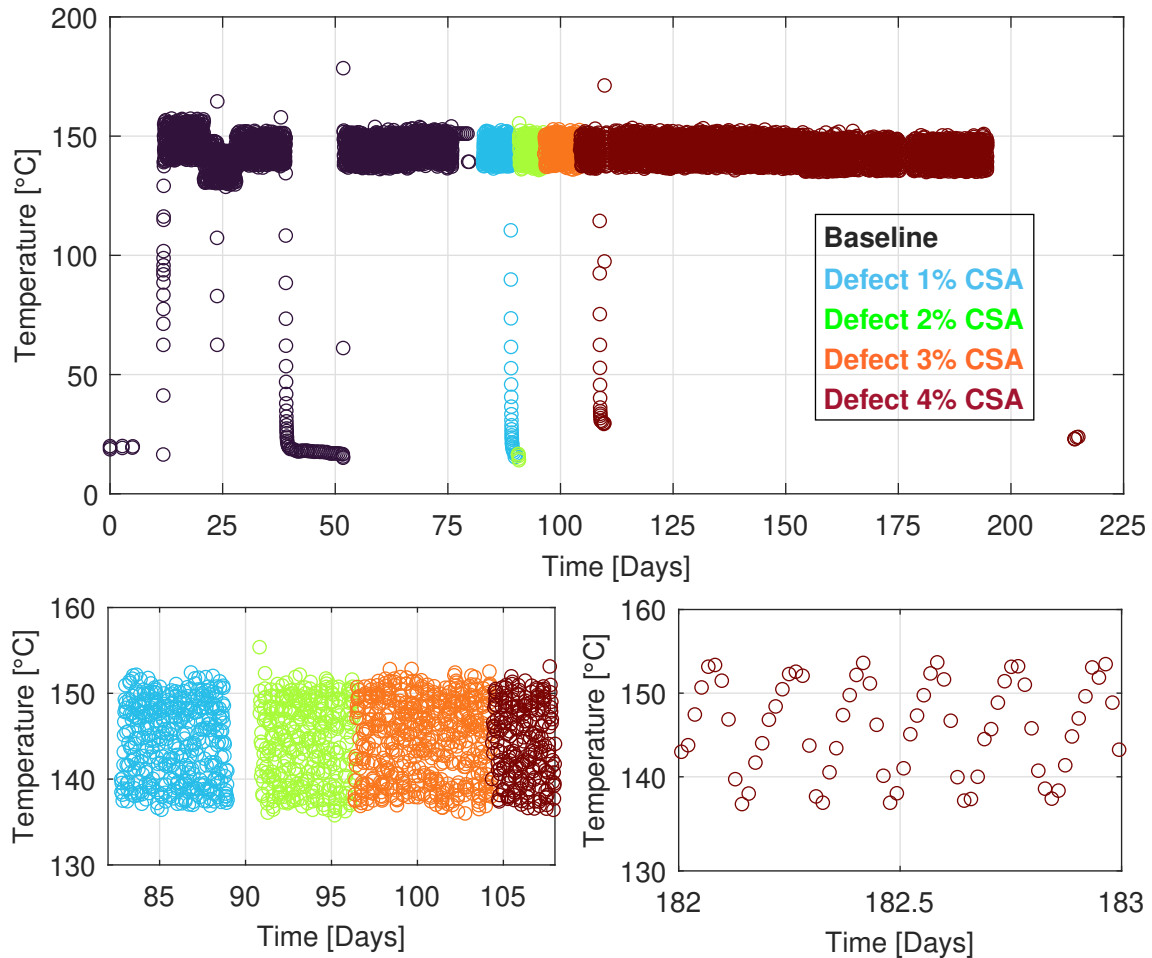
FIGURE 6.5: Average pipe temperature recorded with each of the 12000 ultrasonic measurements during the monitoring experiment. Measurements are colour-coded to indicate the damage category.

Before each increment in defects, the pipe temperature was returned to ambient temperature to collect ultrasonic measurements for the entire temperature range. After adding the final defect of 4% CSA, the ultrasonic measurements were taken for an additional 90 days while the transducer array temperature was maintained at 150°C. This data set served as a basis to evaluate the stability of the transducer array with long-term exposures to high temperatures and to assess the sensitivity to damage detection over time for the SHM application. A summary of the monitoring

data, including the number of ultrasonic signals collected for each increment in the defect, its temperature range, and the dimensions of the saw-cut defects, are given in Table 6.1.

TABLE 6.1: Summary of ultrasonic measurements collected during the guided wave monitoring experiments.

Signal Description	Time (Days)	No. of Meas.	CSA (%)	Defect Size y (mm)	d (mm)
Baseline	1-71	7000	0	0	0
Damage 1	71-79	530	1	24.2	1.3
Damage 2	79-85	380	2	30	2
Damage 3	85-93	530	3	34.5	2.6
Damage 4	93-203	5230	4	37.6	3.2

The pulse-echo waveform in the forward direction was obtained by combining the ultrasonic measurements from the transducer rings. An example of the pulse-echo measurement from the transducer array and the TOA analysis of the experimental setup is shown in Figure 6.6. Two examples of ultrasonic measurements are shown from the baseline and Damage 4 datasets acquired using the centre frequency 60 kHz at a temperature of around 150°C. These are presented as a time series of filtered responses normalised to the first Forward Pipe-end reflection ($FP1$) that can be seen at 3.5ms (5.7m). This is followed by a reflection at 3.8ms (6.2m) comprising the overlapping echoes of the second Backward Pipe-end reflection ($BP2$) due to imperfect backward cancellation and the second Forward Pipe-end reflection ($FP2$). A zoomed-in view in the time series shows the reflection from the Defect ($FD1$) around 2.9ms (4.7m) however, the change is relatively small and can be masked by the noise.

These signals are also translated into an A scan[1] using the envelope derived from the Hilbert transform so the noise floor can be visualised in dB scale relative to the $FP1$ reflection. From the A-scan, the coherent noise floor is seen around $-30dB$ relative to the $FP1$ reflection. For the detection of defects using a single measurement, a threshold of $6dB$ is generally required, which in this case was $-24dB$. Although the $FD1$ signal in this example measurement was above the noise floor with $-27.4dB$ but below the threshold, highlighting the need for advanced signal processing techniques.

---

[1]Distance on the x-axis converted using the group velocity of the $T(0, 1)$ wave mode.
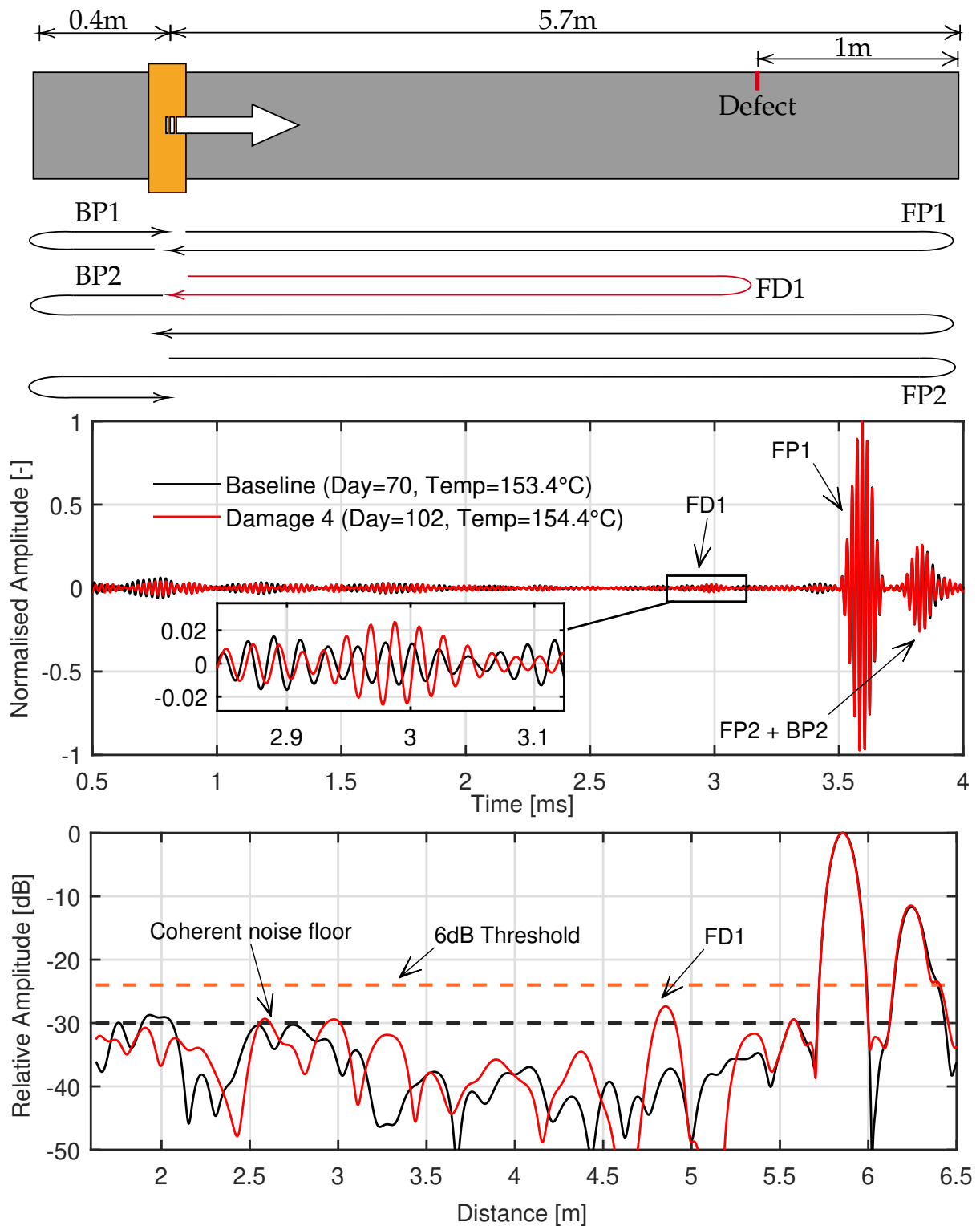
FIGURE 6.6: Schematic of the measurement setup used for acquiring high-temperature ultrasonic signals and time of flight analysis on an example ultrasonic signal to show the expected ultrasonic guided wave response - Forward and Backward Pipe-end echoes (FP1 and BP1) and their second reflections (FP2 and BP2) and the echo from the Defect (FD1).

6.3.3 Effect of Temperature on UGW Measurements

Pulse-echo measurements from the transducer array were analysed at increasing temperatures from ambient to 150°C. Selected high temperature measurements between 25°C and 150°C acquired with excitation frequencies of $40kHz$, $50kHz$ and $60kHz$ are shown in Figure 6.7.
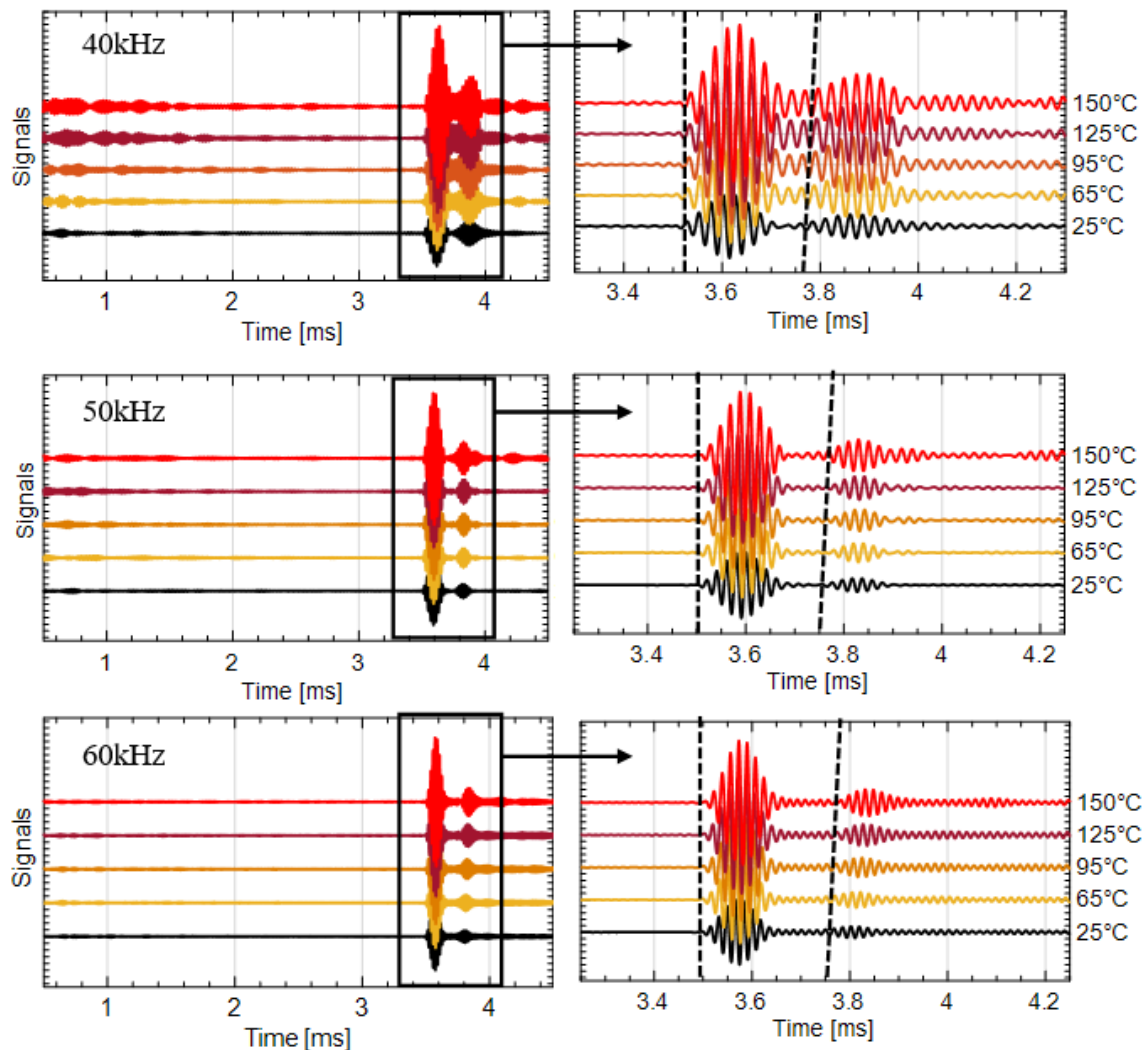
FIGURE 6.7: Pulse-echo UGW measurements at increasing temperatures of up to 150°C for excitation frequencies of 40, 50 and 60 kHz.

In the waterfall plots for each frequency dataset, the signal amplitude of the HT measurements is normalised to the $FP1$ reflection of their respective signal at 25°C to highlight the signal variations with increasing temperatures. The time of arrival of $FP1$ and $FP2$ is marked by dashed lines, and it can be seen that the wave propagates at a slightly reduced velocity as observed with the later arrival of the second wave packet. Since no reflections were expected before $3ms$, the time window between $0.5ms$ and $3ms$ is considered coherent noise. It can be seen that the coherent noise

increased with increasing temperatures and was more prominent with excitation frequencies of $40kHz$ and $50kHz$. This coherent noise may have resulted from the mode conversion due to $BP1$ reflection or flexural modes being excited by the transducer array due to the uneven influence of temperature on the transducers.

The performance of the transducer array is characterised by analysing the change in signal amplitude, phase, SCNR and time of arrival of the $FP1$ reflection from the HT measurements. The effect of increasing temperatures on FOMs is shown in Figure 6.8.
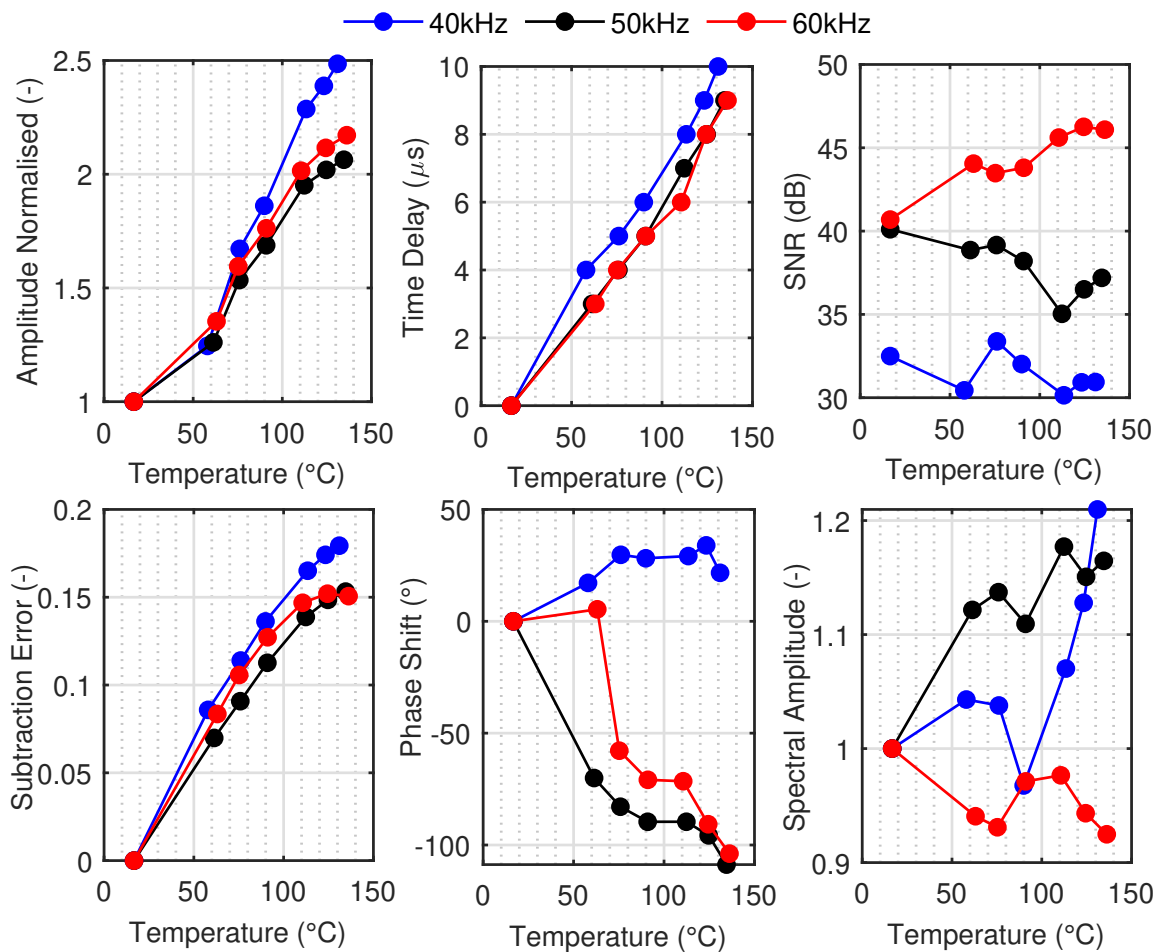
FIGURE 6.8: Pipe-end signal amplitude, phase, SNR, and arrival time as a function of temperature with excitation frequency of 40, 50 and 60 kHz.

The peak-to-peak signal amplitude displayed a linear increase with temperature for all three excitation frequencies. The amplitude of the signal at ambient temperature was $125mV (40kHz)$, $130mV (50kHz)$ and $100mV (60kHz)$, which at 150°C increased by a factor of 2-2.5. This increase in amplitude is potentially a combined effect of the change in material properties of the transducer components, their thermal expansion, and (or) expansion of the transducer array frame or springs, which may have led to an increase in coupling force to the transducers.

The phase delay and arrival time also showed a linear trend with temperature for all three excitation frequencies. This change is due to the combined effect of temperature on the transducer array and the waveguide. However, because the waveguide length did not have a uniform temperature distribution, it is difficult to analyse the contribution of the waveguide alone. However, the delay in arrival time at 150°C relative to ambient temperature was around 10μs for all three excitation frequencies. The phase delay at 150°C relative to the ambient temperature for $40kHz$, $50kHz$, and $60kHz$ was -150°, -160°and -200°, respectively.

The SNR of the transducer array at ambient temperature was in the range of 34 to 40 dB. The SNR response to increasing temperature was nearly linear, except for slight deviations observed at 75°C and 100°C. This is probably due to the interference of phase-shifted excitation signals from different transducers. The SNR for the excitation of $40kHz$ and $50kHz$ at 150°C decreased by $\approx 6dB$, while it increased by a similar level for $60kHz$. This response resulted from the higher coherent noise observed with $40kHz$ and $50kHz$ which can also be seen with an increase in the variation in spectral amplitude of more than 15% in comparison of <8% for $60kHz$. Nevertheless, the SNR at 150°C for the three frequencies was higher than $30dB$ and highest for $60kHz$ at $43dB$. Thus, the following defects sensitivity studies only considered measurements with $60kHz$ excitation frequency.

6.3.4 Defect Sensitivity at High Temperatures

A subset of the monitoring database was created using only high-temperature measurements to analyse the defect detection sensitivity of the transducer array at high temperatures. This subset included 3260 measurements with increasing defect size, collected over a 90-day period from Day 30 to Day 120. The temperature for these measurements ranged between 138-154°C. To characterise defect sensitivity, a single baseline measurement with 60kHz excitation frequency is compared with four measurements corresponding to each defect size acquired at a similar temperature ($\Delta T < 0.5C$) as the baseline considered to reduce any temperature influences. The measurements are shown in Figure 6.9 and an increasing amplitude of the $FD1$ defect reflection is highlighted. The amplitude of the defect reflection is above the noise floor only for the sizes of the defects of 3% and 4% CSA. For the 4% CSA defect size, the defect reflection is $6dB$ above the noise floor of $-35dB$, suggesting that it can be detected with a single baseline measurement collected at the same temperature. The defect reflections from 1% and 2% were masked by coherent noise. However, this may be improved by more sophisticated defect detection and temperature compensation methodologies.
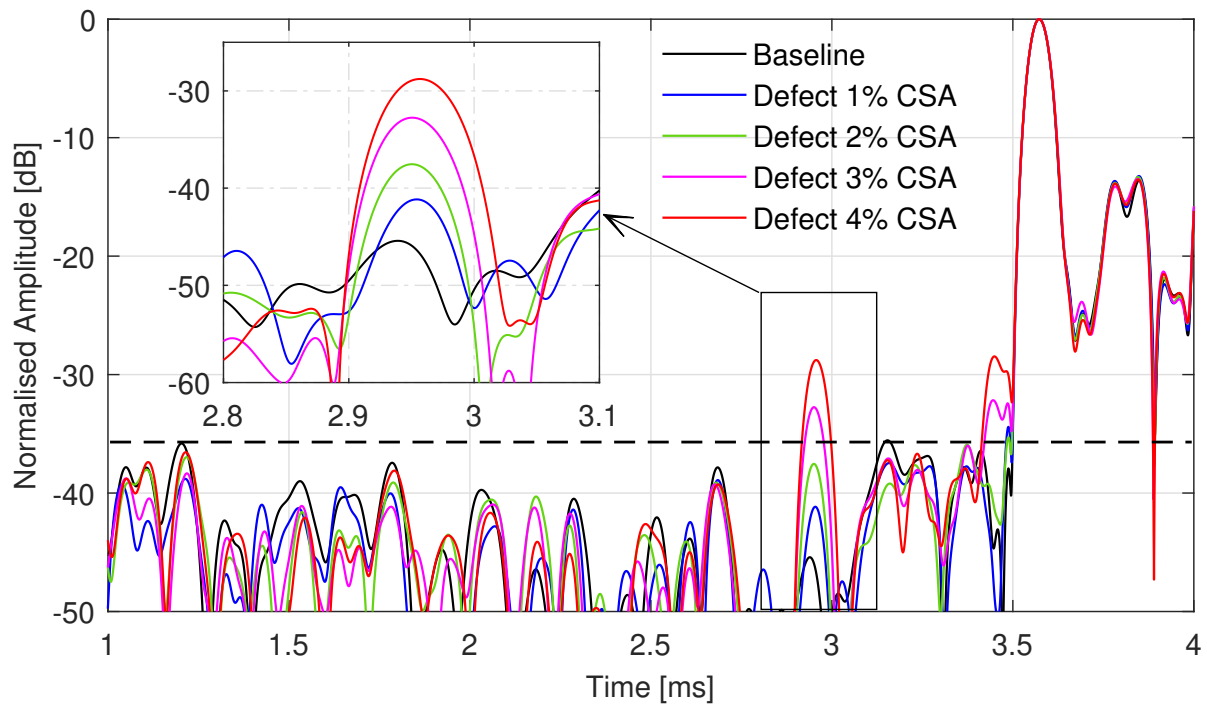
FIGURE 6.9: Ultrasonic measurements at 150°C with increasing defect size. Measurements are normalised to pipe-end reflection at 3.6 ms and the increasing reflections from the introduced defect at 2.9 ms.

The OBS and BSS methodologies described in Chapter 2 are applied to this monitoring data set. For each of the 1000 measurements, an optimum baseline measurement was selected that minimised RMS of the residual signal after subtraction. An example of the residual signal from OBS and BSS for each defect category is given in Figure 6.10. The residual signals are plotted as relative amplitudes to the $FP1$ reflection. The residual signal was in the -45 to -50dB range. An increase in the signal residual from the $FD1$ defect reflection at $2.9ms$. The residual signal amplitude for the 1% CSA defect was still within the residual noise. The 2% CSA defect signal had a residual of $3dB$ above the noise floor.
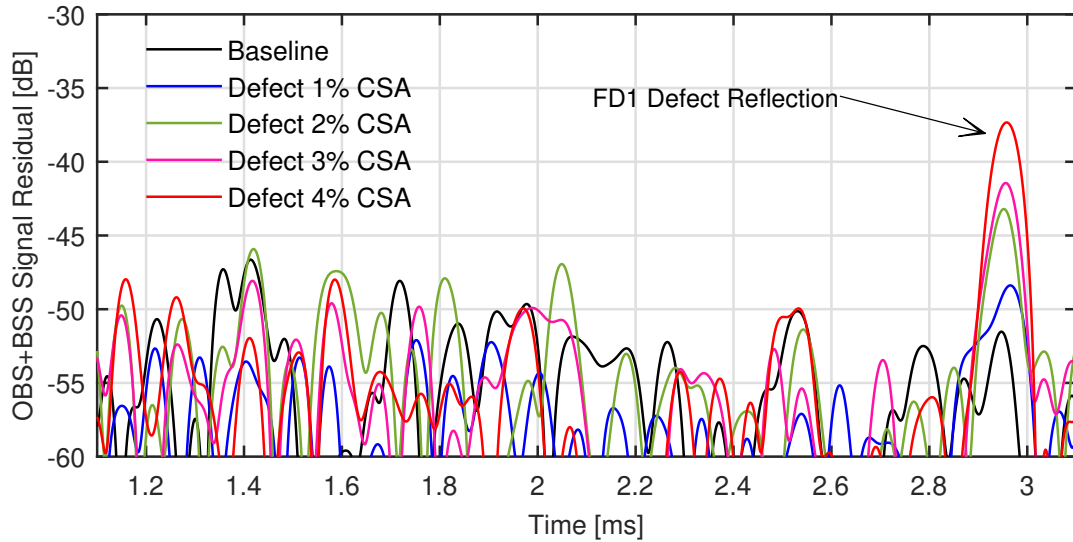
FIGURE 6.10: Residual signals after optimum baseline selection and baseline subtraction; applied to measurements from increasing defect size in the temperature range of 140-150°C.

Two hundred measurements from each defect category were selected for analysis of the defect monitoring capability of the transducer array. This monitoring data set consisted of measurements recorded in the 120-150°C temperature range. The SNR of the time window where the defect signal was expected is shown in Figure 6.11. The SNR within the baseline ranges within the $\pm 5dB$ range, and this defines the coherent noise floor. The measurements corresponding to the 1% CSA defect were within the noise floor. The 2% CSA defect signal crossed the threshold, but only for temperatures below 135°C. The measurements corresponding to the 3% and 4% defects were clearly distinguishable.
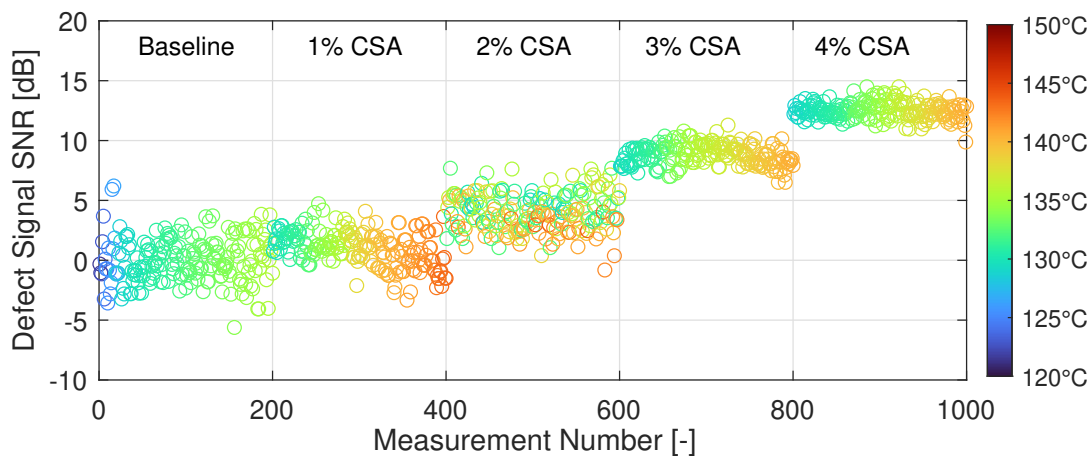
FIGURE 6.11: SNR of the defect reflection over the 120 day monitoring period at temperatures ranging from 120-150°C calculated from 200 measurements of each defect category.

DTW algorithm from Matlab [252] was used to apply signal stretching to improve the temperature compensation algorithm. The residual signals after applying DTW are shown in Figure 6.12. The residual signal level was in the range of -55 to -50dB, which was an improvement of $\approx 5dB$ compared to just OBS alone. However, the residual signal from the defect was also reduced by around $2dB$. This reduction in residual level is caused by
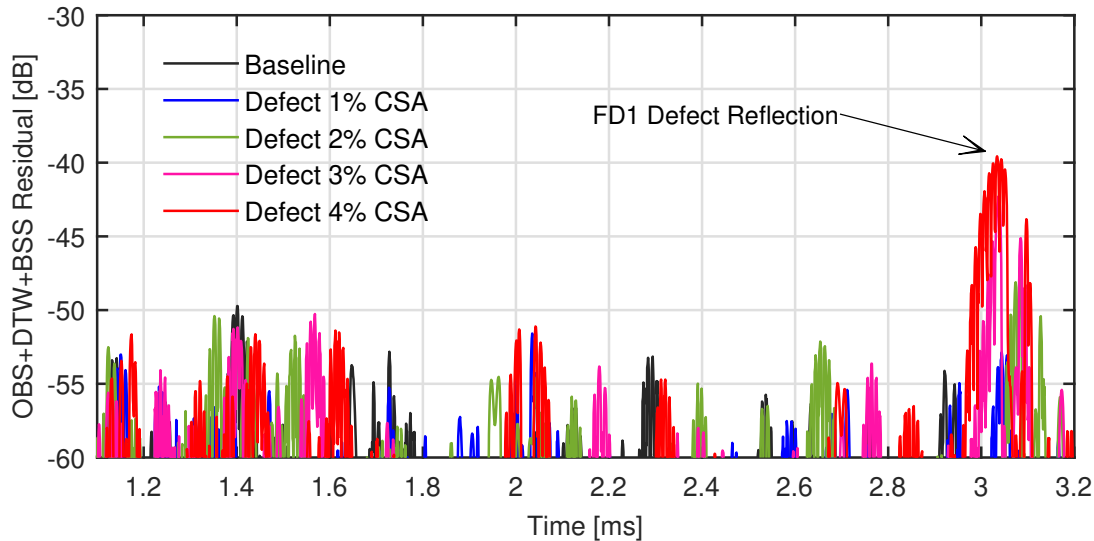
FIGURE 6.12: Residual signals after optimum baseline selection and baseline subtraction with dynamic time warping; applied to measurements from increasing defect size in the temperature range of 140-150°C.

The maximum residual signal levels from the subtraction of the baseline signal using OBS are compared with that of OBS with DWT for all defect categories in Figure 6.13. A reduction of $\approx 2.5dB$ was achieved in residual signal levels within the baseline data set, which is associated with coherent noise. Although the variance in the baseline residual signal of $\pm 5dB$ was similar with both approaches, the number of outliers possibly caused by phase differences was significantly reduced. The residual signal level in the case of OBS increased with increasing defect size, but only the 4% CSA defect was outside the variance within the baseline. However, with DTW, there was a significant step change in the residual level with DTW even for the smallest 1% CSA defect. The variance within each category was more pronounced with DWT, possibly due to a generally reduced residual signal level, as explained earlier. Both approaches showed a similar residual level for 2-4% CSA with DWT significantly outperforming for the smallest defect, provided that baseline outliers are ignored.
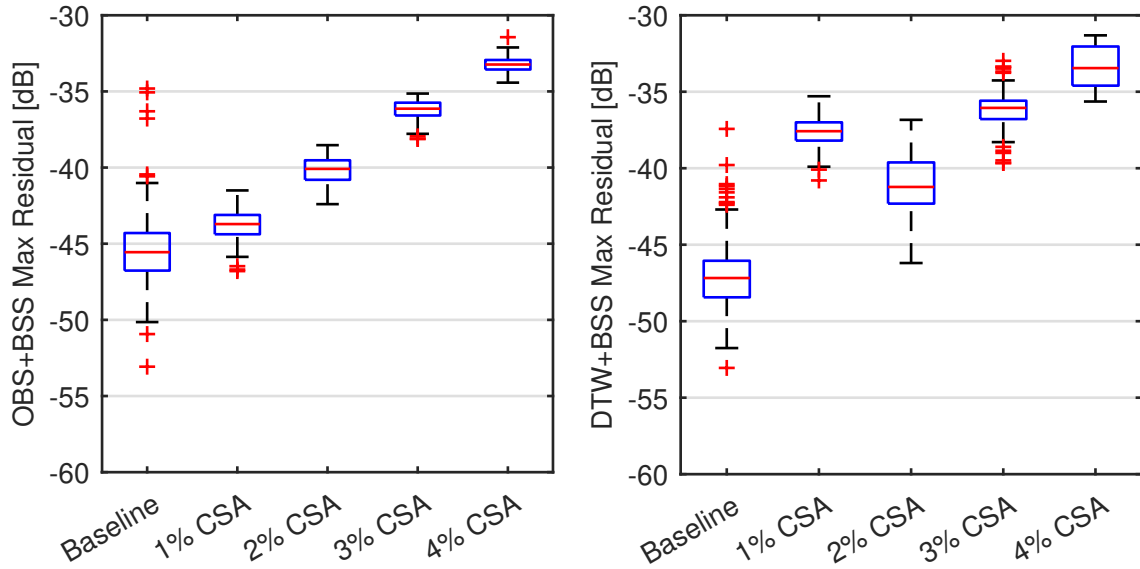
FIGURE 6.13:   Comparison of residual signal level from baseline signal subtraction using (left) OBS and (right) OBS with DWT.

The analysis was extended to all the monitoring data, including the measurements recorded at a finer resolution. A combination of OBS, DTW and BSS was used to derive the residual signal. The SNR of the $FD1$ reflection time window was computed against the RMS of the residual signal. Two hundred measurements and the corresponding SNR for each defect category are presented in Figure 6.14. The baseline spread was still around $5dB$, however, the smallest defect in 1% CSA had a step change of $4dB$. This suggests that if ultrasonic measurements are available at finer temperature increments of around 0.25°C, the sensitivity to defects can be greatly improved.
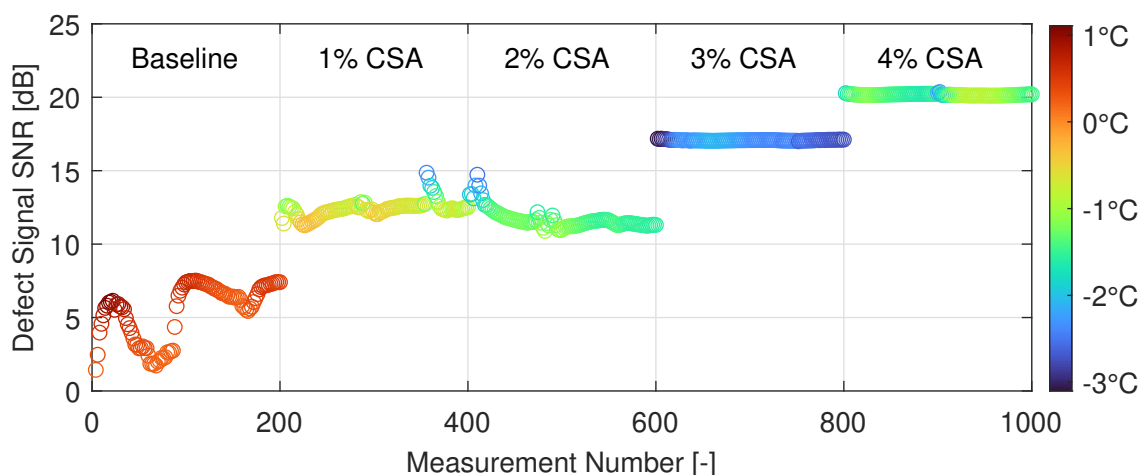
FIGURE 6.14: Maximum SNR of the defect reflection calculated using the entire 210 day monitoring dataset in temperatures ranging from 120-150°C. The color coding shows different in temperature with the selected baseline.

6.3.5 System Thermal Stability

Ultrasonic stability was evaluated by analysing the monitoring data set from Day 110 to Day 200. This data set was associated with a 4% CSA defect and included 8000 ultrasonic measurements taken in the temperature range of 130°C to 155°C. As described earlier, due to on-off control of the temperature regulator, the transducer array experienced six thermal cycles of ±6°C each day.

The signal amplitude and SNR of the $FP1$ reflection were analysed from these HT ultrasonic measurements. These FOM are analysed to assess the stability of the performance of the transducer array and are plotted as a time function in Figure 6.15. The signal amplitude is normalised to the value (245 mV) at the beginning of the monitoring period. No signal amplitude degradation was observed, demonstrating the thermal stability of the transducer array. The SNR varied by less than $3dB$. The nearly linear relationship between the signal response (both amplitude and SNR) with increasing temperatures is evident in the precise colour segmentation in both plots.
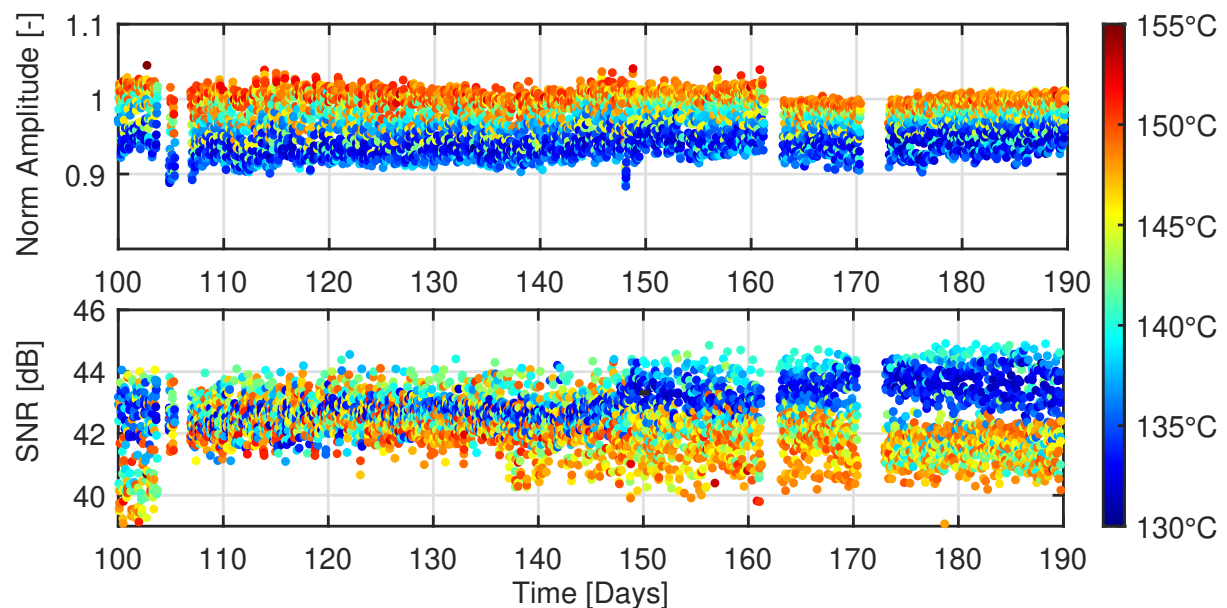
FIGURE 6.15: Signal amplitude and SNR of pipe end reflection in the temperature range of 130-155°C over the final 90 days of the monitoring period.

These results demonstrate the stability of the transducer array for SHM application to HTPs operating at temperatures up to 155°C. Ultrasonic measurements corresponding to each excitation frequency at the start and end of the 210-day thermal soak test were compared as shown in Figure 6.16. A stable response can be seen for all frequencies. However, the 4% CSA defect was masked within the much higher coherent noise with $40kHz$ excitation.
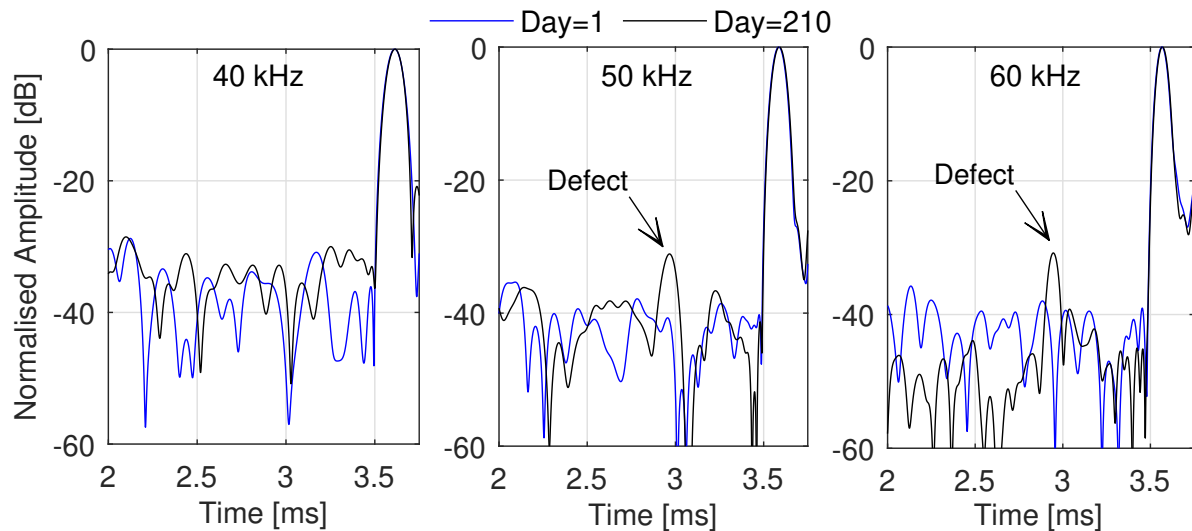
FIGURE 6.16: Ultrasonic measurements at the start and end of the monitoring experiment showing signal stability and defect reflection.

6.4 Performance characterisation in a Power Plant

6.4.1 System Installation

The UGW system was installed in a functioning gas-fuelled power station operated by SSE in Medway, Rochester, UK; to assess the performance in real operation conditions. The installation process and the monitoring data collection were carried out according to the business operations of the plant. The transducer array was mounted on a 4-inch Schedule 40 pipe in the IP Economiser to IP Steam Drum Line. This pipeline was chosen because of its temperature rating of 160°C suitable for the HT transducer array; however, it had a complex set of features. The pipe was 2.9 m long with two 90°1.5D bends on either side, as shown in Figure 6.17.

The welds between the straight and curved sections are labelled $BW1$ and $BW2$. The transducer array was installed 0.5m in front of $BW1$ and had $BW2$ 1.7m away in the forward direction. Within the straight section of the pipe, a T-piece was present at 1m and is referred to as TP. There were circumferential girth welds on either side of the TP feature, labelled $W1$ and $W2$, 0.8m, and 1.1m from the transducer array, respectively.

FIGURE 6.17: Installation of the transducer array in an operational power plant showing the installed location and key pipe features.

The transducer array was installed during a routine outage when the pipeline was at ambient temperatures. The insulation of the pipe was removed to gain access to the pipe surface and the surface scale was removed with a wire brush to achieve better transducer coupling; however, the surface was not even. Four thermocouples were installed at the four quadrants of the transducer array. The pipe insulation was restored to either end of the transducer array and an insulation sheet covered the top to avoid direct water ingress in rainy conditions as this was located on the roof in the open air. The thermocouple and high-temperature cables from the transducer array were fed along a support beam to the platform level above. They were connected to a custom-built data logger placed away from HT, which consisted of a mini-computer, a Teletest Pulser-Receiver unit, a Pico TC-08 temperature logger, and data storage drives. The same Python data acquisition scripts developed for laboratory experiments were used. The data logger was powered by a 110V power supply that was available on-site.

6.4.2 Monitoring Data Collection

The monitoring trial was carried out over a period of 425 days. The data logger was programmed to collect UGW measurements and the corresponding pipe temperature at intervals of 30 minutes, resulting in approximately 50 measurements each day. Due to the lack of network connectivity on site, the data logger measurements were not remotely accessible. Data was recovered from the logger by visiting the installation site on Day 55, Day 230, and Day 425. More than 11,000 ultrasonic measurements were collected during the 425-day monitoring period, while the transducer array was exposed to live operating conditions. The pipeline temperature corresponding to each of the ultrasonic measurements during the field monitoring trial is shown in Figure 6.18.
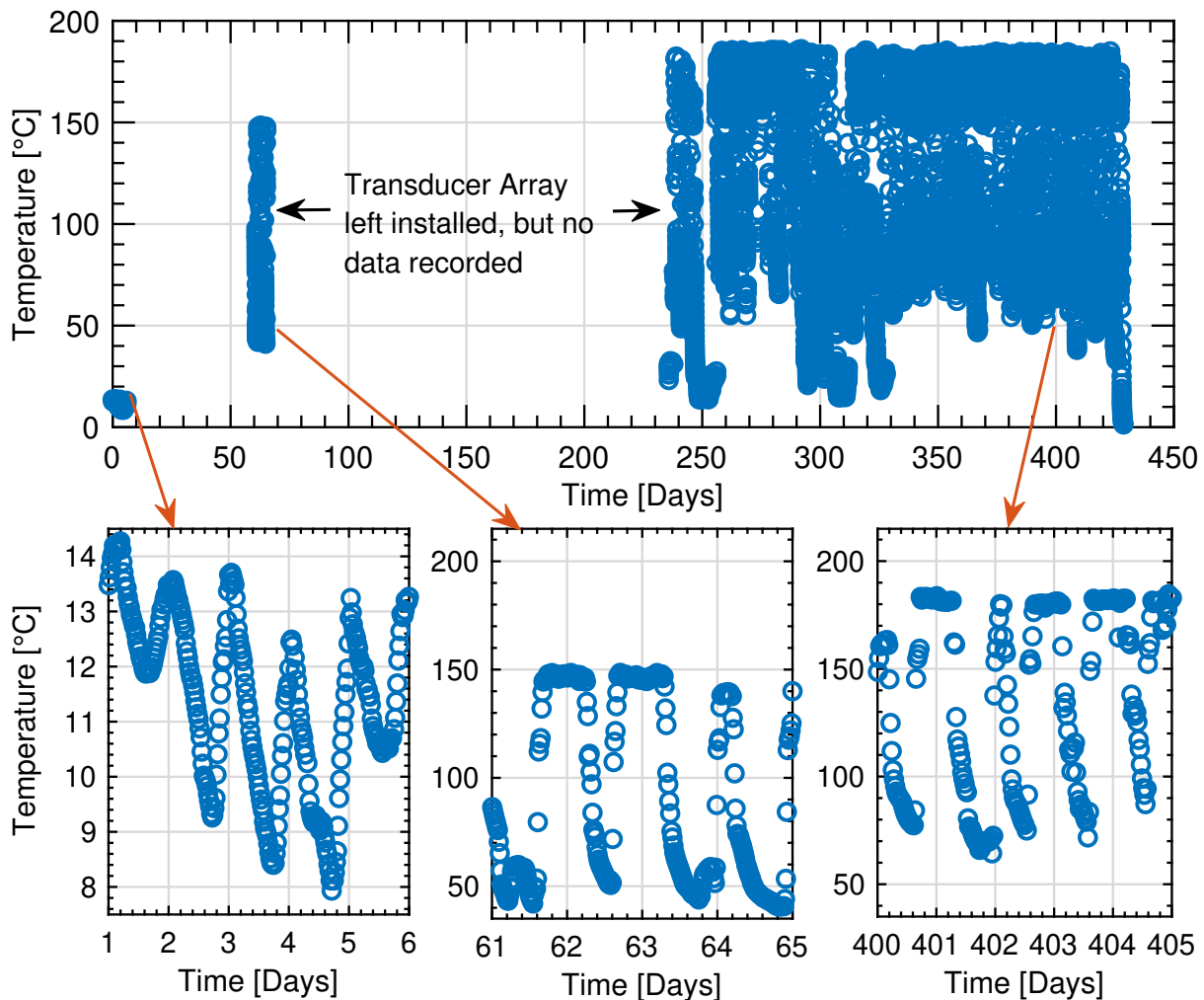
FIGURE 6.18: Pipe temperature measurements during the in-service monitoring trial. The zoomed views at the bottom show the daily temperature fluctuations experienced by the transducer array due to the plant operating schedule.

The gas-fired power plant operated reactively to meet grid generation demands, which resulted in regular temperature cycles during the monitoring period. From the temperature time-series data, it can be observed that the plant was operational for approximately six to eight hours each day. The transducer array therefore experienced a daily thermal cycle with temperature swings between 50°C and 150°C or 70°C and 180°C according to the operation parameters of the plant.

The first 400 measurements were recorded during the routine outage when the system was installed. These measurements were recorded at ambient pipe temperatures ranging from 8°C to 14°C. On the first data retrieval visit on Day 55, an issue with the data logger was observed. The problem was associated with a power outage on Day 10, just before the plant would go operational, as informed by the plant operator. The power outage interrupted the data logger and did not restart, resulting in no measurements being collected between Day 10 and Day 55. The data logger was restarted on Day 55 and measurements were taken at temperatures ranging from 50°C to 150°C. There was no reported outage between Day 10 and Day 55 so it is assumed that the transducer array experienced daily thermal cycles of similar temperature range.

After 500 measurements on Day 70, a similar data logger error had occurred. However, this was not identified until Day 230, when the second data retrieval visit was made. This issue led to another measurement gap, although the transducer array was left installed and exposed to operating temperature conditions. To avoid this issue, the data logger was programmed to restart at the end of each day. When the data logger was restarted on Day 230, the operating temperatures of the pipe ranged from 70°C to 180°C. This change in operational temperature may have occurred anytime between Day 70 and Day 230, and no further data from the plant operators was available to confirm that. However, more than 10,000 measurements were collected from Day 230 to Day 425 in this temperature range. In summary, more than 11,000 measurements were recorded during the 425-day monitoring period, in which the transducer array was exposed to a daily thermal cycle with a temperature range between 8°C and 180°C.

6.4.3 Ultrasonic Measurement and Analysis

A schematic of the measurement setup and an example of the ultrasonic measurement are shown in Figure 6.19. The TOA analysis and the reflection from the known features are annotated in the example measurement. The reflections from the circumferential girth welds, $W1$ and $W2$, can be observed at 0.5ms and 0.7ms, respectively. The $BW1$ feature was in the backward direction, but its reflection can be seen at 0.3ms due to imperfect backward cancellation. The reflection of $BW2$ can be

seen at 1.5*ms*. The *BW*2 reflection is relatively low in amplitude and appears distorted due to the attenuation from the *TP* feature. In addition, the non-axisymmetric T-piece and pipe bend introduced mode conversion. Therefore, signals beyond the *W*2 feature are complicated with coherent flexural noise, which challenges their interpretation. Therefore, the analysis of the stability of the transducer array will only consider the W1 and W2 reflections.
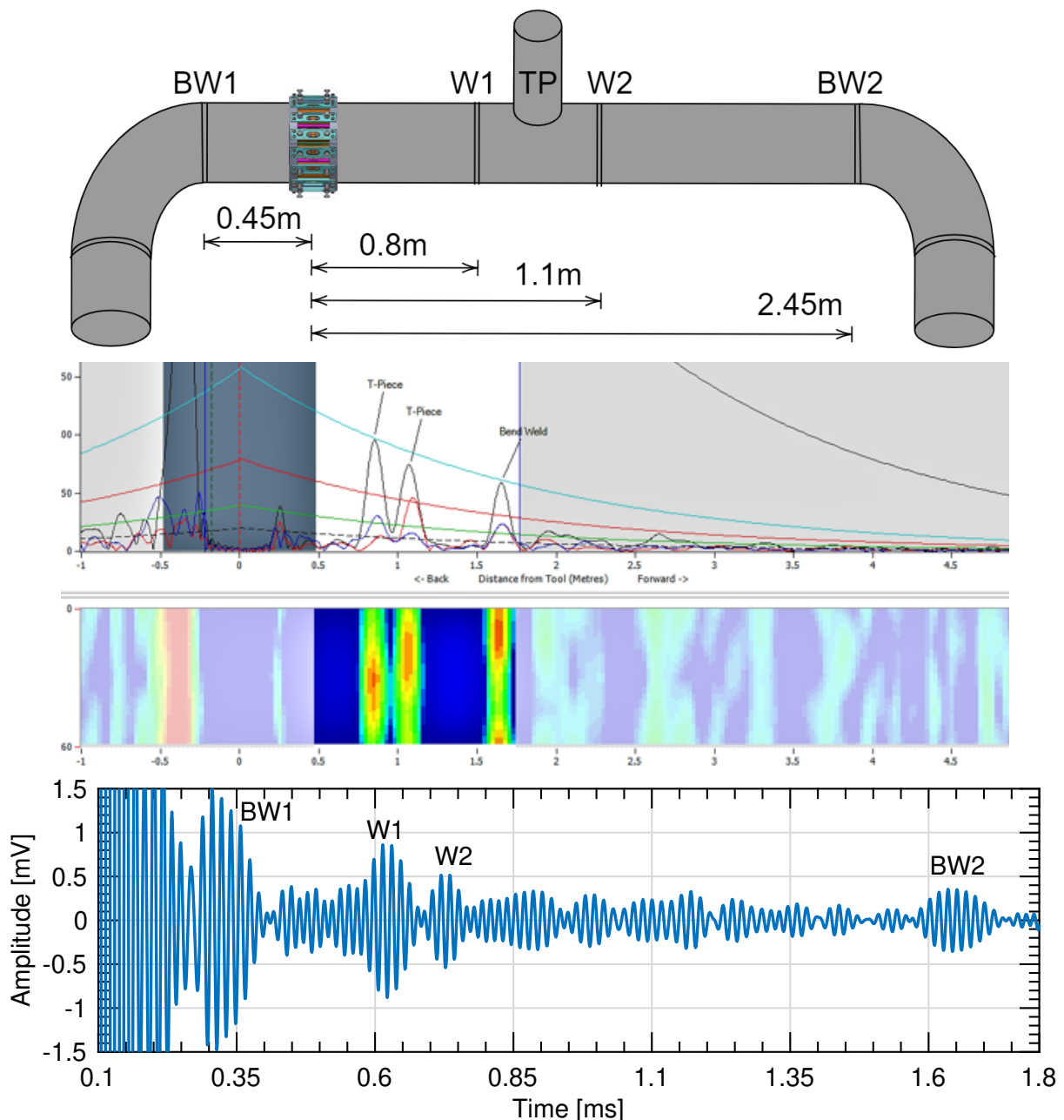
FIGURE 6.19: Illustration of the pipe in the power plant used to acquire high temperature guided wave measurements showing key pipe features with an example measurement presented as A-scan and C-scan.

6.4.4 Performance in Operational Conditions

The performance of the transducer array was evaluated by analysing the ultrasonic pulse-echo measurements over time. The transducer array was used to excite an axisymmetric $T(0,1)$ wave, and the analysis focused on the ultrasonic reflections from known pipe features, including $W1$, TP, $W2$, $BW1$, and $BW2$. These ultrasonic measurements were normalised to the $W1$ reflection to compensate for amplitude changes and visualise the stability of the ultrasonic response over time. As a result, a consistent ultrasonic response over time can be seen through the distinct $W1$ and $W2$ reflections of the TP pipe feature at $0.8m$ and $1.1m$, respectively. The amplitude and SNR of the reflection of the $W1$ feature were analysed over time. The normalised signal amplitude and SNR of $W1$ reflection as a function of temperature over 425 days are shown in Figure 6.20. A subset of randomly selected ultrasonic measurements from the period up to Day 70 is also shown.
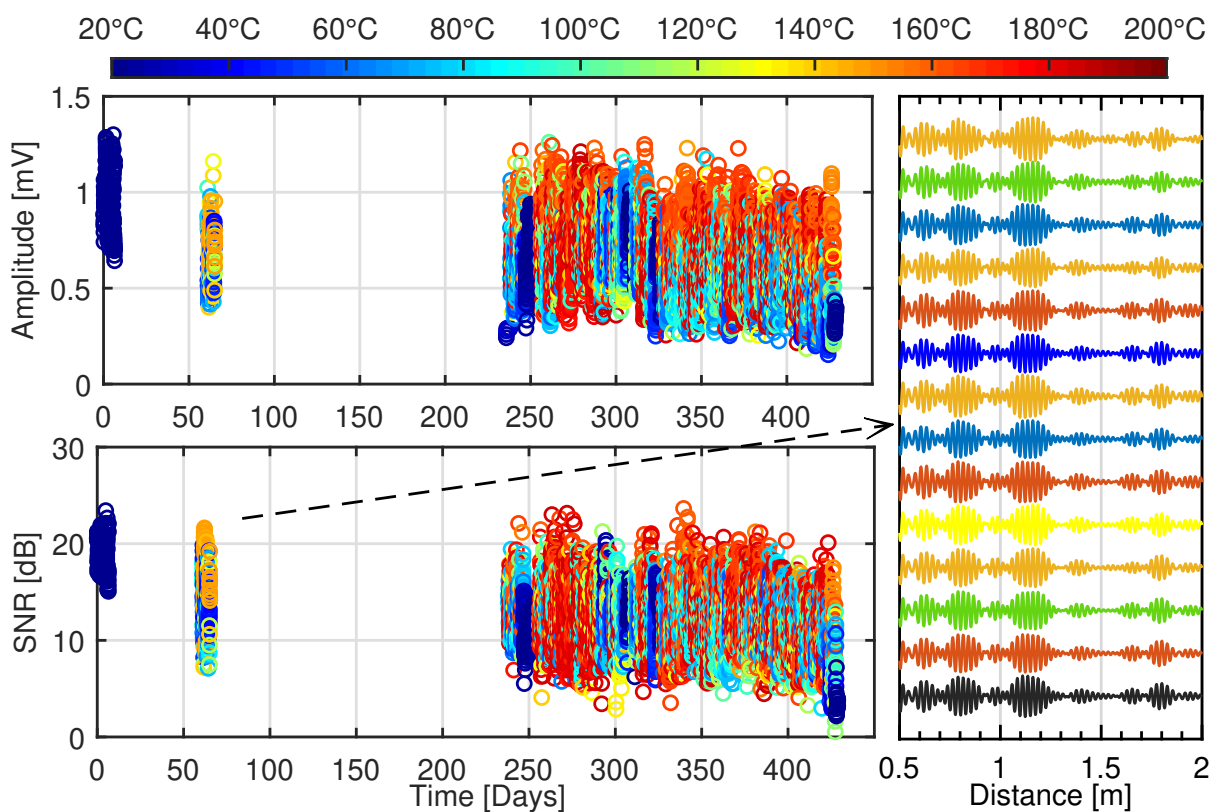
FIGURE 6.20: Signal amplitude and SNR of pipe weld reflection in the temperature range of 20-190°C over the 435 days monitoring trial and example high temperature measurements between Day 60-70.

From the start of the monitoring experiment to Day 10, the maximum amplitude of the $W1$ reflection was $1mV$ and varied by $\pm 0.25mV$ under ambient temperature conditions. The corresponding SNR was $20dB$ and varied by $\pm5dB$. On Day 55, when

data collection was resumed, an amplitude drop of around 20% and a reduction in SNR of *6dB* were observed under ambient temperature conditions. However, both SNR and amplitude increased with increasing temperatures, and at 150°C, their values were relative to those under ambient temperature conditions on Day 1. From Day 230 to Day 425, a gradual decrease in amplitude and SNR can be observed, which is more significant after Day 300. As the transducer array displayed a stable response with long-term exposure at 150°C, it is believed that continuous thermal cycling from ambient temperatures up to 180°C during plant operation accelerated the thermal ageing which degraded the transducer performance. At the end of the monitoring experiment, the amplitude and SNR were reduced by 50% and 15*dB*, respectively.

6.4.5 System Stability Analysis

To assess the system stability, ultrasonic measurements from the monitoring dataset with minimal signal residual were selected for ambient and high temperature range. The measurements are shown in Figure 6.21. The signal amplitude is normalised against the $W1$ reflection from the measurements from the start of the monitoring period. of respective.
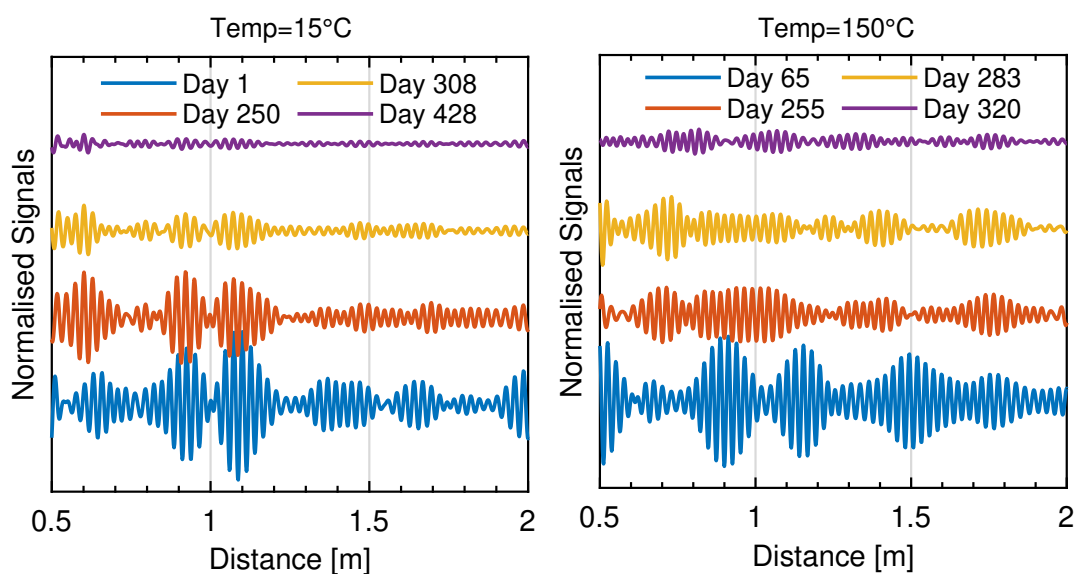
FIGURE 6.21: Selected ultrasonic measurements at ambient and high temperature during the monitoring trial. The signal amplitude is normalised against the pipe weld reflection at the beginning of the monitoring period.

The ambient temperature measurements at $\approx$ 15°C show consistent $W1$ and $W2$ reflections up to Day 250. A significant drop in amplitude can be seen in the measurement on Day 308, whereas, on Day 428, no reflections were observed. From the measurements at 150°C, the $W1$ and $W2$ reflections can be seen up to Day 65.

However, in measurements from Day 255 onwards, a decrease in amplitude together with increased coherent noise masked the reflections. This is possibly associated with non-uniform degradation or failure of some transducers in the array due to accelerated ageing that would led to generation of non-axisymmetric wave modes.

The degradation in ultrasonic performance was further investigated by analysing the ultrasonic measurements from each of the sixteen channels, which accounted for three transducers. The signal amplitude of the $W1$ reflection normalised with the respective value at Day 1 as measured by individual channels is shown in Figure 6.22. All channels were operational from the response on Day 55, with their amplitudes increasing with temperature, as expected. However, on Day 255 the analysis indicated that channels CH2, CH5, CH7, CH9, CH11, CH12 and CH15 had declined. Their reduction in signal amplitude was around 30% or 60%, suggesting a failure of one or two of the three transducers connected to each channel.
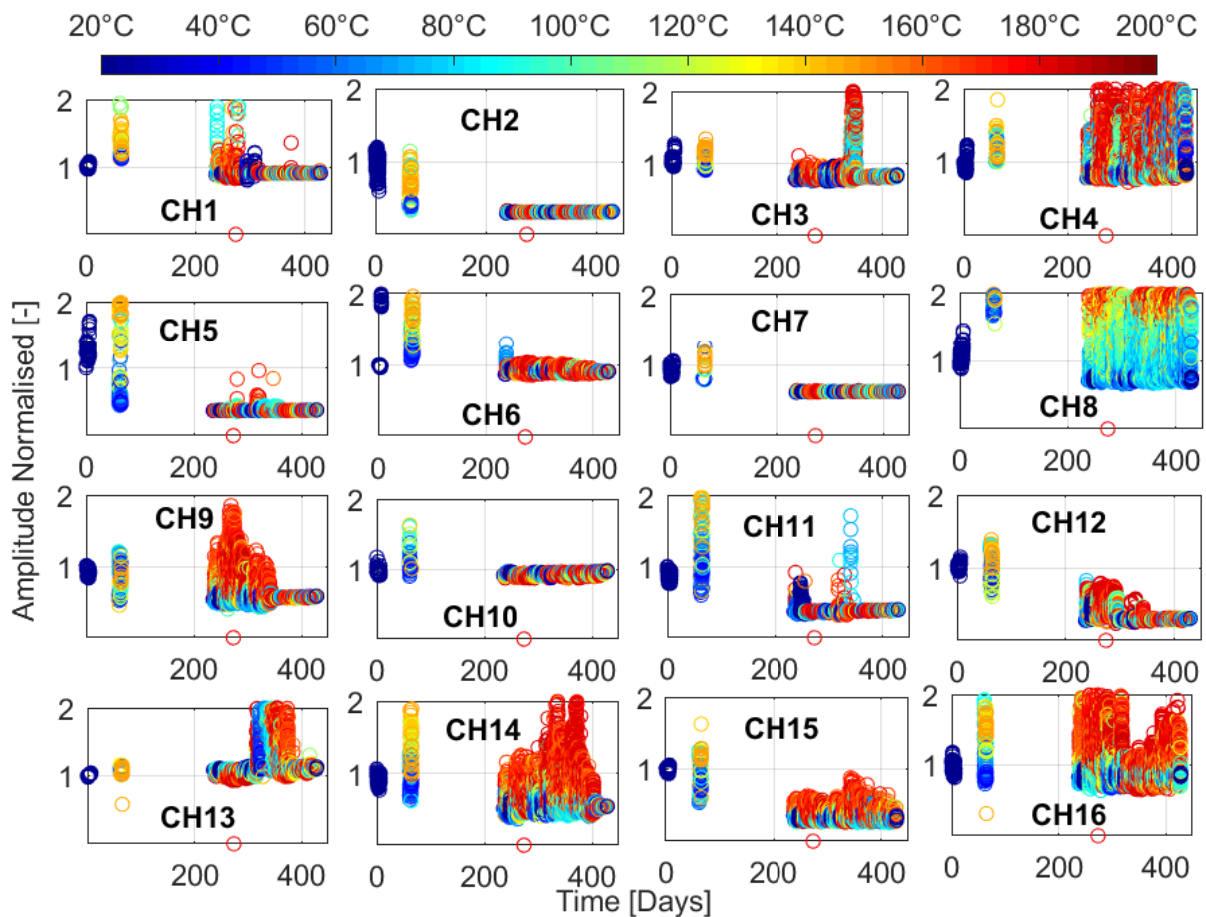
FIGURE 6.22: Normalised signal amplitude measured from transducers in each of the sixteen channels over the 425 day monitoring period.

The remaining nine channels showed consistent signal amplitude and slight degradation of up to 10% throughout the monitoring period. It is important to note

that for two stable channels, including CH3, CH6, CH10, and CH13, the response of the signal amplitude to increasing temperatures was not linear as expected. On the contrary, the channels CH4, CH8, CH14 and CH16 showed a very stable response during the 425-day monitoring period. These channels were in symmetric positions in each quadrant, suggesting that there may have been buckling of the transducer array fixture that resulted in uneven or reduced dry-coupling force to the transducers. This may also have been aggravated by any nonuniformity in the pipe cross section resulting in a nonuniform force distribution around the array. The coupling force was not monitored, so the hypothesis could not be confirmed. This analysis confirmed that non-uniform degradation due to failure of some transducer and changes in dry coupling force led to reduction of ultrasonic output and increased generation of non-axisymmetric modes reduced the SCNR for $T(0,1)$ operation.

After the monitoring test, the transducer array was retrieved and disassembled for inspection. The mechanical fixture and fastners of the transducer collar had become stuck and needed extensive force to be dismantled from the pipe. Some transducer wear plate had adhered to the surface of the pipe and cracked during dismantling. Closer inspection of other transducers revealed crack-type damage to the face plate of the transducer, as highlighted in Figure 6.23.
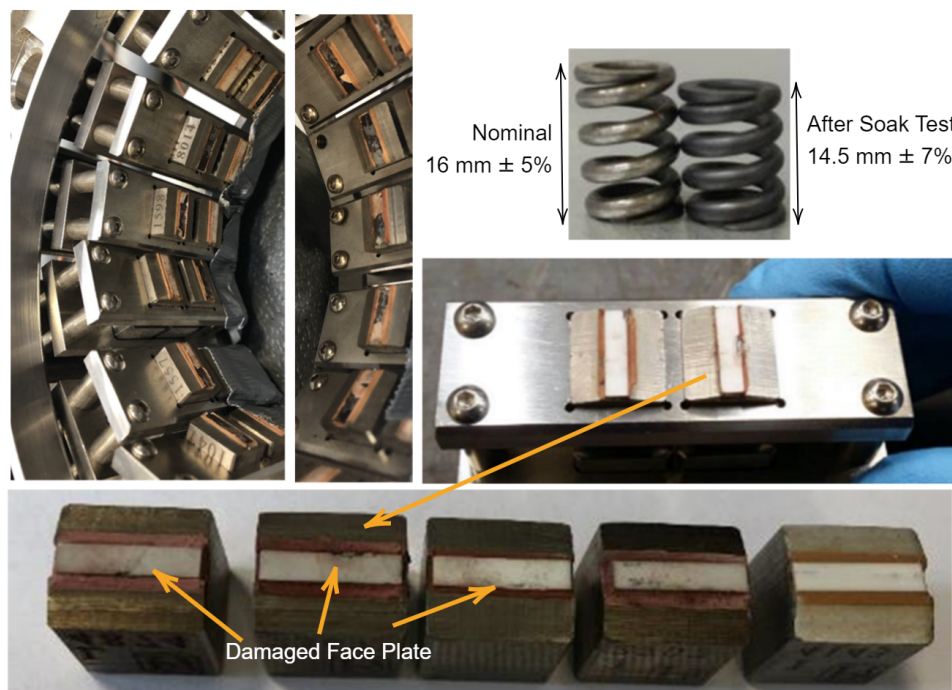
FIGURE 6.23: Transducer collar array after the monitoring trial showing damaged transducers with cracked face plate and transducer holder springs showing loss in compression force.

This failure could have resulted from excessive coupling forces on the transducer, continuous thermal cycles, expansion of adhesives, residual thermal stress, or a combination of these. Since most of the transducers had visual signs of damage, no ultrasonic experiments were performed with these. The springs used in the transducer collar were examined after the monitoring test and revealed a reduction in length 10%. This was equivalent to a loss of $\approx$ 100N (50%) in the dry coupling force to the transducer that will have impacted the ultrasonic output. Long-term exposure to high levels of stress and temperature may have resulted in thermally activated plastic creep in the springs. This problem was not evident in the initial laboratory experiment due to a more gradual heating rate and a much lower dwell temperature of 150°C.

6.5 Summary

This chapter investigated the ultrasonic performance of an GWT system with HT Teletest transducers for SHM application to HTP. Monitoring experiments were carried out under various extreme conditions, within the temperature limits of the system to prevent deterioration. A 200-day monitoring experiment was carried out with simulated EOCs such as high temperature and introduction of defects. Ultrasonic FOM including torsional $T(0,1)$ signal amplitude, signal-to-coherent noise and defect sensitivity as a function of temperature. The signal amplitude and SNR were highly stable during the monitoring period, with a variation of less than 5% and $1dB$, respectively. The defect sensitivity was also demonstrated to be at 4% CSA. A combination of OBS, DTW, and BSS techniques was used to improve the sensitivity to defects and produced encouraging results even for the smallest 1% CSA defect introduced. This validated the performance of the transducer array for SHM application to HTPs, highlighting its thermal stability, consistent ultrasonic performance, and the application of temperature compensation techniques to enhance the sensitivity to defects in a range of EOC. Operational testing in a HTP in a power plant, which included a complex pipe configuration, revealed reduced signal amplitudes and SNR due to its complex geometry. During the 425-day monitoring period, the extreme EOCs had exceeded the rated temperature limits, leading to gradual deterioration of the transduction system and failure of some transducers. The analysis highlighted shortcomings in the transduction system for higher-temperature use, including the mechanical collar fixture for further improvements.

Chapter 7

HT-PUT Material Selection and Characterisation

7.1 Introduction

This chapter is dedicated to the selection and characterisation of HT-PWAS for the design of PUT intended to operate at temperatures of 350°C and 600°C. Two HT piezoelectric materials are selected for these target temperatures based on their TS-mode performance and commercial availability. Their design optimisation for TS-mode operation and HT performance characterisation is carried out using the experimental and numerical methodologies demonstrated on the PZT-5A material in Chapter 4. Their HT-FOMs, including elastic, dielectric, and piezoelectric properties, are characterised at respective target temperatures and also compared with the reference material PZT-5A. Their performance stability is analysed over a 1000-hour period to assess their suitability for HT-SHM application at the target operational temperatures.

7.1.1 Motivation

The piezoelectric material is the active and primary component of an HT-UGW transducer; therefore, the selection of a suitable material and its performance characterisation are critical to the PUT design. The properties of the piezoelectric material, including the elastic, dielectric, and electromechanical properties, are anisotropic and depend on the mode of operation, the direction of polarisation, and the cut of the crystal for single crystals. The temperature response of these anisotropic properties can vary and degrade due to various failure mechanisms described in Chapter 2.

Piezoelectric materials operating in TS-mode are required for the design of PUT for the application of UGW. Therefore, characterising the HT response of their TS-mode properties is crucial for their verification and evaluation of operational effectiveness. The temperature coefficients of these TS-mode properties are useful for accurate numerical analysis, as demonstrated in Chapter 4. These HT-FOMs for the TS-mode operation have been characterised and well documented for widely used materials as reviewed in Chapter 3. However, not all TS-mode properties and their temperature characteristics are available, may deviate from those reported due to differences in electrodes and polarisation, or may not be available for the entire temperature range considered. These FOMs must also be characterised at the target operating temperatures for extended periods to assess thermal stability. A stable response will ensure that its use in PUT will provide a consistent ultrasonic output for HT-SHM application.

7.1.2 Aims and Objectives

The purpose of this chapter was to select and validate piezoelectric materials for their application in HT-UGW transducers for continuous operation at temperatures of 350°C and 600°C. The key objectives of this chapter are:

(1) Review of commercially available HT piezoelectric materials and their TS-mode FOMs relevant for UGW-PUT application.

(2) Selection of candidate piezoelectric materials and compatible electrode materials for target operating temperatures of 350°C and 600°C.

(3) Characterisation of TS-mode FOMs of the candidate piezoelectric materials up to their target operating temperatures to assess their suitability for HT-UGW transducer design.

(4) Evaluation of the stability of TS-mode FOMs at the target operating temperature for extended periods to assess their suitability for HT-SHM application.

7.2 Design of HT Piezoelectric Plates

7.2.1 Selection of Piezoelectric Materials

The selection of the piezoelectric material is based on its electromechanical properties described in Chapter 2. A recommended FOM for ultrasonic application is the product of piezoelectric charge (d_{ij}) and voltage coefficients (g_{ij}) [253]. A higher value of this FOM gives a higher electromechanical coupling coefficient k, defining the ratio of stored electrical energy to applied mechanical energy and vice versa. The maximum recommended operational temperature (T_{max}) is also considered to avoid domain-related thermally activated ageing behaviour in ferroelectric materials. Previous studies have suggested that temperatures above $1/2T_c$ can accelerate thermal ageing and degradation of properties [254]. Unless specified in the material datasheets, T_{max} was assumed to be $1/2T_c$. For single crystals, the phase transition temperature was taken into account.

From the HT piezoelectric materials reviewed in Chapter 3, only a subset was commercially available and had T_{max} suitable for the intended target temperatures of 350°C and 600°C. These candidate piezoelectric materials, along with their FOM and T_{max} are shown in Figure 7.1. The PZT-5A piezoelectric material used in the Teletest transducer is marked in blue for reference.
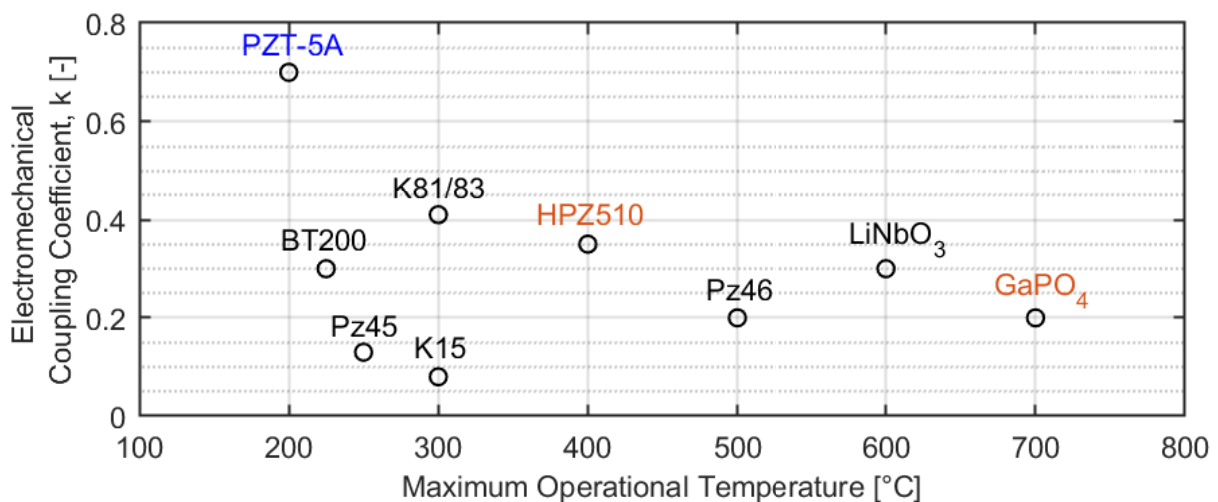
FIGURE 7.1: Commercially available HT piezoelectric materials, their maximum operating temperature and TS-mode electromechanical coupling factor.

The candidate materials included Pz32, Pz45, Pz46 from Ferroperm [255]; K81, K83 from Keramos [256]; K15 - Piezo Technologies [257]; HPZ510 from Ionix Advanced Technologies [258]; BT200 (BS-PT based material) from TRS Technologies [259];

LiNbO$_3$ from Roditi [143]; *GaPO*$_4$ from Piezocryst [260]. The electromechanical coupling factors for these candidate materials were taken from their data sheets.

The K-81, K-83 and K-15 materials were modified lead titanate. They were not selected as previous studies on lead titanate-based materials have reported sudden dielectric loss at 350°C and significant thermal degradation especially at low frequencies [122, 123]. Pz46 and HPZ510 were modified bismuth titanate, with *k* of HPZ510 ≈50% higher than Pz46. The T_{max} of 500-550°C specified for Pz46 is ignored and assumed not for continuous operation with a T_c of 650°C. Thus, HPZ510 was selected for continuous operation at 350°C. For the target temperature of 600°C, *GaPO*$_4$ was chosen as *LiNbO*$_3$ is known to suffer chemical decomposition at 600°C due to oxygen loss [132].

7.2.2 Selection of Electrode Materials

The high-temperature electrode materials reviewed in Chapter 3 were considered for the selected HPZ510 and *GaPO*$_4$ piezoelectric materials. Electrode materials with CTE similar to those of candidate piezoelectric materials were considered to ensure compatibility and avoid the requirement of an additional electrode matching layer. For the *HPZ*510 plate, an electrode of gold was chosen as the CTE of gold (14.2 ppm/°C) matched well with the CTE of HPZ510 (13.5 ppm/°C). For *GaPO*$_4$, platinum was chosen as the electrode material, as it has excellent conductive properties, resists oxidation and has demonstrated HT performance without degradation up to 650°C [173]. The CTE of Pt (9 ppm/°C) matched well with the CTE of *GaPO*$_4$ (12.78 ppm/°C).

7.2.3 Fabrication of Piezoelectric Plates

Piezoelectric plates of the selected HPZ510 material were manufactured by Ionix Advanced Technologies Ltd. and *GaPO*$_4$ by Piezocryst Advanced Sensorics GmbH. Rectangular plates with nominal dimensions of $L = 13mm$, $W = 3mm$ and $T = 0.5mm$. The plate dimensions were similar to those of PZT-5A PWAS characterised in Chapter 4 and were chosen to avoid any mode coupling and achieve clean vibration in TS-mode for accurate characterisation. As a length-to-thickness ratio of less than ten can introduce additional vibration modes [62].

The *GaPO*$_4$ plates were obtained in the $Y - cut(YXl)0°$ configuration as a previous study on different crystal orientations has identified $Y - cut$ to achieve a pure shear mode vibration [261]. The HPZ510 plate was manufactured with polarisation along

the $W = 3mm$ dimension. The piezoelectric plates manufactured from materials $GaPO_4$ and HPZ510 are shown in Figure 7.2.

(A)   (B)
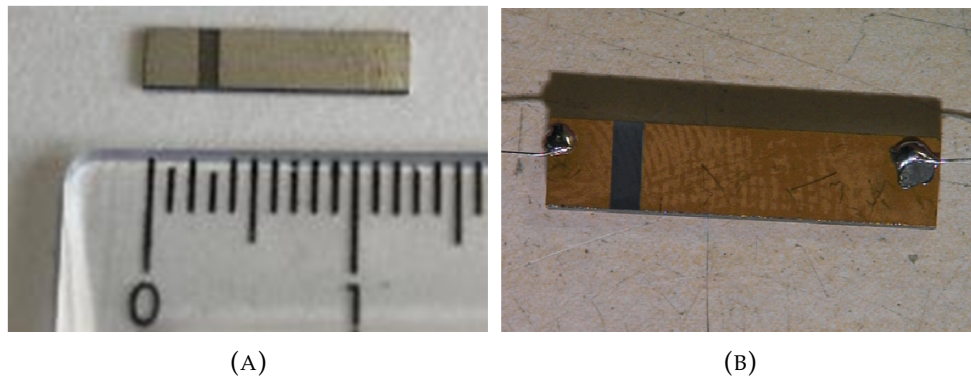
FIGURE 7.2: Piezoelectric plate samples used for material characterisation showing (a) $GaPO_4$ with Platinum coating and (b) HPZ510 with Gold coating.

Platinum and gold electrodes were applied to the $GaPO_4$ and HPZ510 piezoelectric plates in a wrap-around electrode configuration using the magnetron sputtering technique PVD. The manufacturer recommended electrode thickness of $100nm$ was used. The electrode for ground connection was applied to one of the two large faces (13mm x 3mm), its adjacent end face (3mm x 0.5mm), and part of the second large face (2mm x 3mm). The input voltage electrode was applied on the second large face (10mm x 3mm) with a 1mm gap from the ground electrode, which was achieved by applying a micromasking tape before sputtering.

7.3 Electromechanical Characterisation

7.3.1 Characterisation of TS-mode FOMs using EMIS

The HT-EMIS methodology described in Chapter 4 was used to measure the electromechanical impedance response of the HPZ510 and $GaPO_4$ plates at increasing temperatures. The EMI spectrum was measured for five samples of each candidate piezoelectric material. The EMIS measurements on each HPZ510 and $GaPO_4$ plates sample were performed at temperature increments of 25°C up to 525°C and 600°C[1], respectively.

The EMIS response from each of the samples was analysed to extract the characteristic resonance (f_r) and anti-resonance frequencies (f_a). The characteristic frequencies and

---

[1]Although $GaPO_4$ is capable of operating at even higher temperature the high temperature characterisation was limited to the target temperature of 600° due to the limitations of the test instrument used.

capacitance (measured at $1kHz$) were then used to calculate the elastic, dielectric and piezoelectric FOM of the candidate piezoelectric materials as described in Chapter 2. The exact dimensions of the samples were measured with an accuracy of $0.01mm$ using a digital calliper. The dimensions of the plate at high temperatures used to derive HT-FOM were estimated using the anisotropic CTEs from their datasheet.

The following TS-mode FOM were characterised as a function of temperature using HT-EMIS: electrical permittivity $\epsilon_{11}^T/\epsilon_0$; elastic constants S_{55}^D, S_{55}^E; piezoelectric coefficients d, g; and electromechanical coupling factor k. The derived HT FOMs of the candidate piezoelectric materials were analysed and compared with PZT-5A for performance comparison. The derived temperature coefficients were also compared with those available in the literature. A sample of each HPZ510 and $GaPO_4$ material was examined for 1000 hours of dwell time at their respective target temperatures of 350°C and 600°C. These measurements were analysed to evaluate their thermal ageing behaviour and evaluate their long-term reliability for the SHM application.

7.3.2 FEA of HPZ510 and GaPO4 PWAS

The piezoelectric plate model described in Chapter 4 was modified for selected high-temperature piezoelectric materials HPZ510 and $GaPO_4$. The geometry of the plate was set up to model the piezoelectric plate of 0°rotated Y-cut $GaPO_4$ (YXl)0°piezoelectric plate with its thickness aligned with the geometric Y axis. The dimensions of the $GaPO_4$ plate were y = 0.5 mm, x = 13 mm, and z = 3 mm. The HPZ510 piezoelectric plate was modelled with the same dimensions but with the plate width aligned along the geometric Z axis to achieve the width polarisation.

$GaPO_4$ material belongs to the 32-point trigonal group, such as quartz. Because of its crystal symmetry, several elements of the property matrices are zero, and some others are related, as shown in Equation (7.1).

$$
\begin{bmatrix}
s_{11}^E & s_{12}^E & s_{13}^E & s_{14}^E & 0 & 0 \\
s_{12}^E & s_{11}^E & s_{13}^E & -s_{14}^E & 0 & 0 \\
s_{13}^E & s_{13}^E & s_{33}^E & 0 & 0 & 0 \\
s_{14}^E & -s_{14}^E & 0 & s_{44}^E & 0 & 0 \\
0 & 0 & 0 & 0 & s_{44}^E & s_{14}^E \\
0 & 0 & 0 & 0 & s_{14}^E & \frac{1}{2}(s_{11}^E - s_{12}^E)
\end{bmatrix}
\begin{bmatrix}
d_{11} & -d_{11} & 0 & d_{14} & 0 & 0 \\
0 & 0 & 0 & 0 & -d_{14} & -2d_{11} \\
0 & 0 & 0 & 0 & 0 & 0
\end{bmatrix}
\\
\begin{bmatrix}
\epsilon_{11}^T & 0 & 0 \\
0 & \epsilon_{11}^T & 0 \\
0 & 0 & \epsilon_{33}^T
\end{bmatrix}
\tag{7.1}
$$

The numerical modelling approach of the transducer was validated for the current Teletest transducer design in Chapter 5. Furthermore, the piezoelectric plate models

for the selected HPZ510 and $GaPO_4$ high-temperature materials were experimentally validated in Chapter 7.

7.3.3 Vibrational Response Characterisation using SDLV

The vibration response characterisation of PZT-5A PWAS described in Chapter 4 and the design hypothesis related to the influence of the electrode configuration verified in Chapter 5 are also applicable to HPZ510, as both materials are ferroelectrics with polarisation defined in a particular dimension of the plate. $GaPO_4$ is a single crystal, and this study selected a particular configuration (Y-cut (YXl)0°) for TS-mode. Therefore, SLDV in this study focused on the vibration response characterisation of the $GaPO_4$ plate. The influence of wear plate on the vibration response is also characterised and compared with the simulated response.

The methodology described in Chapter 4 was followed to characterise the 3D vibrational response of the $GaPO_4$ piezoelectric plates of both electrode configurations and a wraparound electrode sample bonded with an Alumina face plate. Thin wires were soldered to the platinum surface electrodes for electrical connection. As a much lower displacement was expected, a retroreflective glass beads tape was attached to the surface of the piezoelectric plates to enhance levels of reflection from the surface. The $GaPO_4$ devices under test are shown in Figure 7.3. The measured vibration response as a function of frequency was compared with those simulated by the model.

Parallel electrode   Wraparound with face plate

FIGURE 7.3: $GaPO_4$ PWAS samples used for SLDV measurements (a) PWAS with parallel electrode (b) PWAS with wraparound electrode bonded to Alumina wear plate.

7.4 Results and Discussion

7.4.1 Electromechanical Impedance Response

The measured electromechanical impedance frequency spectrum of HPZ510 and $GaPO_4$ materials at ambient temperatures is shown in Figure 7.4. The response of PZT-5A from Chapter 4 is overlayed for comparison. The frequency plots are presented in a logarithmic scale to emphasise the weaker excitable harmonics and spurious/unwanted modes. A series of TS-mode harmonics can be seen at higher frequencies and are progressively weaker than the fundamental mode. The fundamental TS-mode harmonic and its overtones can be seen at around 2 MHz, 7 MHz, and 11 MHz, respectively.
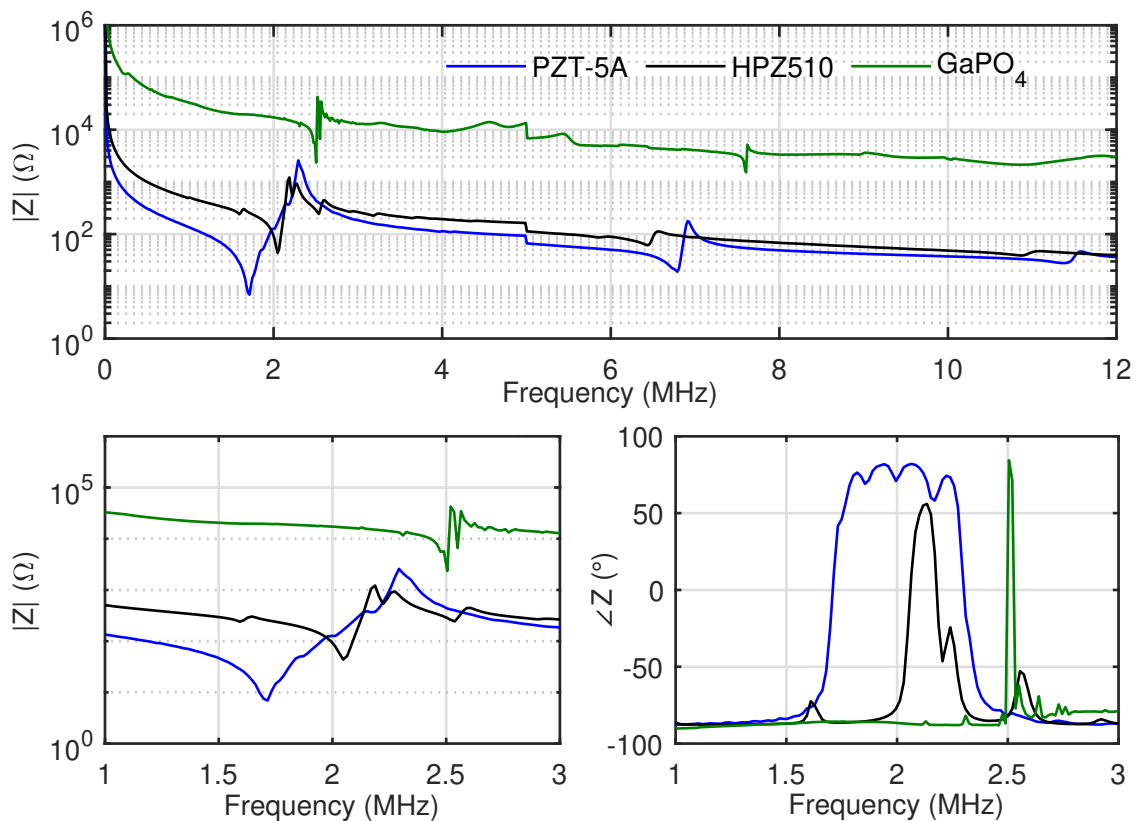
FIGURE 7.4: Impedance spectrum of PZT, HPZ510 and $GaPO_4$ samples measured in the frequency range of 40 Hz to 12 MHz at ambient temperatures.

The EMIS resonance response appears rougher, such as the serrations observed in the phase response of PZT-5A and the amplitude response of both the HPZ510 and the $GaPO_4$ samples. These are associated with the harmonics of the lower frequency modes, which may be excited by or coupled with the strong TS-mode. A spurious peak is observed at around 4.5 MHz for all three materials and is believed to be due to the parasitic impedance of the test fixture.

The room temperature EMI response simulated from the $GaPO_4$ piezoelectric plate model was compared to the measured impedance spectra as shown in Figure 7.5. The comparison shows a good correlation between the simulated and measured EMI amplitude. The modelled response simulated two resonances in the TS mode around 2.5 MHz and 7.6 MHz, consistent with the measured response.
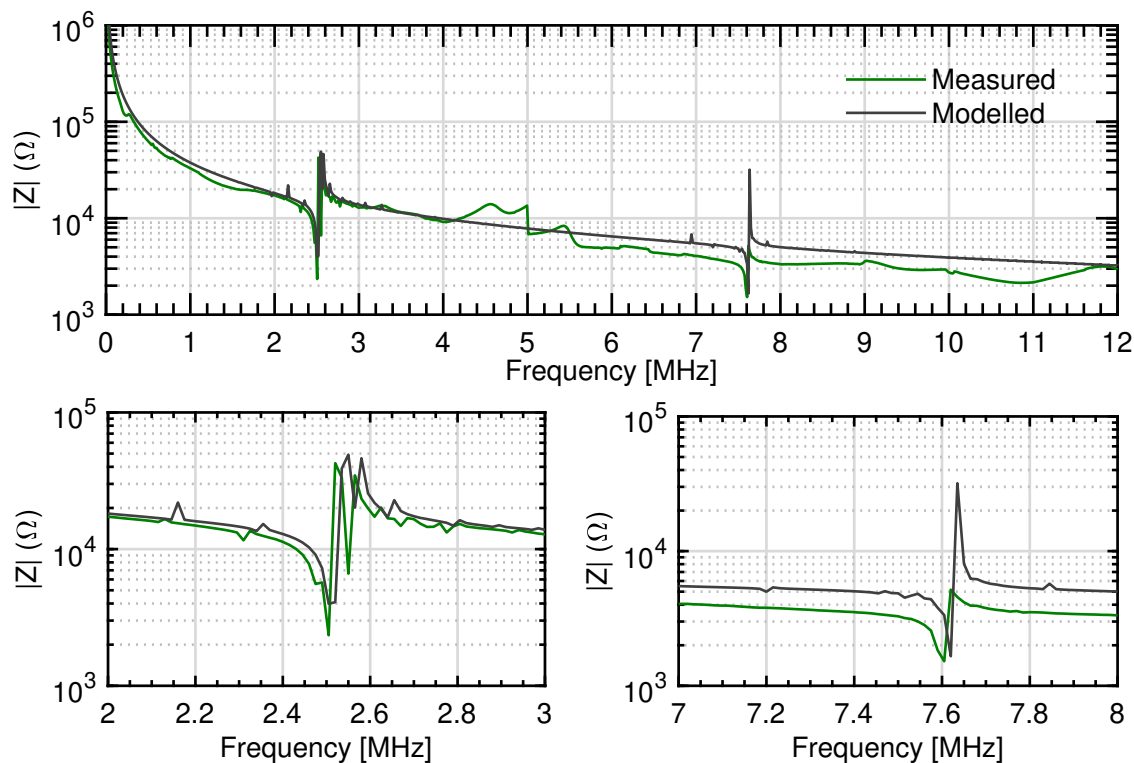
FIGURE 7.5: Comparison of the simulated and measured EMI responses of the fundamental TS-mode resonance and its overtone.

The model also successfully simulated the coupling of TS-mode resonance with high overtone contour and undesired modes, which can be seen around the antiresonance frequency of the fundamental resonance. These unwanted modes generally have lower frequencies, and their influence becomes smaller for overtones, as observed with the cleaner second overtone. A slight frequency change in the simulated EMI affected both the fundamental and the second resonance frequencies, although the disparity in the second resonance was comparatively higher. This frequency shift may have resulted from the mass loading effect of the deposited piezoelectric plate electrode or the connecting wires, which are not included in the model. This hypothesis agreed with a previous study in which the mass loading effect was more significant with high overtone resonances [262].

Resonance frequencies in the TS mode were also analysed using the frequency thickness coefficient of the data sheet and the nominal thickness of the piezoelectric plate. A comparison of the calculated, measured, and modelled resonances is provided in Table 7.1. The modelled phase of the impedance is always $\pm\pi/2$ since the piezoelectric material is assumed to be lossless in the model. The fundamental resonance of the thickness-shear mode and anti-resonance were used to calculate the thickness-shear coupling factor k_{26}. A slight variance in the measured resonances was observed in comparison to those predicted by the model. However, the coupling factor k_{26} only varied by a mere 0.25%.

TABLE 7.1: Comparison of measured and simulated TS-mode resonance frequencies.

Parameter	Baseline	Measured	Simulated	Error (%)
F_r n=1 (MHz)	$2.53^{(a)}$	2.52	2.51	0.4
F_r n=3 (MHz)	$7.59^{(b)}$	7.61	7.62	0.2
k_{26} (-)	0.183-0.192 [263]$^{(c)}$	0.164	0.169	2.9

$^{(a, b)}$ Calculated using the nominal thickness of the piezoelectric plate and frequency thickness coefficient from the material data sheet.

$^{(c)}$ The reported value is for a different geometry and a different electrode configuration.

The CTEs (α_{ij}) of $GaPO_4$ is a second-rank tensor with only two independent coefficients α_{11} and α_{33} and is temperature dependent. Material properties for $GaPO_4$ and their temperature coefficients are available in the literature [260] and are given in Appendix A.2.1. These properties and their temperature coefficients were added as piecewise cubic interpolation within COMSOL.

For HPZ510, the properties of the TS-mode were not available in the datasheet. Only properties for the 31 and 33 operation modes were available at discrete temperatures of 25°C, 200°C and 400°C. Therefore, for the HT-modeling of the HPZ510 piezoelectric plate, the properties of the material in the TS mode derived from HT-EMIS were used for the model.

7.4.2 TSM FOM at Ambient Temperatures

The calculated coefficients are then compared with those reported in the literature, and the relative errors are listed in Table 7.2. The data sheet for the HPZ510 material provided by Ionix [258] did not provide any TS-mode FOM apart from the relative dielectric constant K^T, which is comparable to the measured value. Other modified Bismuth Titanate materials $D2$ and $D2+$ have previously been reported to have a TS mode k_{eff} of 0.46 [264].

For $GaPO_4$, the measured d_{26} was approximately three times the value provided in the data sheet provided by Piezocryst Gmbh [260]. The coupling factor was not available in the datasheet, but previous work on TS-mode using $GaPO_4$ provided a k_{26} value of 0.192 [265], which matched very well with the measured value of 0.195. The BAW phase velocity previously reported for the Y-cut pure slow shear mode $GaPO_4$ by Wallnofer was 2550 m/s, Philippot was 2527 m/s, and Palmier was 2546 m/s [261] and is consistent with our measured value of 2538 m/s. The measured elastic coefficients are in good agreement with those previously reported [265]. There is a considerably more significant difference in the measured k_{26}. This is due to the difference in PWAS geometry, since the previous study used a circular plate with gold electrodes [265]. The deviation is attributed to the electric field concentration at the electrode corners in a rectangular design, which is reduced in circular designs. The variation between the measured and modelled electromechanical coupling factor k_{26} is less than 3%. This shows that the model can accurately predict the electromechanical resonances and the associated constitutive piezoelectric properties of the selected piezoelectric materials. These FOMs indicate its performance as an ultrasonic transducer.

TABLE 7.2: TS-mode electromechanical properties of candidate materials derives from EMIS compared with those reported in datasheets and literature.

Property	k	d	g	K^T	K^S	V_s	Z_L
Units	[-]	[pC/N]	[Vm/N]	[-]	[-]	[m/s]	[$MRayl$]
HPZ510							
Measured	0.35	139.5	31.2	506	443	2024	14.16
Datasheet [258]	-	-	-	515	-	-	-
K15 [266]	0.08	14	10	140	-	4000	28
$GaPO_4$							
Measured	0.195	27.2	60.7	50.5	48.6	2538	9.1
Datasheet [260]	-	9	-	6.1	5.8	-	-

To compare the performance of the candidate materials at ambient temperature, their electromechanical, elastic and dielectric properties are compared to PZT-5A in Figure 7.6. Blue, black, and green bars represent the properties of PZT-5A, HPZ510, and $GaPO_4$. This colour scheme is maintained throughout the results.
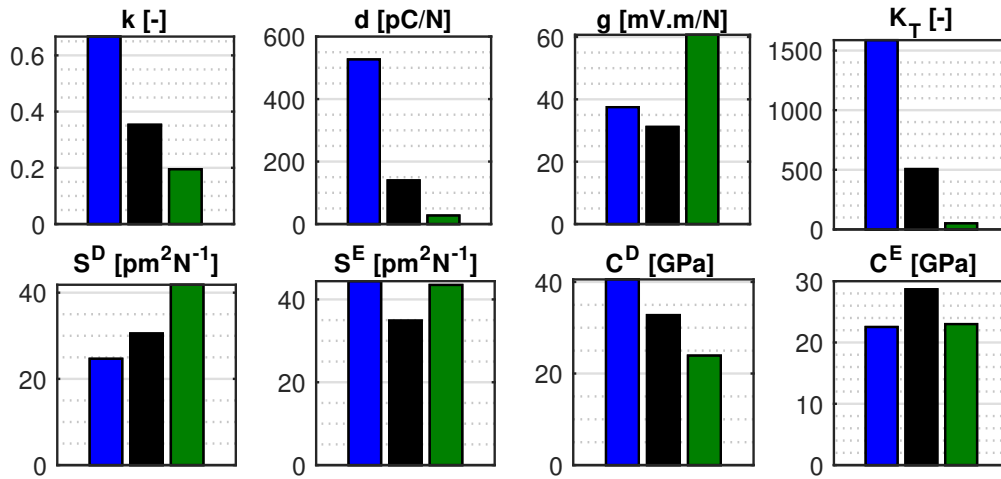
FIGURE 7.6: Comparison of TS-mode electromechanical, dielectric and elastic properties of candidate piezoelectric materials at ambient conditions.

The electromechanical coupling factor of TS-mode, *k* of HPZ510 and *GaPO₄*, is approximately 50% and 30%, compared to PZT, respectively. The charge constant *d* of HPZ510 and *GaPO₄* is around 25% and 5% of the corresponding value of PZT-5A. On the other hand, the charge coefficient *g* of *GaPO₄* is almost 1.5 times higher than that of PZT-5A and HPZ510. This indicates that the *GaPO₄* material is a worse actuator but a significantly better sensor under ambient conditions.

7.4.3 Vibrational response characterisation

The vibrational frequency response of the *GaPO₄* plate was analysed in the 20-120 kHz range. The analysis was carried out on *GaPO₄* plates with parallel and wrapped around electrode configuration. The analysis on wrapped around electrode configuration was extended to evaluate influence of a sandwiched Alumina wear plate. In-plane and out-of-plane displacement fields in the $\vec{Y}$ and $\vec{X}$ directions were averaged across the length-width face of the piezoelectric plate and compared to the measurements from SLDV.

For the *GaPO₄* model with parallel electrode configuration, A good correlation was achieved between the measured and modelled spectrum of the electromechanical displacement field in terms of resonance frequencies and operating modes of vibration, as shown in Figure 7.7. The displacement patterns suggest the desired thickness-shear vibration mode was dominant and a near-linear response was observed within the frequency range of interest. The measurements also show first-order and second-order eigenmodes of displacement appear through the thickness of the plate with higher out of plane displacement at 21kHz, 35kHz, 59kHz and 104kHz. However, their amplitude was at least an order of magnitude lower than

in-plane displacement. The model also displayed the out-of-plane displacement in the 35kHz and 105kHz range. The measured out-of-plane displacement were lower as the model does not consider added mass from the electrodes and the electrical connections to the $GaPO_4$ elements.
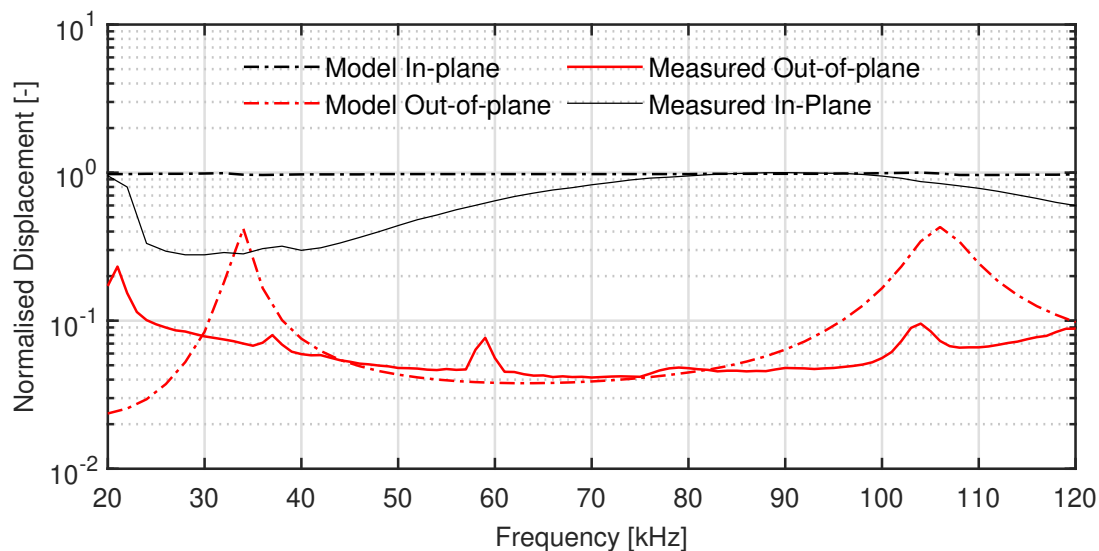
FIGURE 7.7: Frequency response of Y-cut $GaPO_4$ piezoelectric plate with parallel electrodes showing simulated and measured in-plane and out-of-plane vibration.

The $GaPO_4$ model with the wraparound electrode configuration predicted significant out-of-plane displacement within the same frequency range as shown in Figure 7.8. Additional resonances were observed in the measured response near 31, 58, 72 and 98 kHz. These lower amplitude out-of-plane vibrations are believed to be introduced due to longitudinal mode coupling associated with the boundary effects of the wrapped-around electrode configuration. The simulated response closely matched the measured response. A slight shift in the simulated frequency response is depicted, which increases almost linearly with the increase in frequency. This is possible because the added mass from the electrodes and electrical connections is not included in the model.
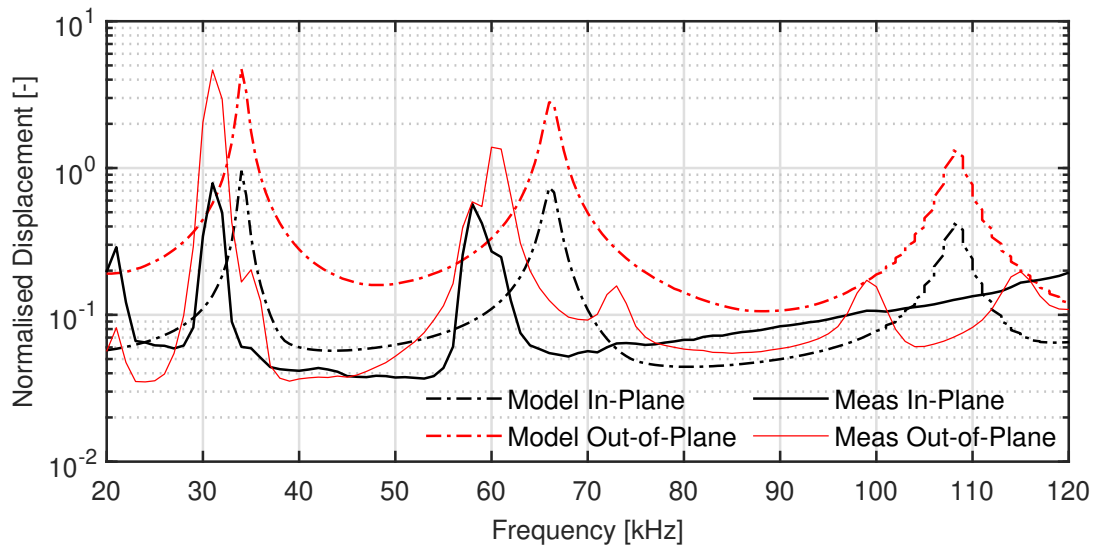
FIGURE 7.8: Frequency response of Y-cut $GaPO_4$ piezoelectric plate with wrapped-around electrodes showing simulated and measured in-plane and out-of-plane vibration.

The $GaPO_4$ piezoelectric plate model with wraparound electrode was advanced to study the influence of the Al_2O_3 wear plate on the electromechanical response of the piezoelectric element. With the addition of face plate the out-of-plane vibration in the 60kHz and 70kHz range were suppressed due to the increased flexural stiffness. However, out-of-plane resonances at 34kHz and 89 kHz were still visible as shown in Figure 7.9.
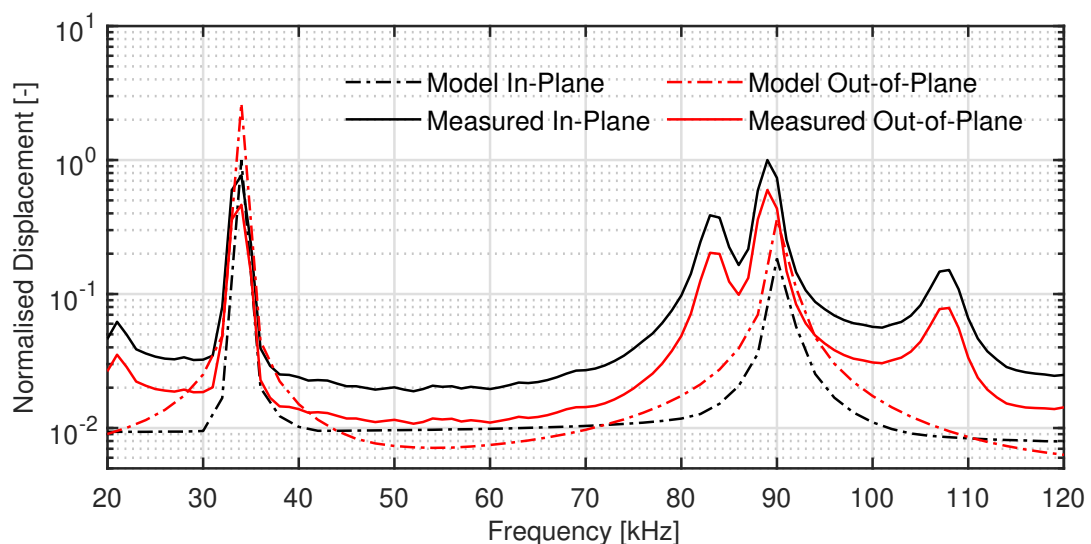
FIGURE 7.9: Frequency response of Y-cut $GaPO_4$ piezoelectric plate with wrapped-around electrode attached to Alumina wear plate showing simulated and measured in-plane and out-of-plane vibration.

Resonance frequencies and corresponding vibration mode shapes for the three models are shown in Figure 7.10. The measured and simulated vibration modes and resonance frequencies appear to be in good agreement. The out-of-plane resonances of parallel electrode were weaker in amplitude compared with the wrap-around configuration. The resonance frequencies were simulated with an error of less than 5%. The two resonance observed at 35kHz and 105kHz have uniform out-of-plane displacement across the surface so an adequate backing can suppress them. With the wrap-around configuration, the longitudinal mode coupling and significant out-of-plane displacement can be seen around 30, 60 and 100 kHz and the mode shape suggest imbalanced out-of-plane displacement.
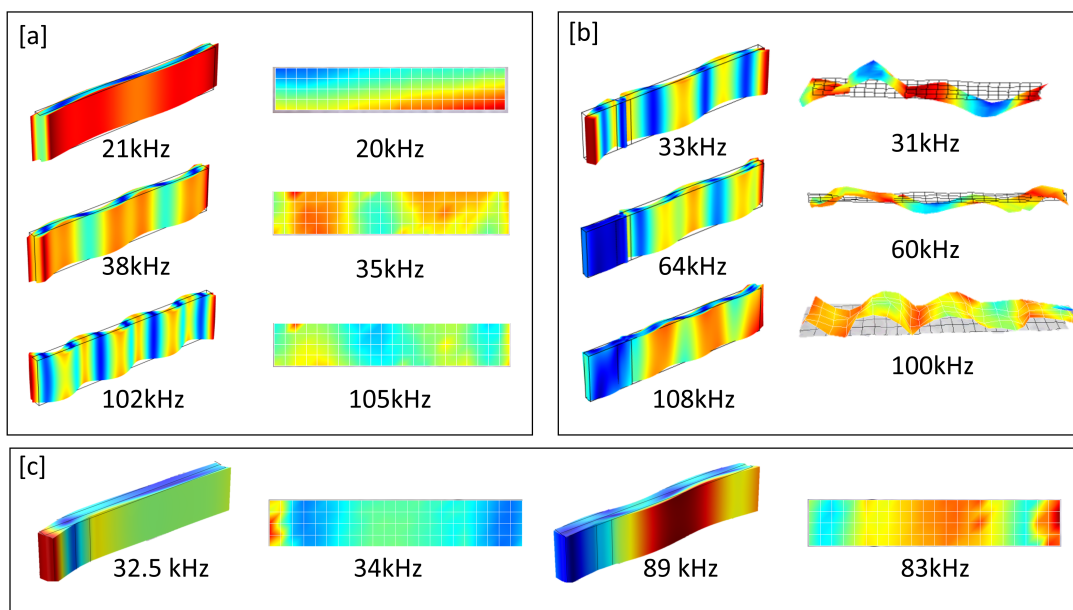
FIGURE 7.10: Comparison of simulated (left) and measured (right) vibration modes of the $GaPO_4$ piezoelectric plate with (a) parallel electrode configuration and (b) wrapped-around electrode configuration, (c) wrapped-around electrode configuration with alumina wear plate.

7.4.4   HT-EMI Response of HPZ510

The high-temperature EMI response of HPZ510 material was measured at temperatures up to 525°C in increments of 25 °C. The measured response at each temperature step is provided in Appendix A.3.1. HPZ510 lost its piezoelectric response at 525°C, which was expected with the T_c of 514°C provided by the supplier. Measurements at selected temperatures and the respective simulated response are shown in Figure 7.11. The comparison shows that the simulated high-temperature response matched well with the respective measurements.
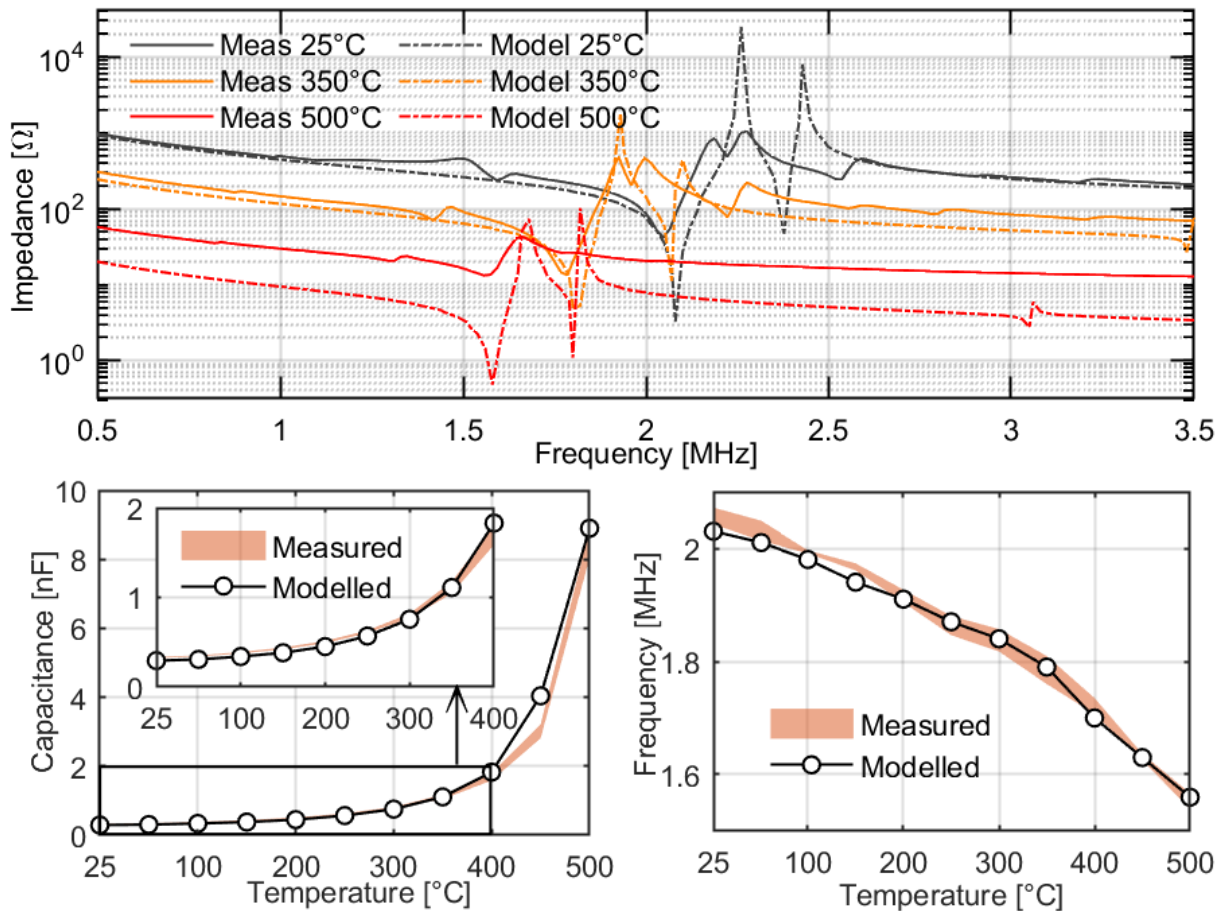
FIGURE 7.11: Comparison of HT-EMI measurements and simulated response of HPZ510 piezoelectric plate at temperatures up to 500°C.

The HPZ510 high-temperature impedance response showed a decreasing trend of the resonance peak with a negative frequency shift, which was more significant for the TS-mode harmonics. This relates to the increase in permittivity and capacitance of the material. The temperature coefficient of the resonance frequency predicted by the model is 27.89 ppm/°C, which matches well with the 27.3 ppm/°C calculated from the measured response with an error of less than 2%. The capacitance data from the model were extracted by computing the integral of the total electric energy on the edge of the electrode. The increased capacitance at higher temperatures was observed in both measured and simulated responses.

7.4.5 HT-EMI Response of $GaPO_4$

The measured and simulated HT-EMI response of $GaPO_4$ and the effect of increasing temperature on the resonance frequency and capacitance are shown in Figure 7.12. The comparison is shown for 200°C, 400°C and 600°C. The complete set of high temperature measurements in the entire frequency range are provided in Appendix

A.3.2. The measured impedance amplitude at HT has been reduced by a factor of ten compared to the response at ambient temperature. No mode coupling was observed around the antiresonance frequency. This has resulted from the HT conductive adhesive used to attach an electrical connection to the plate. $GaPO_4$ did not show any significant frequency change, indicating no change in the structural properties of the material. A linear drop in impedance amplitude was observed with increased temperature; however, the sample remained piezoelectric until 600°C. The change in measured capacitance is around 100 times more than in the simulation. This is due to the combined effect of the dielectric losses in $GaPO_4$ and the parasitic capacitance from the electrical connections and measurement setup.
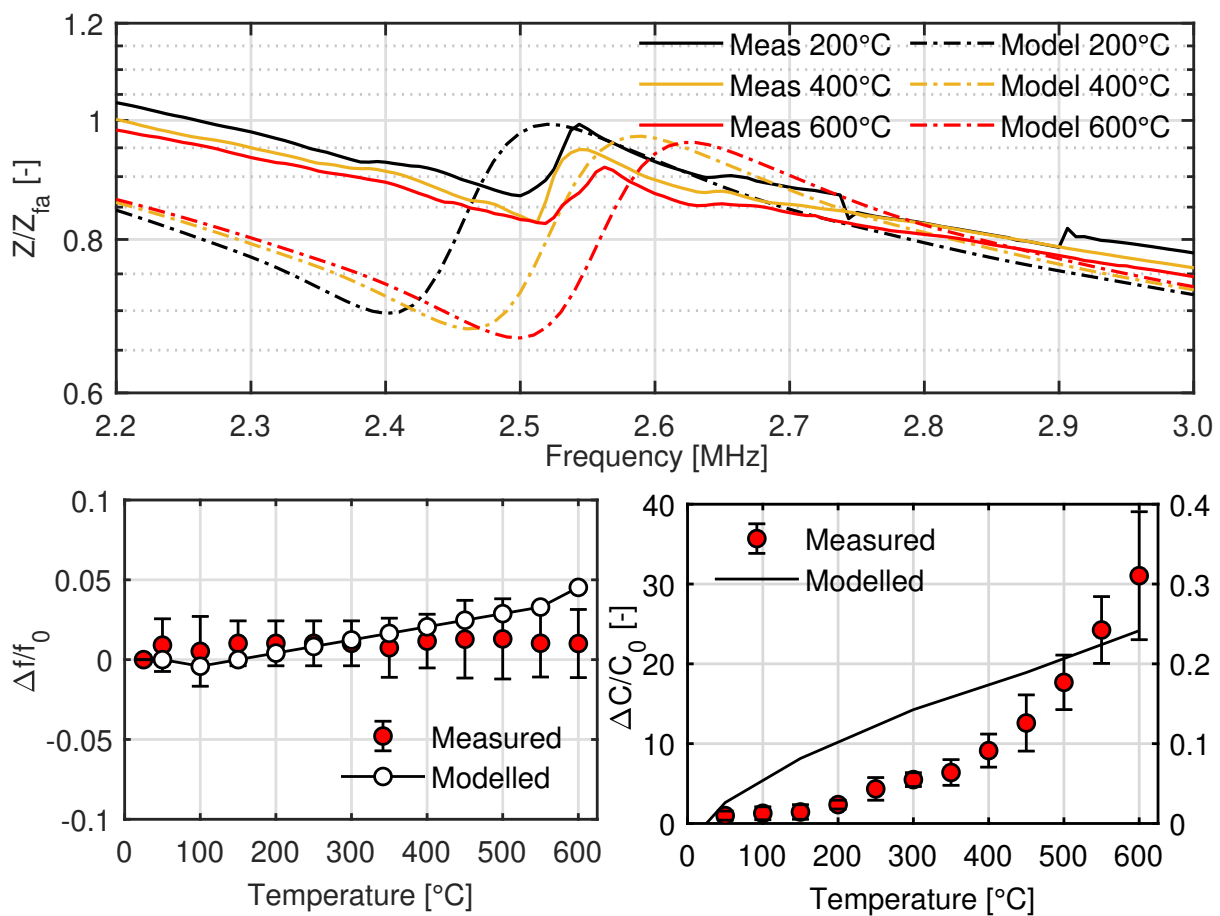
FIGURE 7.12: Comparison of (a) measured and (b) simulated HT-EMI response of $GaPO_4$ with resulting (c) change of frequency and (d) capacitance at temperatures up to 600°C.

The first-order temperature coefficients were derived from the measured HT properties and are compared with those available in the literature in Table 7.3. A relative error of approximately 3% was observed for the four critical FOM for the TS-mode transducer.

TABLE 7.3: Temperature coefficients of TS-mode $GaPO_4$ elastic and piezoelectric properties

Property	[263]	Measured	Rel Error (%)
		$Tp_{ij}^{(1)}[K^{-1}]$	
C_{66}^E	44.9e-6	46.4e-6	3.23
S_{66}^E	-26.9e-6	-27.8e-6	3.34
f_r	19.9e-6 - 35.7e-6 [a]	27.3e-6	1.8 [b]
k_{26}	4.52e-4	4.69e-4	3.62

[a] Values reported with and without the correction from stay capacitance
[b] Error calculated based on the average of the two reported values

The material properties calculated from the HT-EMI measurements in Figure 7.13 are compared with those calculated using first-, second-, and third-order temperature coefficients provided in the datasheet. The temperature dependence of the elastic constants exhibits a stable state up to 600°C with a variation of less than 3%. The measured k_{26} is extremely consistent, showing less than 1% variation up to 600°C. This demonstrates excellent temperature-independent behaviour and the accuracy of the simulations.
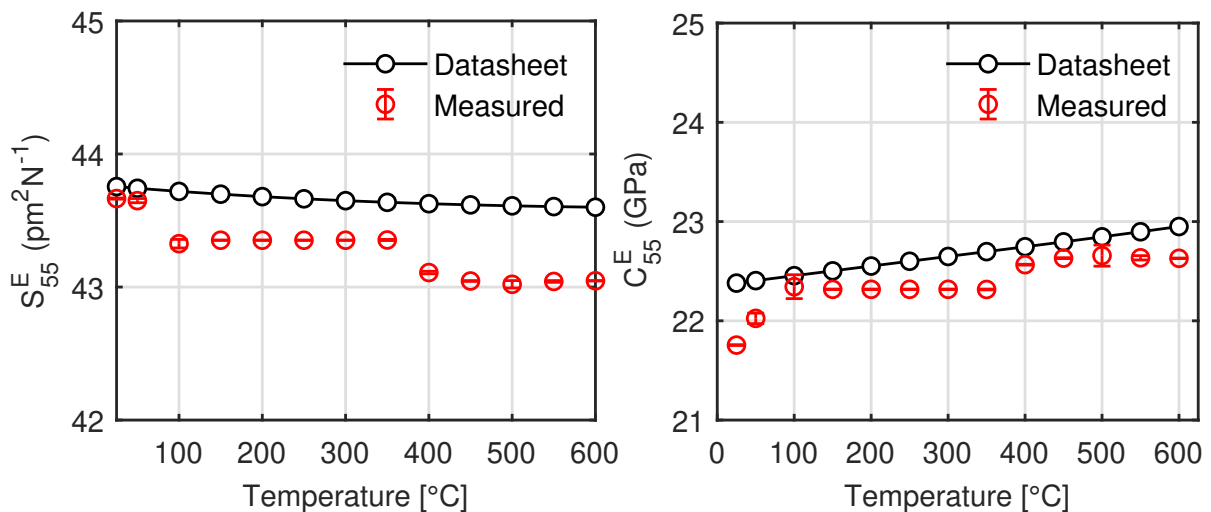
FIGURE 7.13: Assessment of the measured elastic constant S_{66}^E and C_{66}^E with those calculated using the temperature coefficients provided in the literature.

7.4.6 High temperature TSM electromechanical properties

The HT-FOM of both candidate piezoelectric materials were derived from the EMI measurements as described in Section 2.2.2 and compared with PZT-5A.

Dielectric Properties

As piezoelectric materials are predominantly capacitive, it is crucial to analyse their capacitance at increasing temperatures. Static capacitance C_T measured at 1 kHz was used to calculate the values of the relative dielectric constant K_{11}^T ($\frac{\epsilon_{11}^T}{\epsilon_0}$). The static capacitance and the dielectric constant of all candidate materials are analysed as a function of temperature in Figure 7.14. Temperature-dependent K^T for ferroelectric materials is dominated by polarisation rotation, domain wall mobility, phase transitions, and ionic conduction caused by mobile charge carriers [120]. The K^T of PZT and HPZ510 remained consistent up to 200°C and 250°C, respectively, below their respective T_c. However, K^T increased sharply as the temperature approached T_c, as the Curie-Weiss law also predicts this phenomenon. For HPZ510, there is a significantly large increase in capacitance, consistent with the significant decrease in impedance amplitude observed in Figure 7.11. This results from the high shunt capacitance of the material and can lead to a significant loss in the sensing capability of the material.
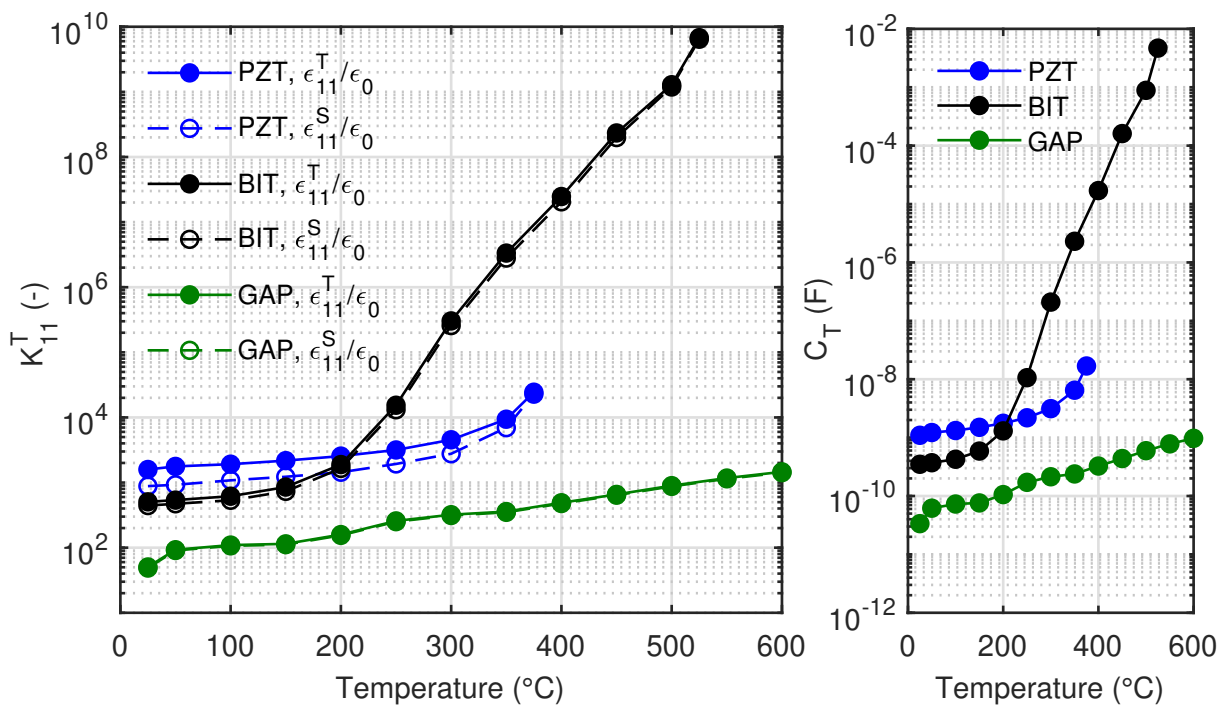
FIGURE 7.14: Comparison of the dielectric constants and capacitance of the candidate materials at high temperature.

On the other hand, $GaPO_4$ showed a consistent response of up to 600°C. Both C_T and K_{11}^T show a linear increase but are significantly lower than the other candidate materials. It follows the dielectric temperature behaviour for non-ferroelectric piezoelectric crystals described by the Clausius-Mosotti equation [120]. For materials with small electromechanical coupling, such as $GaPO_4$, the piezoelectric and dielectric constants generally have a negligible effect on the temperature response of devices that use the material; only the temperature coefficients of the elastic constants and the thermal expansion coefficients are significant.

Characteristic Resonance Frequencies

The characteristic resonance (f_r) and anti-resonance (f_a) frequencies of the fundamental TS mode derived from high temperature impedance measurements are shown in Figure 7.15. The resonance frequencies of PZT and HPZ510 were found to show a linear behaviour as a function of temperature. The difference between f_a and f_r decreased with increasing temperature and decreased as the temperature approached their respective T_c.
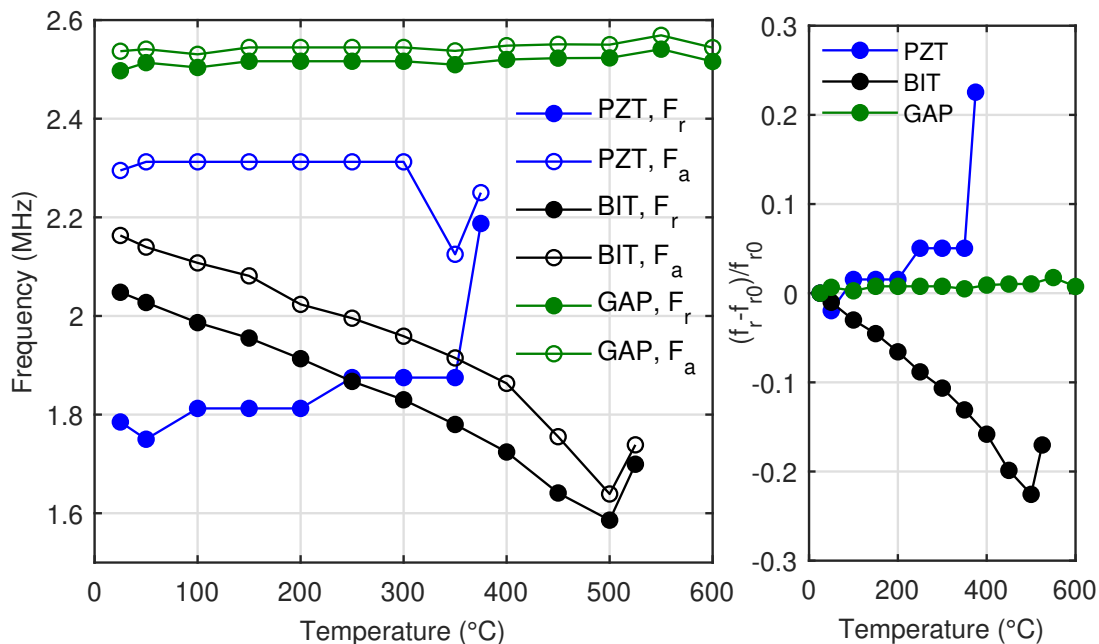
FIGURE 7.15: Characteristic resonance and anti-resonance frequency of the fundamental TS-mode as a function of temperature for candidate materials.

Temperature coefficients of frequency (TCF) were found to be on the order of 350 ppm/°C and -475 ppm/°C for PZT and HPZ510, over a temperature range of 25°C to 300°C and 500°C, respectively. $GaPO_4$ exhibited a stable temperature frequency characteristic up to 600°C with a TCF≈0.

Elastic Properties

The elastic compliance of the materials with constant electric displacement (S_{jj}^D) and constant electric field (S_{jj}^E) is calculated as a function of temperature and is shown in Figure 7.16. The subscript j for PZT and HPZ510 is 5 and 6 for $GaPO_4$. The measured elastic compliance constants for PZT remained consistent up to 300°C with a variation of less than 2% for S_{55}^D and 10% for S_{55}^E. For HPZ510, the elastic constants increased monotonically with increasing temperature. An increase of around 30% for S_{11}^D and S_{33}^D was reported in the HPZ510 datasheet. Measurements showed an increase of 41% for S_{55}^E in the same temperature range. The elastic constants increased by approximately 65% at 500°C. For both PZT and HPZ510, a sharp increase in the elastic constant S_{55}^D was observed as the temperature approached their respective T_c. Above T_c, the sudden drop in elastic compliance is due to the diminishing resonance as the material loses its piezoelectric behaviour.
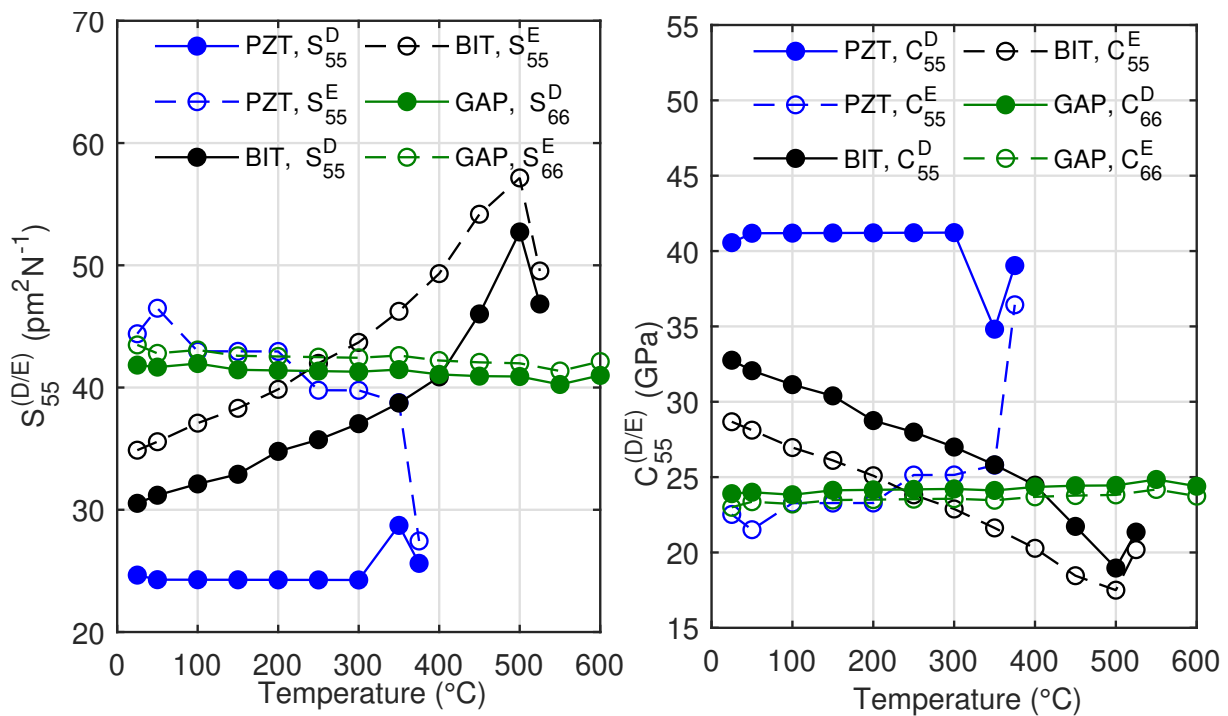
FIGURE 7.16: Characteristic resonance and anti-resonance frequency of the fundamental TS-mode as a function of temperature for candidate materials.

A proportional decrease in elastic constants S_{66}^E was observed with increasing temperature and a small dependence at low temperatures for $GaPO_4$. At 600°C, S_{66}^D and S_{66}^E had decreased by approximately 5% of their respective values at 35°C. Highly stable elastic properties are seen in most single crystals [135]. The temperature response of elastic constants C_{ij}^D and C_{ij}^E is inversely proportional to S_{66}^D and S_{66}^E, respectively, due to their inverse relation.

Electromechanical and Piezoelectric Properties

The piezoelectric coefficients d_{ij}, g_{ij}, and k_{ij} for the TS mode were determined for all candidate materials as a function of temperature. The TS mode is represented by subscript $(i, j) = (1, 5)$ for PZT-5A and HPZ510 while $(i, j) = (2, 6)$ for $GaPO_4$. The variations of these coefficients with increasing temperature for all candidate materials are shown in Figure 7.17. Variations are represented as P_T/P_0 versus temperature, where P_T is the property measured at temperature T, and P_0 is measured at 25°C.
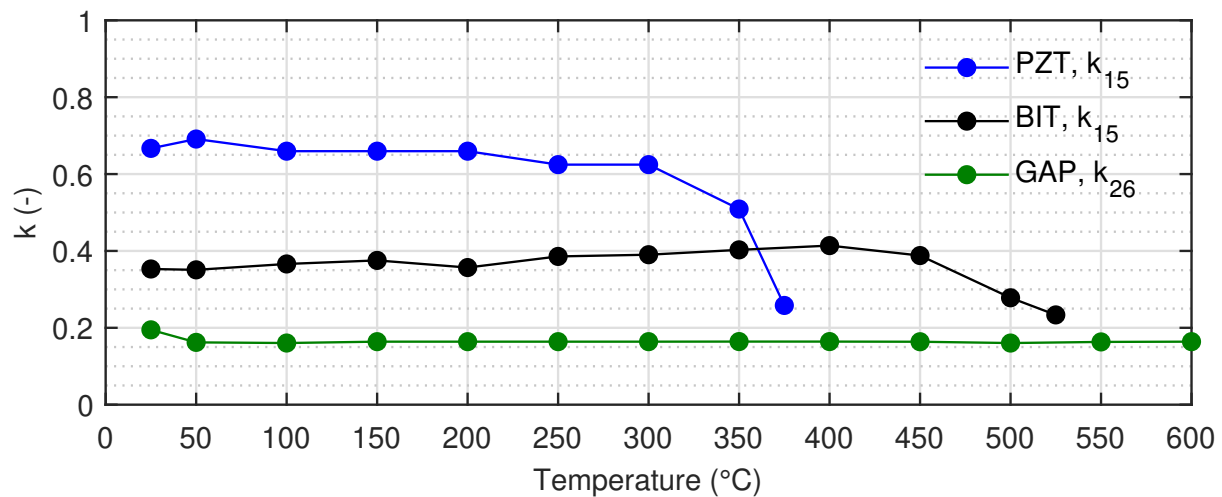
FIGURE 7.17: Electro-mechancal coupling, k as a function of temperature for candidate materials.

The charge constant d for all materials increased linearly with temperature. For PZT-5A, the d_{15} value increased by 70% from 526 pC/N at 25°C to 914 pC/N at 350°C. For HPZ510, the temperature response is much more significant and follows the trend observed with its dielectric constant, as seen in Figure 7.18. The d_{15} for HPZ510 increased by a factor of 100 from its ambient temperature value of 139 pC/N. The charge constant d_{26} for $GaPO_4$ increased by 35% from its room temperature value of 27.2 pC/N to 121 pC/N at 600°C.
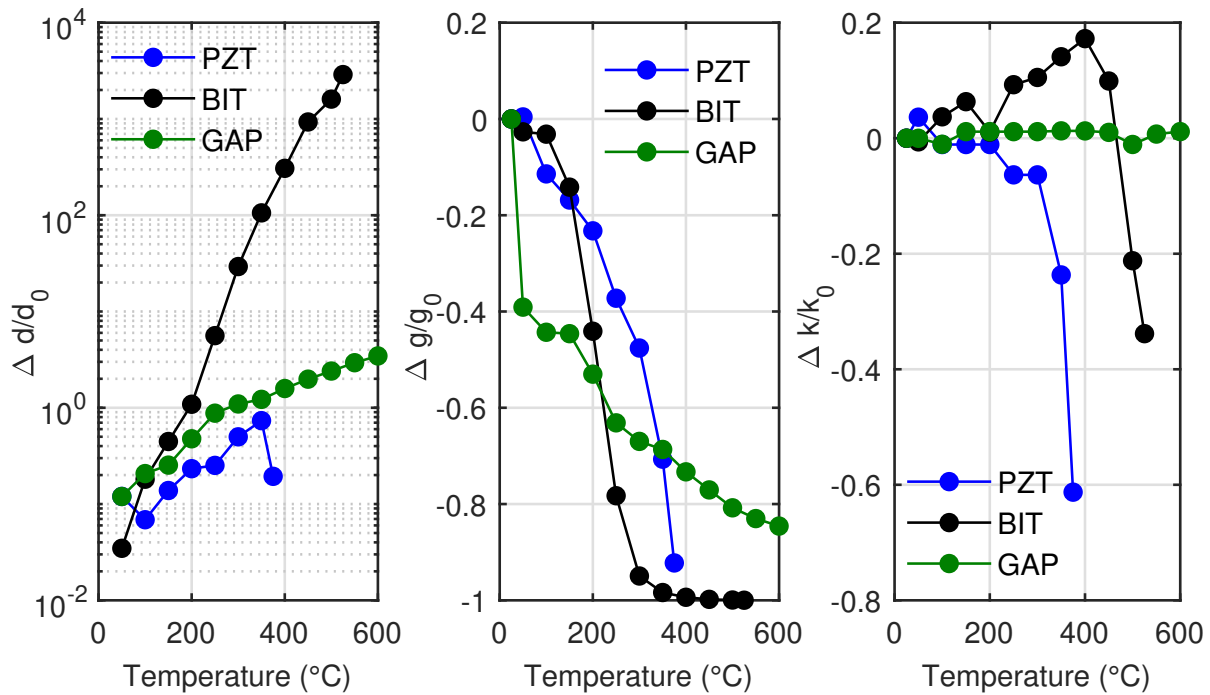
FIGURE 7.18: Piezoelectric material properties d, g and k as a function of temperature for the candidate materials.

The value of g_{15} for PZT reduced by 70% from 37.5 mVm/N to 11 mVm/N at 350°C. Compared to PZT-5A, g_{15} for HPZ510 showed a sharper decline of 100% from 31.2 mVm/N to 0.5 mVm/N in the same temperature range. For $GaPO_4$, g_{26} decreased more gradually from 60 mVm/N to 10 mVm/N at 600°C. It should be noted that the values of g are less temperature dependent than those of d, as d is closely related to the dielectric permittivity. By analysing the temperature-dependent coefficients g and d of all materials, it can be observed that they become better transmitters but significantly worse receivers as the temperature increases. Therefore, as a transducer, its performance will degrade.

The variation in the coupling factor k_{15} for both PZT and HPZ510 displayed linear behaviour with increasing temperature as they approached their respective T_c, after which they decreased sharply. For PZT, k_{15} decreased by 10% from 0.69 to 0.51 at 350°C. HPZ510 increased linearly from 0.35 at 25°C to 0.41 at 450°C, approximately increasing 18%. The temperature coefficients of k_{31} reported in the HPZ510 datasheet are 0.18 at 25°C and 0.20 at 400°C. The coupling factor k_{26} of $GaPO_4$ is exceptionally consistent, showing less than 2% variation up to 600°C.

7.4.7 Thermal Stability Analysis

The ageing response of HPZ510 and $GaPO_4$ was evaluated at 400°C and 600°C, respectively, for 1000 hours. The variation of their dielectric (K_{11}^T), elastic (S_{jj}^D) and piezoelectric (d_{ij}, g_{ij}, k_{ij}) properties over time at temperature is shown in Figure 7.19. Variations P/P_0 are plotted as a function of time, where P_0 is the property measured at the target temperature during the start of the ageing experiment, and P_t is the property measured at the target temperature at time t.

For HPZ510, the three piezoelectric coefficients d_{15}, g_{15} and k_{15} and the elastic constant S_{55}^D show a gradual decline during the initial 250 hours at 400°C. Properties degrade by approximately 20% from their initial values at 400°C. After this gradual decline, a stable response was demonstrated for the remaining 750 hours.
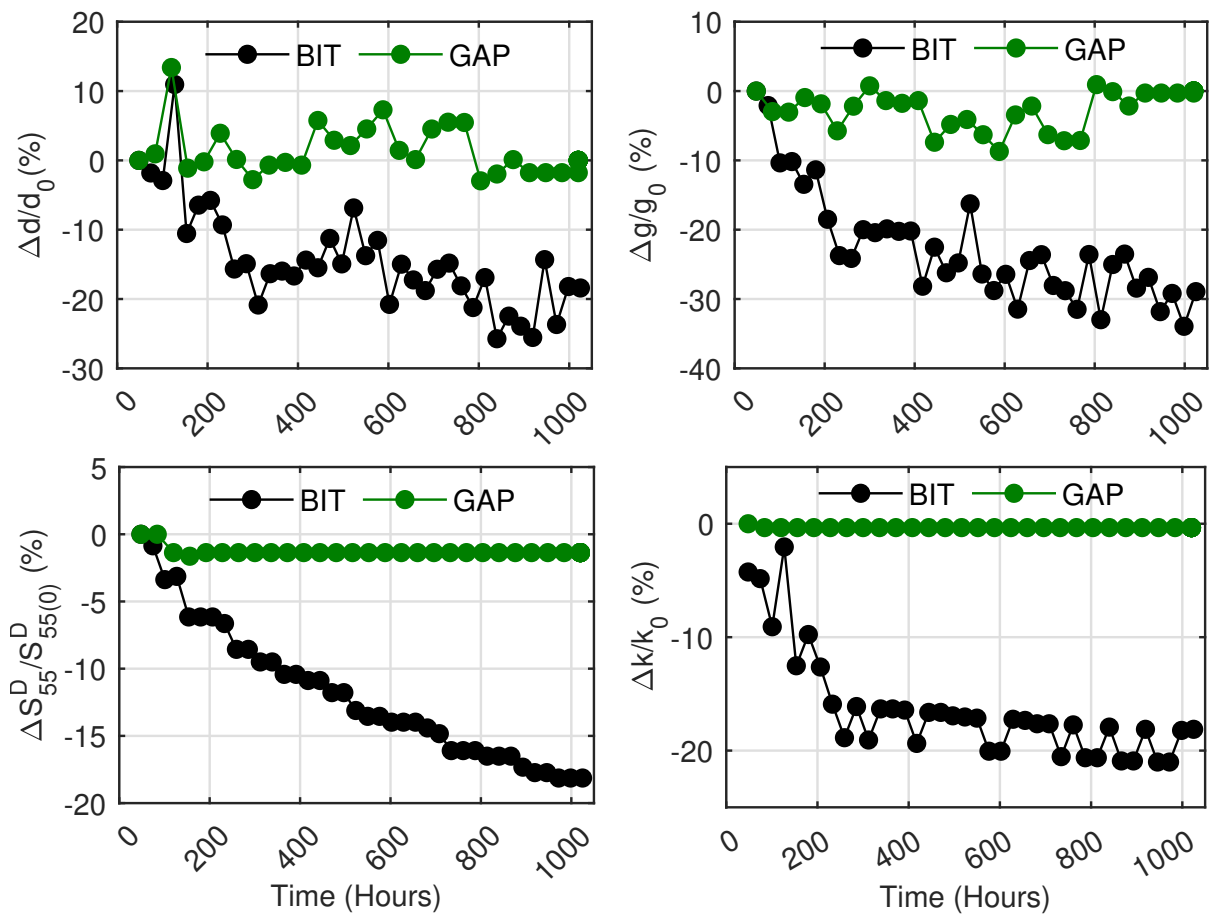
FIGURE 7.19: Comparison of piezoelectric material FOMs of BIT at 400°C and $GaPO_4$ at 600°C over a period of 1000 hours.

On the other hand, $GaPO_4$ showed a more consistent response from the beginning, with variations less than 10% in d and g and less than 2% in its values S_{55}^D and k. Compared to the elastic and piezoelectric properties, the temperature sensitivity of

the dielectric properties is much higher. Therefore, the responses of K^T for both materials varied by around 20% over time and were possibly associated with minor temperature variations in the furnace due to temperature control.

7.5 Summary

This chapter addressed the selection and characterisation of HT piezoelectric materials for their use in the design of HT-UGW transducers. Commercially available piezoelectric materials were reviewed for target operating temperatures of 350°C and 600°C. HPZ510, a modified Bismuth Titanate ($m - Bi_4Ti_3O_{12}$) and Gallium Phosphate ($GaPO_4$) materials were chosen based on their TS-mode FOMs and recommended operating temperatures. These materials were used to fabricate PWAS with appropriate polarisation or crystal cut to obtain the desired TS-mode operation. Their TS-mode performance was verified by characterising their dielectric, elastic, and piezoelectric properties as a function of temperature using EMIS.

Characterised material properties were used to model $m - Bi_4Ti_3O_{12}$ and $GaPO_4$ piezoelectric plates using the multiphysics FEA approach developed in Chapter 4. The model was able to simulate the high-temperature response of both materials, which was demonstrated by comparing it with the measured frequency and the electromechanical response. The model was also used to evaluate the vibration response of the Y cut plate $GaPO_4$ and the bonded wear plate and the simulated vibration frequency response matched well with the measurements using SLDV.

The high temperature TS-mode FOMs of HPZ510 and $GaPO_4$ demonstrated their suitability for use in HT-UGW transducers for application at temperatures up to 350°C and 600°C, respectively. Their performance for SHM application was verified through a thermal ageing experiment that was carried out for a period of 1000 hours. HPZ510 showed an initial settlement period of 250 hours, after which performance was stable. $GaPO_4$ demonstrated an extremely stable high temperature response up to 600°C, although FOM suggested a much weaker ultrasonic performance compared to PZT-5A and HPZ510. The experimental and numerical characterisation verified the HPZ510 and $GaPO_4$ materials for the design of HT-UGW transducers for SHM application at 350°C and 600°C, respectively.

Chapter 8

Design, Development and Characterisation of HT-PUT

8.1 Introduction

This chapter presents the design, development, and characterisation of HT-UGW transducers for SHM application at 350°C and 600°C. The design of the transducer is based on the improvements made to the Teletest transducer and the hypothesis formulated from the numerical FEA studies in Chapter 5. The materials $HPZ510$ and $GaPO_4$, which are characterised and validated for continuous operation at 350°C and 600°C in Chapter 7 are used as active piezoelectric elements. Passive transducer materials for the transducer backing and face plate are selected to ensure compatibility with these piezoelectric materials.

A methodology for the assembly of the transducer is devised based on the adhesive bonding of the active and passive layers of the transducer. This included the selection of adhesives based on their electrical characteristics, suitability for continuous operation at the target operational temperatures, and compatibility with the transducer layers.

The prototype PUTs are manufactured using $PZT-5A$, $HPZ510$, and $GaPO_4$ and their ultrasonic performance is characterised using the methodology established in Chapter 4. Ultrasonic characteristics in the time, frequency, and space domains are used to assess their mode purity and SNR for UGW application. The characterisation is extended to high temperatures and over extended periods to qualify their performance for HT-SHM application.

8.1.1 Motivation

The transduction of directional axisymmetric UGW in pipes requires an array of PUT. All PUT within the array should have a comparable performance to achieve high SNR and wavemode purity. Furthermore, for the HT-SHM application in HTPs, transducers must maintain their ultrasonic performance in the desired temperature range and over time. PUT have complex multilayered constructions, and each layer or its interfaces can influence ultrasonic performance, making them susceptible to degradation at high temperatures.

Degradation in ultrasonic performance can be associated with a variation in signal amplitude or frequency response at high temperatures, both of which affect their UGW performance by limiting the inspection range or sensitivity to defect detection. Changes in the transducer frequency response are generally due to degradation of the bonding or changes in the stiffness of the materials. Numerical and experimental studies have shown that even partial debonding of the transducer layers can result in excessive ringing due to reduced damping [198]. This ringing can distort ultrasonic signals by adding noise and thus affect the sensitivity for defect detection. Thermal stresses caused by differential thermal expansion between transducer layers can also result in variations in their ultrasonic response [167]. Excess differential thermal expansion can even cause permanent damage, such as a crack-type defect in the transducer layers. Such a failure can result in the diffraction of ultrasonic waves and significantly affect the transducer performance.

Transducer performance can also drift or worsen when exposed to high temperatures over time as a result of thermal ageing and fatigue caused by cyclic thermal stresses. This can affect their performance for HT-SHM applications. These problems can be minimised by selecting appropriate temperature resistant transducer materials with closely matched CTEs and suitable assembly techniques [267]. However, the selection and validation of piezoelectric materials in Chapter 7 minimised the risk of ultrasonic degradation.

It is critical for the design and assembly of the transducer to use compatible materials and their manufacturing process to achieve consistent performance. To validate their design for the HT-SHM application, it is crucial to characterise their electromechanical and ultrasonic response and any variation with long-term exposure to high temperature.

8.1.2 Aims and Objectives

This chapter aims to design and validate HT-UGW transducers for SHM application at 350°C and 600°C through numerical and experimental characterisation. The manufacturing of prototype transducers required the selection of adhesive materials and the development of an assembly procedure to provide a reliable electrical and mechanical connection between the transducer layers. The characterisation of piezoelectric materials $HPZ510$ and $GaPO_4$ in Chapter 7 displayed a suitable and stable high-temperature performance over time. This chapter focuses on the effects of temperature on the complete transducer, including passive transducer layers and their bonding.

The key objectives of this study are:

(1) Design and numerical analysis of HT-PUT using $HPZ510$ and $GaPO_4$ piezoelectric materials and hypothesis formulated in Chapter 5.

(2) Selection of compatible HT adhesives for the construction of PUT.

(3) Development of an assembly procedure for the manufacture of HT-PUT and the construction of prototype transducers.

(4) Verification of the assembly procedure by assessing the performance variation among a batch of manufactured PUT prototypes.

(5) Experimental ultrasonic characterisation of manufactured HT-PUT prototypes following the methodology established in Chapter 4:

    (a) UGW transmission and reception performance (signal amplitude and SNR) for torsional wave mode in UGW frequency range (20-120 kHz).

    (b) Thermal response of the transducer by evaluating performance FOMs at increasing temperatures up to the target temperature.

    (c) Examination of the reliability of the transducer at the target temperature for an extended period to examine its suitability for SHM application.

8.2 Design and FEA of HT-UGW Transducer

8.2.1 Transducer design with parallel electrode configuration

The findings of Chapter 5 highlighted that the design of the piezoelectric plate with a parallel electrode and polarisation along the width can significantly increase the SNR of the transducer by avoiding unwanted out-of-plane vibration caused by wraparound electrodes. This study aims to realise a transducer design with a parallel electrode piezoelectric plate and redesigned the wear plate and the backing layer to facilitate the electrical connections. The wear plate was designed to be longer than the piezoelectric plate and metallised on the surface in contact with the piezoelectric plate. This allowed the attachment of the wire to the wear plate to provide electrical continuity with the electrode of the piezoelectric plate. The backing layer of the transducer was designed to accommodate the piezoelectric element, the wear plate, and the electrical wiring, as illustrated in the transducer cross section in Figure 8.1.
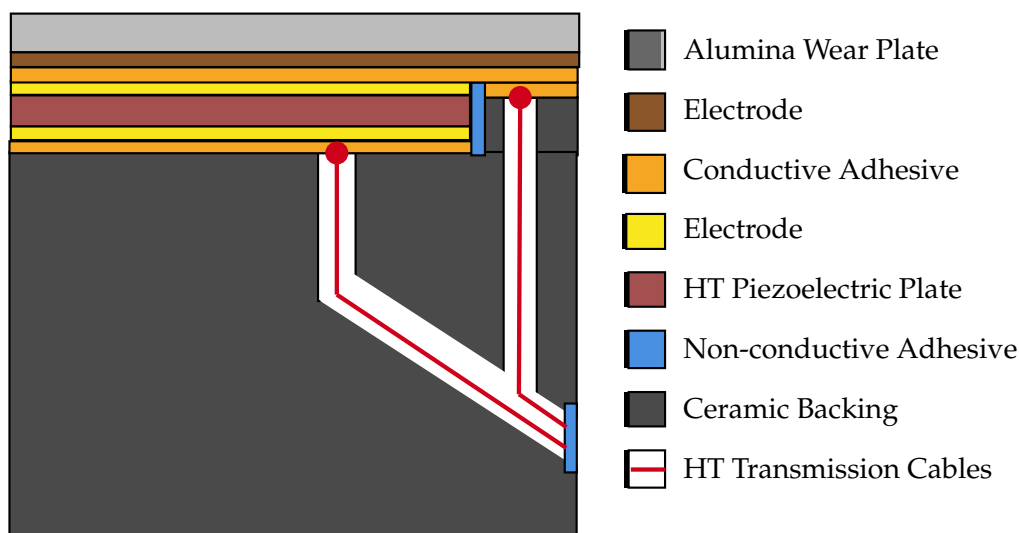
FIGURE 8.1: Cross-sectional schematic of the proposed HT-UGW transducer design showing the active piezoelectric plate with parallel electrodes and passive transducer layers.

The piezoelectric plates were designed with HPZ510 and $GaPO_4$ materials qualified in Chapter 7 and used for HT-UGW transducer variants for operation at 350°C and 600°C, respectively. Other design parameters considered for the piezoelectric plate include the dimensions of the plate, the electrode configuration, and the direction of polarisation. For the wear plate and backing layer, the selection of material compatible with these piezoelectric materials is described in Section 8.2.2. The physical parameters of these passive layers are governed by the dimensions of the piezoelectric plate and are described in Section 8.3.1.

8.2.2 Material Selection

For the design of an HT-UGW transducer, only materials with an operational temperature limit much higher than the hot standby temperature requirement of 350°C and 600°C were considered. Material selection for these transducer components requires careful consideration of their CTEs to ensure compatibility with the chosen piezoelectric materials $HPZ510$ and $GaPO_4$.

Selection of wear plate material

The transducer wear plate will be in direct contact with the pipe surface and is therefore required to be resistant to corrosion and wear. The material must also be mechanically stable under the dry coupling force of the transducer, resulting in pressures of around 5 MPa with 200N of normal force. The mechanical stability of the wear plate depends on the hardness of the material, the surface roughness, and the hardness of the material in contact. It is also preferable that the wear plate be electrically non-conductive to isolate the piezoelectric materials from the metallic pipe substrate, and it reduces electrical cross-talk between transducers of an array. With this criterion, the ceramic materials were the most suitable for the wear plate because of their high dielectric strength, thermal stability, and resistance to wear and corrosion. A list of potential ceramic candidates and their CTE and elastic properties are listed in Table 8.1. Aluminium oxide (Al_2O_3) was chosen as its CTE of 8.4 ppm/°C matched closely with that of HPZ510 (9 ppm/°C) and $GaPO_4$ (12.3 ppm/°C) piezoelectric materials.

Selection of backing layer material

The function of the backing layer is to support the piezoceramic structure and to act as a buffer when a normal load is applied to the dry coupling of the transducer. The CTE of the backing material should also be closely matched to the CTE of the piezoelectric plate. Materials with a high Young's modulus are preferred to withstand the load required for transducer coupling and any thermal stresses caused by mismatching CTE. The backing layer should also be able to suppress any out-of-plane vibration of the piezoceramic seen in Chapter 7. For high-frequency operation, materials with high density are generally used as backing to reduce damping and improve axial resolution. However, for the given non-resonant transducer design with less efficient high-temperature piezoelectric materials, it is desirable to maximise their ultrasonic output. The machinability of the material was also considered, as the material will need to be machined to house the wiring, piezoelectric wafer and wear plate.

Ceramics have high Young's moduli and can withstand the high stresses caused by CTE mismatch. Several ceramic materials met these requirements and their physical and thermal properties are given in Table 8.1. These candidate ceramic materials possess a spread of densities. Aluminium Nitride offers high thermal conductivity since it is commonly used as an electronic substrate material. Tungsten carbide is an incredibly tough ceramic and its machining requires specialist manufacturing processes. Aluminium oxide appears to be a good choice of material; however, thick layers of Al_2O_3 (greater than a few millimetres) can only be manufactured using the sintering process. This is due to the high modulus of Al_2O_3, which poses manufacturing challenges for the machining features on the substrate. Zirconium dioxide is a promising candidate material as it has a similar CTE and a density relatively close to that of steel.

TABLE 8.1: Properties of candidate ceramic backing and wear plate materials

Material	T_{max} (°C)	CTE (ppm/°C)	ρ (kg/m^3)	Z (MRayl)	E (GPa)	ν (-)	Rank
MACOR	800	9-11.2	2520	-	66.9	0.29	1
Aluminium Oxide	2072	8.4	3970	26.28	390	0.235	2
Beryllium Oxide	2507	8	2850	24.4[1]	345	0.26	4
Zirconium Dioxide	2715	13.5	5800	36.4[2]	150	0.27	3
Tungsten Carbide	2870	6	15800	58.44	550	0.24	5
Aluminium Nitride	2200	5.3	3260	36.7	308	0.28	6

[1] Calculated using the bulk modulus of 210 GPa.
[2] Calculated using the bulk modulus of 222 GPa and the density of 6000 kgm^{-3}.

Macor, on the other hand, is a machined glass ceramic and remains continuously stable at 800°C. Macor is composed of approximately 55% fluorophlogopite mica and 45% borosilicate glass. It is highly rigid, has low thermal conductivity, and is also an electrical insulator. The CTE of Macor is 9.3 ppm/°C up to 300°C and 11.2 ppm/°C up to 600°C [268]. Macor's CTE are compatible with HPZ510 (9 ppm /°C) and $GaPO_4$ (12.3 ppm/°C), making it an excellent ceramic alternative to stainless steel for the backing layer.

Selection of adhesives

The selection of suitable adhesives for transducer bonding is critical to ensure the reliable performance of the transducer over EOC. The adhesive bond must be elastic to allow the piezoelectric element to vibrate and be compatible CTE with those of the selected piezoelectric and passive materials. Their CTE should also be compatible with the selected piezoelectric and passive materials. The temperature and pressure required for the adhesive application should also be considered, as too high a temperature or pressure could damage the transducer layers. The target operational temperatures excluded most epoxy-based adhesive materials, as they lose thermal stability at glass transition temperatures less than 200°C. A list of suitable commercially available candidate adhesive materials is given in Table 8.2. This includes their recommended maximum operating temperature, number of components, thermal conductivity, electrical resistivity, CTEs, and curing regime.

TABLE 8.2: Properties of candidate adhesive materials for transducer assembly.

Adhesive	T_r (°C)	Base	CTE (ppm/°C)	Curing (°C, h)
Conductive Materials				
Duralco 124	343	Silver	-	-
Duralco 952	1093	Ni	4	-
Duralco 954	1093	Al/SS	10	-
Pyroduct 597A	927	Silver	17.28	25, 2 & 200, 2
Resbond 931C	1370	Graphite	7.4	-
Non-conductive Materials				
Cotronics 989	1650	Alumina	8.1	150, 4
Duralco 4703	343	-	39	-
Cermabond 571	1760	Magnesium Oxide	12.6	200, 2
Cotronics 7030	982	SiO_2	13.5	150, 4

One-part adhesives were preferred over two-component adhesives to achieve a more straightforward and repeatable transducer assembly procedure. Mixing of two-part adhesives can introduce variability in batches of transducers unless precision dispensing systems and curing in a vacuum chamber are used. Otherwise, it may lead to the introduction of trapped air, which has a detrimental effect on the ultrasonic performance of the transducer, as indicated in previous studies [269].

High-temperature epoxies such as Duralco 124 and Duralco 4703 have a recommended maximum temperature close to the desired target temperature of 350°C for the HPZ510 transducer variant. The remaining candidate adhesive

materials are ceramic-based or metal-based one-component adhesives with a maximum operational temperature above 600°C, the target temperature for the $GaPO_4$ transducer. The same conductive and nonconductive adhesives for the HPZ510 and $GaPO_4$ HT-PUT transducer assembly were selected for simplicity. This allowed for a similar transducer fabrication procedure whereby batches of both transducers could be manufactured together to minimise process variability and facilitate consistent performance comparison. After considering CTE for material compatibility, Resbond 931C and Cotronics 989 adhesives were selected as conductive and non-conductive adhesive materials for the fabrication of HPZ510 and $GaPO_4$ HT-UGW transducers.

8.2.3 Transducer design analysis

An eigenfrequency analysis of the Macor backing block was performed to assess the natural frequencies that could limit the electromechanical performance of the transducer. The first five resonances within the backing and their mode shapes are shown in Figure 8.2. The resonances were outside the desired operating range for UGW and in the 189-280kHz frequency range. The resonances were also compared with those of a stainless steel backing of the same design, and the eigenfrequencies are compared in Table 8.3.
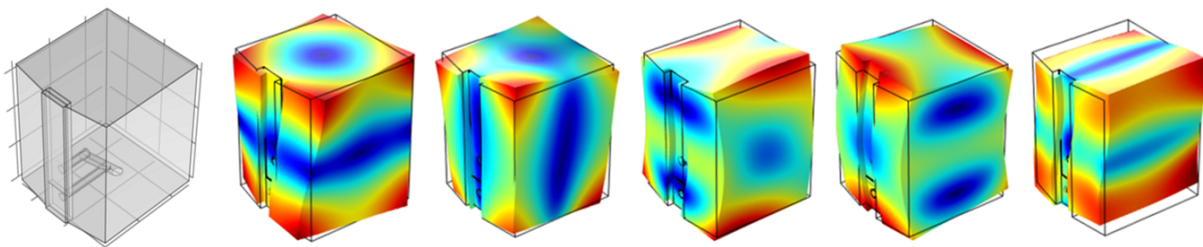
FIGURE 8.2: Vibrational response of the Macor backing layer at eigenfrequencies.

TABLE 8.3: Comparison of eigenfrequencies of Macor and Steel backing layer.

Mode	1	2	3	4	5
SS	107kHz	141kHz	146kHz	154kHz	158kHz
Macor	189kHz	250kHz	252kHz	269kHz	280kHz

An electromechanical frequency analysis was performed in the 20-120kHz range to assess transducer performance. Simulations were carried out for the design of the transducer with PZT-5A, HPZ510, and $GaPO_4$ materials. A comparison of the in-plane shear displacement, capacitance, and impedance amplitude as a function of operating

frequency is shown in Figure 8.3. The shear displacement and charge of HPZ510 and
$GaPO_4$ were orders of magnitude lower than those of PZT-5A, in line with their lower
charge coefficient and dielectric properties as characterised in Chapter 7. The absence
of resonance in the impedance response confirmed their non-resonant behaviour in the
operating frequency range.
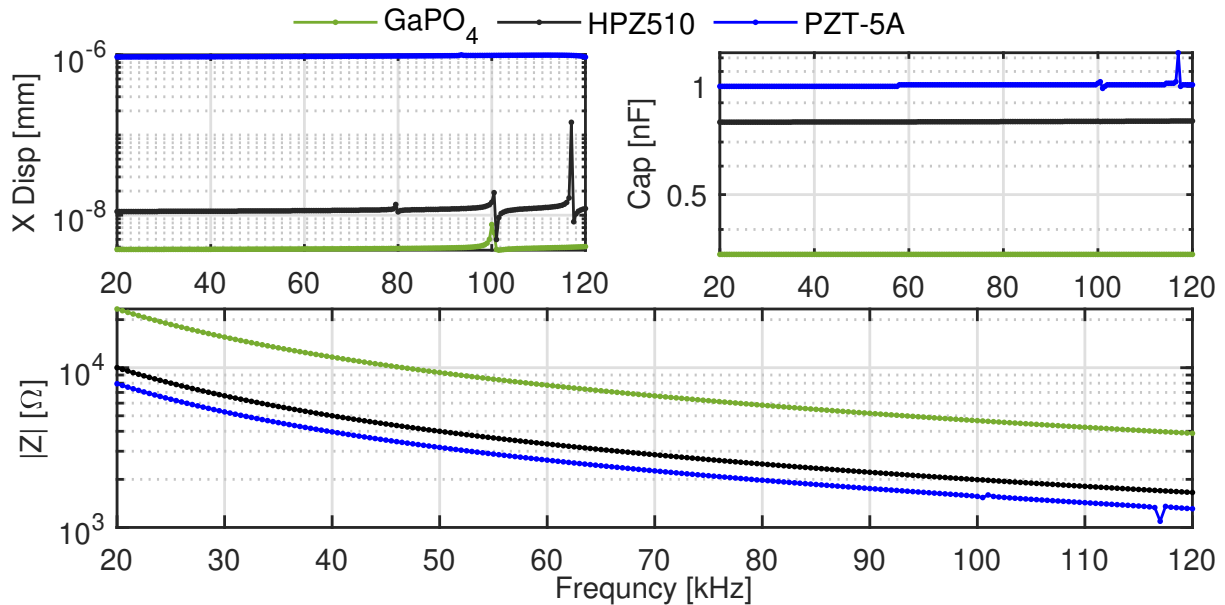
FIGURE 8.3: Electromechanical response of the proposed transducer design with
width polarised parallel electrode piezoelectic plates of PZT-5A, HPZ510 and
$GaPO_4$ materials.

A time domain analysis was performed by applying a five-cycle toneburst excitation of
150V signal amplitude and centre frequency of 70kHz. The average displacement of the
wear plate with the transducer with $GaPO_4$ is compared with that of the wraparound
electrode to assess the improvement with the proposed parallel electrode configuration.
The simulated in-plane shear and out-of-plane displacements as a result of the applied
electrical signal are shown in Figure 8.4. The simulated results are also compared with
those of the optimised PZT-5A transducer in Chapter 5 as a reference.
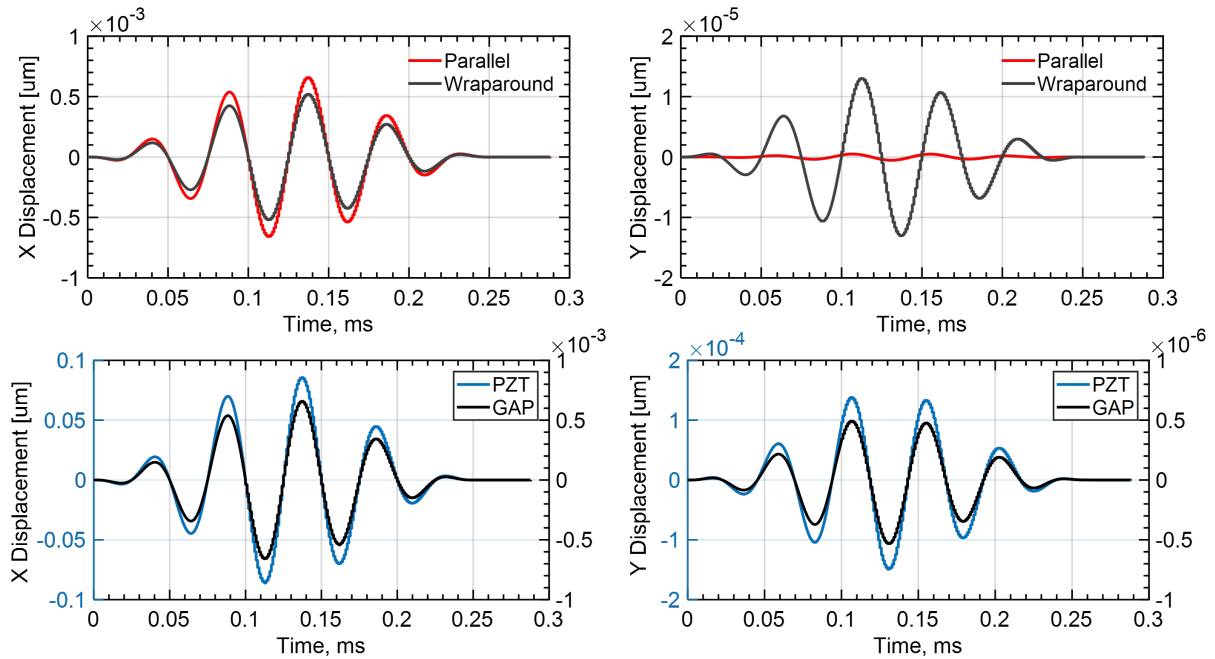
FIGURE 8.4: Simulated ultrasonic output showing in-plane (X) and out-of-plane (Y) displacement from the (top) $GaPO_4$ transducer with parallel and wraparound electrode configuration and (bottom) their comparison with PZT transducer.

The charge accumulated with $GaPO_4$ of the parallel and wraparound electrode was $2.1pC$ and $1.65pC$. The ratio of displacements in the plane to out of the plane suggests a $15dB$ improvement with the proposed electrode configuration, which is of similar order as seen with optimisation studies with the PZT-5A material in Chapter 5. However, the displacement fields generated by $GaPO_4$ in the in-plane direction were significantly less than those of the PZT-5A transducer by a factor of 100 and 300, that is, 40 and 50dB, respectively. The decrease in electrical displacement is associated with the lower piezoelectric properties and the higher electromechanical impedance of $GaPO_4$. This suggests that a similar order of gain will be required in the pulser receiver to achieve the same ultrasonic performance.

8.3 Construction of HT-PUT Prototypes

This section presents the construction of prototype HT-UGW transducers. Two variants of the transducer design are built using HPZ510 and $GaPO_4$ piezoelectric materials for operation at 350°C and 600°C.

8.3.1 Manufacturing of transducer components

The piezoelectric materials HPZ510 and $GaPO_4$ characterised in Chapter 7 were used as active elements. PWAS with parallel electrode configuration for both materials were acquired from their suppliers. The piezoelectric elements and all passive components used for the construction of the prototype transducers are shown in Figure 8.5.
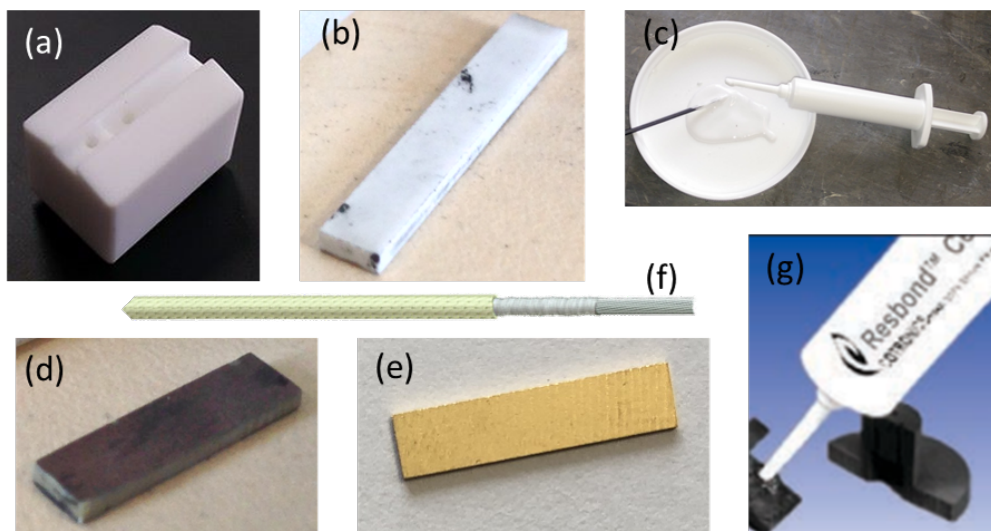
FIGURE 8.5: Components manufactured and used for transducer assembly: (a) MACOR backing block, (b) Alumina wear plate, (c) Resbond 989F non-conductive adhesive, (d) Gallium Phosphate piezoelectric plate with platinum electrode, (e) Bismuth Titanate piezoelectric plate with Gold electrode, (f) Glass fibre insulated pure nickel wire, and (g) Resbond 931C conductive adhesive.

The transducer wear plates were manufactured using 96% Al_2O_3 by Almath Crucibles Ltd [270]. Wear plates were manufactured as rectangular slabs of nominal dimensions 15*mm* x 3*mm* x 0.5*mm*. They were metallized on a 15*mm* x 3*mm* surface to serve as an electrode once attached to the piezoelectric element. The metallisation of the Alumina plate was achieved by applying a titanium adhesion layer followed by a sputter coating of a gold electrode layer.

The Macor transducer backing layer was manufactured by Precision Ceramics Ltd. The backing layer was made as a 16.5*mm* x 13*mm* x 12.5*mm* block. The block was machined with two through holes to provide access for routing the high-temperature cables for

live and ground electrical connections to the piezoelectric plate. The top surface of the block was machined with a recess to hold the piezo-wear plate sub-assembly. The recess was designed with a width of 3.5*mm* to allow enough clearance to account for the manufacturing tolerance of the piezoelectric plate and the backing block.

A pure nickel wire braided with glass fibre by Thermocoax [271] with a maximum rated temperature of 700°C was selected for ground and live connections to the piezoelectric element. It offers excellent resistance to oxidation and is therefore suitable for long-term use at high temperatures. This high-temperature cable was obtained as a 20 m roll with a cable diameter of 1 mm and a diameter of 0.2 mm nickel conductor. The diameter of the cable was chosen to allow movement inside the MACOR backing through holes.

A complete list of components required for the construction of prototype transducers is given in Table 8.4. The table also indicates the material used to fabricate these transducer components, their maximum recommended operating temperature, key design features, and their supplier.

TABLE 8.4: Components used for manufacturing of transducer prototypes.

Transducer Component	T_{max} (°C)	Material	Design	Supplier
Wear Plate	1650	96% Al_2O_3	15mm x 3mm x 0.5mm plate with Au Coating on one 13mm x 3mm face	Almath Crucibles Ltd
Conductive Adhesive	1370	Resbond 931C	Graphite based adhesive	
Piezoelectric Plate	350	HPZ510	13mm x 3mm x 0.5mm plate polarised along 3mm with parallel Au electrodes	Ionix Advanced Technologies Ltd
Piezoelectric Plate	600	$GaPO_4$	13mm x 3mm x 0.5mm Y-cut (YXl)0°plate with parallel Pt electrodes	Piezocryst Advanced Sensorics Gmbh
Non-conductive Adhesive	1650	Resbond 989F	Alumina based adhesive	
Backing Block	800	MACOR	Machined 16.5mm x 13mm x 12.5mm block with recess and access holes	Precision Ceramics Ltd.
Wiring	700	Ni	1 mm diameter cable and 0.2 mm conductor diameter	Thermocoax

8.3.2 Transducer Fabrication Procedure

The fabricated transducer components were assembled to manufacture the prototype HT-UGW transducers. A transducer assembly procedure was devised for the selected adhesives and their required surface preparation, adhesive application, and curing process. The sequence of assembly steps was intended to minimise fabrication time and allow for early identification of failures. The transducer assembly procedure is shown in Figure 8.6.
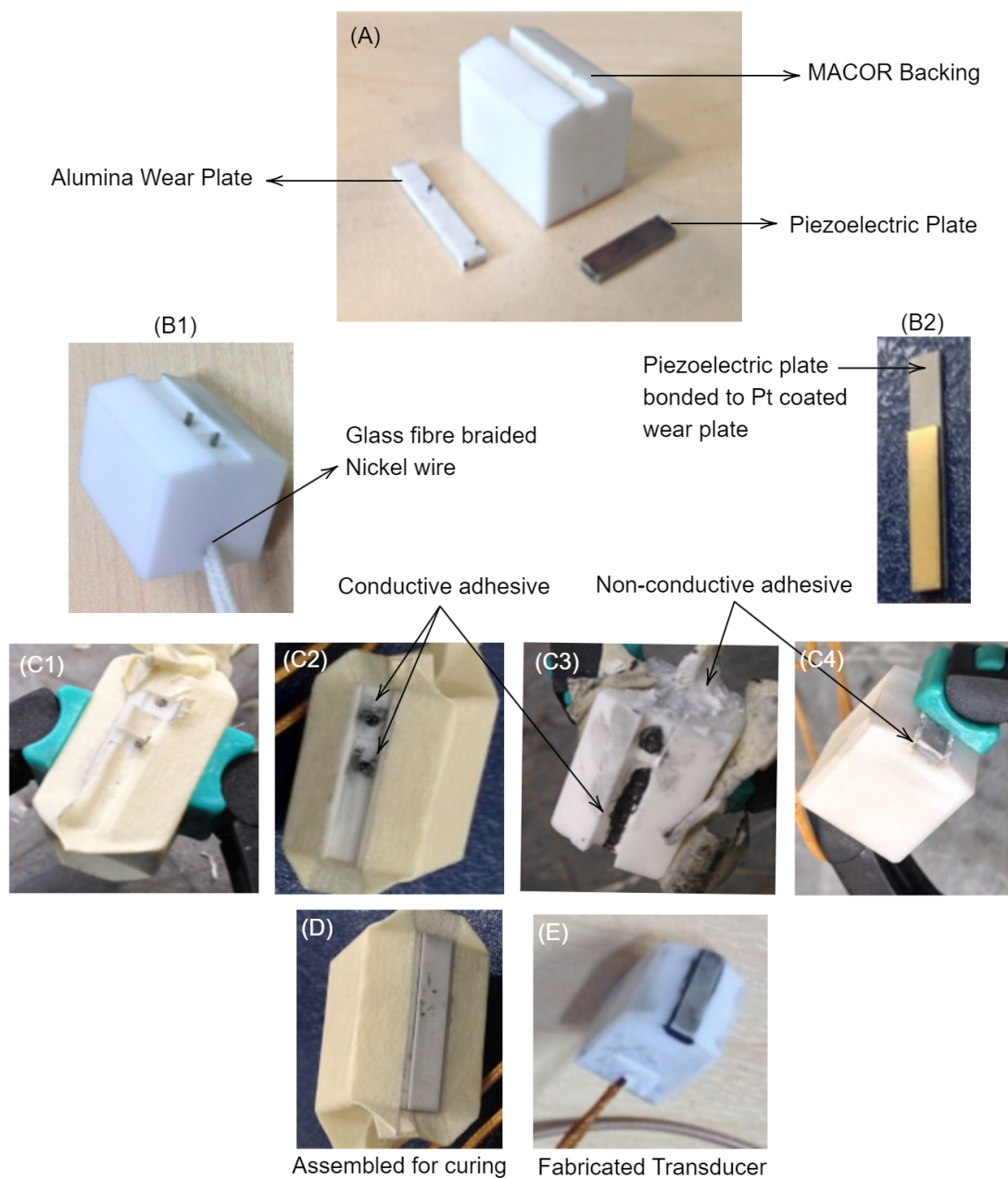
FIGURE 8.6: Fabrication of HT-UGW transducer prototypes showing the assembly of transducer layers and electrical connections.

The first bonding step was to attach the Piezoelectric plate to the Alumina wear plate using the conductive Resbond 931C adhesive. Surface preparation was carried out for both rectangular plates by cleaning them with acetone. Subsequently, a thin bond line thickness was achieved by applying a controlled amount of adhesive using a syringe. Once the piezoelectric and wear plates were joined, they were carefully aligned and pressed against each other using a clamp while the adhesive was cured at room temperature. This formed the piezo-wear plate sub-assembly. Visual inspection and electrical continuity tests were performed once the adhesive between the piezo element and the wear plate had cured. This test ensured that the conductive adhesive did not flow through the sides and made electrical contact between the two electrodes of the piezo element. If that was the case, excess adhesive from the edges was removed using super-fine grade sandpaper (FEPA P800). Extra care was taken during this step to avoid damaging the bonded subassembly.

Two pure nickel wires braided with glass fibre, each $15cm$ in length, were used for ground and live connections to the piezoelectric element. These two wires were fed through the side of the Macor backing to the top surface, where the insulation $20mm$ was stripped. The wire exit holes were filled with non-conductive adhesive and cured at room temperature for a 24-hour period. The excess wires were cut off once the adhesive was cured, and the top surface was flushed flat using fine sandpaper. The conductive adhesive was applied to the slot on top of the Macor block. The piezo-wear plate sub-assembly was placed in this slot while ensuring flat-level fitting. Next, the two sub-assemblies were gently pressed against each other using a clamp. Finally, the piezo-wear plate assembly edges were filled with non-conductive adhesive to seal and prevent electrical connection between the two electrodes during the curing process. The transducer assembly was completed in two steps, with a curing cycle following each step. A total of 48 hours were needed to complete the assembly procedure for a batch of transducers.

8.3.3 Manufactured Transducer Prototypes

A batch of 20 transducers was manufactured to verify the assembly procedure and assess the variance in transducer performance of the prototypes. This batch of transducers was manufactured using a PZT-5A PWAS polarised along the width direction of the same dimensions as HPZ510 and $GaPO_4$. The availability of PZT-5A PWAS allowed for a large number of prototype builds. Their ultrasonic performance was characterised using the methodology described in Chapter 4. The variability in dimensions of the piezoelectric plate and the amplitude of the ultrasonic signal and

SNR in transmission, reception and pulse echo mode at a single excitation frequency of 80kHz are shown in Figure 8.7.
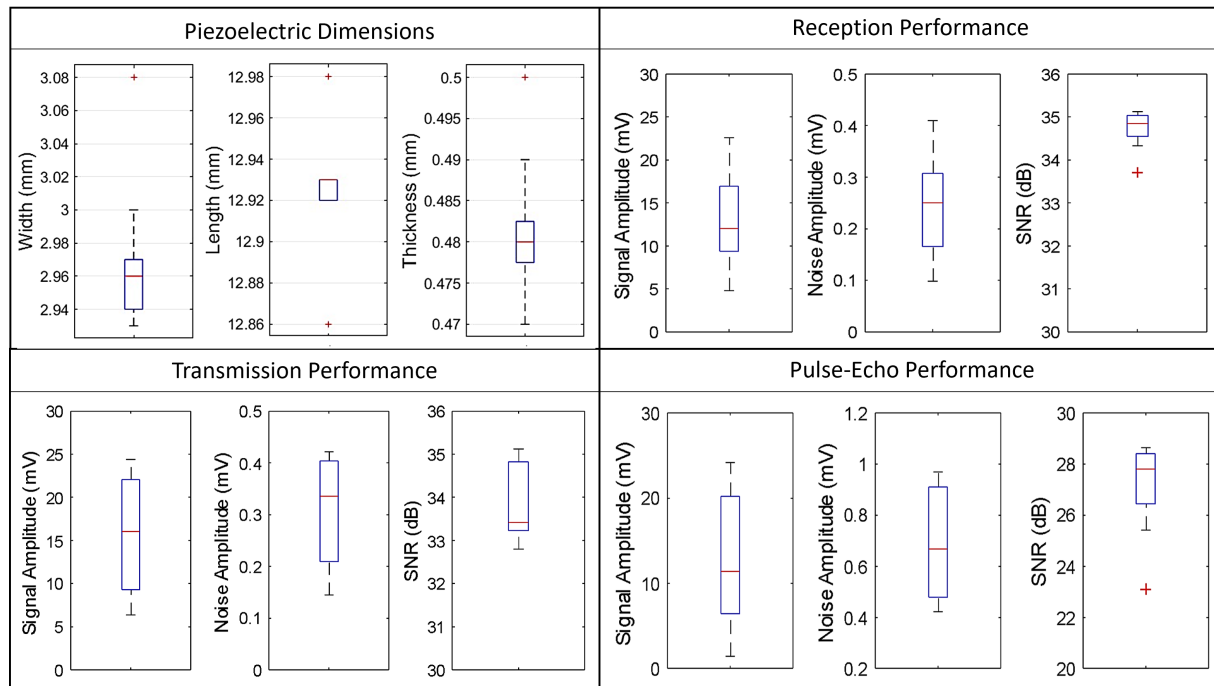
FIGURE 8.7: Variability in the dimensions of the piezoelectric plates and corresponding variance in the ultrasonic reception, transmission and pulse-echo performance of the manufactured transducer prototypes.

The peak-to-peak amplitude of the Tx, Rx and PE signals had an average of 16 mV, 11 mV, and 12 mV, with a variation between transducers of around 50%. These signal amplitudes were translated into SNR of $33dB$, $34.5dB$, and $28dB$, respectively. The variation in SNR was less than $1dB$, indicating consistency in the ultrasonic performance of the transducer with respect to the frequency response. The variation in signal amplitude could be due to variability in the coupling forces applied between measurements, tolerances within the components of the transducer, or variations in the manual assembly process.

Five HT-UGW transducer prototypes using HPZ510 and $GaPO_4$ piezoelectric materials for high-temperature characterisation. The performance of the manufactured PZT-5A variant is compared with the HPZ510 and $GaPO_4$ transducers for the like-for-like evaluation of transducers that used the same transducer components and assembly procedure in addition to the piezoelectric material. Furthermore, the PZT-5A variant used a width-polarised parallel electrode PWAS that according to the analysis in Chapter 5 reduced unwanted out-of-plane vibration. The ultrasonic response of the PZT-5A variant is also compared with the Teletest transducer described in Chapter 2 to verify this hypothesis.

8.4 Transducer Ultrasonic Performance Characterisation

8.4.1 Transducer Test Fixture

A custom transducer holder and dry coupling fixture was designed to test up to five transducers simultaneously inside the furnace by accommodating the bar waveguide and providing a dry coupling force. The jig is shown in Figure 8.8 and was built with A2 Grade 18/8 Stainless Steel parts and allowed operation up to 600°C. The jig consisted of a stainless steel transducer holder with machined slots to accommodate five transducers on one side and compression springs on the other side. Each transducer was supported by a spring to provide a normal dry coupling force. Another stainless steel retainer block with machined slots for compression springs was placed on the back of the transducer holder. Retainer blocks were positioned using two 5*mm* diameter alignment pins that passed through them at either end. The depth of the spring slots was designed so that a 10*mm* gap separated the two blocks. Two clamping steel plates enclosed the transducer holder and the bar waveguide. Two screws are applied to compress the springs in the transducer holder, providing the dry coupling force to the transducers under test.
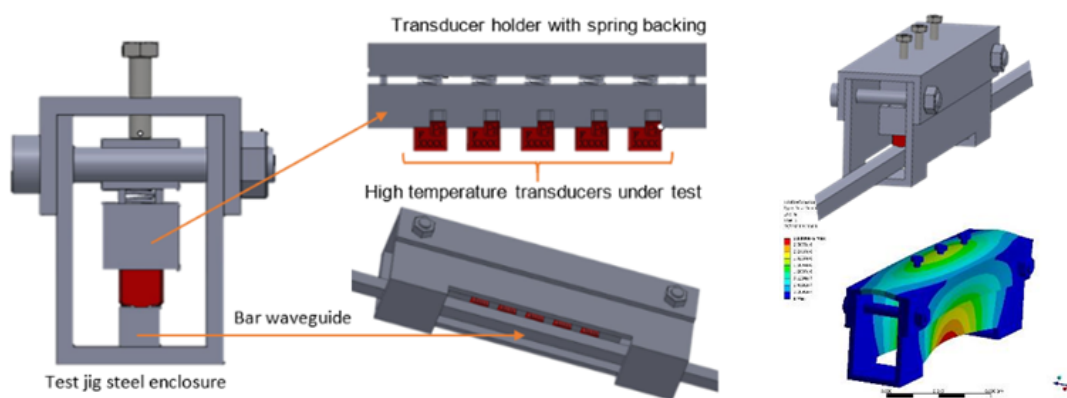
FIGURE 8.8: Test fixture for HT-UGW measurements of multiple transducers.

Previous studies on the coupling force requirement for PUT with a similar contact area have shown that a normal dry coupling load of 150N is sufficient to achieve adequate acoustic coupling between the transducer and the waveguide [246]. The spring rate of 20 N/mm and the separation of 10*mm* between the transducer holder and the spring retainer blocks allowed visual calibration. Once the two retainer blocks were in contact, the springs were compressed by 10*mm*, providing the required coupling force of 200N to each transducer under test. The counterforce on the steel plates of the jig would be 1000N when the five transducers were spring loaded with a force of 200N each. An FEA stress analysis study confirmed the stability of the test jig under load.

8.4.2 Experimental Setup

The ultrasonic performance of the transducer prototypes was characterised based on the methodology described in Chapter 4 with an additional apparatus for high temperature measurements as shown in Figure 8.9. A heat source was applied to the test transducer for the HT measurements. The HT-PUTs under test were dry coupled using a custom-built jig that applied a normal load. A k-type thermocouple was placed next to the transducers to measure the temperature using a Pico TC-08 temperature logger [272]. An automated Python script was written to continuously acquire ultrasonic measurements and record the transducer temperature before and after each measurement.
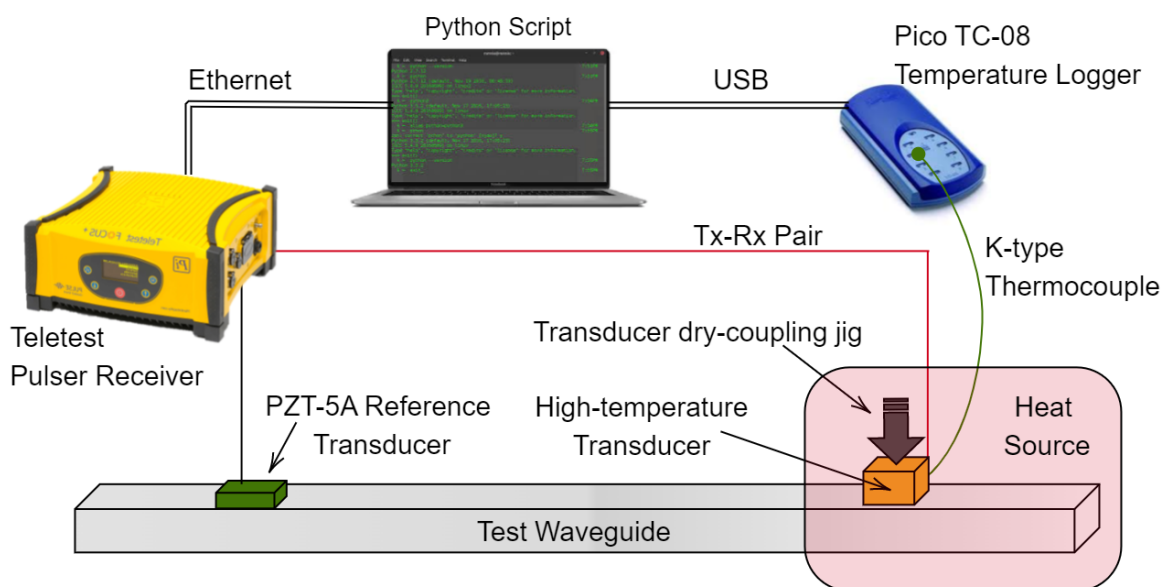
FIGURE 8.9: Illustration of the experimental apparatus used for ultrasonic guided wave measurements of a piezoelectric transducer.

Ultrasonic measurements were acquired in the pitch catch configuration where a PZT-5A PWAS was used as a reference transducer. This reference transducer was attached to the waveguide using a cyanoacrylate adhesive and would remain in ambient temperature conditions. The reference transducer and the HT transducer under test were installed in the bar waveguide and connected to independent channels of the Teletest Focus Pulser-Receiver unit. The Pulser-Receiver unit provided the electrical excitation and collected the received ultrasonic measurements. The two transducers served as a transmit-receiver pair for pitch-catch ultrasonic measurements.

The HT-UGW measurements from the prototype transducers used the described test fixture to accommodate the transducers under test and the bar waveguide inside a

Carbolite LHT6/30 furnace [273]. The bar waveguide was first inserted through the vent access hole on top of the furnace for the experimental setup. The test fixture was installed at the end of the bar waveguide and located the transducers under test inside the furnace. The experimental setup is shown in Figure 8.10.

Square steel bar with PZT-5A reference transducer attached to the bar-end above (not visible)

Furnace access vent   Transducer Cables

Thermocouple

Cross-section view of transducer test jig

Carbolite LHT6-30 furnace   Transducers test jig   Transducers under test
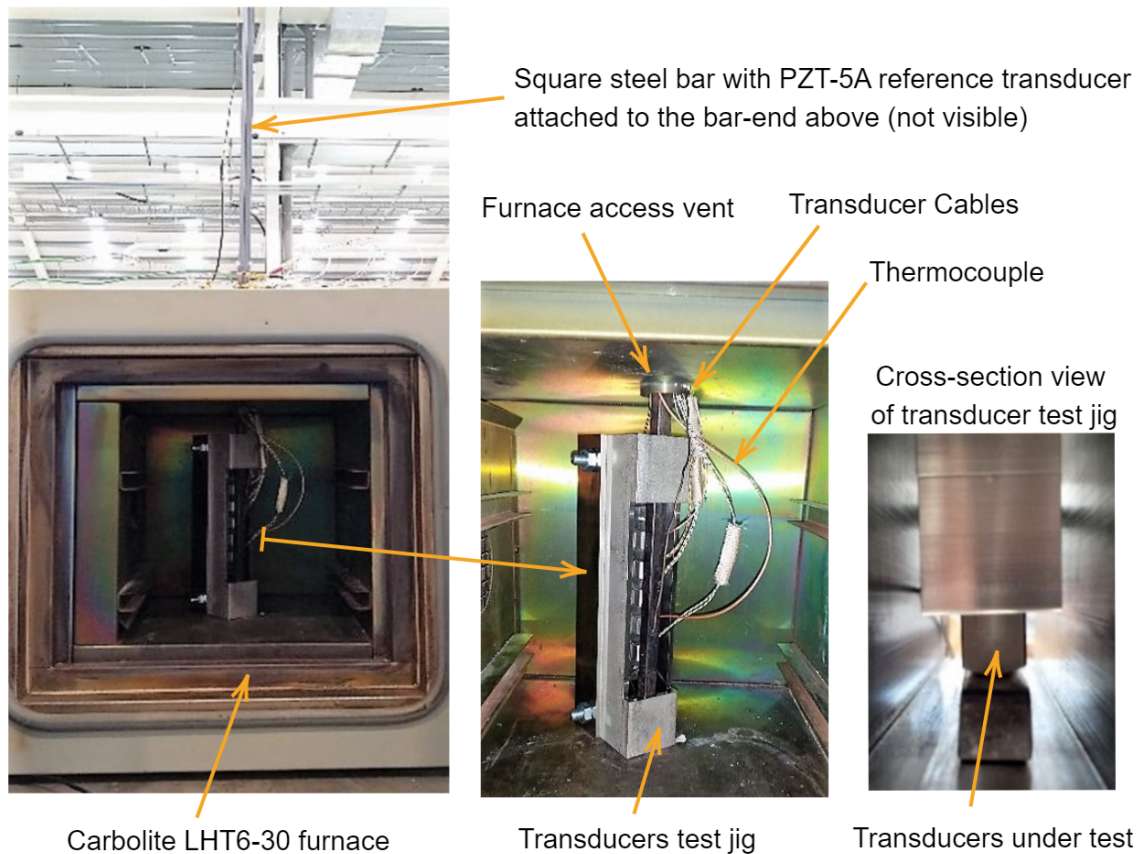
FIGURE 8.10: Transducer holder designed for ultrasonic guided wave measurements using multiple transducers under test at high temperature.

The reference PZT-5A transducer was placed outside the furnace at ambient temperatures to ensure that only the temperature behaviour of the test transducer was captured by ultrasonic measurements. The transducers under test and the reference transducer were connected to independent channels of the pulser-receiver unit. Ultrasonic pitch-catch measurements were performed using the reference transducer and one test transducer at a time.

8.4.3 Ultrasonic Guided Wave Measurements

The ultrasonic pitch catch measurements allowed for the characterisation of the transmission and reception performance of the transducer under test independently. The transmission data set consisted of ultrasonic measurements in which the HT transducer was used as an actuator and the reference transducer as a sensor. The reception dataset was collected by switching the transmit-receive pair, whereby the reference transducer was used as an actuator and the HT transducer as a receiver. The measured UGW signals transmitted or received by the HT transducer will be referred to as Tx and Rx, respectively. Three sets of Tx and Rx measurements were performed to characterise the responses of the prototype transducers to frequency, high temperature, and thermal ageing. A summary of these ultrasonic measurements is given in Table 8.5.

TABLE 8.5: Summary of measurements for transducer ultrasonic characterisation.

Dataset	Transducer DUT	Fc [kHz]	T_o [°C]	Time at T_o [hours]	Meas No.	Rx Gain [dB]
Frequency Response	Teletest Transducer	20-80	25	-	122	30
	PZT-5A	20-80	25	-	122	30
	HPZ510	20-80	25	-	122	30
	$GaPO_4$	20-80	25	-	122	40
High Temperature	PZT-5A	70	250	-	16	30
	HPZ510	70	350	-	16	30/40
	$GaPO_4$	70	600	-	24	60
Thermal Ageing	HPZ510	70	350	200	2400	30/40
	$GaPO_4$	70	600	200	2400	60

Ultrasonic pitch catch measurements used an excitation signal of a ten-cycle Hanning window-modulated sine wave of centre frequency between 20 and 80 kHz. The pulser-receiver used a sampling frequency of 1 MHz, a pulse repetition frequency of 10Hz, and a lowpass filter of 150kHz. A receiver gain of 30dB or 40dB was used for the HPZ510 and $GaPO_4$ transducers under test. An average of 256 acquisitions were taken to reduce incoherent noise.

To characterise the transducer frequency response, frequency sweep measurements were collected at ambient temperatures using excitation signals with centre frequencies ranging from 20 to 80 kHz in 1 kHz steps. The frequency sweep measurements contained 61 ultrasonic measurements for both the Tx and Rx datasets.

These frequency sweep measurements were analysed to examine the ultrasonic transducer FOM, including wave mode purity, signal amplitude and SNR within the frequency range of interest for UGW. The time-frequency analysis of the ultrasonic measurements was performed as described in Chapter 2.

To assess transducer performance at high temperatures, ultrasonic measurements were collected using a 70 kHz excitation signal at increasing temperatures with intervals of 50°C up to 350°for the HPZ510 variant and 600°for the $GaPO_4$ transducer variant. The furnace was programmed to heat up at a rate of 5°C/min. A dwell time of 15 minutes was used to ensure that the temperature reached equilibrium before high temperature ultrasonic measurements were recorded. The transducer performance metrics were derived as a function of temperature to analyse any deviation with increasing temperatures.

Following the HT-UGW measurements, one HPZ510 and $GaPO_4$ transducer prototypes were selected for long-term thermal testing at their respective target temperatures. The Tx and Rx data sets were recorded at high target temperatures for more than 200 hours with less than five minutes between each data acquisition. The thermal soak test data were analysed to examine the stability of transducer performance and investigate any degradation over time. This analysis was performed by characterising the ultrasonic performance FOMs as a function of time at target temperature to examine their HT-SHM application.

8.5 Results and analysis

8.5.1 Transducer Frequency and UGW Response

The transmission and reception data sets for the $PZT - 5A$, HPZ510 and $GaPO_4$ transducer variants were analysed by evaluating the signal transmitted to and from the reference PZT-5A wafer transducer. The amplitude and SNR of the transmitted and received ultrasonic signals were characterised as a function of frequency and compared with the current Teletest transducer, as shown in Figure 8.11. The signal amplitude shows a near-linear frequency response range of 30-80 kHz. The signal amplitude in the 20-30kHz range is significantly lower due to the destructive interference of the ten-cycle excitation signal (λ=0.1-0.15m) with the reflection from the end of the 1.5 m bar waveguide.
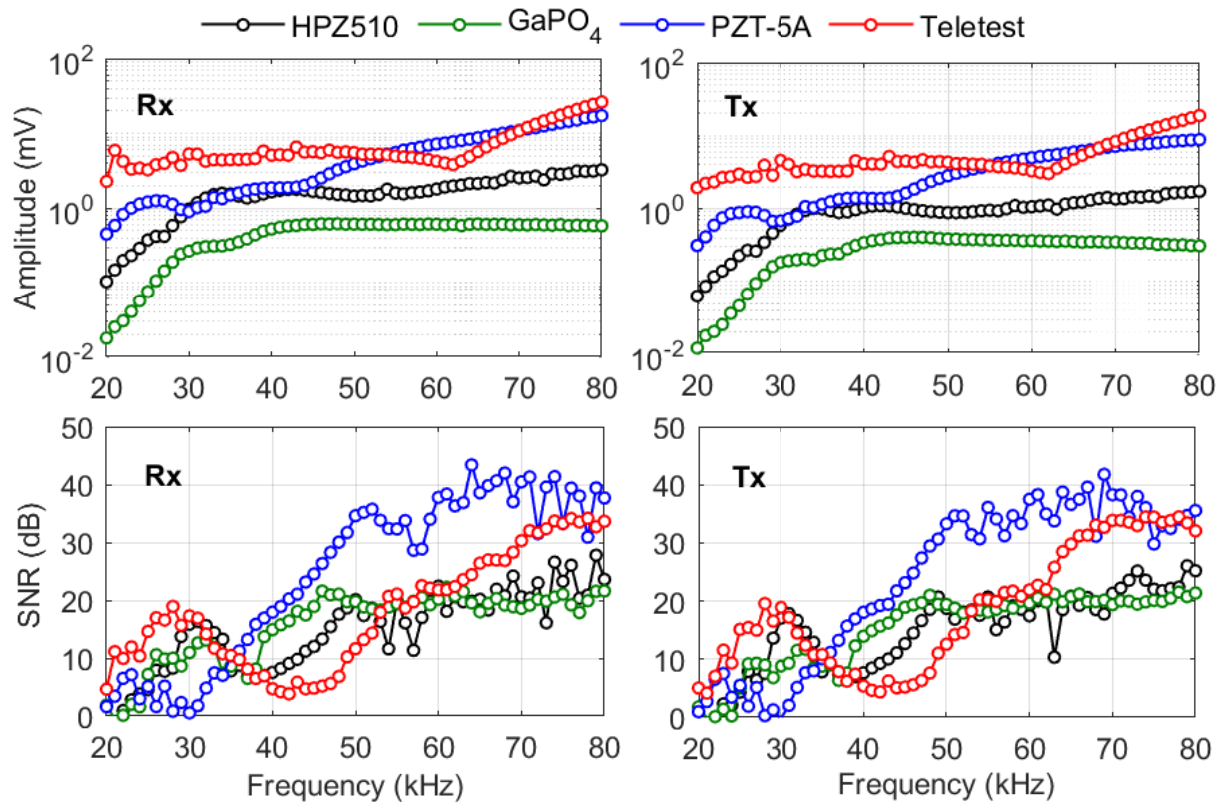
FIGURE 8.11: The transmission and reception signal amplitude and SNR as a function of frequency measured using HT-PUT variants using PZT-5A, HPZ510 and $GaPO_4$ piezoelectric materials.

The PZT-5A transducer variant displayed a lower signal amplitude compared to the Teletest transducer. The amplitude and SNR of the Teletest transducer showed an uneven response in the 45kHz and 65kHz region, which may be associated with additional wave modes excited due to the wraparound electrode or the eigenfrequency within the backing of the transducer, as hypothesised in Chapter 5. The PZT-5A transducer variant displayed a uniform frequency response and an increase in SNR of approximately 10dB in the 40-60kHz frequency range.

The signal amplitudes transmitted and received by HPZ510 and $GaPO_4$ are lower than those of the PZT-5A variant by one and two orders of magnitude. It can be seen that the Tx amplitudes are slightly lower for all transducers than their respective Rx amplitudes. This difference is due to the better ultrasonic response of bonded PZT-5a PWAS used as a reference in all measurements. The Rx and Tx signals at 70 kHz using the Teletest transducer are 10.92 mV and 7.15 mV, respectively. The corresponding values for the HPZ510 transducer are 2.53 mV and 1.36 mV, and for the $GaPO_4$ transducer, 0.60 mV and 0.35 mV. The much lower values for $GaPO_4$ are due to the lower piezoelectric charge coefficient and piezoelectric voltage coefficient, as

characterised in Chapter 7. The signal amplitudes translated into SNR of 30dB for the PZT-5A variant and 20-24dB for the HPZ510 and $GaPO_4$ transducer variants.

TFR analysis of the UGW measurements was performed to assess the excited wave mode response of the prototype transducers. As described in Chapter 4, three distinct UGW modes exist in the bar waveguide within the test frequency range. The group velocity of these wave modes and the travel distances from the transducer were used to calculate the expected arrival time of these wave modes.

The group velocity dispersion curves were used to simulate the TFR response of the UGW measurements on the waveguide, as shown in Figure 8.12. The three UGW modes are colour coded for comparison with the TFR analysis performed on the transmission and reception data collected using the Teletest, PZT-5A, HPZ510 and $GaPO_4$ transducers. The arrival of the first transmitted shear wave ($V_g = 3000m/s$) across the 1.5m bar is expected to be at 0.5ms. The second reflection with a travel distance of 4.5m is expected at $\approx$1.5 ms. The longitudinal wave reflection with a velocity of 5000 m/s is expected to arrive at 0.9 ms.

The signal amplitudes are normalised against the current Teletest transducer to aid in comparison and to identify wave modes excited by the transducer under test. All transducer variants displayed low signal amplitudes with excitation frequencies below 30 kHz. This suggests that the macor backing does not provide sufficient damping that causes the transducers to ring. However, above 40 kHz, the transmitted signals and reflections are distinctly visible. The TFR of the Teletest transducer indicates the presence of the longitudinal wave mode seen at 1 ms and its reflection overlapping with the shear wave at 1.5 ms and after that. The HT-PZT-5A transducer using a parallel electrode significantly decreases the amplitude of longitudinal waves by $\approx$45%, thus demonstrating the increased purity of the wave mode.

From the TFR of the HPZ510 transducer, the longitudinal mode excitation is visible at frequencies above 65 kHz, although the amplitude is -20 dB compared to the torsional wave mode. For the $GaPO_4$ transducer, the time-frequency response shows that the transducer is exciting both the longitudinal and the shear modes of similar amplitudes. This is likely due to the crystal cut or the extremely low shear coupling coefficient of the $GaPO_4$ material. However, the uniform frequency response of the developed HPZ510 and $GaPO_4$ transducers in the 40-80kHz range confirms their suitability for UGW applications.
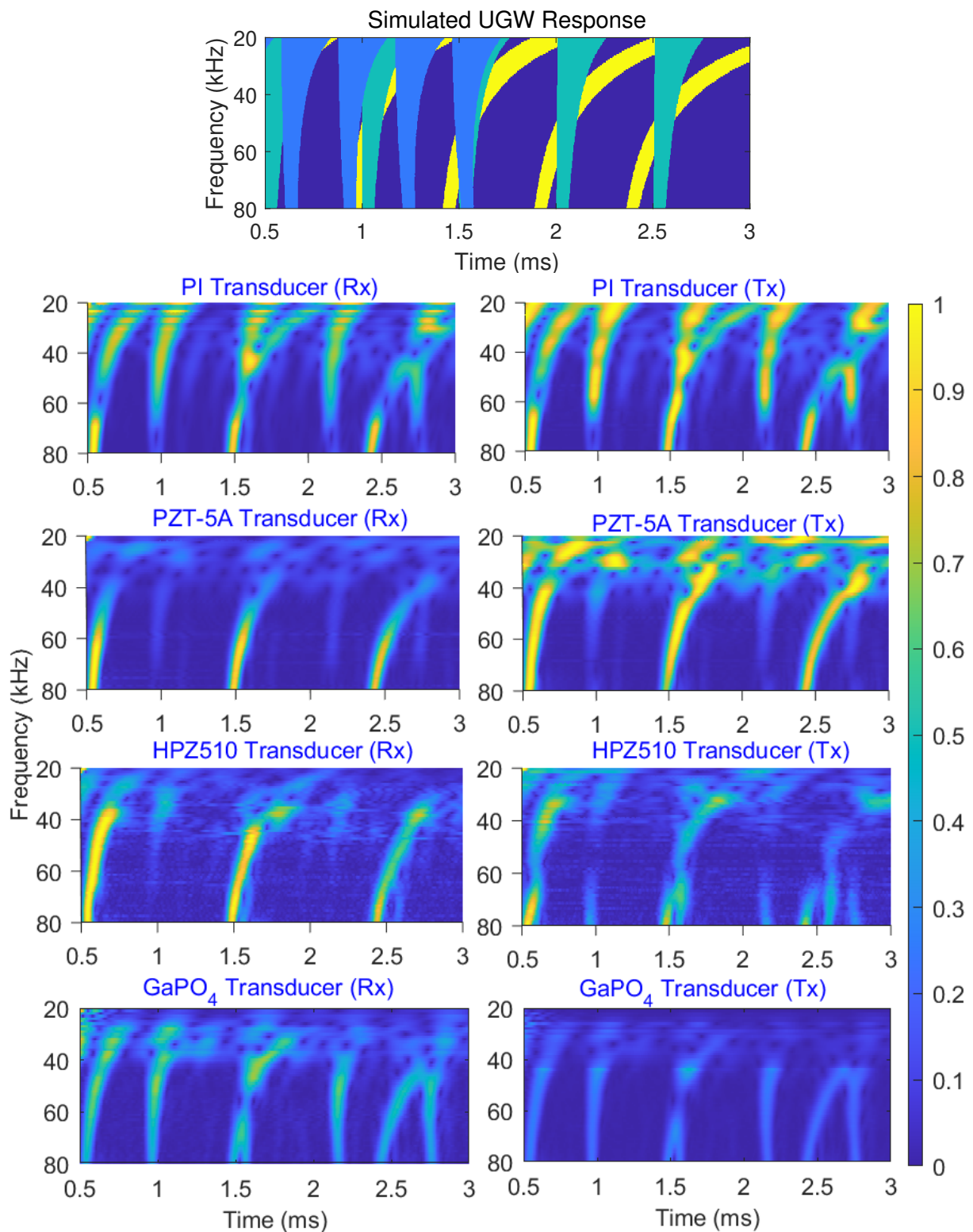
FIGURE 8.12: TFR analysis of the transmitted and received signals from transducers under test showing multiple UGW reflections. All signals are normalised to the signal amplitude of the Teletest transducer.

8.5.2 Transducer High-temperature Reponse

The high temperature UGW measurements of the HPZ510 transducer in transmit and receive mode are shown as a waterfall plot in Figure 8.13. Each Tx and Rx measurement shows the directly transmitted shear wave at 0.4 ms and the reflections from the ends of the bar at 1.4 and 2.3 ms. The signal amplitudes for high temperature measurements are normalised to the amplitude of the directly transmitted shear wave at 0.4 ms at 25°C. The normalised plot highlights the increase in coherent noise between reflections with increasing temperature above 250°C. At temperatures above 150°C, the first arriving shear mode at 0.4 ms is followed by additional waves. The amplitude of these waves gradually increases with temperature to 350°C, where their amplitude is -6dB compared to that of shear waves. These are most likely flexural waves, which are around 100-200 m/s slower than shear waves, and can be seen to separate over time for the corresponding reflections of shear waves. However, the transducer was operational up to its target temperature of 350°C without a significant reduction in signal amplitude.
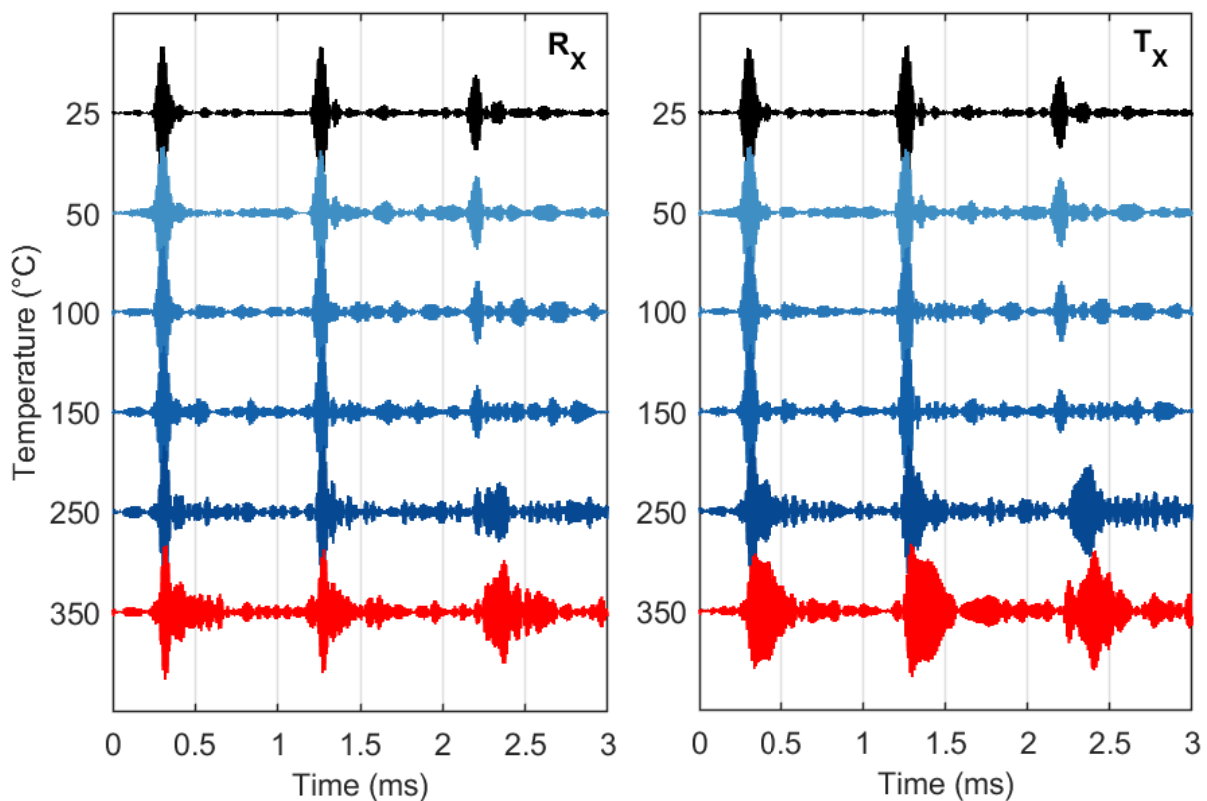
FIGURE 8.13: Normalised pitch-catch ultrasonic measurements showing reception (left) and transmission (right) by the *HPZ510* transducer at increasing temperatures up to 350°C.

The high-temperature transmission and reception UGW measurements using $GaPO_4$ transducers at temperatures up to 600°C are shown in Figure 8.14. The Tx response shows a decrease in the excitation performance of the $GaPO_4$ transducer with an increase in temperature. This decrease in SNR was caused by low signal amplitudes masked by noise for the target temperature of 600°C. Unlike the transmission response, the reception response of the $GaPO_4$ transducer was more stable up to the target temperature of 600°C. However, an increase in the coherent noise level was observed at 600°C. An increase in temperature results in thermal expansion of the structure and shifts in wave velocity [46]. These phenomena and thermal gradient along the waveguide resulted in signal interference and new reflections which increased the coherent noise for both transducer variants.
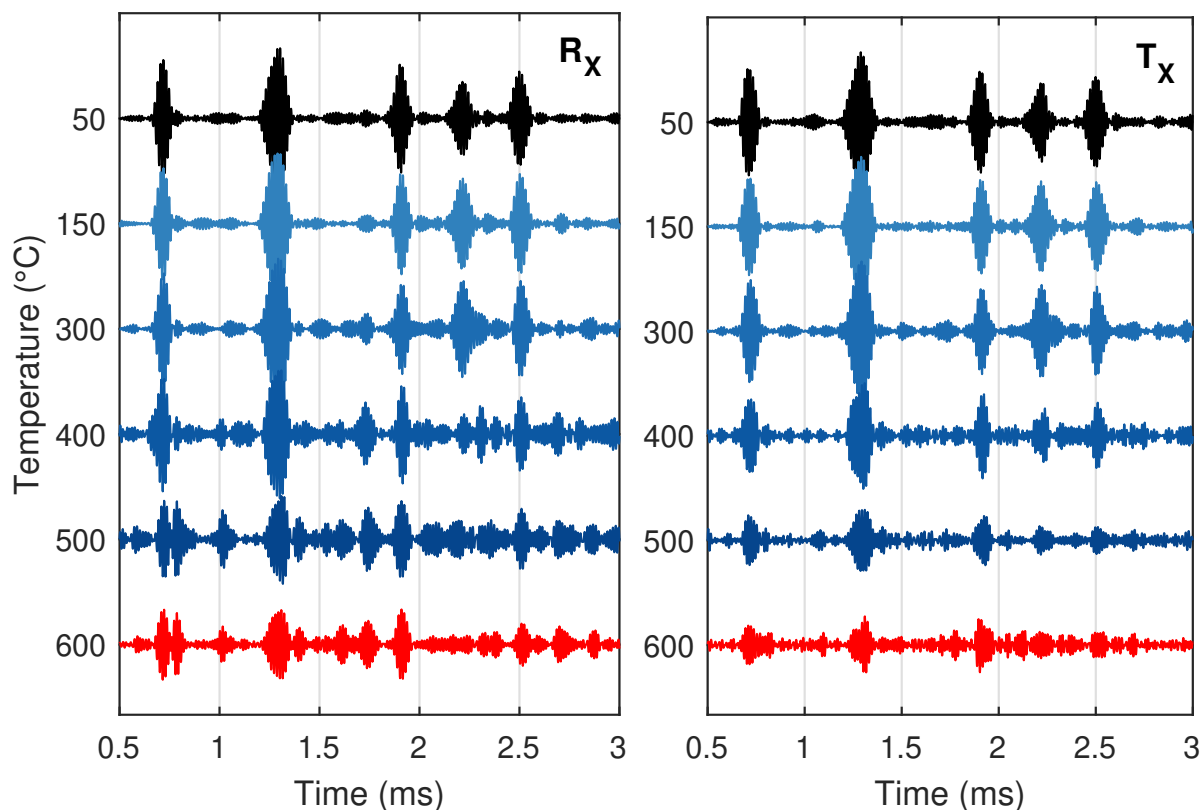
FIGURE 8.14: Normalised pitch-catch ultrasonic measurements showing reception (left) and transmission (right) by the $GaPO_4$ transducer at increasing temperatures up to 600°C.

These high temperature pitch catch measurements were used to characterise transducer performance FOMs as a function of temperature. The analysed FOMs included the signal amplitude, the time of arrival, the signal-to-noise ratio, the phase change, and the spectral amplitude. These FOM are analysed for the PZT-5A, HPZ510 and $GaPO_4$ transducer variants at temperatures up to 250°C, 350°C and 600°C, respectively. The transmission and reception performance of HT-PUTs as a function

of temperature are shown in Figure 8.15. The FOMs at high temperatures were normalised to their respective values at ambient temperature to analyse any deviation with increasing temperatures.
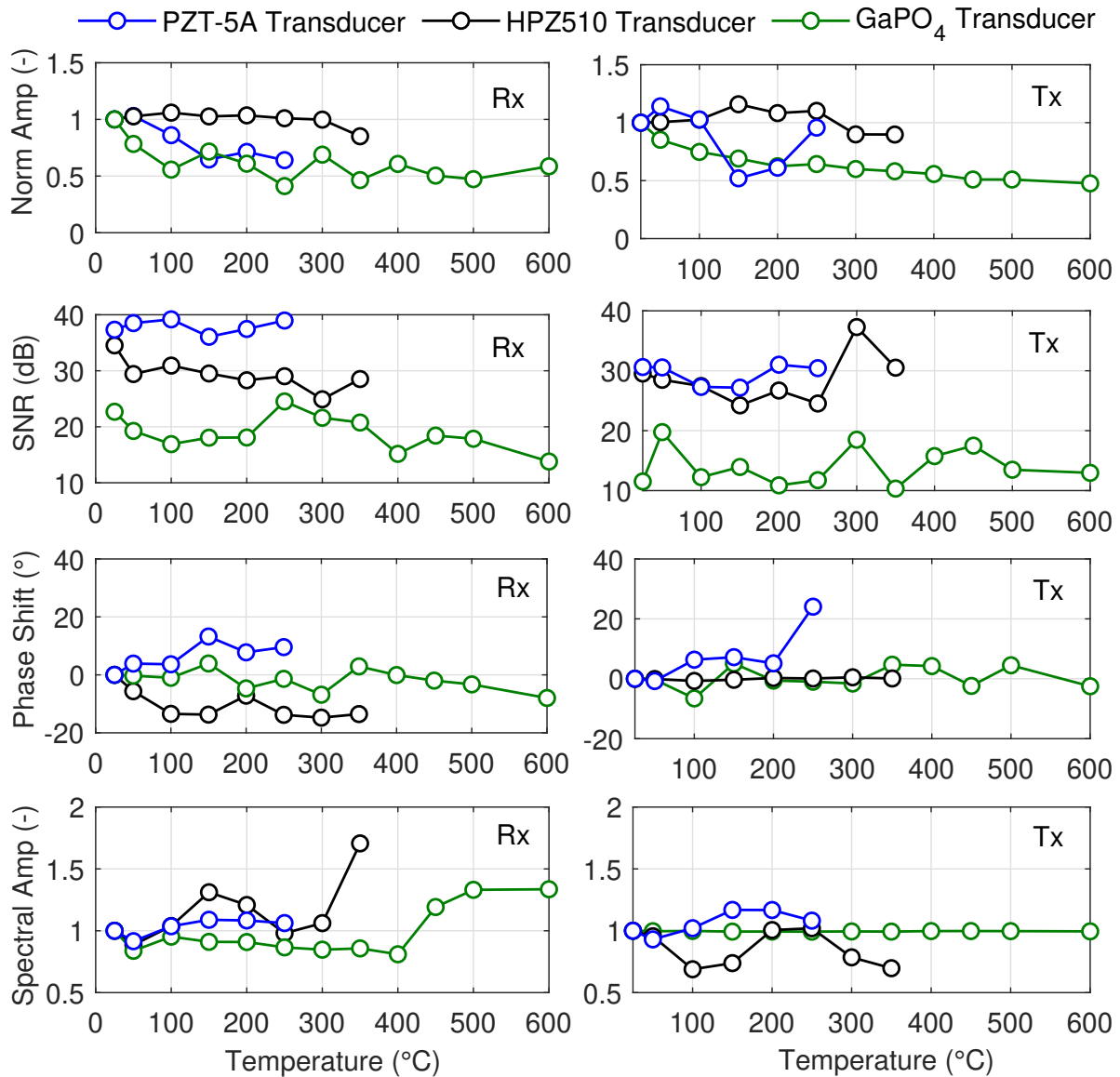
FIGURE 8.15: Comparison of HT-UGW transducer performance figures of merit for PZT-5A, HPZ510 and *GaPO*$_4$ transducer variants at temperatures up to 250°C, 350°C and 600°C, respectively.

The signal amplitude of the HT-PZT-5A transducer decreased linearly by 45% up to 250°C and diminished near the curie temperature of 325°C. The signal amplitude of the HPZ510 transducer remained stable to 300°C, after which a slight decrease of 20% was observed at 350°C. The signal amplitude with the *GaPO*$_4$ transducer decreased by 50% at 100°C compared to ambient temperatures, but was stable up to the target temperature of 600°C.

The SNR of the HT-PZT-5A transducer was stable at around 40 dB up to 250°C, while for the HPZ510 transducer, the SNR decreased from 36 dB at 25°C to 30 dB at 350°C. The SNR of the $GaPO_4$ transducer was maintained at around 17 dB with a minor variation of ± 2 dB up to 600°C. The phase change of the received signals showed a near linear behaviour with temperature and was in the 15°C range for HPZ510 and 10°C for the $GaPO_4$ transducer. The spectral amplitude was analysed as a significant variation that would indicate coherent noise due to unwanted modes or ringing of the transducer. The spectral amplitude of the HPZ510 transducer is stable up to 300°C but spikes at 350°C, which is related to the unwanted wave modes seen in Figure 8.13. For the $GaPO_4$ transducer, no significant change in spectral amplitude was observed up to 400°C, after which a gradual increase was observed up to 600°C.

The FOM for the transmission dataset were also analysed as a function of temperature. Generally, FOM of the transmission response of the transducer under test showed a similar response as a function of temperature. For example, the amplitude of the Tx signal for the $GaPO_4$ transducer also gradually decreased to about 50% at 600°C as its Rx response. However, its low transmission efficiency results in significantly more degradation in SNR.

8.5.3 Transducer Ageing Response

One of each HPZ510 and $GaPO_4$ transducer prototype was used for thermal soak measurements. Ultrasonic measurements were collected more frequently, resulting in a finer temperature resolution, with measurements collected roughly every 5°C. For the HPZ510 transducer, once the target temperature of 350°C was achieved, ultrasonic measurements were collected for 200 hours to analyse performance stability for the monitoring application.

The FOM of the HPZ510 transducers, including signal amplitude, SNR, phase shift, signal subtraction error, and spectral amplitude, were analysed as a function of time at high temperatures and are shown in Figure 8.16. The FOM are shown as scatter plots, where each point represents data analysed from an ultrasonic measurement over time, and its colour indicates the temperature of the transducer corresponding to that measurement. The signal amplitude decreased with an increase in temperature and dropped by 40% at 250°C. With a further increase in temperature, the signal amplitude increased slightly and reverted to 80% of its corresponding value at ambient temperatures at 350°C. At 350°C, the signal amplitude was maintained at the 80% level for 200 hours. The corresponding SNR of the transducer increased by nearly 7 dB with increasing temperature, reached 30 dB at 350°C, and was also stable during the 200-hour monitoring period.
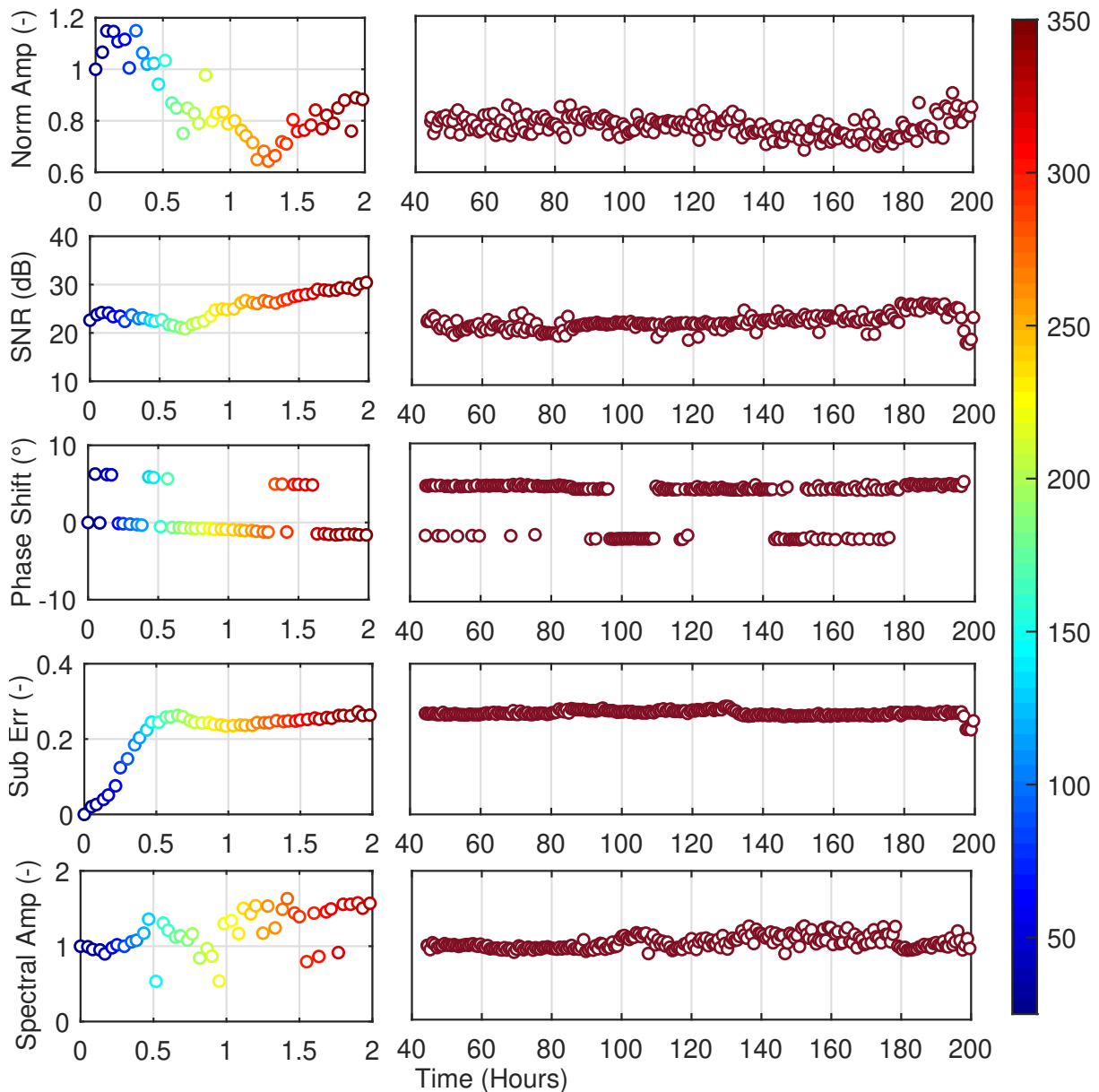
FIGURE 8.16: Thermal ageing response of the ultrasonic signal performance of *HPZ510* transducer measured at increasing temperatures up to 350°C and 350°C for over 200 hours.

The high temperature FOM for the $GaPO_4$ transducer as a function of time is shown in Figure 8.17. The amplitude and SNR decreased with increasing temperature, and at 600°C, their values decreased by 40% and 2 dB of their respective ambient temperature values. However, they were stable at 60% and 20 dB at 600°C during the monitoring period of 200 hours. A variability of ±10% for signal amplitude and ±3 dB for SNR was observed during the monitoring period and is most likely due to temperature fluctuations in the furnace.
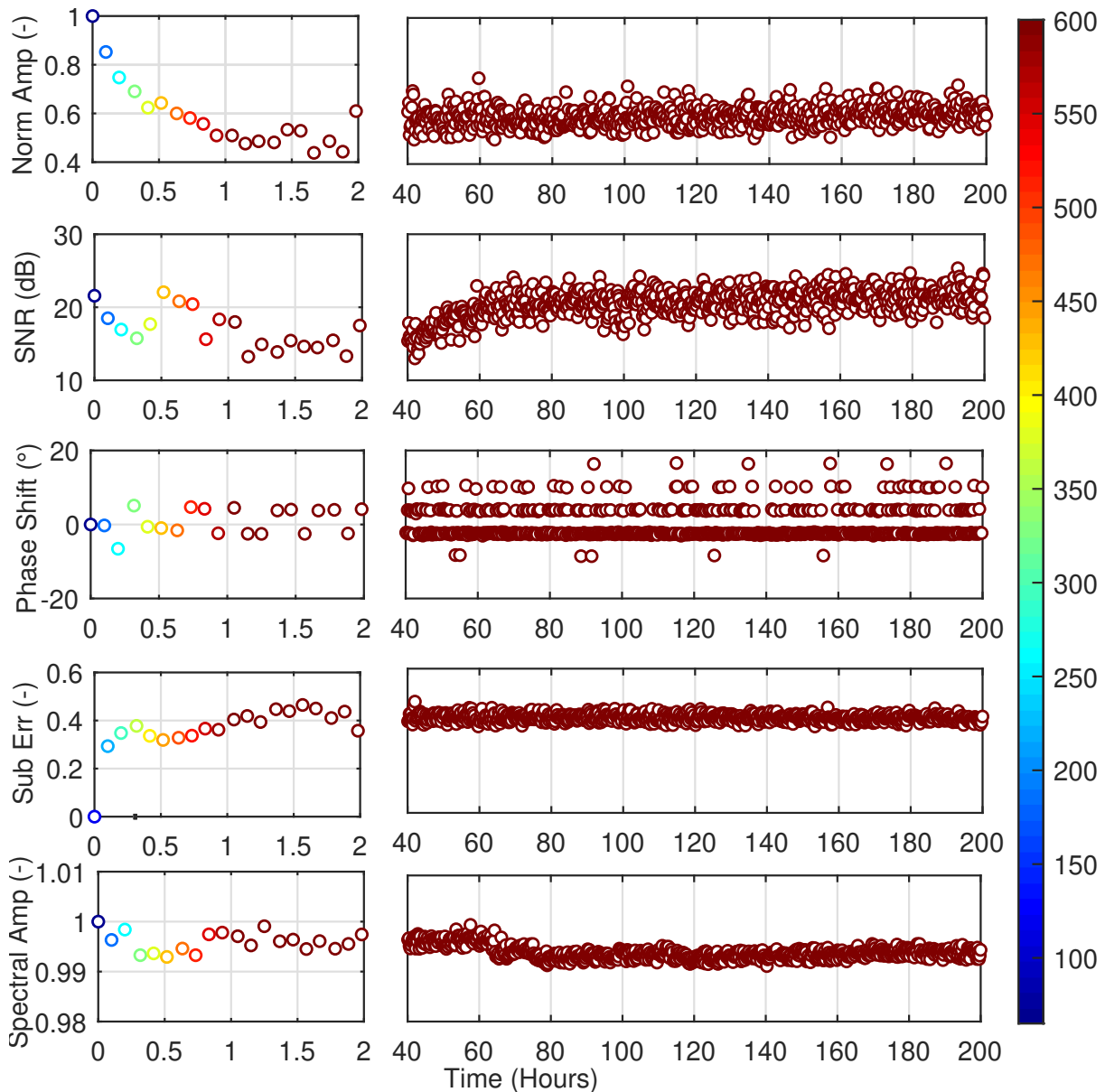
FIGURE 8.17: Thermal ageing response of the ultrasonic signal performance of *GaPO₄* transducer measured at increasing temperatures up to 600°C and 600°C for over 200 hours.

The subtraction error and spectral amplitude varied with increasing temperature but were stable at the target operating temperature and over the monitoring period. No significant changes in the analysed transducer FOMs confirm the ultrasonic and frequency response of the transducer *GaPO₄* for continuous operation at 600°C.

8.6 Summary

This chapter developed and characterised HT-UGW transducers for SHM application at temperatures up to 350°C and 600°C. The transducer design was based on the HPZ510 and $GaPO_4$ piezoelectric materials verified in Chapter 7. Compatible passive transducer materials and adhesives were selected for the transducer design. Numerical FEA analysis of the transducer confirmed non-resonant shear operation in the UGW frequency range suitable for the generation of the torsional wave mode. Transducers are fabricated and their ultrasonic characterisation was carried out extending the characterisation methodology described in Chapter 4 to high temperatures. The torsional ultrasonic output within the transducer batch varied by $\pm$ 50% possibly due to differences in the adhesive layers; but a consistent SNR within $\pm$1dB was achieved, verifying the assembly method. Comparison of the PZT-5A variant with the Teletest transducer showed that the proposed design reduced the signal amplitude by $\approx$ 60% but achieved a significant improvement in SNR of more than 10dB. The proposed design also eliminated the signal degradation seen in Teletest transducer around 60kHz, however, at an expense of worse performance in frequencies below 40kHz.

The high temperature variants of the transducer were manufactured using HPZ510 and $GaPO_4$ and an experimental setup was developed to evaluate their HT-UGW measurements at temperatures up to 350°C and 600°C, respectively. The UGW measurements were analysed in the time, frequency and time-frequency domains to assess their signal amplitude, mode purity, SNR, and wave mode response. The transducers achieved a flat frequency response in the UGW frequency range. The signal amplitude and SNR for the HPZ510 variant are reduced by 20% and 5 dB (to 24dB) at 350°C. Similarly, there was a reduction in the signal amplitude and SNR of the $GaPO_4$ variant reduced by 40% and 2dB (to 18dB) at 600°C. The variant with $GaPO_4$ also showed an increase in coherent noise at temperatures above 400°C. For both transducers, the change in phase shift, spectral amplitude, and signal subtraction error up to their target temperatures was less than 10°, 20% and 10%, respectively.

The ultrasonic performance of the transducers was also analysed at their target temperature for a monitoring period of more than 200 hours to assess their reliability over time. The performance of the analysed transducer FOMs was highly stable, with less than 10% variability during the monitoring period, and no deterioration was observed. Thus, manufactured HT-UGW transducers using HPZ510 and $GaPO_4$ materials have shown sufficient signal strength, mode purity, and SNR to be considered for SHM application to HTPs operating at temperatures up to 350°C and 600°C, respectively.

Chapter 9

Conclusions and Recommendations for Future Work

9.1 Thesis Review

This thesis investigated the feasibility of using the UGW piezoelectric transducer for the application of SHM in HTPs. The HT-UGW transducers were designed for operation at medium-high temperatures up to 350°C and ultra-high temperatures up to 600°C. The design of the transducer has been optimised for operation in TS-mode mode for the transduction of the fundamental torsional wave mode in the frequency range of 20-120 kHz in metallic pipes.

Chapter 1 introduced the thesis by presenting the industrial needs of the UGW based SHM system for HTPs. Contributions to knowledge and publications arising from the thesis were presented and the structure of the thesis was illustrated.

Chapter 2 presented the fundamental background and terminology related to UGW on cylindrical pipe-like structures. Piezoelectric theory was introduced to understand its characteristics and application for the design of ultrasonic transducers. The ultrasonic signal processing techniques used in the thesis were also described.

Chapter 3 presented a review of the literature on HT-PUT design and their SHM application. The review focused on the numerical and experimental analysis of the HT transducer for low-frequency ultrasonic application. The enabling technologies for the HT-SHM application including temperature compensation and diagnostic algorithms were also reviewed.

Chapter 4 presented a hybrid numerical and experimental approach for the design characterisation of HT-UGW piezoelectric transducer. Design characterisation was focused on the TS-mode mode for transduction of the $T(0,1)$ wave mode at high temperatures. The numerical methodology was based on multiphysics FEA and the

experimental methodology included electromechanical characterisation by EMIS, vibrational analysis using SLDV, and UGW measurements on a waveguide. The proposed numerical methodology was experimentally validated using the Teletest transducer. The characterisation of the Teletest transducer design also identified issues related to the excitation of spurious modes arising from the electrode configuration of the piezoelectric plate and the natural frequency of the backing layer. The high-temperature performance and limitation of the Teletest transducer also served as a benchmark for new transducer designs.

In Chapter 5, the validated PWAS model in Chapter 4 was used to investigate the influence of several transducer design parameters on the electromechanical performance of the operation in TS-mode and the excitation of $T(0,1)$ UGW. This included the dimensions of the piezoelectric plate, the polarisation, the electrode design, and the dimensions of the backing layer. Parametric analysis focused on optimising signal amplitude, increasing SNR by reducing out-of-plane vibration, and avoiding resonances in the operating frequency range for UGW. The optimal performance was achieved with a width-polarised, wrapped-around electrode configuration. The simulated vibration modes and the frequency response of the electrical displacement were experimentally validated through 3D SLDV. The results showed that the accuracy of the model in simulating the dynamic electromechanical behaviour, including the vibrational modes and frequency response, matched well with the measured response. Furthermore, the electro-mechanical performance was compared with that of the current Teletest transducer. The results of this study lead to the development of an optimised transducer for UGW SHM application.

In Chapter 6, an experimental approach was applied to characterise the performance of an UGW system for SHM of HTPs. Long-term high-temperature monitoring experiments were carried out in a laboratory setting with simulated defects and in a live-operating power plant to evaluate the performance of the system in a range of EOCs. Ultrasonic SHM data was collected while the transducer array was exposed to more than 1000 thermal cycles of temperatures up to 150°C over 180 days in the simulated environment and over a year at 180°C in the power plant. This experimental study showed that the transducer array provided a highly stable T(0,1) signal output with a consistent SNR variation less than 2dB and 4% CSA defect sensitivity at temperatures up to 150°C. This confirmed that the UGW system including the transducer array and the defect monitoring approach is suitable for SHM of HTPs operating at temperatures up to 150°C. Monitoring trials at the power plant also demonstrated the stability of the system, but performance degradation was observed over time, likely due to accelerated degradation due to extreme EOCs and

collar array design.

Chapter 7 focused on the selection and characterisation of HT piezoelectric materials for continuous operation at 350°and 600°C. HPZ510 and $GaPO_4$ piezoelectric materials were selected after review of commercially available materials. The electromechanical characterisation of these materials was performed through EMIS and their dielectric, elastic and piezoelectric properties and temperature dependence were derived and assessed. The temperature dependence of the elastic constants was found to exhibit a stable state of up to 600°C with a variation of less than 3%. Multiphysics FEA models of the chosen piezoelectric materials were developed and validated through experiments. Numerical studies showed a good agreement on the change in frequency and electromechanical response, which are critical to evaluating their performance for HT applications. Finally, HT ageing experiments demonstrated excellent temperature stability and validated their use for HT-PUT design.

Finally, in Chapter 8, the findings of the design optimisation FEA studies from Chapter 5 are used to develop HT-UGW transducers for improved TS-mode performance. High-temperature conductive and non-conductive adhesives are selected, and a transducer assembly methodology is developed for bonding the active and passive layers of the transducer. The assembly procedure minimised the fabrication time, allowed early identification of failures, and demonstrated consistency among the prototypes developed with amplitude and SNR variability less than $2mV$ and $1dB$, respectively. HPZ510 and $GaPO_4$ transducer were manufactured for continuous operation at 350°C and 600°C. The ultrasonic performance of the manufactured prototypes was characterised at increasing temperatures up to their respective target temperatures and then at the target operating temperatures for a period of 200 hours. The results indicate that the proposed design reduces the signal amplitude by around 60%; however, it significantly increases the SNR by more than 10 dB throughout the 40 to 80 kHz frequency range and eliminates degradation around 60 kHz caused by the resonance of the stainless steel backing. Thus, the developed transducer design is validated for a wide range of HT-UGW applications.

9.2 Key findings

It has been shown that a unified numerical and experimental approach can be applied to design and characterise a low-frequency (20-120 kHz), high-temperature, torsional guided wave piezoelectric ultrasonic transducer.

The main findings of the thesis are:

- Information about unwanted out-of-place vibration mode arising from the wrapped-around electrode configuration of the piezoelectric plate and the natural frequency of the backing layer in the existing Teletest transducer.

- Performance characteristics of an UGW system for SHM application to HTPs, including stability of the torsional signal response at temperatures up to 180°C under simulated and live operating conditions in a power plant.

- The application of optimal baseline selection and baseline signal subtraction for temperature compensation and defect detection can achieve a defect sensitivity of 4% CSA at temperatures up to 150°C.

- Application of the numerical multiphysics approach FEA for the analysis of high temperature piezoelectric materials. The simulated electromechanical and vibrational frequency response of the piezoelectric models of PZT-5A, HPZ510 and $GaPO_4$ demonstrated a good correlation with the measured response.

- Influence of the direction of polarisation and electrode configuration on the TS-mode performance of a piezoelectric plate. Numerical analysis demonstrated an improvement of 11 dB in SNR with a transverse width polarised piezoelectric plate compared to the existing design and an additional improvement of 5 dB with a parallel electrode.

- Validation of the HPZ510 piezoelectric material for continuous operation at medium-high temperatures of up to 350°C in TS-mode. The development of the UGW transducer using HPZ510 achieved torsional signal amplitudes of 2.53 mV (Rx), 1.36 mV (Tx) and corresponding SNR of 20 dB.

- Validation of $GaPO_4$ piezoelectric material for TS-mode operation using y-cut configuration. $GaPO_4$ based UGW transducer designed for continuous operation at ultra-high temperatures of 600°C demonstrated a torsional signal amplitude of 0.6 mV (Rx), 0.35 mV (Tx) and corresponding SNR of 24 dB. Information on mode coupling in $GaPO_4$ single crystal with y-cut configuration.

9.3 Further Work

The presented HT-PUT were designed and characterised for shear mode operation for transduction of the torsional wave mode in the frequency range of 20-120 kHz at temperatures of up to 600°C. However, it may be desirable to operate in a different UGW mode or in a higher frequency range or even higher temperatures for a given industrial requirement. Although the numerical and experimental techniques discussed were used to create and analyse HT-UGW transducers, they can be applied to any PUT design configuration.

9.3.1 Advancements in FEA of HT-PUT

The numerical analysis of the piezoelectric materials and transducers performed in this work was limited to the electrical boundary conditions of the transducer. Thermal characteristics were introduced with high-temperature piezoelectric material properties only. The influence of temperature on external mechanical loads, for example, the mechanical assembly of the transducer, the thermal properties of the adhesives, or the dry coupling force of the transducer collar, was not included. Further research should include investigation of thermal stresses due to these external factors and influence on the electromechanical frequency response of the transducer. In addition to the mechanical load, the effect of the measurement system can also be introduced to further emulate the electrical setup and improve the accuracy of the simulated results.

The numerical FEA studies focused on the characterisation of the electromechanical frequency and vibration response and accurately predicted the resonance frequencies, vibration modes, and their coupling with unwanted contour modes as seen in the case for $GaPO_4$. This work also demonstrated the suitability of the FEA technique for understanding the influence of different design parameters. However, to further improve the accuracy of the simulated results, material losses, such as friction, damping, and dielectric dissipation, can be introduced. These can be extracted from the measured EMI response of the piezoelectric material. For high frequency application, other considerations such as the mass loading effect of electrodes and internal heating of the piezoelectric material may need to be introduced.

The excitation of UGW on cylindrical pipe-like structures is very well understood. For complex structures, the developed transducer models can be further evaluated through transient time-domain analysis to analyse guided wave excitation and interaction with the structure.

9.3.2 Transducer Design Optimisation

The transducer design was optimised for a 20-120 kHz broadband frequency response. The transducer design could be further optimised if a narrower frequency range is desired. The use of higher frequencies above 500 kHz could enable resonant transducer design which can significantly increase the ultrasonic performance and defect sensitivity. However, the temperature influences for resonance operation are worse and will need consideration for design. Electrical impedance matching circuitry can also optimise ultrasonic performance, but it will be restricted to a specific frequency range depending on the tuning parameters of the circuit.

9.3.3 Guided Wave System Optimisation

The HT-SHM studies performed using a complete UGW system in Chapter 5 were performed using existing transducers at temperatures of up to 150 °C. These studies were carried out in parallel with the development of the transducer reported in Chapter 8. Further experimental investigation of the developed transducers in an array configuration is required as part of a complete UGW system. The developed HT-UGW transducers developed for 350°C and 600°C have a similar physical profile and can be housed in the same collar with some modifications to the transducer holder modules. Long-term monitoring trials in the power plant revealed degradation in the springs and their compression force. Further evaluation of temperature-resistant springs should be carried out to provide consistent dry coupling force to the transducer over temperature variation. This should consider any thermal expansion and additional force that may be exerted on the transducer to prevent any mechanical failure of the transducer.

The presented UGW system used a transducer array for pulse-echo operation. There are several options to optimise the ultrasonic performance of the array. The number of transducers in an array can be increased for higher ultrasonic output although the array density is limited to the transducer size and electrical drive limits of the pulser-receiver electronics. The increase in number of channels used for multiplex across the transducer array can also improve the performance of the ultrasonic output and defect sensitivity through post-processing techniques such as full matrix capture. To compensate for transducer degradation or temperature variability, it can also allow the application of different excitation signals to selected transducers to maintain the output of the axisymmetric torsional signal. To further improve the ultrasonic performance of the system, a separate transmitter and receiver array could comprise transducers that are designed for optimised transmission and reception operation.

This study only considered simple temperature compensation and defect detection signal processing techniques to characterise the performance of the Teletest system for the HT-SHM application. For industrial applications, it will be beneficial to improve the sensitivity of the system to defect detection by applying advanced signal processing and data analytics techniques such as machine learning or AI models for temperature compensation and defect monitoring. The ultrasonic signal compensation methods can be applied using the known understanding of the effect of temperature on the transducer ultrasonic output. The high-temperature transducer response characterised by the transducer of Chapter 8 and the impedance amplitude and phase response characterised in Chapter 7 can be considered to improve the temperature compensation.

Appendix A

Appendices

A.1 Calculation of Contact Surface Area

A.1.1 Hertzian Contact Theory

The Hertzian contact theory was developed by Heinrich Hertz and is a fundamental concept in solid mechanics and contact mechanics [247]. It has been widely applied in various fields of engineering and physics. It is particularly applicable to situations where two solids come into contact under pressure. This theory is applied to calculate the contact surface area in this study where a piezoelectric transducer is dry-coupled to a carbon steel pipe using a normal force. The theory assumes perfect elasticity i.e. both the contacting bodies are elastic and deform elastically within the range of stresses and strains experienced during the contact. The materials are assumed to be homogeneous (uniform composition) and isotropic (uniform properties in all directions) within the region of contact. It also neglects friction and surface roughness and does not apply to adhesive contact situations. This theory can approximate the size and shape of the contact area between the two bodies. It also provides equations to calculate the distribution of stress and strain within the contact region, typically in terms of the applied load and the geometrical properties of the contacting bodies.

A.1.2 Contact Area between Cylinder and Plate

Hertzian contact theory can be applied to calculate the contact surface area between a cylinder and a flat plate. In this calculation, contact of a cylinder of radius R and a flat plate is considered as illustrated in Figure A.1. The contacting cylindrical and plate bodies have elastic moduli E_1, E_2 and Poisson's ratio ν_1, ν_2. A normal load F is transmitted to the flat surface through a contact zone.
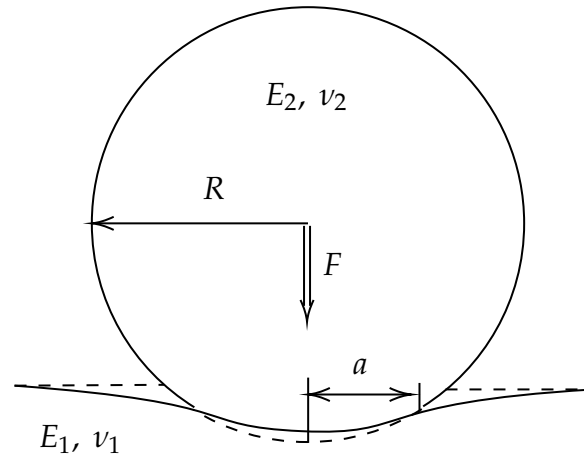
FIGURE A.1: Illustration of the contact between a cylinder and a flat plate.

Assuming a cylindrical contact that has a symmetric pressure distribution, the equation for the contact radius (*a*) is given by:

$$a = \left(\frac{3FR}{4E^*}\right)^{1/3} \tag{A.1}$$

where F is the applied force, R is the radius of the pipe, and E^* is the reduced modulus of elasticity which is calculated as:

$$\frac{1}{E^*} = \frac{1 - v_1^2}{E_1} + \frac{1 - v_2^2}{E_2} \tag{A.2}$$

where E_1, E_2 are the elastic moduli and v_1, v_2 are the Poisson's ratio of the piezoelectric plate and the pipe, respectively.

Once the contact radius a is determined, the contact surface area A can be calculated using the formula for the contact area of a cylinder:

$$A = 2\pi a L \tag{A.3}$$

where L is the length of the contact area, which is the dimensions of the piezoelectric plate along the axial direction of the cylindrical pipe.

This theory and model have been used in Chapter 5 to estimate the actuation area of a piezoelectric PZT-5A plate installed on a carbon steel pipe. For Carbon Steel and PZT-5A, the Elastic moduli are 240 GPa and 60 GPa, whereas the Poisson's ratios are 0.26 and 0.34, respectively. With a nominal contact force of 200N applied on the PZT-5A installed on a 4-inch pipe (ϕ=114.3mm), the contact radius is $\approx$0.0116mm.

A.2   Material Properties used for FEA

A.2.1   Gallium Phosphate

TABLE A.1: $GaPO_4$ material properties used for the model [260]

Material Property	Property Value (at 25°C)	Temperature Coefficients		
		$T_{ij}^1[10^{-6}K^{-1}]$	$T_{ij}^2[10^{-9}K^{-2}]$	$T_{ij}^3[10^{-12}K^{-3}]$
Piezoelectric constants [a], [b]			$d_{ij}[pC/N]$	
d_{11}	4.5	(-)	(-)	(-)
d_{14}	1.9	(-)	(-)	(-)
Elastic Constants $S_{ij}[10^{-12}m^2/N]$				
S_{11}^E	17.93	22.4	30.5	62.4
S_{12}^E	-4.82	-210.5	-0.1	-271.3
S_{13}^E	-3.19	181.6	78.2	322.2
S_{14}^E	-2.36	482.2	315.5	7.9
S_{33}^E	11.35	147.9	14.1	261.5
S_{44}^E	27.04	18.7	54.7	52
S_{66}^E	45.51	-26.9	24	-8.3
Relative Dielectric Constants [c]			$\epsilon_{ii}^T[-]$	
ϵ_{11}^T	6.1	(-)	(-)	(-)
ϵ_{33}^T	6.6	(-)	(-)	(-)
Thermal expansion coefficients $\alpha_{ii}[10^{-6}K^{-1}]$				
α_{11}	12.78	10.6	-16.1	12.3
α_{33}	3.69	5	-5.4	3.6

[a] Signs following standard IEEE 176-1987 for the right-handed crystal.

[b] d_{11} value is constant up to 700°C, and d_{14} is 1.6 at 500°C.

[c] Measured at 1 kHz.

The elastic properties of $GaPO_4$ and CTEs as a function of temperature were derived using the reported temperature coefficients and are shown in Figure A.2.
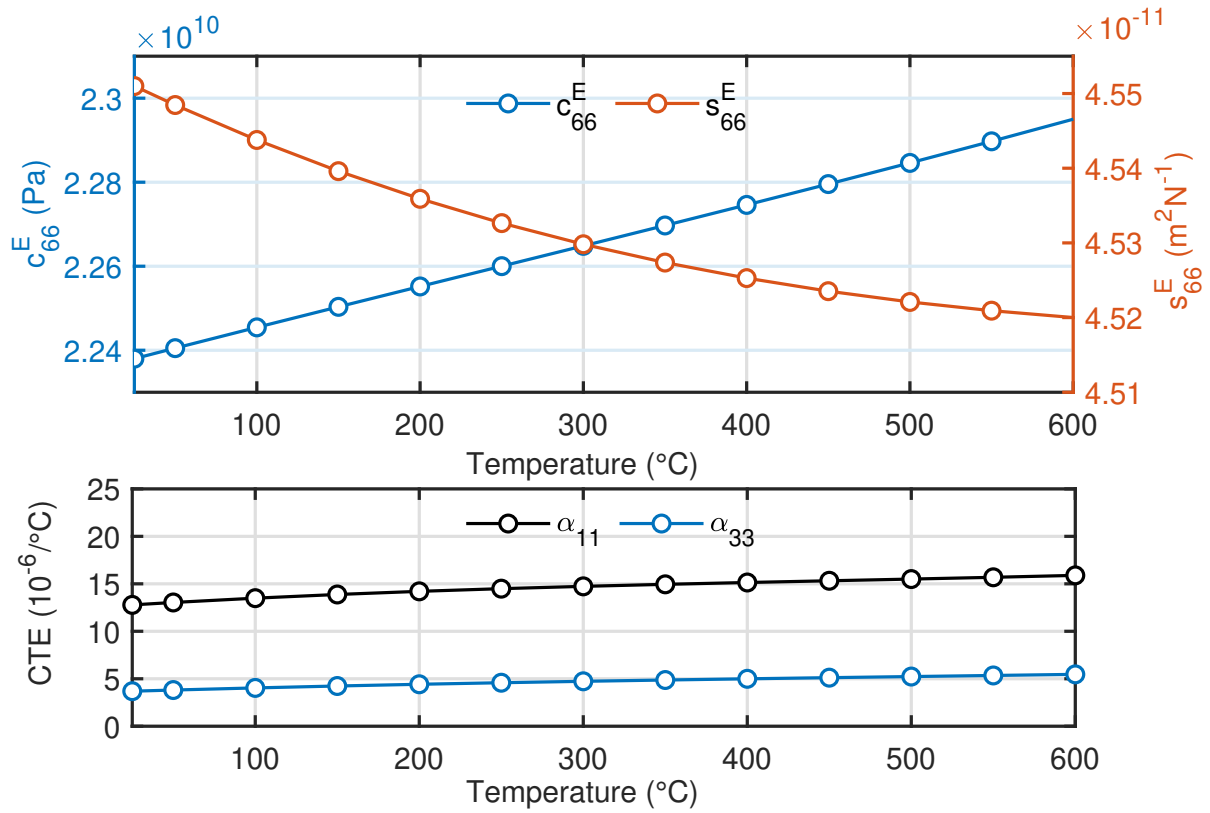
FIGURE A.2: The elastic compliance and the CTEs of $GaPO_4$ material as a function of temperature derived using the temperature coefficients.

A.2.2 Transducer Passive Layers

TABLE A.2: Physical material properties of transducer materials used for FEA studies.

Material	Density [kg/m^3]	Young's Modulus [GPa]	Poisson's Ratio
99.5% Al_2O_3	3890	375	0.21
96% Al_2O_3	3720	300	0.21
Macor	2520	66.9	0.29
PZT-5A	7750	66	0.31
HPZ510	7950	95.2	0.25
$GaPO_4$	3570	85	0.28

A.3   High temperature EMI Measurements

A.3.1   HPZ510 - Modified Bismuth Titanate
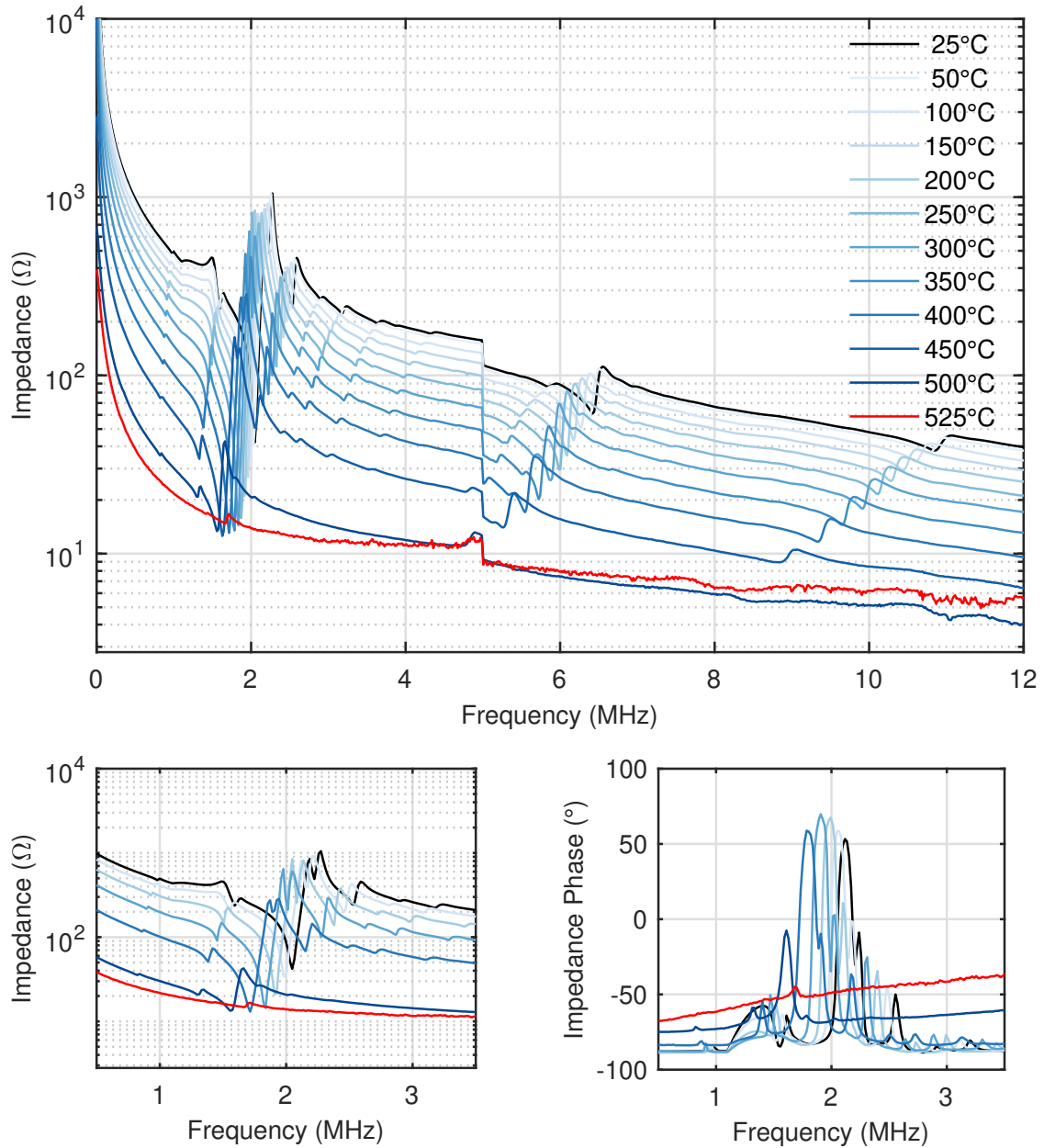
FIGURE A.3: Electromechanical impedance measurements of the HPZ510 plate showing the impedance amplitude and phase at temperature increments of 50°C up to 525°C.

A.3.2 $GaPO_4$ - Gallium Phosphate
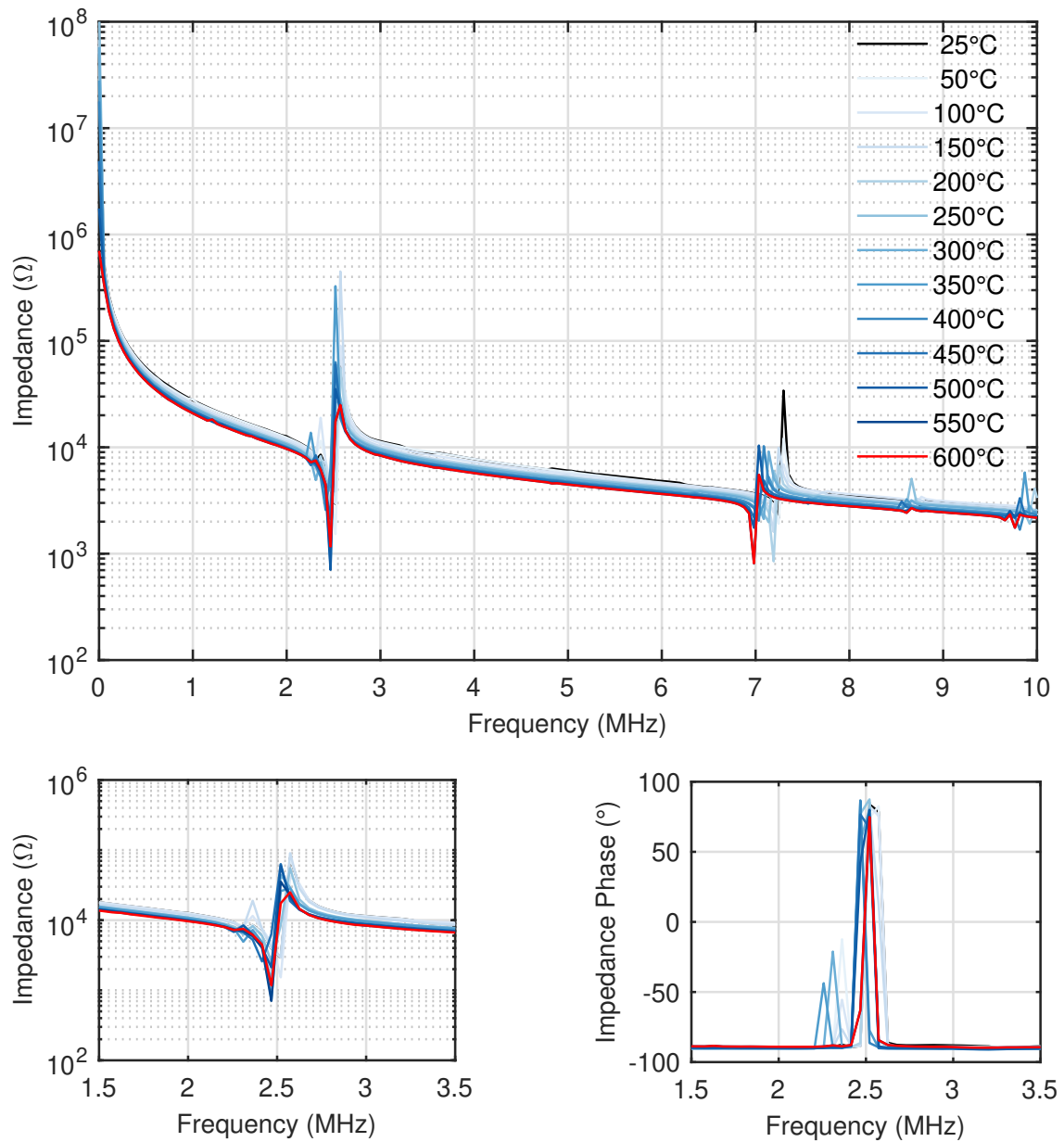
FIGURE A.4: Electromechanical impedance measurements of the $GaPO_4$ plate showing the impedance amplitude and phase at temperature increments of 50°C up to 600°C.

A.3.3 PZT-5A - Lead Zirconate Titanate
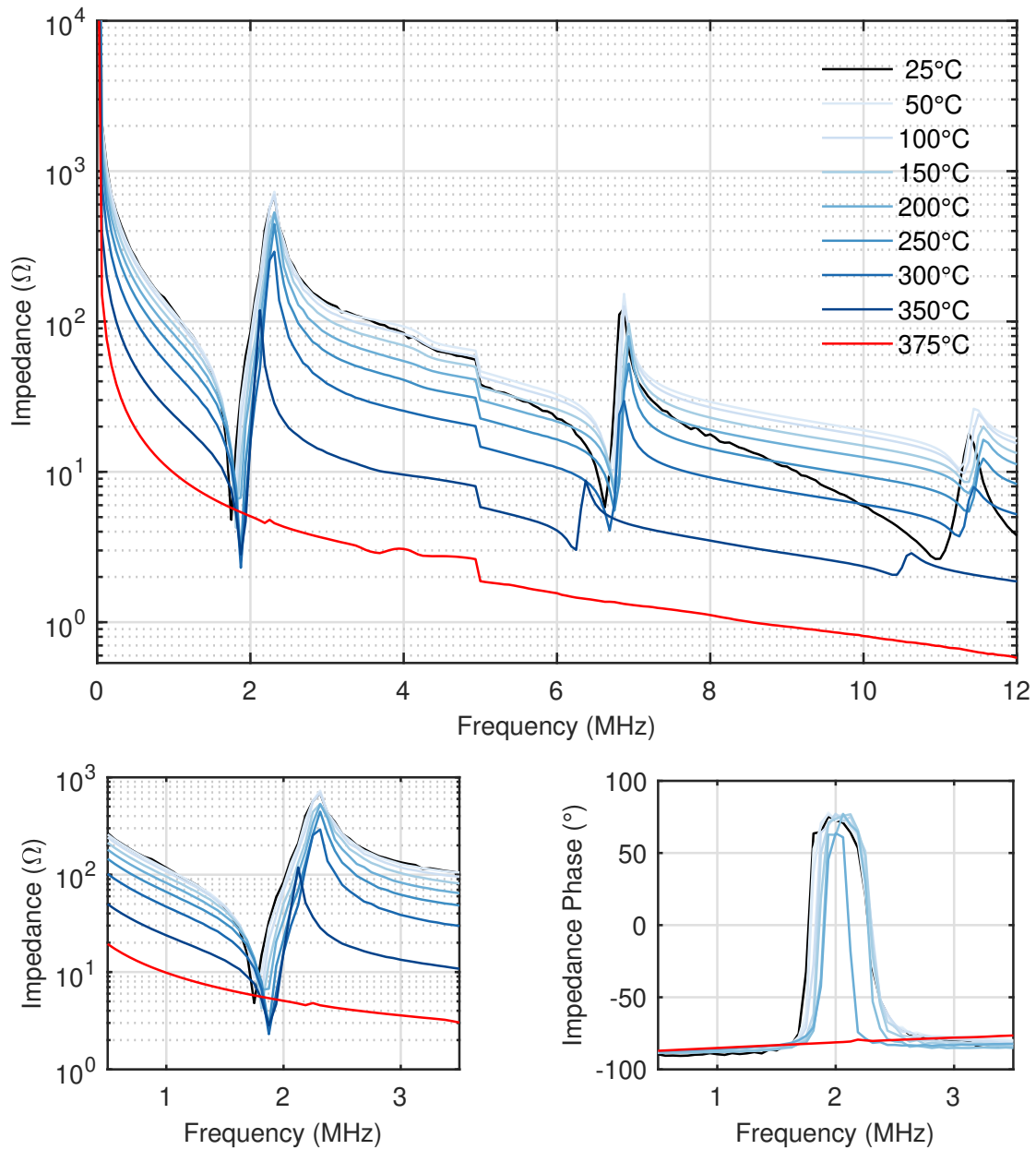
FIGURE A.5: EMI measurements of the PZT-5A plate used in the Teletest transducer at temperature increments of 50°C up to 375°C.

A.4 Additional Transducer FEA Results

A.4.1 Comparison of Macor and Stainless Steel Backing
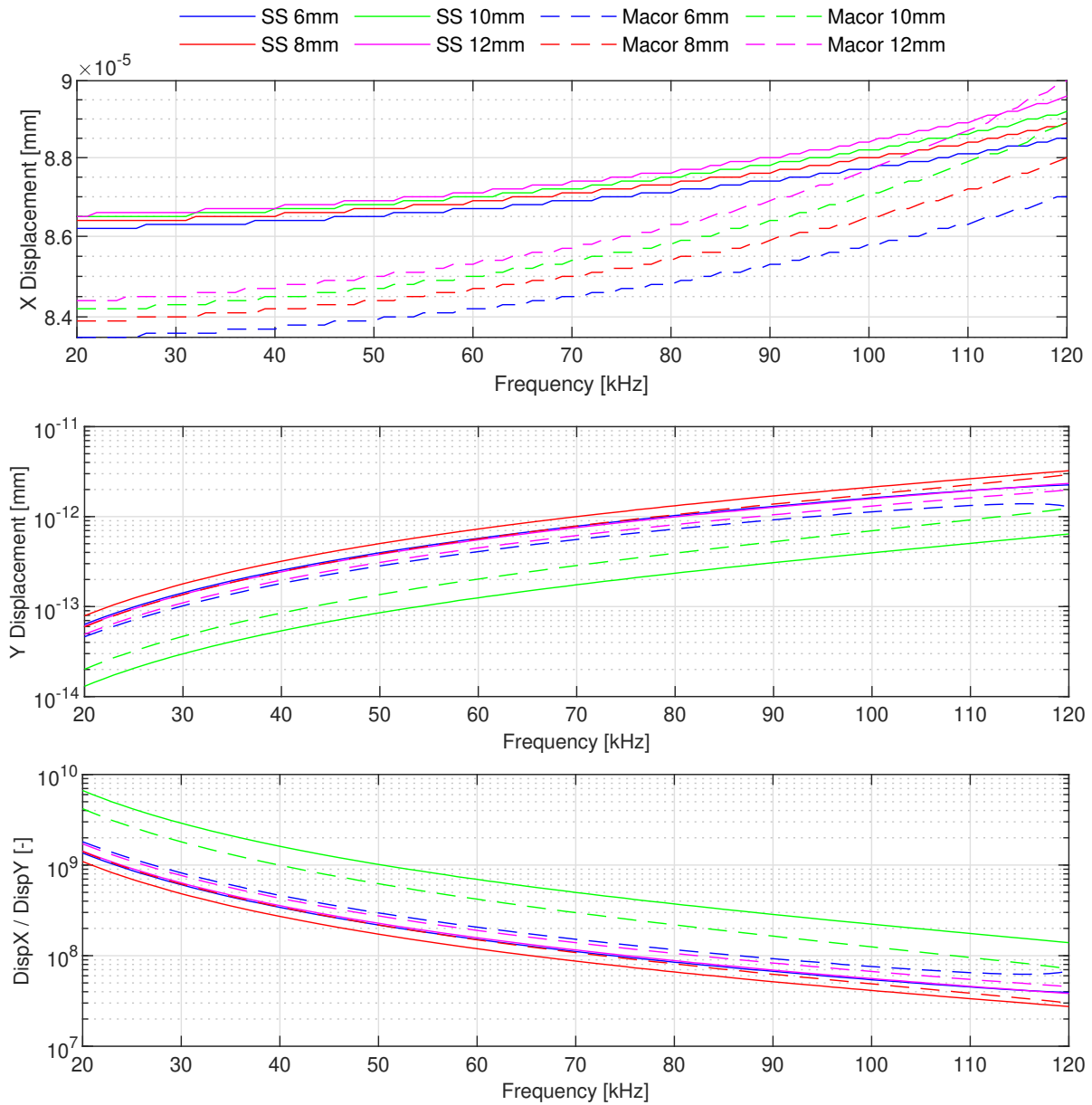
FIGURE A.6: Comparison of in-plane shear and out-of-plane displacement of width polarised parallel electrode PZT-5A transducers with stainless steel and macor backing of different thickness showing both materials have better response for a square backing shape.

A.4.2   Length Polarised Wraparound Parametric Study
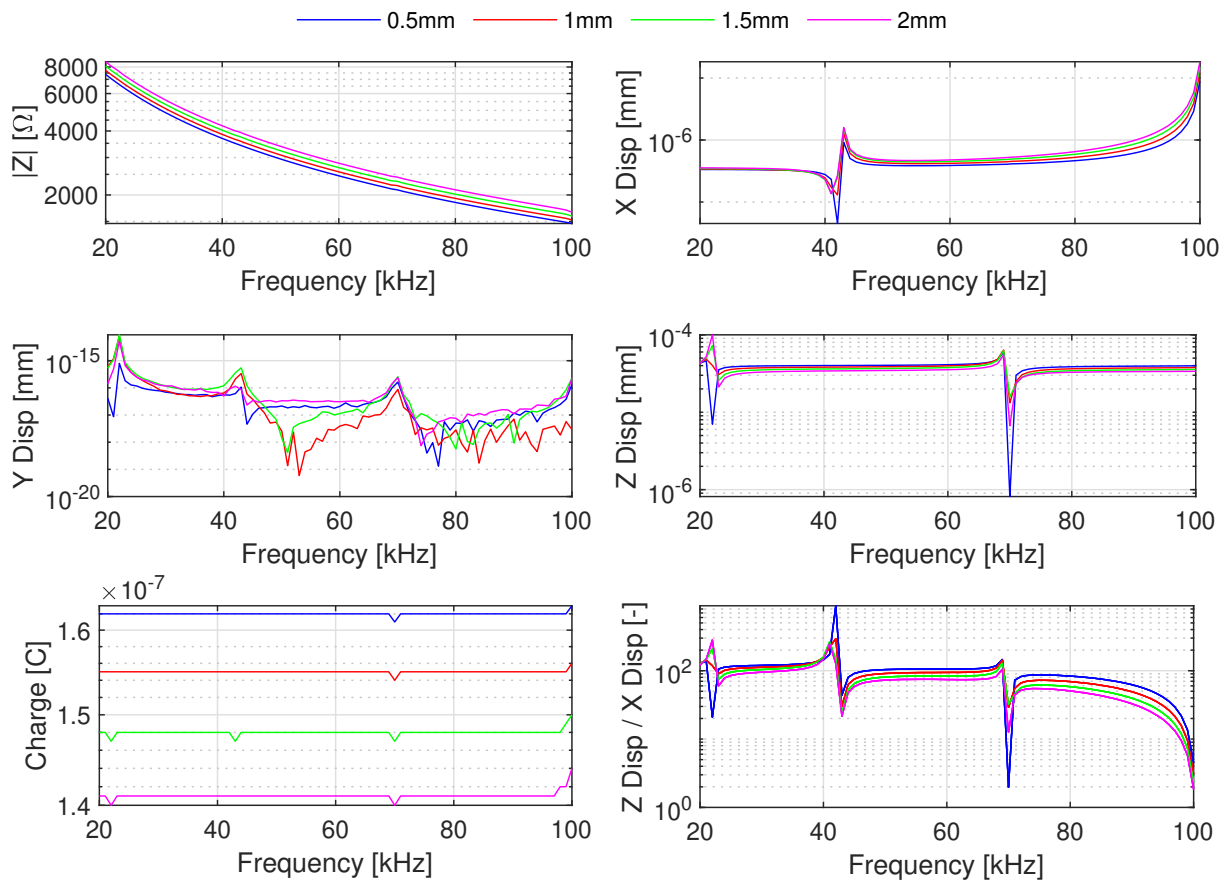
FIGURE A.7: Results from parametric study on length polarised wraparound electrode on PZT-5A response showing the impedance, in-plane-shear and out-of-plane displacement and charge as a function of operating frequency.

References

[1] Statistical review of world energy 2021. [Online]. Available: https://www.bp.com/en/global/corporate/energy-economics/statistical-review-of-world-energy.html

[2] "Energy mix - our world in data," https://ourworldindata.org/energy-mix?, (Accessed on 05/20/2023).

[3] G. V. Tsiklauri, R. J. Talbert, B. E. Schmitt, G. A. Filippov, R. G. Bogojavlensky, and E. I. Grishanin, "Supercritical steam cycle for nuclear power plant," *Nuclear Engineering and Design*, vol. 235, no. PNNL-SA-39686, 2005.

[4] T. Zhang, "Methods of improving the efficiency of thermal power plants," in *Journal of Physics: Conference Series*, vol. 1449, no. 1. IOP Publishing, 2020, p. 012001.

[5] B. Tramošljika, P. Blecich, I. Bonefačić, and V. Glažar, "Advanced ultra-supercritical coal-fired power plant with post-combustion carbon capture: analysis of electricity penalty and co2 emission reduction," *Sustainability*, vol. 13, no. 2, p. 801, 2021.

[6] "Thermal power station | thermal energy | engie," https://www.engie.com/en/activities/thermal-energy/thermal-power-stations, (Accessed on 09/22/2023).

[7] I. Le May, T. Da Silveira, and S. Cheung-Mak, "Uncertainties in the evaluation of high temperature damage in power stations and petrochemical plant," *International journal of pressure vessels and piping*, vol. 59, no. 1-3, pp. 335–343, 1994.

[8] S. H. Bush, "Failure mechanisms in nuclear power plant piping systems," *Journal of Pressure Vessel Technology*, vol. 114, no. 4, pp. 389–395, 1992, 24 citations (Crossref) [2022-11-19] _eprint: https://asmedigitalcollection.asme.org/pressurevesseltech/article-pdf/114/4/389/5623373/389_1.pdf. [Online]. Available: https://doi.org/10.1115/1.2929244

[9] B. Gaur and A. Babakr, "Piping failure in a superheated steam service–a case study," *Matériaux & Techniques*, vol. 101, no. 2, p. 206, 2013.

[10] R. Viswanathan, "An overview of failure mechanisms in high temperature componentd in power plants," *Electric Power Research Institute*, vol. 122, pp. 246–255, 2000.

[11] M. Sabouri, H. Hoseiny, and H. Faridi, "Corrosion failure of superheat steam pipes of an ammonia production plant," *Vacuum*, vol. 121, pp. 75–80, 2015.

[12] L. Y. Geng, J. M. Gong, D. Liu, and Y. Jiang, "Damage analysis and life prediction of a main steam pipeline at elevated temperature based on creep damage mechanics," in *2009 International Conference on Sustainable Power Generation and Supply*, 2009, pp. 1–6.

[13] Age of electric power generators varies widely - today in energy - u.s. energy information administration (EIA). [Online]. Available: https://www.eia.gov/todayinenergy/detail.php?id=1830

[14] I. Animah and M. Shafiee, "Condition assessment, remaining useful life prediction and life extension decision making for offshore oil and gas assets," *Journal of loss prevention in the process Industries*, vol. 53, pp. 17–28, 2018.

[15] European Commission. Joint Research Centre. Institute for the Protection and the Security of the Citizen., *Corrosionrelated accidents in petroleum refineries: lessons learned from accidents in EU and OECD countries.* Publications Office, 2013, ZSCC: NoCitationData[s0].

[16] "Norco refinery explosion 1988 - process safety integrity," https://processsafetyintegrity.com/events/1988-05-05_norco/, (Accessed on 09/30/2023).

[17] "Bbc news | world | asia-pacific | accident at japan nuclear plant," http://news.bbc.co.uk/1/hi/world/asia-pacific/3547828.stm, (Accessed on 09/30/2023).

[18] S. Xu, W. Meng, C. Wang, Z. Sun, and Y. Zhang, "Failure analysis of tp304h tubes in the superheated steam section of a reformer furnace," *Engineering Failure Analysis*, vol. 79, pp. 762–772, 2017.

[19] M. Naï *et al.*, "Root-cause analysis of superheater-tube failure," *Materiali in tehnologije*, vol. 51, no. 1, pp. 503–507, 2017.

[20] B. Hull and V. John, "Non-destructive testing," 1 1988. [Online]. Available: https://www.osti.gov/biblio/6503058

[21] R. Hanke, T. Fuchs, and N. Uhlmann, "X-ray based methods for non-destructive testing and material characterization," *Nuclear Instruments and Methods in Physics Research Section A: Accelerators, Spectrometers, Detectors and Associated Equipment*, vol. 591, no. 1, pp. 14–18, 2008.

[22] H. G. Ramos and A. L. Ribeiro, "Present and future impact of magnetic sensors in NDE," *Procedia Engineering*, vol. 86, pp. 406–419, 2014-01-01. [Online]. Available: https://www.sciencedirect.com/science/article/pii/S187770581402013X

[23] Non-destructive techniques based on eddy current testing - PubMed. [Online]. Available: https://pubmed.ncbi.nlm.nih.gov/22163754/

[24] W. M. Alobaidi, E. A. Alkuam, H. M. Al-Rizzo, and E. Sandgren, "Applications of ultrasonic techniques in oil and gas pipeline industries: A review," *American Journal of Operations Research*, vol. 05, no. 4, p. 274, 2015, number: 04 Publisher: Scientific Research Publishing. [Online]. Available: http://www.scirp.org/journal/PaperInformation.aspx?PaperID=57745&#abstract

[25] M. H. Wood, A. V. Arellano, and L. Van Wijk, "Corrosion related accidents in petroleum refineries," *European Commission Joint Research Centre, report no. EUR*, vol. 26331, 2013.

[26] D. Santos, M. A. Machado, J. Monteiro, J. P. Sousa, C. S. Proença, F. S. Crivellaro, L. S. Rosado, and T. G. Santos, "Non-destructive inspection of high temperature piping combining ultrasound and eddy current testing," *Sensors*, vol. 23, no. 6, 2023. [Online]. Available: https://www.mdpi.com/1424-8220/23/6/3348

[27] J. L. Tai, R. Grzejda, M. T. H. Sultan, A. ukaszewicz, F. S. Shahar, W. Tarasiuk, and A. Rychlik, "Experimental investigation on the corrosion detectability of a36 low carbon steel by the method of phased array corrosion mapping," *Materials*, vol. 16, no. 15, 2023. [Online]. Available: https://www.mdpi.com/1996-1944/16/15/5297

[28] J. L. Rose, "Ultrasonic guided waves in structural health monitoring," in *Key Engineering Materials*, vol. 270. Trans Tech Publ, 2004, pp. 14–21.

[29] E. H. Ling and R. H. Abdul Rahim, "A review on ultrasonic guided wave technology," *Australian Journal of Mechanical Engineering*, vol. 18, no. 1, pp. 32–44, 2020.

[30] International Institute of Welding, "Non-destructive testing Long-range inspection of above-ground pipelines and plant piping using guided wave testing with axial propagation," International Organization for Standardization,

Genoa, IT, Standard ISO 18211:2016, 2016. [Online]. Available: https://www.iso.org/standard/61765.html

[31] M. Clough, S. Dixon, M. Fleming, and M. Stone, "Evaluating an sh wave emat system for pipeline screening and extending into quantitative defect measurements," in *AIP Conference Proceedings*, vol. 1706, no. 1. AIP Publishing LLC, 2016, p. 160001.

[32] E. Kannan, B. Maxfield, and K. Balasubramaniam, "Shm of pipes using torsional waves generated by in situ magnetostrictive tapes," *Smart Materials and Structures*, vol. 16, no. 6, p. 2505, 2007.

[33] L. Zhu, Y. Wang, and F. Sun, "Single torsional guided wave excitation in pipes by frequency selection using magnetostrictive sensor technology," *ICEMI 2013*, vol. 2, pp. 872–876, 2013, ISBN: 9781479907571.

[34] N. Lunn, S. Dixon, and M. Potter, "High temperature emat design for scanning or fixed point operation on magnetite coated steel," *NDT & E International*, vol. 89, pp. 74–80, 2017.

[35] M. Kogia, T.-H. Gan, W. Balachandran, M. Livadas, V. Kappatos, I. Szabo, A. Mohimi, and A. Round, "High temperature shear horizontal electromagnetic acoustic transducer for guided wave inspection," *Sensors*, vol. 16, no. 4, 2016. [Online]. Available: https://www.mdpi.com/1424-8220/16/4/582

[36] "Sonyks guided wave testing (gwt) of pipelines | eddyfi," https://www.eddyfi.com/en/product/sonyks-guided-waves-pipeline-inspection, (Accessed on 05/20/2023).

[37] "Teletest focus+ launched - twi," https://www.twi-global.com/media-and-events/insights/teletest-focus-launched-493, (Accessed on 09/23/2023).

[38] J. Fong and M. Evans, "Guided wave testing (gwt) of high temperature piping," in *ASNT Annual Conference 2015*, 2015, pp. 41–45.

[39] R. Charchuk, C. Werstiuk, M. Evans, and E. Sjerve, "High temperature guided wave pipe inspection," in *Proceedings of Proceedings of the 4th International CANDU In-service Inspection Workshop and NDT in Canada 2012 Conference, Toronto, ON, Canada*, 2012, pp. 18–21.

[40] K. Worden, C. R. Farrar, G. Manson, and G. Park, "The fundamental axioms of structural health monitoring," *Proceedings of the Royal Society A: Mathematical,*

Physical and Engineering Sciences, vol. 463, no. 2082, pp. 1639–1664, 2007-06-08, publisher: Royal Society.

[41] C. R. Farrar and K. Worden, "An introduction to structural health monitoring," *Philosophical Transactions of the Royal Society A: Mathematical, Physical and Engineering Sciences*, vol. 365, no. 1851, pp. 303–315, 2007-02-15, publisher: Royal Society.

[42] Z. Liu and Y. Kleiner, "State-of-the-art review of technologies for pipe structural health monitoring," *IEEE Sensors Journal*, vol. 12, no. 6, pp. 1987–1992, 2012-06. [Online]. Available: http://ieeexplore.ieee.org/document/6121894/

[43] "Gul product & services catalogue," https://www.guided-ultrasonics.com/wp-content/uploads/2023/04/GUL-Catalogue2022_rev0-ENG-Web.pdf, (Accessed on 09/23/2023).

[44] "Ultrasonic guided wave testing equipment, monitoring, mss guided wave inspection system; gwa," https://www.gwanalysis.com/mssprobe.html, (Accessed on 09/23/2023).

[45] A. Dhutti, T.-H. Gan, and J. Kanfoud, "iperm a structural health monitoring device for pipelines," 2019. [Online]. Available: https://api.semanticscholar.org/CorpusID:164214736

[46] A. J. Croxford, P. D. Wilcox, B. W. Drinkwater, and G. Konstantinidis, "Strategies for guided-wave structural health monitoring," *Proceedings: Mathematical, Physical and Engineering Sciences*, vol. 463, no. 2087, pp. 2961–2981, 2007. [Online]. Available: https://doi.org/10.1098/rspa.2007.0048

[47] P. Cawley, F. Cegla, and A. Galvagni, "Guided waves for ndt and permanently-installed monitoring," *Insight-Non-Destructive Testing and Condition Monitoring*, vol. 54, no. 11, pp. 594–601, 2012.

[48] "Products and services ionix advanced technologies," https://ionixadvancedtechnologies.co.uk/products/, (Accessed on 09/24/2023).

[49] "Rosemount wireless permasense wt210 corrosion and erosion monitoring system | emerson gb," https://www.emerson.com/en-gb/catalog/rosemount-sku-permasense-wt210-corrosion-erosion-monitoring-system-en-gb, (Accessed on 09/23/2023).

[50] "Teletest technical brief: Monitoring with teletest high-temperature permamount," https://www.eddyfi.com/doc/Downloadables/

technical-brief-monitoring-with-teletest-high-temperature-permamount-01. pdf, (Accessed on 09/23/2023).

[51] "gpims system - guided ultrasonics limited," https://www.guided-ultrasonics. com/monitoring/gpims-system/, (Accessed on 09/23/2023).

[52] Guilded ultrasonics ltd. gPIMSő. [Online]. Available: https://www. guided-ultrasonics.com/gpims/

[53] Teletest focus+ | eddyfi. [Online]. Available: https://eddyfi.com/en/product/ focus

[54] S. C. Olisa, M. A. Khan, and A. Starr, "Review of current guided wave ultrasonic testing (gwut) limitations and future directions," *Sensors*, vol. 21, no. 3, 2021. [Online]. Available: https://www.mdpi.com/1424-8220/21/3/811

[55] K. Uchino, "The development of piezoelectric materials and the new perspective," in *Advanced Piezoelectric Materials*. Elsevier, 2017, pp. 1–92.

[56] J. Holterman and P. Groen, *An introduction to piezoelectric materials and components*. Stichting Applied Piezo, 2012.

[57] J. F. Tressler, S. Alkoy, and R. E. Newnham, "Piezoelectric sensors and sensor materials," *Journal of electroceramics*, vol. 2, no. 4, pp. 257–272, 1998.

[58] X. Gao, J. Yang, J. Wu, X. Xin, Z. Li, X. Yuan, X. Shen, and S. Dong, "Piezoelectric actuators and motors: Materials, designs, and applications," *Advanced Materials Technologies*, vol. 5, no. 1, p. 1900716, 2020, 37 citations (Crossref) [2021-11-13] _eprint: https://onlinelibrary.wiley.com/doi/pdf/10.1002/admt.201900716.

[59] H. Jaffe and D. Berlincourt, "Piezoelectric transducer materials," *Proceedings of the IEEE*, vol. 53, no. 10, pp. 1372–1386, 1965.

[60] A. Meitzler, H. Tiersten, A. Warner, D. Berlincourt, G. Couqin, and F. Welsh III, "Ieee standard on piezoelectricity," 1988.

[61] M. De Jong, W. Chen, H. Geerlings, M. Asta, and K. A. Persson, "A database to enable discovery and design of piezoelectric materials," *Scientific data*, vol. 2, no. 1, pp. 1–13, 2015.

[62] T. C. Tavernor, a W, and a W, "Aspect Ratio dependence of d15 measurements in Motorola 3203 material," *Journal of the European Ceramic Society*, vol. 21, pp. 9–12, 2001.

[63] B. EN, "50324-2: 2002, piezoelectric properties of ceramic materials and componentspart 2: Methods of measurement," *British Standards*, 2002.

[64] J. Yang *et al.*, *An introduction to the theory of piezoelectricity*. Springer, 2005, vol. 9.

[65] M. J. Schulz, M. J. Sundaresan, J. Mcmichael, D. Clayton, R. Sadler, and B. Nagel, "Piezoelectric materials at elevated temperature," *Journal of Intelligent Material Systems and Structures*, vol. 14, no. 11, pp. 693–705, 2003.

[66] R. Georges Sabat, B. K. Mukherjee, W. Ren, and G. Yang, "Temperature dependence of the complete material coefficients matrix of soft and hard doped piezoelectric lead zirconate titanate ceramics," *Journal of Applied Physics*, vol. 101, no. 6, 2007.

[67] I. Ohno, K. Harada, and C. Yoshitomi, "Temperature variation of elastic constants of quartz across the α-β transition," *Physics and Chemistry of Minerals*, vol. 33, pp. 1–9, 2006. [Online]. Available: https://doi.org/10.1007/s00269-005-0008-3

[68] D. Damjanovic, "Materials for high temperature piezoelectric transducers," *Current Opinion in Solid State and Materials Science*, vol. 3, pp. 469–473, 1998. [Online]. Available: https://doi.org/10.1016/S1359-0286(98)80009-0

[69] H. Shekhani and K. Uchino, "Evaluation of the mechanical quality factor under high power conditions in piezoelectric ceramics from electrical power," *Journal of the European Ceramic Society*, vol. 35, no. 2, pp. 541–544, 2015.

[70] X. P. Qing, H.-L. Chan, S. J. Beard, T. K. Ooi, and S. A. Marotta, "Effect of adhesive on the performance of piezoelectric elements used to monitor structural health," *International Journal of Adhesion and Adhesives*, vol. 26, no. 8, pp. 622–628, 2006.

[71] M. Islam and H. Huang, "Effects of adhesive thickness on the lamb wave pitch-catch signal using bonded piezoelectric wafer transducers," *Smart Materials and Structures*, vol. 25, no. 8, p. 085014, 2016.

[72] X. Liu, Y. Xu, X. Wang, Y. Ran, and W. Zhang, "Effect of adhesive and its aging on the performance of piezoelectric sensors in structural health monitoring systems," *Metals*, vol. 10, no. 10, 2020. [Online]. Available: https://www.mdpi.com/2075-4701/10/10/1342

[73] T. Wandowski, J. Moll, P. Malinowski, S. Opoka, and W. Ostachowicz, "Assessment of piezoelectric sensor adhesive bonding," in *Journal of Physics: Conference Series*, vol. 628, no. 1. IOP Publishing, 2015, p. 012114.

[74] X. Liu, Y. Xu, N. Li, X. Wang, and W. Zhang, "Effect of adhesive debonding on the performance of piezoelectric sensors in structural health

monitoring systems," *Sensors*, vol. 19, no. 23, 2019. [Online]. Available: https://www.mdpi.com/1424-8220/19/23/5070

[75] "Onscale solve - the cloud engineering simulation platform | onscale," https://onscale.com/, (Accessed on 10/03/2023).

[76] D. Chen, L. Wang, X. Luo, C. Fei, D. Li, G. Shan, and Y. Yang, "Recent development and perspectives of optimization design methods for piezoelectric ultrasonic transducers," *Micromachines*, vol. 12, no. 7, p. 779, 2021.

[77] B. Fu, T. Hemsel, and J. Wallaschek, "Piezoelectric transducer design via multiobjective optimization," *Ultrasonics*, vol. 44, pp. e747–e752, 2006. [Online]. Available: https://doi.org/10.1016/j.ultras.2006.05.087

[78] G. Rus, S.-C. Wooh, and R. Gallego, "Design of ultrasonic wedge transducer," *Ultrasonics*, vol. 43, no. 5, pp. 391–395, 2005. [Online]. Available: https://doi.org/10.1016/j.ultras.2004.10.002

[79] J. L. Rose, *Ultrasonic Guided Waves in Solid Media*. Cambridge University Press, 2014-08-11, google-Books-ID: tIHRAwAAQBAJ.

[80] J. Zemanek, "An experimental and theoretical investigation of elastic wave propagation in a cylinder," *The Journal of the Acoustical Society of America*, vol. 51, no. 1, pp. 265–283, 1972-01-01, ZSCC: 0000347 68 citations (Crossref) [2021-08-17] Publisher: Acoustical Society of America.

[81] A. H. Meitzler, "Mode coupling occurring in the propagation of elastic pulses in wires," *The Journal of the Acoustical Society of America*, vol. 33, no. 4, pp. 435–445, 1961.

[82] J. Krautkrämer and H. Krautkrämer, "Wave physics of the sound field," *Ultrasonic Testing of Materials*, pp. 58–92, 1990.

[83] P. Wilcox, M. Lowe, and P. Cawley, "The effect of dispersion on long-range inspection using ultrasonic guided waves," *Ndt & E International*, vol. 34, no. 1, pp. 1–9, 2001.

[84] M. Lowe, B. Pavlakovic, and P. Cawley, "A model for predicting the properties of guided ultrasonic waves, and illustration of its application to ndt," 1999.

[85] P. Bocchini, A. Marzani, and E. Viola, "Graphical user interface for guided acoustic waves," *Journal of Computing in Civil Engineering*, vol. 25, no. 3, pp. 202–210, 2010.

[86] C. Hakoda, J. Rose, P. Shokouhi, and C. Lissenden, "Using Floquet periodicity to easily calculate dispersion curves and wave structures of homogeneous waveguides," *AIP Conference Proceedings*, vol. 1949, no. April, 2018.

[87] M. J. S. Lowe and P. Cawley, "Long range guided wave inspection usage current commercial capabilities and research directions," p. 40.

[88] J. Li and J. L. Rose, "Excitation and propagation of non-axisymmetric guided waves in a hollow cylinder," *The Journal of the Acoustical Society of America*, vol. 109, no. 2, pp. 457–464, 02 2001. [Online]. Available: https://doi.org/10.1121/1.1315290

[89] M. J. Lowe, D. N. Alleyne, and P. Cawley, "Defect detection in pipes using guided waves," *Ultrasonics*, vol. 36, no. 1, pp. 147–154, 1998-02. [Online]. Available: https://linkinghub.elsevier.com/retrieve/pii/S0041624X97000383

[90] F. B. Cegla and B. Herdovics, "Guided wave testing," Apr. 20 2021, uS Patent 10,983,096.

[91] D. N. Alleyne and P. Cawley, "The excitation of lamb waves in pipes using dry-coupled piezoelectric transducers," *Journal of Nondestructive Evaluation*, vol. 15, no. 1, pp. 11–20, 1996-03.

[92] D. N. Alleyne, P. Cawley, A. Lank, and P. Mudge, "The lamb wave inspection of chemical plant pipework," in *Review of Progress in Quantitative Nondestructive Evaluation*. Springer, 1997, pp. 1269–1276.

[93] P. Cawley and D. Alleyne, "The use of lamb waves for the long range inspection of large structures," *Ultrasonics*, vol. 34, no. 2-5, pp. 287–290, 1996.

[94] A. Demma, P. Cawley, M. Lowe, and A. G. Roosenbrand, "The reflection of the fundamental torsional mode from cracks and notches in pipes," *The Journal of the Acoustical Society of America*, vol. 114, no. 2, pp. 611–625, 07 2003. [Online]. Available: https://doi.org/10.1121/1.1582439

[95] S. H. Cho, H. W. Kim, and Y. Y. Kim, "Megahertz-range guided pure torsional wave transduction and experiments using a magnetostrictive transducer," *IEEE Transactions on Ultrasonics, Ferroelectrics, and Frequency Control*, vol. 57, no. 5, pp. 1225–1229, 2010.

[96] M. Ratassepp, S. Fletcher, and M. J. S. Lowe, "Scattering of the fundamental torsional mode at an axial crack in a pipe," *The Journal of the Acoustical Society of America*, vol. 127, no. 2, pp. 730–740, 02 2010. [Online]. Available: https://doi.org/10.1121/1.3277185

[97] A. Løvstad and P. Cawley, "The reflection of the fundamental torsional mode from pit clusters in pipes," *NDT E International*, vol. 46, pp. 83–93, 2012. [Online]. Available: https://www.sciencedirect.com/science/article/pii/S096386951100171X

[98] D. Alleyne and P. Cawley, "The effect of discontinuities on the long-range propagation of lamb waves in pipes," *Proceedings of the Institution of Mechanical Engineers, Part E: Journal of Process Mechanical Engineering*, vol. 210, no. 3, pp. 217–226, 1996.

[99] A. Galvagni and P. Cawley, "The reflection of guided waves from simple supports in pipes," p. 13.

[100] P. Cawley, M. J. Lowe, F. Simonetti, C. Chevalier, and A. G. Roosenbrand, "The variation of the reflection coefficient of extensional guided waves in pipes from defects as a function of defect depth, axial extent, circumferential extent and frequency," *Proceedings of the Institution of Mechanical Engineers, Part C: Journal of Mechanical Engineering Science*, vol. 216, no. 11, pp. 1131–1144, 2002-11.

[101] R. Carandente, J. Ma, and P. Cawley, "The scattering of the fundamental torsional mode from axi-symmetric defects with varying depth profile in pipes," *The Journal of the Acoustical Society of America*, vol. 127, no. 6, pp. 3440–3448, 2010-06. [Online]. Available: https://doi.org/10.1121/1.3373406

[102] E. Rojas, A. Baltazar, and C. Treesatayapun, "Investigation on damage identification in a pipe using torsional guided waves," in *AIP Conference Proceedings*, vol. 1806, no. 1. AIP Publishing, 2017, p. 0300Mohimi2014a18.

[103] A. Demma, P. Cawley, M. Lowe, and A. G. Roosenbrand, "The reflection of the fundamental torsional mode from cracks and notches in pipes," p. 16.

[104] A. Løvstad and P. Cawley, "The reflection of the fundamental torsional guided wave from multiple circular holes in pipes," *NDT & E International*, vol. 44, no. 7, pp. 553–562, 2011.

[105] A. Mazzeranghi and D. Vangi, "Methodology for minimizing effects of temperature in monitoring with the acousto-ultrasonic technique," *Experimental Mechanics*, vol. 39, no. 2, pp. 86–91, 1999. [Online]. Available: http://link.springer.com/10.1007/BF02331110

[106] Y. Lu and J. E. Michaels, "A methodology for structural health monitoring with diffuse ultrasonic waves in the presence of temperature variations," *Ultrasonics*, vol. 43, no. 9, pp. 717–731, 2005-10. [Online]. Available: https://linkinghub.elsevier.com/retrieve/pii/S0041624X05000429

[107] G. Konstantinidis, P. D. Wilcox, and B. W. Drinkwater, "An investigation into the temperature stability of a guided wave structural health monitoring system using permanently attached sensors," *IEEE Sensors Journal*, vol. 7, no. 5, pp. 905–912, 2007. [Online]. Available: https://doi.org/10.1109/JSEN.2007.894908

[108] K. M. Prabhu, *Window functions and their applications in signal processing*. Taylor & Francis, 2014.

[109] F. J. Harris, "On the use of windows for harmonic analysis with the discrete fourier transform," *Proceedings of the IEEE*, vol. 66, no. 1, pp. 51–83, 1978.

[110] Z. Maekawa, J. Rindel, and P. Lord, *Environmental and architectural acoustics*. CRC Press, 2010.

[111] P. Y. Ktonas and N. Papp, "Instantaneous envelope and phase extraction from real signals: Theory, implementation, and an application to EEG analysis," *Signal Processing*, vol. 2, no. 4, pp. 373–385, 1980-10-01. [Online]. Available: https://www.sciencedirect.com/science/article/pii/0165168480900791

[112] D. G. Manolakis and V. K. Ingle, *Applied digital signal processing: theory and practice*. Cambridge university press, 2011.

[113] T. Clarke, P. Cawley, P. D. Wilcox, and A. J. Croxford, "Evaluation of the damage detection capability of a sparse-array guided-wave shm system applied to a complex structure under varying thermal conditions," *IEEE transactions on ultrasonics, ferroelectrics, and frequency control*, vol. 56, no. 12, pp. 2666–2678, 2009.

[114] L. Bandyopadhyay, S. Chaulya, and P. Mishra, "Intrinsic safety for hazardous area," in *Wireless Communication in Underground Mines*. Springer, 2010, pp. 299–378.

[115] L. Yu and V. Giurgiutiu, "Advanced signal processing for enhanced damage detection with piezoelectric wafer active sensors," *Smart Structures and Systems*, vol. 1, no. 2, pp. 185–215, 2005.

[116] P. Wilcox, A. Croxford, J. Michaels, Y. Lu, and B. Drinkwater, "A comparison of temperature compensation methods for guided wave structural health monitoring," in *AIP conference proceedings*, vol. 975, no. 1. American Institute of Physics, 2008, pp. 1453–1460. [Online]. Available: https://doi.org/10.1063/1.2902606

[117] R. Gorgin, Y. Luo, and Z. Wu, "Environmental and operational conditions effects on lamb wave based structural health monitoring systems: A review," *Ultrasonics*, vol. 105, p. 106114, 2020.

[118] K. Shinekumar and S. Dutta, "High-temperature piezoelectrics with large piezoelectric coefficients," *Journal of Electronic Materials*, vol. 44, no. 2, pp. 613–622, 2015. [Online]. Available: https://link.springer.com/article/10.1007/s11664-014-3534-2

[119] R. Kazys, A. Voleisis, and B. Voleisiene, "High temperature ultrasonic transducers," *Ultrasound*, vol. 63, no. 2, pp. 7–17, 2008.

[120] S. Zhang and F. Yu, "Piezoelectric materials for high temperature sensors," *Journal of the American Ceramic Society*, vol. 94, no. 10, pp. 3153–3170, 2011. [Online]. Available: http://doi.wiley.com/10.1111/j.1551-2916.2011.04792.x

[121] Y. Wang, J. Wu, D. Xiao, J. Zhu, P. Yu, L. Wu, and X. Li, "Piezoelectric properties of (li, ag) modified (na0.50 k0.50) nbo3 lead-free ceramics with high curie temperature," *Journal of alloys and compounds*, vol. 459, no. 1-2, pp. 414–417, 2008. [Online]. Available: https://doi.org/10.1016/j.jallcom.2007.04.287

[122] R. Tickoo, R. Tandon, K. Bamzai, and P. Kotru, "Dielectric and piezoelectric characteristics of samarium modified lead titanate ceramics," *Materials Science and Engineering: B*, vol. 103, no. 2, pp. 145–151, 2003. [Online]. Available: https://www.sciencedirect.com/science/article/pii/S0921510703001788

[123] V. Rahangdale and V. Deshpande, "Study of dielectric and ferroelectric properties of lead titanate glass–ceramics," *Transactions of the Indian Institute of Metals*, vol. 67, pp. 701–707, 2014.

[124] Z. Liu, H. Wu, Y. Yuan, H. Wan, Z. Luo, P. Gao, J. Zhuang, J. Zhang, N. Zhang, J. Li, Y. Zhan, W. Ren, and Z.-G. Ye, "Recent progress in bismuth-based high curie temperature piezo-/ferroelectric perovskites for electromechanical transduction applications," *Current Opinion in Solid State and Materials Science*, vol. 26, no. 5, p. 101016, 2022. [Online]. Available: https://www.sciencedirect.com/science/article/pii/S1359028622000365

[125] Y. Dong, K. Zou, R. Liang, and Z. Zhou, "Review of bisco3-pbtio3 piezoelectric materials for high temperature applications: fundamental, progress, and perspective," *Progress in Materials Science*, vol. 132, p. 101026, 2023. [Online]. Available: https://www.sciencedirect.com/science/article/pii/S0079642522001074

[126] J. W. Griffin, G. J. Posakony, R. V. Harris, D. L. Baldwin, A. M. Jones, and L. J. Bond, "High temperature ultrasonic transducers for in-service inspection of liquid metal fast reactors," in *2011 IEEE International Ultrasonics Symposium*. IEEE, 2011, pp. 1924–1927.

[127] Y. Meng, G. Chen, and M. Huang, "Piezoelectric materials: Properties, advancements, and design strategies for high-temperature applications," *Nanomaterials*, vol. 12, no. 7, 2022. [Online]. Available: https://www.mdpi.com/2079-4991/12/7/1171

[128] C. Long, B. Wang, W. Ren, K. Zheng, H. Fan, D. Wang, and L. Liu, "Significantly enhanced electrical properties in cabi2nb2o9-based high-temperature piezoelectric ceramics," *Applied Physics Letters*, vol. 117, no. 3, 2020.

[129] S. Sherrit, "Smart material/actuator needs in extreme environments in space," in *Smart Structures and Materials 2005: Active Materials: Behavior and Mechanics*, vol. 5761. SPIE, 2005, pp. 335–346.

[130] A. D. Suprock and B. R. Tittmann, "Development of high temperature capable piezoelectric sensors," *AIP Conference Proceedings*, vol. 1806, no. 1, p. 050007, 02 2017. [Online]. Available: https://doi.org/10.1063/1.4974601

[131] F. Chen, L. Kong, W. Song, C. Jiang, S. Tian, F. Yu, L. Qin, C. Wang, and X. Zhao, "The electromechanical features of linbo3 crystal for potential high temperature piezoelectric applications," *Journal of Materiomics*, vol. 5, no. 1, pp. 73–80, 2019. [Online]. Available: https://www.sciencedirect.com/science/article/pii/S2352847818300923

[132] D. Fraser and A. Warner, "Lithium niobate: A high-temperature piezoelectric transducer material," *Journal of Applied Physics*, vol. 37, no. 10, pp. 3853–3854, 1966. [Online]. Available: https://doi.org/10.1063/1.1707937

[133] R. Hauser, L. Reindl, and J. Biniasch, "High-temperature stability of linbo/sub 3/based saw devices," in *IEEE Symposium on Ultrasonics, 2003*, vol. 1. IEEE, 2003, pp. 192–195.

[134] S. Zhang, F. Li, F. Yu, X. Jiang, H.-Y. Lee, J. Luo, T. R. Shrout, S. Zhang, F. Li, F. Yu *et al.*, "Recent developments in piezoelectric crystals," *Journal of the Korean Ceramic Society*, vol. 55, no. 5, pp. 419–439, 2018.

[135] F.-p. Yu, F.-f. Chen, S. Hou, H.-w. Wang, Y.-a. Wang, S.-w. Tian, C. Jiang, Y.-l. Li, X.-f. Cheng, and X. Zhao, "High temperature piezoelectric single crystals: Recent developments," in *2016 Symposium on Piezoelectricity, Acoustic Waves, and Device Applications (SPAWDA)*. IEEE, 2016, pp. 1–7.

[136] Q. Zheng, B. Shi, Z. Li, and Z. L. Wang, "Recent progress on piezoelectric and triboelectric energy harvesters in biomedical systems," *Advanced Science*, vol. 4, no. 7, p. 1700029, 2017.

[137] T. R. Shrout, S. Zhang, R. Eitel, C. Stringer, and C. Randall, "High performance, high temperature perovskite piezoelectrics," in *Applications of Ferroelectrics, 2004. ISAF-04. 2004 14th IEEE International Symposium on*. IEEE, 2004, pp. 126–129. [Online]. Available: https://doi.org/10.1109/ISAF.2004.1418353

[138] P. Krempl, G. Schleinzer, W. Wallno *et al.*, "Gallium phosphate, gapo 4: a new piezoelectric crystal material for high-temperature sensorics," *Sensors and Actuators A: Physical*, vol. 61, no. 1, pp. 361–363, 1997. [Online]. Available: https://doi.org/10.1016/S0924-4247(97)80289-0

[139] M. Kostan, A. Mohimi, C. Nageswaran, A. Dhutti, T.-H. Gan, L. Wrobel, and C. Selcuk, "High temperature gallium orthophosphate transducers for ndt," *Procedia Engineering*, vol. 168, pp. 987–990, 2016.

[140] M. Kostan, "Design and fabrication of gapo4 ultrasonic transducer for ndt at high temperatures," Ph.D. dissertation, Brunel University London, 2018.

[141] M. Kostan, A. Mohimi, C. Nageswaran, V. Kappatos, L. Cheng, T.-H. Gan, L. Wrobel, and C. Selcuk, "Assessment of material properties of gallium orthophosphate piezoelectric elements for development of phased array probes for continuous operation at 580 c," in *IOP Conference Series: Materials Science and Engineering*, vol. 108, no. 1. IOP Publishing, 2016, p. 012008.

[142] V. Giurgiutiu, B. Xu, and W. Liu, "Development and testing of high-temperature piezoelectric wafer active sensors for extreme environments," *Structural Health Monitoring*, vol. 9, no. 6, pp. 513–525, 2010.

[143] Roditi, "Lithium Niobate Properties," available at http://www.roditi.com/SingleCrystal/LiNbO3/liNBO3-Properties.html.

[144] "Products," https://www.piezocryst.com/en/products, (Accessed on 10/21/2023).

[145] D. Palmier, R. Gohier, C. Bonjour, G. Martin, A. Zarembovitch, E. Bigler, and E. Philippot, "New results on the thermal sensitivity of bulk and surface modes of gallium orthophosphate GaPO4," in *1995 IEEE Ultrasonics Symposium. Proceedings. An International Symposium*, vol. 1. IEEE, 1995, pp. 605–610.

[146] H. Thanner, P. W. Krempl, R. Selic, W. Wallnöfer, and P. M. Worsch, "GaPO4 high temperature crystal microbalance demonstration up to 720řc," *Journal of thermal analysis and calorimetry*, vol. 71, pp. 53–59, 2003.

[147] M. N. Hamidon, V. Skarda, N. White, F. Krispel, P. Krempl, M. Binhack, and W. Buff, "Fabrication of high temperature surface acoustic wave devices for sensor applications," *Sensors and Actuators A: Physical*, vol. 123, pp. 403–407, 2005.

[148] L. B. Silva and E. J. Santos, "Quartz and gapo 4 pressure transducers for high resolution applications in high temperature: A simulation approach," in *2014 29th Symposium on Microelectronics Technology and Devices (SBMicro)*. IEEE, 2014, pp. 1–4.

[149] F. Krispel, C. Reiter, J. Neubig, F. Lenzenhuber, P. Krempl, W. Wallnofer, and P. Worsch, "Properties and applications of singly rotated gapo/sub 4/resonators," in *IEEE International Frequency Control Symposium and PDA Exhibition Jointly with the 17th European Frequency and Time Forum, 2003. Proceedings of the 2003*. IEEE, 2003, pp. 668–673.

[150] H. Fritze, "High-temperature piezoelectric crystals and devices," *Journal of electroceramics*, vol. 26, pp. 122–161, 2011.

[151] M. P. Da Cunha, R. Lad, T. Moonlight, G. Bernhardt, and D. Frankel, "High temperature stability of langasite surface acoustic wave devices," in *2008 IEEE Ultrasonics Symposium*. IEEE, 2008, pp. 205–208.

[152] S. Zhang, Y. Zheng, H. Kong, J. Xin, E. Frantz, and T. R. Shrout, "Characterization of high temperature piezoelectric crystals with an ordered langasite structure," *Journal of Applied Physics*, vol. 105, no. 11, 2009.

[153] F.-p. Yu, X.-l. Duan, S.-j. Zhang, Y.-g. Yu, T.-f. Ma, and X. Zhao, "Temperature dependence of electro-elastic properties of yttrium calcium oxyborate single crystlals," in *2012 Symposium on Piezoelectricity, Acoustic Waves, and Device Applications (SPAWDA)*. IEEE, 2012, pp. 293–297.

[154] K. Kim, S. Zhang, G. Salazar, and X. Jiang, "Design, fabrication and characterization of high temperature piezoelectric vibration sensor using ycob crystals," *Sensors and Actuators A: Physical*, vol. 178, pp. 40–48, 2012.

[155] R. Cheng, J. Ren, J. Guo, X. Zhang, and S. Guo, "Stable dielectric, elastic, and piezoelectric properties of yb3+: Cngs crystals at high temperature," *Materials Research Bulletin*, vol. 100, pp. 15–17, 2018.

[156] Y. Suhak, M. Schulz, A. Sotnikov, H. Schmidt, S. Ganschow, S. Sakharov, and H. Fritze, "Dielectric, piezoelectric and elastic constants of ca3taga3si2o14 single crystals at elevated temperatures," *Ferroelectrics*, vol. 537, no. 1, pp. 255–263, 2018.

[157] Y. Li, Z. Jia, Y. Yin, Q. Hu, W. Mu, J. Zhang, X. Yu, and X. Tao, "Temperature dependence of the thermal, electrical resistivity, dielectric and piezoelectric properties of cayal3o7 crystal," *Crystals*, vol. 8, no. 1, p. 34, 2018.

[158] N.-I. Kim, Y.-L. Chang, J. Chen, T. Barbee, W. Wang, J.-Y. Kim, M.-K. Kwon, S. Shervin, M. Moradnia, S. Pouladi *et al.*, "Piezoelectric pressure sensor based on flexible gallium nitride thin film for harsh-environment and high-temperature applications," *Sensors and Actuators A: Physical*, vol. 305, p. 111940, 2020.

[159] R. Kazys, A. Voleisis, R. Sliteris, L. Mazeika, R. Van Nieuwenhove, P. Kupschus, and H. A. Abderrahim, "High temperature ultrasonic transducers for imaging and measurements in a liquid pb/bi eutectic alloy," *IEEE Transactions on ultrasonics, ferroelectrics, and frequency control*, vol. 52, no. 4, pp. 525–537, 2005.

[160] T. Kim, J. Kim, R. Dalmau, R. Schlesser, E. Preble, and X. Jiang, "High-temperature electromechanical characterization of aln single crystals," *IEEE Transactions on Ultrasonics, Ferroelectrics, and Frequency Control*, vol. 62, no. 10, pp. 1880–1887, 2015.

[161] B. R. Tittmann, D. A. Parks, S. O. Zhang, B. Tittman, D. A. Parks, and O. Zhang, "High Temperature Piezoelectrics - A Comparison," *13th International Symposium on Nondestructive Characterisation of Materials (NDCM-XIII)*, no. May, pp. 20–24, 2013. [Online]. Available: http://www.ndt.net/?id=15537

[162] D. Parks, B. Tittmann, and M. Kropf, "Aluminum nitride as a high temperature transducer," in *AIP Conference Proceedings*, vol. 1211, no. 1. American Institute of Physics, 2010, pp. 1029–1034.

[163] V. Prisedsky, V. Shishkovsky, and V. Klimov, "High-temperature electrical conductivity and point defects in lead zirconate-titanate," *Ferroelectrics*, vol. 17, no. 1, pp. 465–468, 1977. [Online]. Available: https://doi.org/10.1080/00150197808236768

[164] R. Turner, P. A. Fuierer, R. Newnham, and T. Shrout, "Materials for high temperature acoustic and vibration sensors: A review," *Applied acoustics*, vol. 41, no. 4, pp. 299–324, 1994. [Online]. Available: https://doi.org/10.1016/0003-682X(94)90091-4

[165] Y.-q. Zheng, S.-x. Cui, J.-j. Chen, X.-n. Tu, J. Xin, H.-k. Kong, and E.-w. Shi, "Advances in design, growth and application of piezoelectric crystals with langasite structure," in *Piezoelectricity, Acoustic Waves and Device Applications (SPAWDA), 2012 Symposium on*. IEEE, 2012, pp. 252–259. [Online]. Available: https://doi.org/10.1109/SPAWDA.2012.6464083

[166] H. Fritze, H. Seh, H. Tuller, and G. Borchardt, "Operation limits of langasite high temperature nanobalances," *Journal of the European Ceramic Society*, vol. 21, no. 10, pp. 1473–1477, 2001. [Online]. Available: https://doi.org/10.1016/S0955-2219(01)00044-9

[167] X. Jiang, K. Kim, S. Zhang, J. Johnson, and G. Salazar, "High-temperature piezoelectric sensing," *Sensors (Switzerland)*, vol. 14, no. 1, pp. 144–169, 2013. [Online]. Available: https://doi.org/10.3390/s140100144

[168] D. Richter and H. Fritze, "High-temperature stable electrodes for langasite based surface acoustic wave devices," in *Sensor+Test Conferences*, 2011-06-09, pp. 532–537.

[169] M. P. da Cunha, T. Moonlight, R. Lad, D. Frankel, and G. Bernhard, "High temperature sensing technology for applications up to 1000řc," in *2008 IEEE Sensors*. IEEE, 2008-10, pp. 752–755. [Online]. Available: http://ieeexplore.ieee.org/document/4716550/

[170] S. Firebaugh, K. Jensen, and M. Schmidt, "Investigation of high-temperature degradation of platinum thin films with an in situ resistance measurement apparatus," *Journal of Microelectromechanical Systems*, vol. 7, no. 1, pp. 128–135, 1998-03. [Online]. Available: http://ieeexplore.ieee.org/document/661395/

[171] J.-S. Lee, H.-D. Park, S.-M. Shin, and J.-W. Park, "Agglomeration phenomena of high temperature coefcient of resistance platinum lms deposited by electron beam evaporation," vol. 16, pp. 1257–1259, 1997. [Online]. Available: https://doi.org/10.1023/A:1018562505640

[172] J. D. Wrbanek, K. L. H. Laster, A. Corporation, and B. Park, "Preparation and analysis of platinum thin films for high temperature sensor applications," p. 26, 2005.

[173] M. Pereira da Cunha, T. Moonlight, R. Lad, G. Bernhardt, and D. Frankel, "P4l-1 enabling very high temperature acoustic wave devices for sensor & frequency control applications," in *2007 IEEE Ultrasonics Symposium Proceedings*. IEEE, 2007-10, pp. 2107–2110. [Online]. Available: https://ieeexplore.ieee.org/document/4410103/

[174] A. Mohimi, "High temperature ultrasonic guided wave transducers," May 2014, ph.D. thesis.

[175] A. Mohimi, T.-H. Gan, and W. Balachandran, "Development of high temperature ultrasonic guided wave transducer for continuous in service monitoring of steam

lines using non-stoichiometric lithium niobate piezoelectric ceramic," *Sensors and Actuators A: Physical*, vol. 216, pp. 432–442, 2014.

[176] X. Zhang, Y. Wang, X. Gao, Y. Ji, F. Qian, J. Fan, H. Wang, L. Qiu, W. Li, and H. Yang, "High-temperature and flexible piezoelectric sensors for lamb-wave-based structural health monitoring," *ACS Applied Materials & Interfaces*, vol. 13, no. 40, pp. 47 764–47 772, 2021, pMID: 34582188. [Online]. Available: https://doi.org/10.1021/acsami.1c13704

[177] D. Enciu, I. Ursu, and A. Toader, "New results concerning structural health monitoring technology qualification for transfer to space vehicles," *Structural Control and Health Monitoring*, vol. 24, no. 10, p. e1992, 2017, e1992 STC-16-0066.R2. [Online]. Available: https://onlinelibrary.wiley.com/doi/abs/10.1002/stc.1992

[178] C. Fei, T. Zhao, J. Zhang, Y. Quan, D. Wang, X. Yang, Q. Chen, P. Lin, D. Li, Y. Yang, S. Dong, W. Ren, K. K. Shung, and Q. Zhou, "0.36bisco3-0.64pbtio3 piezoelectric ceramics for high temperature ultrasonic transducer applications," *Journal of Alloys and Compounds*, vol. 743, pp. 365–371, 2018. [Online]. Available: https://www.sciencedirect.com/science/article/pii/S0925838818304122

[179] K. Zou, Q. Yue, J. Li, W. Zhang, R. Liang, and Z. Zhou, "High-performance ultrasonic transducer based on pzt piezoelectric ceramic for high-temperature nde," *Ultrasonics*, vol. 132, p. 107013, 2023. [Online]. Available: https://www.sciencedirect.com/science/article/pii/S0041624X23000896

[180] J. W. Griffin, T. J. Peters, G. J. Posakony, H.-T. Chien, L. J. Bond, K. M. Denslow, S.-H. Sheen, and P. Raptis, "Under-sodium viewing: a review of ultrasonic imaging technology for liquid metal fast reactors," 2009.

[181] V. Vaskeliene, R. Sliteris, R. J. Kazys, E. Zukauskas, and L. Mazeika, "Development and investigation of high-temperature ultrasonic measurement transducers resistant to multiple heatingndash;cooling cycles," *Sensors*, vol. 23, no. 4, 2023. [Online]. Available: https://www.mdpi.com/1424-8220/23/4/1866

[182] C. Fei, X. Liu, B. Zhu, D. Li, X. Yang, Y. Yang, and Q. Zhou, "Aln piezoelectric thin films for energy harvesting and acoustic devices," *Nano Energy*, vol. 51, pp. 146–161, 2018. [Online]. Available: https://www.sciencedirect.com/science/article/pii/S2211285518304579

[183] C. T. Searfass, C. Pheil, K. Sinding, B. R. Tittmann, A. Baba, and D. K. Agrawal, "Bismuth titanate fabricated by spray-on deposition and microwave sintering

for high-temperature ultrasonic transducers," *IEEE Transactions on Ultrasonics, Ferroelectrics, and Frequency Control*, vol. 63, no. 1, pp. 139–146, 2016.

[184] M. Kobayashi, Y. Ono, C.-K. Jen, and C.-C. Cheng, "High-temperature piezoelectric film ultrasonic transducers by a sol-gel spray technique and their application to process monitoring of polymer injection molding," *IEEE Sensors Journal*, vol. 6, no. 1, pp. 55–62, 2006.

[185] M. Sahoo and S. Dutta, "Thick films for high-temperature piezoelectric applications-a future reference," *Journal of Electroceramics*, pp. 1–12, 2023.

[186] J. Yin, S. Chen, V.-K. Wong, and K. Yao, "Thermal sprayed lead-free piezoelectric ceramic coatings for ultrasonic structural health monitoring," *IEEE Transactions on Ultrasonics, Ferroelectrics, and Frequency Control*, vol. 69, no. 11, pp. 3070–3080, 2022.

[187] A.-U. Rehman, C.-K. Jen, and I. Ihara, "Ultrasonic probes for high temperature immersion measurements," *Measurement Science and Technology*, vol. 12, no. 3, p. 306, mar 2001. [Online]. Available: https://dx.doi.org/10.1088/0957-0233/12/3/309

[188] Y. Dong, Q. Yue, D. Cheng, Z. Zhou, R. Liang, and X. Dong, "Ultrasonic transducer with bisco3-pbtio3-based ceramics of operating temperature over 400řc," *Sensors and Actuators A: Physical*, vol. 340, p. 113528, 2022. [Online]. Available: https://www.sciencedirect.com/science/article/pii/S0924424722001662

[189] M. Kobayashi, C.-K. Jen, J. Bussiere, and K.-T. Wu, "High-temperature integrated and flexible ultrasonic transducers for nondestructive testing," *NDT E International*, vol. 42, no. 2, pp. 157–161, 2009. [Online]. Available: https://www.sciencedirect.com/science/article/pii/S0963869508001266

[190] A. Baba, C. T. Searfass, and B. R. Tittmann, "High temperature ultrasonic transducer up to 1000 c using lithium niobate single crystal," *Applied Physics Letters*, vol. 97, no. 23, 2010.

[191] M. H. Amini, A. N. Sinclair, and T. W. Coyle, "High temperature ultrasonic transducer for real-time inspection," *Physics Procedia*, vol. 70, pp. 343–347, 2015, proceedings of the 2015 ICU International Congress on Ultrasonics, Metz, France. [Online]. Available: https://www.sciencedirect.com/science/article/pii/S1875389215008226

[192] S. Bouchy, R. J. Zednik, and P. Belanger, "Ultrasonic transducers for in-service inspection and continuous monitoring in high-temperature environments,"

Sensors, vol. 23, no. 7, 2023. [Online]. Available: https://www.mdpi.com/1424-8220/23/7/3520

[193] D. A. Parks, S. Zhang, and B. R. Tittmann, "High-temperature (> 500/spl deg c) ultrasonic transducers: An experimental comparison among three candidate piezoelectric materials," *IEEE transactions on Ultrasonics, Ferroelectrics, and Frequency control*, vol. 60, no. 5, pp. 1010–1015, 2013.

[194] Y. Du, G. Wu, F. Yu, H. Miao, and X. Zhao, "Beam-focused sh wave transducer based on ysr3(po4)3 piezoelectric crystal for high temperature structural health monitoring," *Journal of Materiomics*, vol. 9, no. 3, pp. 577–586, 2023. [Online]. Available: https://www.sciencedirect.com/science/article/pii/S2352847822001502

[195] B. T. Reinhardt and B. R. Tittmann, "Use of the ferroelectric ceramic bismuth titanate as an ultrasonic transducer for high temperatures and nuclear radiation," *Sensors*, vol. 21, no. 18, 2021. [Online]. Available: https://www.mdpi.com/1424-8220/21/18/6094

[196] K. L. Mcaughey, S. E. Burrows, R. S. Edwards, and S. Dixon, "Investigation into the use of bismuth titanate as a high temperature piezoelectric transducer," in *18th World Conference on Nondestructive Testing*, 2012.

[197] M. H. Amini, A. N. Sinclair, and T. W. Coyle, "Development of a high temperature transducer backing element with porous ceramics," in *2014 IEEE International Ultrasonics Symposium*. IEEE, 2014, pp. 967–970. [Online]. Available: https://doi.org/10.1109/ULTSYM.2014.0237

[198] K. R. Mulligan, N. Quaegebeur, P. Masson, L.-P. Brault, and C. Yang, "Compensation of piezoceramic bonding layer degradation for structural health monitoring," *Structural Health Monitoring*, vol. 13, no. 1, pp. 68–81, 2014.

[199] G. Konstantinidis, B. Drinkwater, and P. Wilcox, "The long term stability of guided wave structural health monitoring systems," in *AIP Conference Proceedings*, vol. 820, no. 1. American Institute of Physics, 2006, pp. 1702–1709.

[200] V. A. Attarian, F. B. Cegla, and P. Cawley, "Long-term stability of guided wave structural health monitoring using distributed adhesively bonded piezoelectric transducers," *Structural Health Monitoring*, vol. 13, no. 3, pp. 265–280, 2014-05-01, publisher: SAGE Publications.

[201] B. Butler, S. Palmer, and G. Primavesi, "Techniques for the generation of ultrasound for extended periods at high temperatures," *Ultrasonics*, vol. 17, no. 6, pp. 249–254, 1979.

[202] M. H. Amini, A. N. Sinclair, and T. W. Coyle, "A new high-temperature ultrasonic transducer for continuous inspection," *IEEE transactions on Ultrasonics, Ferroelectrics, and Frequency control*, vol. 63, no. 3, pp. 448–455, 2016.

[203] N. Bhadwal, M. Torabi Milani, T. Coyle, and A. Sinclair, "Dry coupling of ultrasonic transducer components for high temperature applications," *Sensors*, vol. 19, no. 24, p. 5383, 2019.

[204] A. McNab, K. Kirk, and A. Cochran, "Ultrasonic transducers for high temperature applications," *IEE Proceedings-Science, Measurement and Technology*, vol. 145, no. 5, pp. 229–236, 1998.

[205] P. Wilcox, M. Lowe, and P. Cawley, "Lamb and sh wave transducer arrays for the inspection of large areas of thick plates," in *AIP conference proceedings*, vol. 509, no. 1.　American Institute of Physics, 2000, pp. 1049–1056.

[206] Z. Liu, C. He, B. Wu, X. Wang, and S. Yang, "Circumferential and longitudinal defect detection using t (0, 1) mode excited by thickness shear mode piezoelectric elements," *Ultrasonics*, vol. 44, pp. e1135–e1138, 2006.

[207] A. Kamal and V. Giurgiutiu, "Shear horizontal wave excitation and reception with shear horizontal piezoelectric wafer active sensor (sh-pwas)," *Smart Materials and Structures*, vol. 23, no. 8, p. 085019, 2014.

[208] Q. Huan, M. Chen, and F. Li, "A comparative study of three types shear mode piezoelectric wafers in shear horizontal wave generation and reception," *Sensors*, vol. 18, no. 8, p. 2681, 2018.

[209] G. Boivin, M. Viens, and P. Belanger, "Development of a low frequency shear horizontal piezoelectric transducer for the generation of plane sh waves," vol. 1706, 2016. [Online]. Available: https://doi.org/10.1063/1.4940491

[210] H. Miao, Q. Huan, F. Li, and G. Kang, "A variable-frequency bidirectional shear horizontal (sh) wave transducer based on dual face-shear (d24) piezoelectric wafers," *Ultrasonics*, vol. 89, pp. 13–21, 2018. [Online]. Available: https://doi.org/10.1016/j.ultras.2018.04.010

[211] A. Marzani and S. Salamone, "Numerical prediction and experimental verification of temperature effect on plate waves generated and received by piezoceramic sensors," *Mechanical Systems and Signal Processing*, vol. 30, pp. 204–217, 2012. [Online]. Available: https://www.sciencedirect.com/science/article/pii/S0888327011004547

[212] G. Zhang, "Orientation of piezoelectric crystals and acoustic wave propagation," in *Proceedings of the 2012 COMSOL Conference in Boston, Boston, MA, USA*, 2012, pp. 3–5.

[213] P. N. Bilgunde and L. J. Bond, "Model-assisted approach for probability of detection (pod) in high-temperature ultrasonic nde using low-temperature signals," *Nuclear Technology*, vol. 202, no. 2-3, pp. 161–172, 2018. [Online]. Available: https://doi.org/10.1080/00295450.2017.1419782

[214] T. Meurisse and D. Damjanovic, "Investigating the effects of losses of a piezoelectric transducer in temperature varying environment through finite element analysis," in *2018 IEEE ISAF-FMA-AMF-AMEC-PFM Joint Conference (IFAAP)*, 2018, pp. 1–4.

[215] P. V. Thanh, P. X. Thi, T. Nhung, L. D. Thi, M.-J. Thuy, and N. H. Nhai, "Effect of temperature on ultrasonic velocities, attenuations, reflection and transmission coefficients between motor oil and carbon steel estimated by pulse-echo technique of ultrasonic testing method," 2015. [Online]. Available: https://api.semanticscholar.org/CorpusID:56433064

[216] B. C. Lee and W. J. Staszewski, "Modelling of lamb waves for damage detection in metallic structures: Part ii. wave interactions with damage," *Smart Materials and Structures*, vol. 12, no. 5, p. 815, sep 2003. [Online]. Available: https://dx.doi.org/10.1088/0964-1726/12/5/019

[217] M. E. Mountassir, S. Yaacoubi, G. Mourot, and D. Maquin, "Studies on data correction of structural health monitoring using ultrasonic guided waves: Case of study," *8th European Workshop on Structural Health Monitoring, EWSHM 2016*, vol. 2, pp. 1220–1227, 2016, ISBN: 9781510827936. [Online]. Available: http://www.ndt.net/?id=20150

[218] A. J. Croxford, J. Moll, P. D. Wilcox, and J. E. Michaels, "Efficient temperature compensation strategies for guided wave structural health monitoring," *Ultrasonics*, vol. 50, no. 4, pp. 517–528, 2010-04, ZSCC: 0000363. [Online]. Available: https://linkinghub.elsevier.com/retrieve/pii/S0041624X09001826

[219] T. Clarke, F. Simonetti, and P. Cawley, "Guided wave health monitoring of complex structures by sparse array systems: Influence of temperature changes on performance," *Journal of Sound and Vibration*, vol. 329, no. 12, pp. 2306–2322, 2010.

[220] G. Konstantinidis, B. W. Drinkwater, and P. D. Wilcox, "The temperature stability of guided wave structural health monitoring systems," *Smart*

Materials and Structures, vol. 15, no. 4, p. 967, jun 2006. [Online]. Available: https://dx.doi.org/10.1088/0964-1726/15/4/010

[221] J. B. Harley and J. M. F. Moura, "Scale transform signal processing for optimal ultrasonic temperature compensation," *IEEE Transactions on Ultrasonics, Ferroelectrics, and Frequency Control*, vol. 59, no. 10, pp. 2226–2236, 2012.

[222] S. Mariani, S. Heinlein, and P. Cawley, "Compensation for temperature-dependent phase and velocity of guided wave signals in baseline subtraction for structural health monitoring," *Structural Health Monitoring*, vol. 19, no. 1, pp. 26–47, 2020.

[223] A. C. Douglass and J. B. Harley, "Dynamic Time Warping Temperature Compensation for Guided Wave Structural Health Monitoring," *IEEE Transactions on Ultrasonics, Ferroelectrics, and Frequency Control*, vol. 65, no. 5, pp. 851–861, 2018.

[224] S. Roy, K. Lonkar, V. Janapati, and F.-K. Chang, "A novel physics-based temperature compensation model for structural health monitoring using ultrasonic guided waves," *Structural Health Monitoring: An International Journal*, vol. 13, no. 3, pp. 321–342, 2014-05. [Online]. Available: https://doi.org/10.1177/1475921714522846

[225] J. Moll and C.-P. Fritzen, "Guided waves for autonomous online identification of structural defects under ambient temperature variations," *Journal of Sound and Vibration*, vol. 331, no. 20, pp. 4587–4597, 2012. [Online]. Available: https://www.sciencedirect.com/science/article/pii/S0022460X12003495

[226] N. R. Aditya Chilukuri and K. Balasubramaniam, "In-situ pitting corrosion detection using high-frequency t(0,1) guided wave mode in gas distribution tubes at operating temperatures," *Journal of Structural Integrity and Maintenance*, vol. 6, no. 4, pp. 247–256, 2021. [Online]. Available: https://doi.org/10.1080/24705314.2021.1892573

[227] S. Mariani, S. Heinlein, and P. Cawley, "Location specific temperature compensation of guided wave signals in structural health monitoring," *IEEE Transactions on Ultrasonics, Ferroelectrics, and Frequency Control*, vol. 67, no. 1, pp. 146–157, 2020.

[228] S. Mariani, Y. Liu, and P. Cawley, "Improving sensitivity and coverage of structural health monitoring using bulk ultrasonic waves," *Structural Health Monitoring*, vol. 20, no. 5, pp. 2641–2652, 2021.

[229] S. Mariani and P. Cawley, "Change detection using the generalized likelihood ratio method to improve the sensitivity of guided wave structural health monitoring systems," *Structural Health Monitoring*, vol. 20, no. 6, pp. 3201–3226, 2021.

[230] A. Bagheri, E. Pistone, and P. Rizzo, "Outlier analysis and artificial neural network for the noncontact nondestructive evaluation of immersed plates," *Research in Nondestructive Evaluation*, vol. 26, no. 3, pp. 154–173, 2015-07-03.

[231] M. Gul and F. Necati Catbas, "Statistical pattern recognition for Structural Health Monitoring using time series modeling: Theory and experimental verifications," *Mechanical Systems and Signal Processing*, vol. 23, no. 7, pp. 2192–2204, 2009.

[232] S. Heinlein, "Structural health monitoring of pipes using permanently installed guided wave sensors," Ph.D. dissertation, 2018.

[233] R. Georges Sabat, B. K. Mukherjee, W. Ren, and G. Yang, "Temperature dependence of the complete material coefficients matrix of soft and hard doped piezoelectric lead zirconate titanate ceramics," *Journal of Applied Physics*, vol. 101, no. 6, p. 064111, 03 2007. [Online]. Available: https://doi.org/10.1063/1.2560441

[234] "Comsol multiphysicső software - understand, predict, and optimize," https://www.comsol.com/comsol-multiphysics, (Accessed on 08/26/2023).

[235] F. Moser, L. J. Jacobs, and J. Qu, "Modeling elastic wave propagation in waveguides with the finite element method," *NDT & E International*, vol. 32, no. 4, pp. 225–234, 1999-06-01, 355 citations (Crossref) [2021-11-27]. [Online]. Available: https://www.sciencedirect.com/science/article/pii/S0963869598000450

[236] "Piezoceramic crystals | ebl products," https://eblproducts.com/products/piezoceramic-crystals/, (Accessed on 10/08/2023).

[237] L. B. Silva and E. J. Santos, "Modeling high-resolution down-hole pressure transducer to achieve semi-distributed measurement in oil an d gas production wells," *Journal of Integrated Circuits and Systems*, vol. 14, no. 2, pp. 1–9, 2019.

[238] Soft PZT. [Online]. Available: https://www.ceramtec.com/ceramic-materials/soft-pzt/

[239] "Datasheet soft pz27," https://www.ferropermpiezoceramics.com/wp-content/uploads/2021/10/Datasheet-soft-pz27.pdf, (Accessed on 08/06/2023).

[240] "K-350 - piezoelectric ceramic for hydrophone and accelerometer applications," https://piezotechnologies.com/k350/#:~:text=Piezo%20Technologies'%20K%

2D350%20is,driven%20at%20medium%20power%20levels., (Accessed on 08/06/2023).

[241] "Piezoceramic crystals | ebl products," https://eblproducts.com/?page= piezoceramic-crystals, (Accessed on 08/06/2023).

[242] "Vibrometry products - psv-500-3d scanning vibrometer - polytec," https://www.polytec.com/uk/vibrometry/products/full-field-vibrometers/ psv-500-3d-scanning-vibrometer, (Accessed on 08/26/2023).

[243] C. Desilets, D. Powell, N. Abboud, and G. Wojcik, "Effect of wraparound electrodes on ultrasonic array performance," in *1998 IEEE Ultrasonics Symposium. Proceedings (Cat. No. 98CH36102)*, vol. 2. IEEE, 1998, pp. 993–997.

[244] P. Gerber, A. Roelofs, C. Kügeler, U. Böttger, R. Waser, and K. Prume, "Effects of the top-electrode size on the piezoelectric properties (d33 and s) of lead zirconate titanate thin films," *Journal of applied physics*, vol. 96, no. 5, pp. 2800–2804, 2004.

[245] M. Zennaro, D. J. OBoy, P. S. Lowe, and T.-H. Gan, "Characterization and design improvement of a thickness-shear lead zirconate titanate transducer for low frequency ultrasonic guided wave applications," *Sensors*, vol. 19, no. 8, 2019. [Online]. Available: https://www.mdpi.com/1424-8220/19/8/1848

[246] B. A. Engineer, "The mechanical and resonant behaviour of a dry coupled thickness-shear pzt transducer used for guided wave testing in pipe line," Ph.D. dissertation, Brunel University, 2013.

[247] K. L. Johnson, *Contact mechanics*. Cambridge university press, 1987.

[248] "iperm: Guided wave monitoring tool | iperm | project | fact sheet | h2020 | cordis | european commission," https://cordis.europa.eu/project/id/730648, (Accessed on 10/25/2023).

[249] "iperm: Guided wave pipeline monitoring tool," *Impact*, vol. 2018, no. 9, 2018.

[250] "Integrity assurance ultrasteamline extends high temperature inspection capabilities," https://www.ndt.net/search/docs.php3?id=15234, (Accessed on 10/15/2023).

[251] "70kva heat treatment module - cooperheat heat treatment equipment - stork," https://www.stork.com/en/cooperheat/products/ht-units/70kva-ht-module, (Accessed on 08/06/2023).

[252] "Distance between signals using dynamic time warping - matlab dtw - mathworks united kingdom," https://uk.mathworks.com/help/signal/ref/dtw.html, (Accessed on 10/16/2023).

[253] H. J. Lee, S. Zhang, Y. Bar-Cohen, and S. Sherrit, "High temperature, high power piezoelectric composite transducers," *Sensors (Basel, Switzerland)*, vol. 14, no. 8, pp. 14 526–14 552, 2014-08-08, 89 citations (Crossref) [2021-11-13]. [Online]. Available: https://www.ncbi.nlm.nih.gov/pmc/articles/PMC4179017/

[254] S. W. Gotmare, S. O. Leontsev, and R. E. Eitel, "Thermal degradation and aging of high-temperature piezoelectric ceramics," *Journal of the American Ceramic Society*, vol. 93, no. 7, pp. 1965–1969, 2010-03.

[255] F. Piezoceramics, "High quality components and materials," 2003.

[256] K-Piezo, "K-81," p. 4681, 2011.

[257] P. T. Co, "An overview of the properties of different piezoceramic materials," pp. 3–8, 2012. [Online]. Available: http://www.piezotechnologies.com/knowledge-desk/overview-piezo-materials

[258] Ionix Adcanced Technologies, "HPZ510 Ceramics Datasheet," p. 600, 2014.

[259] High temperature piezoelectric ceramics. [Online]. Available: http://www.trstechnologies.com/Materials/High-Temperature-Piezoelectric-Ceramics

[260] *GaPO4 Material Constants*, Piezocryst Advaced Sensorics GmbH, 2005-11.

[261] P. Davulis, J. Kosinski, and M. P. Da Cunha, "Gapo4 stiffness and piezoelectric constants measurements using the combined thickness excitation and lateral field technique," in *2006 IEEE International Frequency Control Symposium and Exposition*. IEEE, 2006, pp. 664–669.

[262] M. Hamidon, S. Mousavi, M. Isa, A. Ismail, and M. Mahdi, "Finite element method on mass loading effect for gallium phosphate surface acoustic wave resonators," in *Proceedings of the World Congress Engineering*, vol. 1, 2009, pp. 447–452.

[263] A. Zarka, B. Capelle, J. Detaint, D. Palmier, E. Philippot, and O. Zvereva, "Studies of gapo4 crystals and resonators," in *Proceedings of 1996 IEEE International Frequency Control Symposium*. IEEE, 1996, pp. 66–71.

[264] T. Stevenson, D. Martin, P. Cowin, A. Blumfield, A. Bell, T. Comyn, and P. Weaver, "Piezoelectric materials for high temperature transducers and actuators," *Journal of Materials Science: Materials in Electronics*, vol. 26, pp. 9256–9267, 2015.

[265] J. Nosek and M. Pustka, "About the coupling factor of the gallium orthophosphate (gapo/sub 4/) and its influence to the resonance-frequency temperature dependence," in *IEEE International Frequency Control Symposium and PDA Exhibition Jointly with the 17th European Frequency and Time Forum, 2003. Proceedings of the 2003.* IEEE, 2003, pp. 674–678.

[266] "K-15 - high temperature piezoelectric ceramic, high piezoelectric stability," https://piezotechnologies.com/k15/, (Accessed on 10/06/2023).

[267] M. Kobayashi and C.-K. Jen, "Transducers for non-destructive evaluation at high temperatures," in *Ultrasonic Transducers.* Elsevier, 2012, pp. 408–443.

[268] "Properties of macor | morgan technical ceramics," https://www.morgantechnicalceramics.com/en-gb/products/macor-machinable-glass-ceramic/macor-properties/, (Accessed on 09/15/2023).

[269] A. Chaston, "Development of a transducer to be used in long range ultrasonic testing," Ph.D. dissertation, Cardiff University, 2008.

[270] "Almath crucibles ltd | alumina crucibles and refractory ceramics," https://almathcrucibles.com/, (Accessed on 07/29/2023).

[271] "Mineral insulated cable for high voltage at high temperature - engineered thermal products & solutions," https://www.thermocoax.com/mineral-insulated-cable-for-high-voltage-at-high-temperature/, (Accessed on 07/29/2023).

[272] "Tc-08 thermocouple data logger | pico technology," https://www.picotech.com/data-logger/tc-08/thermocouple-data-logger.

[273] "High temperature laboratory oven (lht) - carbolite gero," https://www.carbolite-gero.com/products/ovens/laboratory-ovens/lht/, (Accessed on 10/23/2023).